Distribution Agreement

In presenting this thesis or dissertation as a partial fulfillment of the requirements for an advanced degree from Emory University, I hereby grant to Emory University and its agents the non-exclusive license to archive, make accessible, and display my thesis or dissertation in whole or in part in all forms of media, now or hereafter known, including display on the world wide web. I understand that I may select some access restrictions as part of the online submission of this thesis or dissertation. I retain all ownership rights to the copyright of the thesis or dissertation. I also retain the right to use in future works (such as articles or books) all or part of this thesis or dissertation.

Signature:

_____ _____

Kate K. O'Toole Date

Functional and structural subdomains of the intracellular loop domain of the $GABA_AR$ α1 subunit

By

Kate K. O'Toole
Doctor of Philosophy

Graduate Division of Biological and Biomedical Sciences
Neuroscience

_____
Andrew Jenkins, Ph.D.
Advisor

_____
Ronald Calabrese, Ph.D.
Committee Member

_____
Victor Faundez, Ph.D.
Committee Member

_____
Yoland Smith, Ph.D.
Committee Member

_____
Steve Traynelis, Ph.D.
Committee Member

Accepted:

_____
Lisa A. Tedesco, Ph.D.
Dean of the James T. Laney School of Graduate Studies

_____
Date

Functional and structural subdomains of the intracellular loop domain of the $GABA_AR$ α1 subunit

By

Kate K. O'Toole
B.S., Northern Kentucky University, 2005

Advisor: Andrew Jenkins, Ph.D.

An abstract of
A dissertation submitted to the Faculty of the
James T. Laney School of Graduate Studies of Emory University
in partial fulfillment of the requirements for the degree of
Doctor of Philosophy
Graduate Division of Biological and Biomedical Sciences
Neuroscience

2011

Abstract

Functional and structural subdomains of the intracellular loop domain of the $GABA_AR$ α1 subunit

By Kate K. O'Toole

The $GABA_AR$ functions as a ligand gated ion channel, which permits the flow of anions across the cell membrane, to mediate inhibitory signaling in the central nervous system. To date little is known of the functional importance of the intracellular loop domain of this critical neuronal protein. Recent studies in homologous proteins suggest a role for the intracellular loop domain in controlling the amplitude of channel conductance; therefore, residues within the intracellular loop domain of the $GABA_AR$ α1 subunit were hypothesized to define a portion of the ion channel pore. If charged residues define the permeation pathway, then mutation of integral positions will perturb the electrostatic landscape of the pore to influence ion permeation. First, deletions within the C-terminus of the α1 subunit enhanced the amplitude of macroscopic currents and decreased the apparent affinity of the receptor for GABA, which confirmed that the intracellular loop domain must be intact for proper channel function. Second, a mutagenic screen was conducted of all amino acids harboring ionizable side chains within the intracellular loop domain of the α1 subunit to investigate the functional contribution of individual charged residues. Using whole-cell and single channel voltage clamp recording techniques, charged residues within this domain were shown to control channel gating and anion permeation in a subdomain dependent manner. Third, the importance of the direction of anion flux was investigated. Results showed that currents through the $GABA_AR$ exhibited outward rectification that was inversely related to the open probability of the channel. Finally, secondary structure predictions suggested that the intracellular loop domain is composed of two membrane associated α helices, denoted MA3 and MA4, which are separated by a β strand. Comparison of theoretical and empirical results showed that the predicted functional and structural subdomains overlap. Residues within both MA3 and MA4 control current amplitude and anion permeation, while residues within MA3 determine agonist dependent channel gating and residues within MA4 mediate the rate of desensitization. In sum, these results define the role of the intracellular loop domain in $GABA_AR$ function and expand our knowledge of inhibitory neurotransmission.

Functional and structural subdomains of the intracellular loop domain of the $GABA_AR$ α1 subunit

By

Kate K. O'Toole
B.S., Northern Kentucky University, 2005

Advisor: Andrew Jenkins, Ph.D.

A dissertation submitted to the Faculty of the
James T. Laney School of Graduate Studies of Emory University
in partial fulfillment of the requirements for the degree of
Doctor of Philosophy
Graduate Division of Biological and Biomedical Sciences
Neuroscience

2011

“"The past is not dead, it is living in us, and will be alive in the future which we are now helping to make."”

~William Morris

Table of Contents

Distribution Agreement
Approval Sheet
Abstract Cover Page
Abstract
Cover Page
Dedication
Table of Contents
List of Figures
List of Tables
List of Equations

Chapter 1: Introduction……1
1.1: Overview
1.2: The Pentameric Ligand Gated Ion Channel Superfamily
1.3: The γ-aminobutyric acid type A receptor
    1.3.1: Subunit Diversity
    1.3.2: Structure and Homology Models
    1.3.3: Function
        A: Binding and Gating
        B: Ion Permeation and Selectivity
        C: Trafficking and Phosphorylation
    1.3.4: Clinical Target
        A: Modulation
        B: Dysfunction
1.4: Conclusion

Chapter 2: Experimental Methods and Materials……36
2.1: Overview
2.2: Cell Culture
    2.2.1: HEK293 cells
    2.2.2: Resuscitation of cells
    2.2.3: Preparation of Frozen Stocks
    2.2.4: Passage and Plating
    2.2.5: Vector Expression System
    2.2.6: Mutagenesis
    2.2.7: cDNA Preparation
    2.2.8: Calcium Phosphate Transfection
2.3: Surface Expression
    2.3.1: Confocal Microscopy
    2.3.2: Luminescent Assay
2.4: Electrophysiology
    2.4.1: Solutions

2.4.2: Electrophysiology Circuitry
2.4.3: The Electrophysiology Rig
2.4.4: Achieving the Patch Configurations
2.4.5: The Perfusion System
2.4.6: Whole-Cell Recordings
2.4.7: Whole-Cell Analysis
2.4.8: Single Channel Recordings
2.4.9: Single Channel Analysis
2.5: Statistical Analysis
2.6: Bioinformatics
2.6.1: Sequence Alignment
2.6.2: Secondary Structure Prediction
2.6.3: Homology Model
2.7: Conclusion

Chapter 3: The ILD facilitates channel gating and hinders ion permeation……...81
3.1: Overview
3.2: Introduction
3.3: Results
3.3.1: Deletion of the α1 ILD and C-terminus
3.3.2: Deletion of the α1 ILD did not alter ion selectivity
3.3.3: Truncation of the α1 subunit decreased surface expression
3.4: Discussion
3.4.1: The ILD controls current magnitude
3.4.2: The ILD controls channel gating
3.4.3: The ILD controls ion permeation but not charge selectivity
3.4.4: Which domains are necessary for surface expression?
3.5: Conclusion

Chapter 4: Functional Subdomains of the ILD……...100
4.1: Overview
4.2: Introduction
4.3: Results
4.3.1: Charged residues of the α1 ILD control ion permeation
A: Point mutations increased whole-cell current magnitude
B: Surface expression
C: Single channel currents
D: Ion replacement solutions confirmed anion selectivity of the WT pore
E: Point mutations did not alter charge selectivity
F: Point mutations shifted the relative reversal of anions
4.3.2: Charged residues of the α1 ILD control channel gating
A: ILD charge switch point mutations decreased GABA apparent affinity
B: The α1(K312E) mutation caused a gating impairment
C: ILD charge switch point mutations increased the speed of desensitization

4.4: Discussion
4.4.1: Charge switch mutations revealed functional subdomains of the ILD
A: Defining the Subdomains
B: The MA3 Subdomain
C: The MA4 Subdomain
4.4.2: ILD residues define an anion selectivity filter
4.5: Conclusion

Chapter 5: The $GABA_AR$ exhibits outward rectification at low P_O……..135
5.1: Overview
5.2: Introduction
5.3: Results
5.3.1: Channel gating is voltage dependent
A: Membrane potential determined current magnitude and desensitization
B: IV relationship was dependent on the effective concentration of GABA
C: Asymmetry of currents was independent of Goldman rectification
D: Chloride dependence of gating
5.3.2: Outward rectification of currents occurs at low P_O
A: Extrasynaptic receptors are outwardly rectifying
B: Decreasing P_O enhanced rectification
C: $GABA_AR$ modulation by general anesthetics was voltage dependent
5.3.3: Rectification can be used as a tool to identify ion sensor sites with α1 ILD
5.4: Discussion
5.4.1: Channel open probability is inversely related to degree of outward rectification
A: Rectification is not limited to extrasynaptic $GABA_ARs$
B: P_O modulates degree of rectification
C: The efficacy of drugs that modulate P_O is voltage dependent
5.4.2: Probable causes of rectification
A: Goldman rectification
B: Permeability of chloride
C: Chloride concentration
5.4.3: Gating elements
A: Desensitization
B: Chloride dependence
5.4.4: Ion sensor sites within the permeation pathway
5.4.5: P_O mediated rectification is a universal property of $GABA_ARs$
5.5: Conclusion

Chapter 6: Secondary Structure of the ILD…….179
6.1: Overview
6.2: Introduction
6.3: Results
6.3.1: Sequence alignment revealed conservation of domains
6.3.2: Secondary structure predicted from primary amino acid sequence
6.3.3: Homology model of the α1 subunit
6.4: Discussion
6.5: Conclusion

Chapter 7: Discussion……....202
7.1: Subdomains of the ILD
7.2: Permeation Pathway
7.3: Gating elements
7.4: Conclusion

Appendices……..215
A: Solution Recipes
B: Pipette Programs
C: pClamp Acquisition Parameters
D: Matlab Scripts
E: QuB Protocol

References
Acknowledgements

List of Figures

Chapter 1: General Introduction

Figure 1.1	The $GABA_AR$	3
Figure 1.2	Sequence alignment of pLGIC subunits	4
Figure 1.3	Structure of the extracellular domain	13
Figure 1.4	Protein domain homology	14
Figure 1.5	Canonical rings of charge	22
Figure 1.6	Ion permeation of pLGIC superfamily	23
Figure 1.7	Protein interactions with the ILD	26
Figure 1.8	Phosphorylation of the ILD	27

Chapter 2: Methods

Figure 2.1	Passage and Care of HEK293 cells	42
Figure 2.2	Vector maps of WT constructs	44
Figure 2.3	Immunocytochemistry protocols	50
Figure 2.4	The Confocal Microscope	52
Figure 2.5	Immunocytochemistry controls	54
Figure 2.6	Electronics of compensations	60
Figure 2.7	Whole-cell conductance compensation	63
Figure 2.8	The Rig	66
Figure 2.9	Perfusion controls	68
Figure 2.10	Ramp protocol	70
Figure 2.11	IV relationship is independent of ramp direction	71
Figure 2.12	Ramp protocol verification	72
Figure 2.13	Rectification of currents	74

Chapter 3: The ILD must be intact for proper channel function

Figure 3.1	Putative ion sensor sites	85
Figure 3.2	Deletion constructs	87
Figure 3.3	Concentration response relationships	87
Figure 3.4	Deletion of the α1 ILD enhanced outward rectification	90
Figure 3.5	Truncation of the ILD decreased surface expression	92
Figure 3.6	Quantification of confocal images	93

Chapter 4: Charge switch mutations reveal subdomains

Figure 4.1	Charge switch mutations	102
Figure 4.2	Concentration-response relationships for mutations	104
Figure 4.3	Surface expression of charge switch mutations	109
Figure 4.4	Single channel currents of charge switch mutations	109
Figure 4.5	α1(K378E) decreased chord conductance	110
Figure 4.6	$GABA_AR$ ion channel is anion permeable	112
Figure 4.7	$GABA_AR$ ion channel is cation impermeable	113
Figure 4.8	Mutations did not change charge selectivity of the pore	115
Figure 4.9	Mutations decreased relative anion permeability	118
Figure 4.10	Subdomain dependence of permeability	120
Figure 4.11	α1(K312E) decreased relative partial agonist efficacy	125
Figure 4.12	Charge-switches increased speed of desensitization	127
Figure 4.13	Sequence alignment of synaptic $GABA_AR$ α subunits	129
Figure 4.14	Subdomains of the α1 ILD	130

Chapter 5: Inverse relationship between outward rectification and low open probability

Figure 5.1	Desensitization was faster in outward currents	143
Figure 5.2	Rectification profile for WT $GABA_AR$	145
Figure 5.3	Rectification Index values	146
Figure 5.4	Goldman rectification in altered ionic gradients	148
Figure 5.5	Chloride dependence of concentration-response relationship	151
Figure 5.6	Chloride dependence is independent of driving force	152
Figure 5.7	Incorporation of the γ subunit decreased rectification	155
Figure 5.8	Outward rectification was enhanced at low P_O	157
Figure 5.9	Impaired gating enhanced outward rectification	158
Figure 5.10	Rectification profile for positive allosteric modulators	160
Figure 5.11	Degree of potentiation was voltage dependent	160
Figure 5.12	Rectification profile for the α1(D318K) mutation	163
Figure 5.13	Rectification profile for the α1(D356K) mutation	164
Figure 5.14	Rectification profile for the α1(K374E) mutation	165
Figure 5.15	Theoretical IV relationships when P_{Cl} is not constant	173
Figure 5.16	Chloride permeability was not constant at low P_O	173

Chapter 6: Structural predictions of the ILD

Figure 6.1	Phylogeny of $GABA_AR$ subunits	184
Figure 6.2	Sequence alignment of $GABA_AR$ subunits	186
Figure 6.3	Evolutionary relatedness of $GABA_AR$ domains	188
Figure 6.4	Chou-Fasman predictions of α1 ILD secondary structure	190
Figure 6.5	Jnet secondary structure prediction	191
Figure 6.6	SwissModel homology model of α1 subunit	195
Figure 6.7	Rotated views of putative ILD structure	195
Figure 6.8	Structural subdomains of the ILD	196
Figure 6.9	Summary of secondary structure predictions	200
Figure 6.10	Composite homology model	200

Chapter 7: Discussion

Figure 7.1	Functional and structural subdomains	203
Figure 7.2	Location of integral charged residues	204
Figure 7.3	A putative desensitization gate	210
Figure 7.4	Chloride ions stabilize the open state	212

List of Tables

Table 1.1	Properties and neural expression of common subunits	8
Table 1.2	Genetic mutations that affect expression or function of $GABA_AR$	33
Table 2.1	Mutagenic primers	47
Table 2.2	Physiological solutions	57
Table 2.3	Theoretical reversal potential and junction potential values	57
Table 3.1	Hill fit parameters of deletion/truncation constructs	88
Table 3.2	IV relationship metrics for deletion constructs	88
Table 4.1	Hill fit parameters of charge switch mutations	106
Table 4.2	Single channel properties of charge switch mutations	110
Table 4.3	Reversal potential values for charge switch mutations	121
Table 4.4	Relative shifts in reversal potential	122
Table 5.1	Rectification profile of GABA-elicited currents in WT receptors	146
Table 5.2	IV relationship metrics for low P_O conditions	149
Table 5.3	IV relationship metrics in altered ionic gradients	154
Table 5.4	Rectification profile parameters for charge switch mutations	162
Table 6.1	$GABA_AR$ gene loci	185
Table 6.2	Pairwise comparison of nAChR and $GABA_AR$ subunits	194

List of Equations

Equation 1	Primer melting temperature	45
Equation 2	Whole-cell currents	55
Equation 3	Nernst Equation	58
Equation 4	Ohm's Law	59
Equation 5	Change in command potential	61
Equation 6	Hill Equation	73
Equation 7	Desensitization constant	73
Equation 8	GHK Voltage Equation	73
Equation 9	Rectification Index	74
Equation 10	GHK Current Equation	74
Equation 11	Normalized means	76

Chapter 1

Introduction

1.1: Overview

The homeostatic balance between excitatory and inhibitory inputs is critical to maintain dynamic brain function. If the balance is tipped in either direction, by pharmacologic manipulation or dysfunctions related to disease, neurons lose the ability to respond to stimuli. Soporific states under excess inhibition or epileptic seizures typical of excess excitation are detrimental to organism survival. The γ-aminobutyric acid type A receptor ($GABA_AR$) mediates inhibitory neurotransmission and is therefore a critical clinical target. Full understanding of $GABA_AR$ function is imperative to the study of neuronal activity and the treatment of neural disorders.

The goal of this dissertation work is to determine the contribution of the intracellular loop domain to $GABA_AR$ function. The mature receptor is a complex of five subunits arranged around a central pore (Fig. 1.1A). Each subunit contains three modular protein domains: the extracellular, transmembrane, and intracellular loop domains (Fig. 1.1B). If the central pore of the ion channel extends beyond the plasma membrane into the cytoplasmic space, then charged amino acids of the intracellular loop domain are predicted to make electrostatic interactions with ions to control the permeability of the pore. To test this hypothesis, I measured *in vitro* ion channel activity in transfected mammalian cultured cells via whole-cell and single channel voltage clamp electrophysiology. Site-directed mutagenesis was used to define the function of specific charged residues within the α1 intracellular loop domain. Finally, I used *in silico* prediction methods to determine the structure of the $GABA_AR$ α1 subunit to provide a backbone for functional relationships. The findings presented in this dissertation will show that the $GABA_AR$ α1 intracellular loop domain is necessary for and integral to ion channel function. Furthermore, results will identify the specific charged residues within the α1 intracellular loop

domain that control $GABA_AR$ activity. In this chapter I will describe the structure, function and dysfunction of the $GABA_AR$ and highlight the knowledge gaps that will be filled by my dissertation studies.

1.2: The Pentameric Ligand Gated Ion Channel Superfamily

The $GABA_AR$ is a member of the Cys-loop family of pentameric ligand gated ion channels (pLGIC). This superfamily of proteins is expressed ubiquitously throughout the nervous system and is essential for neural signaling. The primary function of ligand gated ion channels is to translate a chemical message to an electrical output by fluxing ions when active. In particular, pLGICs are permeable to either cations or anions (Keramidas, Moorhouse et al. 2004; Jensen, Schousboe et al. 2005). Cation permeable members of the pLGIC superfamily include the ionotropic serotonin receptor ($5\text{-}HT_3R$) and the nicotinic acetylcholine receptor (nAChR); anion permeable channels include the glycine receptor (GlyR) and $GABA_AR$.

Studies across the pLGIC superfamily allow for parallel comparisons to be made within this genetically related class of proteins. Protein homologs are believed to have diverged from a common evolutionary origin because they perform similar functions and have robust primary sequence conservation. Furthermore, proteins that share function through homology have been shown to have conserved structures (Baker and Sali 2001; Lee, Redfern et al. 2007).

Alignment of primary sequences from *Homo sapiens* revealed regions of strong amino acid conservation among pLGIC α subunits (Fig. 1.2). The extracellular domain and transmembrane domain were highly conserved across all the subunits in the alignment, but the intracellular loop domain showed poor primary sequence conservation (Fig. 1.2). The intracellular loop domain is the most variable domain both in terms of sequence length and side chain identity. Therefore, the lack of primary sequence conservation within the intracellular loop

domain imparts a unique disadvantage to parallel comparison. Without sequence conservation it is difficult to make direct positional comparisons to predict function through homology especially between cationic and anionic channels. Although it is tempting to infer similar intracellular loop domain function across the members of the pLGIC superfamily due to conserved function in other domains, direct analysis of each receptor class and each subunit type is necessary. Furthermore, the diversity of the intracellular loop domain may in fact confer unique function to these otherwise highly-related proteins. Therefore, the focus of my dissertation studies is to characterize the intracellular loop domain of the $GABA_AR$ α1 subunit, in particular, in order to identify a functional role for this domain.

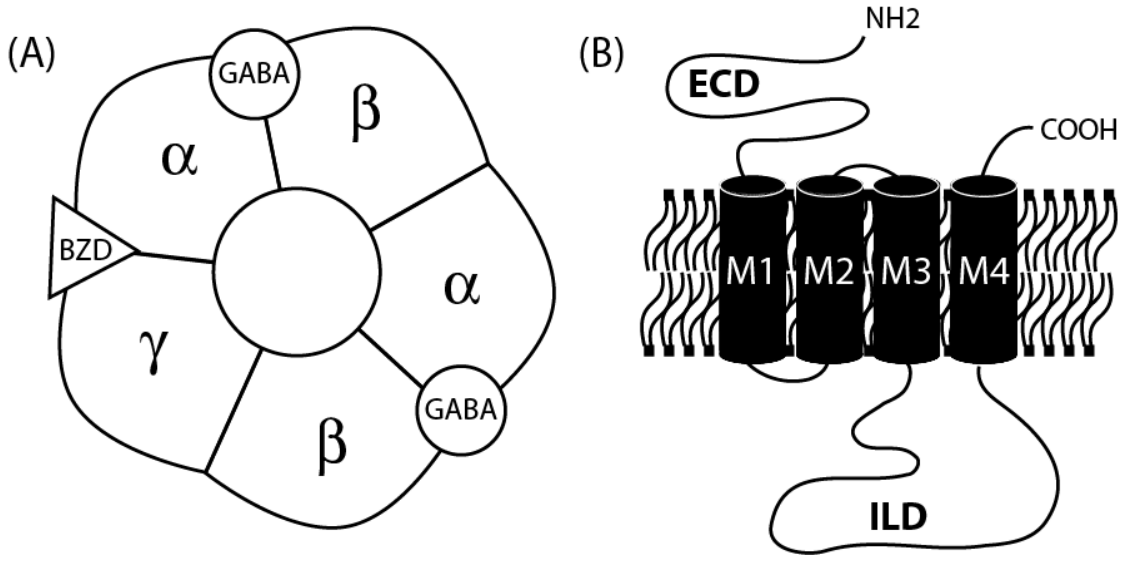

Figure 1.1: The $GABA_AR$. (A) Top down view of five subunits that form the channel depicting the α-β-α-β-γ orientation about the central pore. Binding sites for γ-aminobutyric acid (GABA, circle) and benzodiazepines (BZD, triangle) are indicated. (B) Membrane topography of a single subunit. Both the N-terminus and C-terminus are extracellular. Each subunit is modular with an extracellular domain (ECD), a transmembrane domain comprised of four segments (M1-M4), and an intracellular loop domain (ILD).

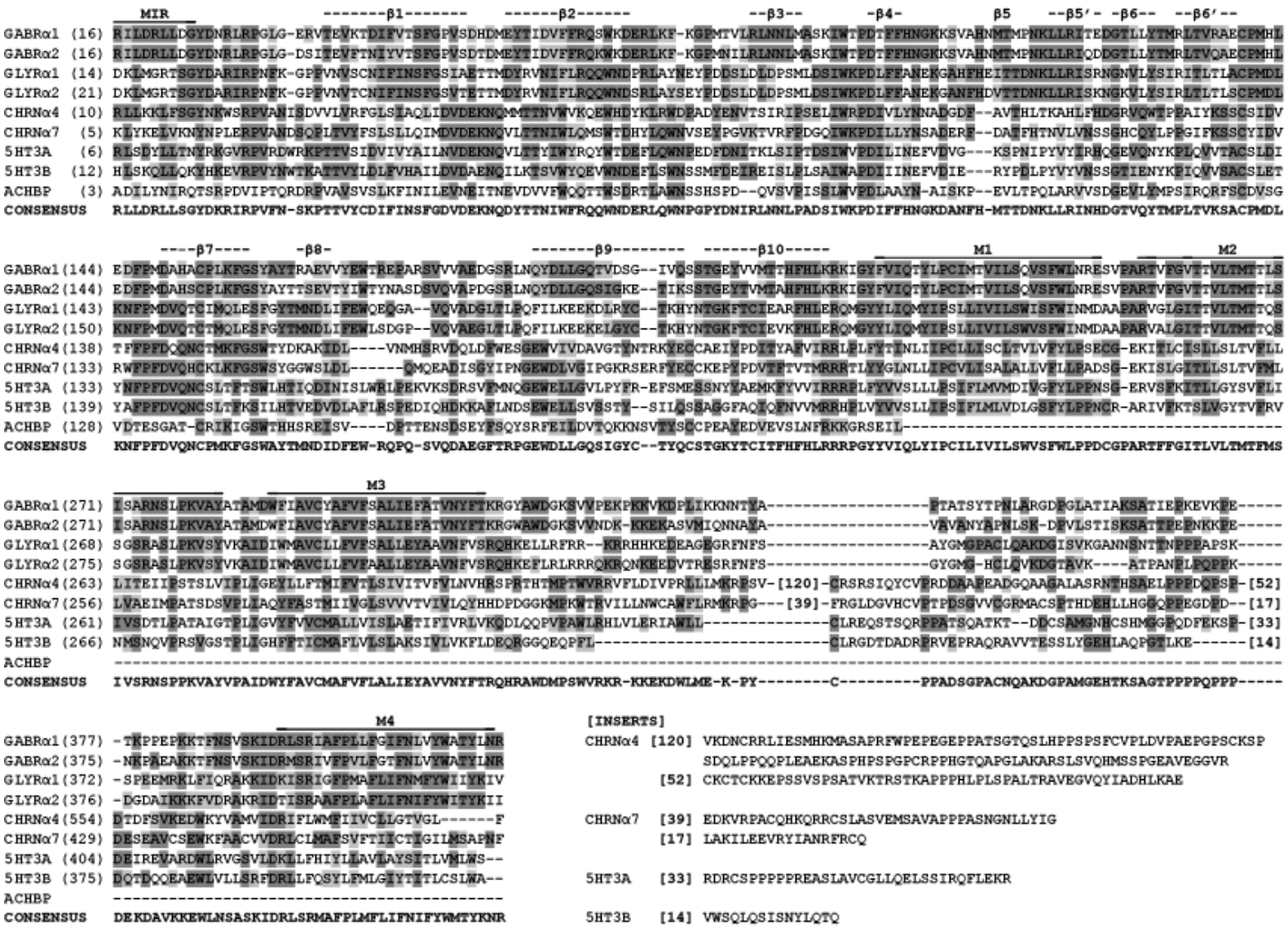
MIR
β1
β2
β3
β4
β5
β5'
β6
β6'
β7
β8
β9
β10
M1
M2
M3
M4
[INSERTS]
CHRNα4 [120] VKDNCRRLIESMHKMASAPRFWPEPEGEPPATSGTQSLHPPSPSFCVPLDVPAEPGPSCKSP
SDQLPPQQPLEAEKASPHPSPGPCRPPHGTQAPGLAKARSLSVQHMSSPGEAVEGGVR
[52] CKCTCKKEPSSVSPSATVKTRSTKAPPPHLPLSPALTRAVEGVQYIADHLKAE
CHRNα7 [39] EDKVRPACQHKQRRCSLASVEMSAVAPPPASNGNLLYIG
[17] LAKILEEVRYIANRFRCQ
5HT3A [33] RDRCSPPPPPREASLAVCGLLQELSSIRQFLEKR
5HT3B [14] VWSQLQSISNYLQTQ

Figure 1.2: Sequence alignment of pLGIC subunits. [Previous page] The *multialign* function in the Bioinformatics toolbox for Matlab was used to generate alignments of primary amino acid sequences. Round brackets (#) give the sequence number and square brackets [#] represent the number of residues that are not shown in the main alignment. Dark grey background shows residues with 100% identity to the consensus sequence and light grey background marks residues that share side-chain property conservation. The predicted secondary structure of the $GABA_AR$ is shown above the alignment for α helices (underlined) and β strands (dashed). The structure of the extracellular domain for the $GABA_AR$ was predicted by Cromer et al., (2005) from comparison to the AChBP structure (PDB ID: 1I9B) to define the residues within the N-terminal α helix (MIR) and β strands (β1-10). The location of the four transmembrane domains (M1-M4) was predicted by Bertaccini and Trudell (2002) from comparison of 10 topology predictions. The extracellular domain and transmembrane domain retained a high degree of primary sequence conservation despite having pores with opposite charge selectivity. The intracellular loop domain showed the most variability both in terms of residues identity and sequence length.

Accession numbers: *GABRα1, NP_000797; GABRα2, NP_000798; GLYRα1, NP_000162; GLYRα2, NP_001112357; CHRNα4, NP_000735; CHRNα7, NP_000737; 5HT3A, NP_000860; 5HT3B, NP_006019; ACHBP, P58154.*

1.3: The γ-aminobutyric acid type A receptor

Upon stimulus, pre-synaptic axon terminals release the neurotransmitter γ-aminobutyric acid (GABA) and $GABA_A$Rs on the post-synaptic cell membrane bind the small molecule, which is also known as a ligand. Ligand binding serves to open the channel gate and allow ions to flow across the postsynaptic membrane. The $GABA_A$R is selectively permeable to anions, chloride in particular; in the adult brain, the extracellular concentration of chloride is greater than the intracellular concentration (Martin and Olsen 2000). Thus, the activated ion channel facilitates chloride influx, which hyperpolarizes the cell membrane to inhibit neurotransmission. The chloride gradient may be switched early in development and in some disease conditions so that GABAergic signals are excitatory (Olsen and Sieghart 2008).

1.3.1: Subunit Diversity

To date there are 16 subunits that combine to form functional $GABA_A$Rs: α1-6, β1-3, γ1-3, δ, ε, π, and θ (Martin and Olsen 2000; Olsen and Sieghart 2008). Most commonly, the $GABA_A$R includes two copies of the α1 subunit, two copies of the β2 subunit and one copy of the γ2 subunit arranged in a α-β-α-β-γ orientation about the pore (McKernan and Whiting 1996) (Fig. 1.1A, Table 1.1). Therefore, the studies presented in this dissertation will focus on the α1β2γ2 receptor. Each subunit confers unique pharmacology and kinetics to the pentamer and each has a unique expression pattern in the brain to generate complex GABAergic signaling (Table 1.1). Studies have used *in situ* mRNA hybridization (Laurie, Seeburg et al. 1992; Wisden, Laurie et al. 1992) and immunoreactivity (Fritschy and Mohler 1995; Pirker, Schwarzer et al. 2000) to determine the distribution of the $GABA_A$R subunits. The α1 subunit is expressed highly throughout the brain (Wisden, Laurie et al. 1992; Fritschy and Mohler 1995). The α2 and α3 subunits are also found throughout the brain, but to a lesser degree than α1; in contrast, the α4, α5, and α6 subunits have a more restricted expression pattern and are primarily concentrated in the hippocampus, thalamus, and cerebellum structures respectively (Pirker, Schwarzer et al.

2000). The β2 and γ2 subunits are also expressed ubiquitously and have the highest expression of their respective subunit classes (Wisden, Laurie et al. 1992). A combination of electrophysiology, pharmacology and electron microscopy experiments have shown that the α1-3 subunits are primarily expressed at the synapse and the α4-6 subunits are expressed extrasynaptically (Nusser, Sieghart et al. 1998; Mody 2001; Galvan, Kuwajima et al. 2006; Mortensen and Smart 2006). The γ2 subunit targets the $GABA_AR$ to the synapse through an interaction with the scaffold protein gephyrin; mice deficient for these proteins exhibit decreased synaptic clustering of $GABA_ARs$ (Essrich, Lorez et al. 1998; Kneussel, Brandstatter et al. 1999).

Recombinant studies showed that $GABA_AR$ subunits have the ability to confer distinct properties to the heteromeric receptor (McKernan and Whiting 1996; Lavoie, Tingey et al. 1997; Martin and Olsen 2000; Teissere and Czajkowski 2001; Picton and Fisher 2007; Mortensen, Ebert et al. 2010); in particular, each of the six α subunits confers a unique sensitivity to GABA (Table 1.1) and distinct kinetics to the receptor (Lavoie, Tingey et al. 1997; Picton and Fisher 2007). The synaptic subunits, α1-3, have a lower affinity for GABA than the extrasynaptic subunits, α4-6, when expressed with the same β and γ subunits in cultured cells (Lavoie, Tingey et al. 1997; Picton and Fisher 2007). Extrasynaptic α subunits confer a high affinity for GABA to permit activation by ambient or spillover concentrations of the neurotransmitter (Mody 2001). The α1 and α2 subunits confer similar kinetics with fast activation and desensitization times; whereas the α3 subunit shows slow transition rates (Picton and Fisher 2007). The extrasynaptic α subunits activate at a moderate rate and differ in their deactivation and desensitization rates; α4 shows fast deactivation and desensitization, the α5 subunit shows fast deactivation and slow desensitization, and the α6 subunit shows slow deactivation and fast desensitization (Picton and Fisher 2007).

Subunits[a]	Percent[a]	Location[a,b]	GABA EC_{50} (μM)
α1β2γ2	43	Synaptic HIP/CTX: Interneurons Purkinje cells	3-17[c] ~20[d]
α2β2/3γ2	18	Spinal cord: Motor neurons HIP: Pyramidal cells	~20[d]
α2βγ1	8	Limbic system, Pancreas, Glia	
α3βγ2/3	17	ACh/MA neurons	~35[d]
α4βδ	3	Thalamus, DG	0.5[c] ~10[d]
α5β3γ2/3	4	Extrasynaptic HIP: Pyramidal cells	11-19[c] ~10[d]
α6βγ2 α6ββδ	2 2	Cerebellar granule cells	~2[d]

[a] McKernan and Whiting, 1996
[b] Martin and Olsen, 2000
[c] Mortensen and Smart, 2006
[d] Picton and Fisher, 2007

Table 1.1: Properties and neural expression of common subunits. The $GABA_AR$ is expressed ubiquitously throughout the brain and may be comprised of a variety of modular subunits which confer unique channel kinetics and pharmacology. The relative percent of each subunit combination found in the rat brain was determined by *in situ* mRNA hybridization and immunoreactivity. GABA apparent affinity values (EC_{50}) refer only to the α subunit. *Table was adapted from (McKernan and Whiting 1996).*

Abbreviations: *ACh, acetylcholine; CTX, cortex; DG, dentate gyrus; HIP, hippocampus; MA, monoamine.*

1.3.2: Structure and Homology Models

Specific domains within the mature protein control each aspect of function to translate the energy of ligand binding to open the channel gate and permit the flow of ions across the post-synaptic membrane. Understanding of the structure of the $GABA_AR$ gives further insight into channel function. Several structures of pLGICs and homologous proteins have been resolved and provide a backbone for making predictions of the structure for the $GABA_AR$ specifically (Unwin 1993; Brejc, van Dijk et al. 2001; Cromer, Morton et al. 2002; Unwin 2005; Bocquet, Nury et al. 2009; Hilf and Dutzler 2009; Corringer, Baaden et al. 2010).

High-resolution structural information for the extracellular domain came from the structure of the homologous acetylcholine binding protein of *Lymnaea stagnalis* (AChBP, Protein Data Bank Accession number (PDB ID): 1I9B; Fig. 1.3, Fig. 1.4A) (Brejc et al., 2001). The AChBP shares primary sequence homology with the extracellular domain of pLGICs (Fig. 1.2). The AChBP amino acid sequence is 25% identical and 52% similar to the $GABA_AR$ α1 subunit, shown by pairwise alignment with the Needleman-Wunsch algorithm (*nwalign* in the Matlab bioinformatics toolbox). Therefore, we can surmise that the extracellular domain of the $GABA_AR$ is structurally homologous to AChBP and is comprised of an N-terminal α helix and ten β strands that are arranged in a β sandwich tertiary structure (Fig. 1.3, Fig. 1.4A).

Finer-Moore and Stroud (1984) proposed that the transmembrane domain segments would have α helical secondary structure and that the central pore of the ion channel would be lined by an amphipathic helix, in which the hydrophilic amino acids face the aqueous pore lumen and the hydrophobic side chains face towards the surrounding lipid environment of the membrane. Bioinformatic analysis of the primary sequence of the nAChR α, β, γ, and δ subunits from *Torpedo californica* suggested a long amphipathic helix and four shorter transmembrane helices; five transmembrane segments predicts an intracellular C-terminus (Finer-Moore and

Stroud 1984). Subsequent analysis refuted this prediction; Ratnam et al. (1986) generated specific antibodies to segments of the nAChR α subunit and showed that the C-terminus was on the extracellular face of the membrane and that the amphipathic helix did not transverse the membrane.

A more complete understanding of the structure of pLGICs has been determined from study of electron micrograph images of nAChR-rich post synaptic membranes from the electric ray, *T. californica* (Unwin 1993; Unwin 1998; Unwin 2000; Unwin 2005) (Fig. 1.4C). Resolution of the nAChR at 9 Å confirmed a pentameric assembly about the central axis. This structure also identified that the pore-lining α helix was kinked to block the pore, presumably at the level of the gate (Unwin 1993). Comparison of receptor structures in the presence (open) and absence (closed) of acetylcholine revealed a rotational conformation change that alleviated the block, which would allow ion flow through the pore (Unwin 1998; Uwin 2000). Resolution of the nAChR at 4 Å (PDB ID: 2BG9) confirmed that the transmembrane domain contained four α helices (M1-M4) and the central pore was lined by M2 (Unwin 2005; Fig. 1.4C). The four transmembrane segments are connected by loops, the M1-2 and M2-3 loops are merely short linkers of 4 and 5 residues respectively, whereas the M3-4 loop is large and variable; in this dissertation the M3-4 loop is referred to as the intracellular loop domain. This seminal work also revealed a partial structure of the intracellular loop domain with an amphipathic membrane associated α helix continuous with M4 (Unwin 2005; Fig. 1.4C). The membrane associated α helix of each subunit forms an intracellular vestibule, closed at the base to prevent direct ion flow, but with lateral apertures approximately the size of a hydrated ion, which define an obligatory path for ion permeation (Unwin 2005).

To date, there is no high-resolution structural information for the $GABA_AR$, but the structures of homologous proteins have provided template coordinates for building homology

models of the receptor (Cromer, Morton et al. 2002; Trudell and Bertaccini 2004; Mokrab, Bavro et al. 2007). The AChBP structure was used as a homology model template to study ligand binding within the orthosteric (GABA) and allosteric (benzodiazepine) sites of the $GABA_AR$ extracellular domain (Cromer et al., 2002) (Fig. 1.1A). The extracellular domain and transmembrane domain of the $GABA_AR$ were first modeled together by Trudell and Bertaccini (2004) from comparison of three crystal structures. As in earlier studies, the AChBP structure served as a template for the extracellular domain. Two structures were used to model the transmembrane domain; a four α helical bundle within the bovine cytochrome c oxidase structure (PDB ID: 2OCC) was used as the template for the transmembrane domain of each subunit and the central pore-forming α helices were modeled after a pentameric bacterial mechanosensitive channel (PDB ID: 1MSL). The specific M2 residues that line the pore lumen have been verified for the $GABA_AR$ by mutating each residue to cysteine and assessing the accessibility of the side chain with polar sulfhydrl reactive agents (Xu and Akabas 1993; Xu and Akabas 1996). The sulfhydrl reactive agents covalently bond to the thiol side chain of cysteine to modify channel activity and the polar reagents were predicted to only be accessible to side chains facing into the water filled pore lumen. More recently, a homology model of the $GABA_AR$ based on the nAChR structure was used to calculate the interaction energy of ion flow (Mokrab, Bavro et al. 2007). Due to poor sequence conservation, the $GABA_AR$ residues comprising the intracellular membrane associated segment were manually assigned. Nonetheless, model analysis predicted large differences in ion permeation through each intracellular portal (Mokrab, Bavro et al. 2007) which suggests that intracellular loop domain control of conductance may be subunit-specific for the heteromeric receptor. Specific analysis of $GABA_AR$ intracellular loop domain residues, such as the experiments undertaken in this dissertation, will inform future model building efforts by identifying the residues that contribute to ion permeation and, therefore, must be accessible to permeant ions in modeled structures.

In the past few years, several structures of prokaryotic homologs in the pLGIC superfamily have been solved (Hilf and Dutzler 2008; Bocquet, Nury et al. 2009; Corringer, Baaden et al. 2010). The homolog from the cyanobacterium *Gloebacter violaceus* (GLIC) has been shown to be proton gated and was crystallized in acidic conditions to yield the open conformation (Bocquet, Prado de Carvalho et al. 2007; Bocquet, Nury et al. 2009) Fig. 1.4B). A closed structure was refined of the pLGIC homolog from the plant pathogen *Erwinia chrysanthemi* (ELIC; (Hilf and Dutzler 2008). Intriguingly, ELIC has been shown to be gated by primary amines, including GABA (Zimmermann and Dutzler 2011). GLIC has recently been used as a substrate to understand receptor modulation by general anesthetics (Nury, Van Renterghem et al. 2011) and ethanol (Howard, Murail et al. 2011). These experiments emphasize the power of combining functional and structural information to fully understand pLGIC activity. The structural information for the intracellular loop domain within these structures, however, remains incomplete. ELIC and GLIC do not contain an intracellular loop domain; rather M3 and M4 are connected by a short linker, less than 10 residues long. Therefore, in my dissertation studies I have used bioinformatics to predict the secondary structure of the $GABA_AR$ α1 subunit in order to provide a structural backbone for my empirical findings.

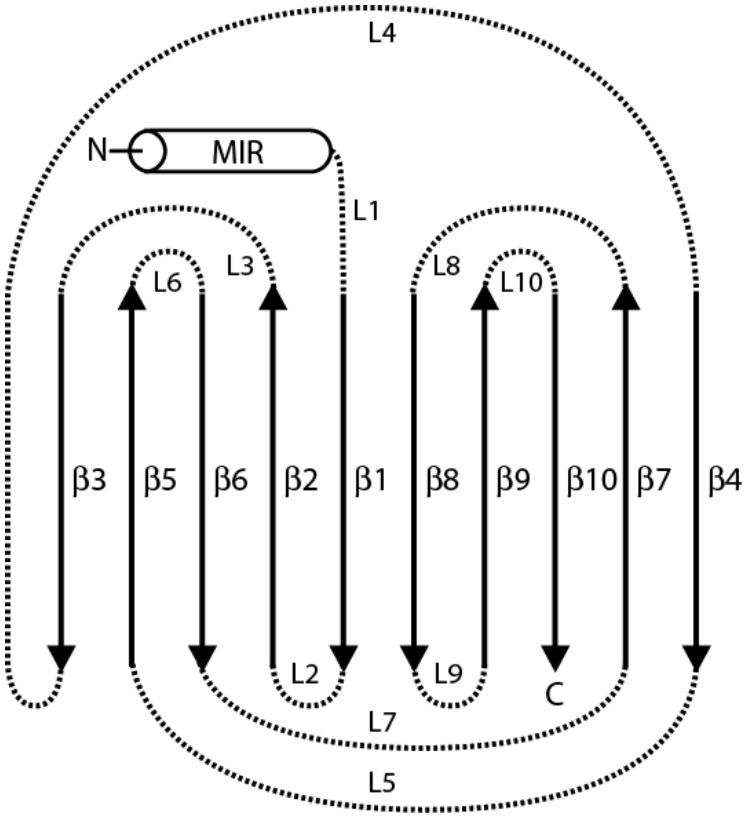

Figure 1.3. Structure of the extracellular domain. Greek key schematic of extracellular domain based on the structure of the *L. stagnalis* AChBP (PDB ID: 1I9B). Relative location of N-terminal α helix (MIR), ten β strands (β1-10), and ten loops (L1-10) within the primary amino acid sequence is indicated. Arrows indicate the location and direction of β strands, the α helix is shown as a cylinder, and dotted lines depict loops. The N-terminus and C-terminus are labeled with N and C respectively. *Adapted from (Brejc, van Dijk et al. 2001).*

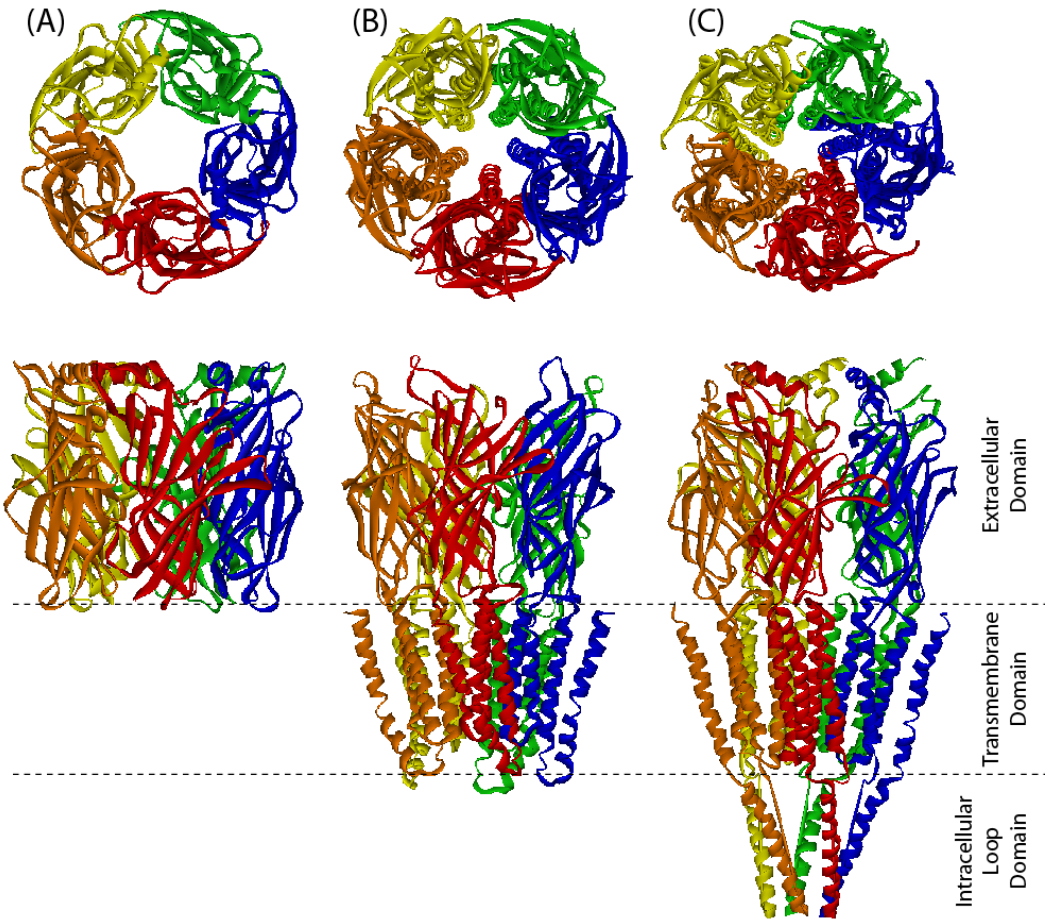

Figure 1.4: Protein domain homology. Top down [top panel] and side views [lower panel] of structures for the (A) *L. stagnalis* AChBP (PDB ID: 1I9B), (B) *G. violaceus* pLGIC (PDB ID: 3EHZ), and (C) *T. californica* nAChR (PDB ID: 29BG). The pentameric quaternary structure is preserved in all three structures. The modular nature of proteins is highlighted by the three discrete domains: Extracellular Domain, Transmembrane Domain, and Intracellular Loop Domain.

1.3.3: Function

1.3.3A: Binding and Gating

Within the pLGIC superfamily the major determinates of ligand binding and channel gating are controlled by residues within the extracellular domain and the transmembrane domain. The GABA binding site resides at extracellular domain interfaces between the α1 and β2 subunits (Fig. 1.1A) (Sigel, Baur et al. 1992; Amin and Weiss 1993; Smith and Olsen 1994; Westh-Hansen, Rasmussen et al. 1997; Boileau, Evers et al. 1999; Westh-Hansen, Witt et al. 1999; Wagner and Czajkowski 2001; Boileau, Newell et al. 2002). The pre-M1 segment, M2-3 linker, and loops 2 and 7 at the interface of the extracellular domain and transmembrane domain within each subunit are regions critical to gating (O'Shea and Harrison 2000; Kash, Jenkins et al. 2003; Kash, Trudell et al. 2004; Xiu, Hanek et al. 2005; Keramidas, Kash et al. 2006; Mercado and Czajkowski 2006).

Site-directed mutagenesis studies (Sigel, Baur et al. 1992; Amin and Weiss 1993; Smith and Olsen 1994; Westh-Hansen, Rasmussen et al. 1997; Westh-Hansen, Witt et al. 1999) and cysteine modification methods (Boileau, Evers et al. 1999; Wagner and Czajkowski 2001; Boileau, Newell et al. 2002) highlighted the residues that define the GABA binding site. The α1(F64) position controls GABA binding shown with photoaffinity labeling and confirmed by site-directed mutagenesis (Sigel, Baur et al. 1992; Smith and Olsen 1994). A systematic mutagenesis study of the extracellular domain identified four residues in the β2 subunit that define the agonist binding site: β2(Y157), β2(T160), β2(T202), and β2(Y205); even conservative point mutations, from threonine to serine and from tyrosine to phenylalanine, induced large, over 50-fold shifts in GABA affinity (Amin and Weiss 1993). A naturally occurring point mutation, α1(I120V), and conservative mutation of the neighboring position, α1(R119K), caused ten to two hundred fold decreases in GABA apparent affinity (Westh-Hansen, Rasmussen et al. 1997; Westh-Hansen, Witt et al. 1999). Finally, the Czajkowski group identified the remaining residues

that define the GABA binding site with the substituted cysteine accessibility method: α1(R66), α1(S68), β2(Y97), β2(L99), β2(S204), β2(R207), and β2(S209) (Boileau, Evers et al. 1999; Wagner and Czajkowski 2001; Boileau, Newell et al. 2002). Residues were systematically mutated to cysteine and then positions that were protected from covalent modification by thiol reactive agents with GABA application were predicted to control agonist binding. Through these studies, residues from both the α1 and β2 subunits were shown to define the orthosteric ligand binding site of the $GABA_AR$.

Several distinct structures within the extracellular domain and transmembrane domain interface are integral for translating ligand binding to channel gating in the $GABA_AR$; reviewed in (Kash, Trudell et al. 2004) and (Xiu, Hanek et al. 2005). The M2-3 linker was first implicated in pLGIC gating from genetic analysis of families with hyperekplexia, a disease in which patients exhibit a pronounced startle response; mutations were shown to decrease agonist efficacy but not antagonist binding in the GlyR (Shiang, Ryan et al. 1993; Langosch, Laube et al. 1994). Decreased agonist efficacy may be due to impaired binding or gating, but normal antagonist binding indicates that the binding site is unperturbed. Mutations within the M2-3 linker therefore most likely impair channel gating. Furthermore, a mutation within the M2-3 linker of the $GABA_AR$ γ2 subunit causes epilepsy by decreasing the magnitude of GABAergic currents (Baulac, Huberfeld et al. 2001), which is also indicative of a gating impairment (Table 1.2). These diseases, hyperekplexia and epilepsy, are prime examples of how an impairment in inhibitory signaling can tip the homeostatic balance to cause detrimental levels of excitation.

It is experimentally very difficult to tease apart the different contributions of binding and gating to channel efficacy because these properties are intrinsically linked, but comparison of the efficacy of two agonists provides an opportunity to address this issue (Colquhoun 1998). If we consider two agonists that have equivalent binding, but differing efficacies, a gating impairment

is predicted to hamper the ability of each agonist to gate the channel, but the relative binding affinity of each would remain the same; therefore relative agonist efficacy values would be different between the native and impaired receptor (Colquhoun 1998). Full and partial agonists bind at the orthosteric site, but have different efficacy in gating the channel. In recombinant receptors, alanine substitutions in the M2-3 linker of the $GABA_AR$ α2 subunit decreased the sensitivity of the receptor for GABA and also decreased the relative efficacy of the partial agonist, piperidine-4-sulfonic acid (P4S), indicative of a gating impairment ((O'Shea and Harrison 2000). The M2-3 linker mediates gating through electrostatic interactions with loop 2 and loop 7 of the extracellular domain (Kash, Jenkins et al. 2003). From comparison of the AChBP structure and primary sequence alignment with the $GABA_AR$ subunits, Kash and Jenkins et al., (2003) identified conserved acidic residues within loops 2 and 7 that were predicted to interact with the basic residues of the M2-3 linker previously implicated in gating. Through careful use of charge switch mutations, this interaction was confirmed in the α1 and β2 subunits (Kash, Jenkins et al. 2003; Kash, Trudell et al. 2004); this experiment highlights the power of using structure predictions from homology models to inform protein function.

Electrostatic coupling between the extracellular domain and transmembrane domain is also contributed by basic residues within the pre-M1 (β10) segment (Keramidas, Kash et al. 2006; Mercado and Czajkowski 2006). Cysteine mutations in the α1 pre-M1 segment modified by positive thiol reactive reagents enhanced the amplitude of GABAergic currents indicating the importance of electrostatic interactions in transducing the energy of ligand binding to open the channel gate (Mercado and Czajkowski 2006). Mutation of an α1 pre-M1 basic residue to alanine decreased the apparent affinity of the receptor for GABA and also decreased the relative efficacy of P4S (Keramidas, Kash et al. 2006).

Comparison of the GLIC and ELIC structures, in the open and closed conformations respectively, has provided high resolution material for investigating the structural rearrangements that occur upon ligand binding and channel gating (Corringer, Baaden et al. 2010). These structures suggest a "twist-deformation" mechanism of structural arrangement. Ligand binding causes the extracellular domains of each subunit to twist counterclockwise around the central axis of the channel. The structures of the hinge region, at the interface of the extracellular and transmembrane domains, translate this movement to move the transmembrane domains clockwise to open the main gate. Substituted cysteine accessibility experiments have shown that the GABA-gate resides at the cytoplasmic end of M2 (Karlin, Akabas et al. 1994; Xu, Covey et al. 1995; Xu and Akabas 1996). This recent structural information has confirmed the importance of the M2-3 linker, loops 2 and 7, as well as, the pre-M1 segment in mediating channel gating. To date, specific residues within the intracellular loop domain have not been implicated in channel gating. In Chapter 4 of this dissertation, I will provide evidence that charge switch mutations within the $GABA_AR$ α1 intracellular loop domain impaired channel gating; these findings were verified with comparison of relative agonist efficacy. Any intracellular loop domain contributions represent a novel determinant of channel gating.

1.3.3B: Ion Permeation and Selectivity

Canonical rings of charged residues, contributed by each of the five subunits, have been hypothesized to interact with permeant ions to control the magnitude of channel conductance and to determine which charge species transverse the membrane through pLGICs; reviewed in (Keramidas, Moorhouse et al. 2004) and (Jensen, Schousboe et al. 2005). The $GABA_AR$ is selectively permeable to anions shown by shifted reversal potential values in asymmetric chloride conditions in both primary cultured neurons (Bormann, Hamill et al. 1987) and recombinant cell culture systems (Jensen, Pedersen et al. 2005). The effective pore diameter of GABA-gated channels was calculated to be 5.6 Å and 6 Å respectively, in cultured spinal neurons (Bormann,

Hamill et al. 1987) and cultured hippocampal neurons (Fatima-Shad and Barry 1993) by determining the relative permeability of anions with increasing diameters.

Imoto et al., (1988) showed that charged residues within M2 control channel conductance; the amplitude of single channel conductance varied directly with the number of charged residues in M2. This seminal work identified three conserved rings of charge in the *T. californica* nAChR subunits, deemed the extracellular, intermediate and cytoplasmic rings (Fig. 1.5, Fig. 1.6) (Imoto, Busch et al. 1988). Selective mutations at these positions also switched the charge selectivity of pLGICs (Keramidas, Moorhouse et al. 2002; Moorhouse, Keramidas et al. 2002; Jensen, Pedersen et al. 2005).

The M1-2 linker contains serine-valine-proline-alanine (SVPA) in the $GABA_AR$ α1 subunit, but serine-glycine-deletion-glutamate (SG-E) in $5\text{-}HT_{3A}R$ and α7 nAChR (Fig. 1.2). Introducing a negative glutamate to the alanine position is sufficient to induce cation selectivity to the α1 GlyR (Keramidas, Moorhouse et al. 2002) and switching the M1-2 linker sequence of only the β subunit was sufficient to confer cation selectivity to the α2β3γ2 heteromeric $GABA_AR$ (Jensen, Timmermann et al. 2002). However, $GABA_AR$ anion selectivity persisted when the identity of the alanine position was neutral, polar and positive, as well as, when the length of the M1-2 linker was augmented with additional alanine residues (Jensen, Pedersen et al. 2005) suggesting that the critical factors for anion selectivity are located elsewhere in the pore.

Crystallization of the AChBP protein with sulfate ions identified an ion coordination site within the extracellular vestibule of the pore (Hansen, Wang et al. 2008). Charge switch mutation of homologous positions in the *T. californica* nAChR subunits decreased single channel conductance (Hansen, Wang et al. 2008) (Fig. 1.6A). Molecular dynamic simulation of a *H. sapiens* nAChR homology model identified two more ion coordination sites by calculating

cation dwell times within the pore (Wang, Cheng et al. 2008). Furthermore, charge switch mutation of extracellular ring residues in the homomeric α1 GlyR selectively decreased the magnitude of outward currents to induce inward rectification (Moorhouse, Keramidas et al. 2002). A possible cause for this rectification is that charged residues that line the pore lumen establish the chloride concentration within the extracellular vestibule to influence the direction of anion flux. Likewise, residues that define the intracellular vestibule could impose similar control on ion permeation; this idea will be explored further in Chapter 5.

Recent evidence shows that residues within the intracellular loop domain also control ion permeation (Davies, Pistis et al. 1999; Kelley, Dunlop et al. 2003; Hales, Dunlop et al. 2006; Deeb, Carland et al. 2007; Livesey, Cooper et al. 2008; Peters, Cooper et al. 2010) (Fig. 1.6B). Fluctuation analysis of recombinant receptors showed that the homomeric 5-HT_{3A}R has a conductance of 310 fS (Brown, Hope et al. 1998). Although the homomeric 5-HT_{3B}R is non-functional when expressed in HEK293 cells and *Xenopus laevis* oocytes, heteromeric expression of the 5-HT_{3A} and 5-HT_{3B} subunits increases channel conductance to 12 pS (Davies, Pistis et al. 1999). Charged residues within the intracellular loop domain of the 5-HT_3R establish the difference in conductance (Kelley, Dunlop et al. 2003; Deeb, Carland et al. 2007; Livesey, Cooper et al. 2008). Kelley et al. (2003) created 5-HT_{3A}/5-HT_{3B} subunit chimeras to narrow the region of the 5-HT_{3B} subunit necessary for current enhancement to a portion of the intracellular loop domain; subsequent mutation, within this region, of three arginine residues of the 5-HT_{3A} subunit to the homologous 5-HT_{3B} residues, 5-HT_{3A}(R432Q, R436D, R440A), accounted completely for the difference in single channel conductance amplitude. The 5-HT_{3A}(R436D) charge switch mutation was shown to control conductance through charge interactions and not steric hindrance by mutating the position to cysteine and assessing the effect of sulfhydrl-reactive reagents of various charge and bulk (Deeb et al., 2007). Increased conductance induced by 5-HT_{3A}(R432Q, R436D, R440A) was caused by an increased relative permeability to calcium

(Livesey, Cooper et al. 2008). Charged intracellular loop domain residues have also been shown to mediate conductance in the nAChR (Hales, Dunlop et al. 2006) and the GlyR (Carland, Cooper et al. 2009). Although the intracellular loop domain has the most heterogeneous primary structure, sequence alignment of cationic pLGICs identified nAChR residues homologous to the 5-HT_{3A}R arginines. The α4β2 nAChR has a single channel conductance of 31 pS; introduction of arginines at homologous positions within the membrane associated stretch significantly decreased the magnitude of conductance (Hales, Dunlop et al. 2006). Sequence conservation between cationic and anion pLGICs is too poor within the intracellular loop domain to draw homology ($GABA_AR$ and GlyR α1 subunits only share 17% and 16% sequence identity, respectively, with the 5-HT_{3A} subunit as determined by pairwise sequence alignment with the Needleman-Wunsch algorithm, *nwalign*, in Matlab). Therefore, Carland et al., (2009) screened charged residues throughout the entire putative membrane associated stretch. Charge switch of four arginine residues of the homomeric α1 GlyR decreased single channel conductance by one third (Carland, Cooper et al. 2009). These data suggest that intracellular control of conductance is ubiquitous throughout the pLGIC superfamily, however, poor primary sequence conservation makes it difficult to make direct positional comparisons especially between cationic and anionic channels. Furthermore, the portion of the intracellular loop domain beyond the membrane associated region has not been investigated for a function role in controlling channel activity. The studies presented in this dissertation not only provide the first evidence for an intracellular contribution to ion permeation for the $GABA_AR$, but also represent the first investigation to functionally characterize the entire region between M3 and M4.

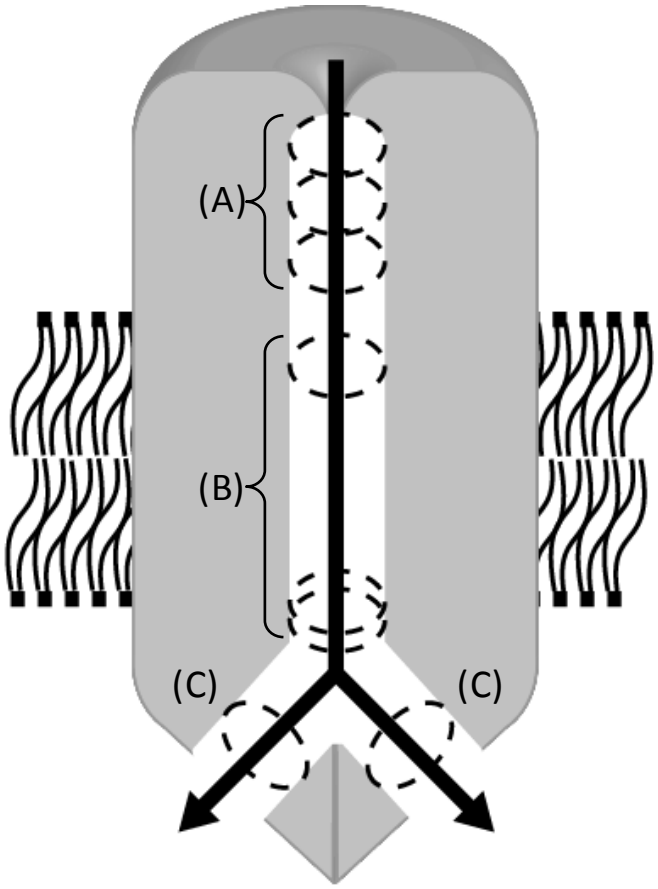

Figure 1.5: Canonical rings of charge within pLGIC superfamily. Cross-section schematic depicts the relative location of charged residues within the permeation pathway. (A) Three rings of charge within the extracellular vestibule coordinate permeant ions in the AChBP structure (Hansen, Wang et al. 2008; Wang, Cheng et al. 2008; Sine, Wang et al. 2010). (B) Charged residues of M2 define the extracellular, intermediate and cytoplasmic rings of charge to mediate channel conductance in nAChR (Imoto, Busch et al. 1988). The intermediate ring forms the selectivity filter to establish the cation or anion permeability of the pore (Jensen, Timmermann et al. 2002; Moorhouse, Keramidas et al. 2002; Jensen, Schousboe et al. 2005). (C) Intracellular charged residues control channel conductance in 5-HT_3R, nAChR, and GlyR (Davies, Pistis et al. 1999; Hales, Dunlop et al. 2006; Carland, Cooper et al. 2009; Peters, Cooper et al. 2010).

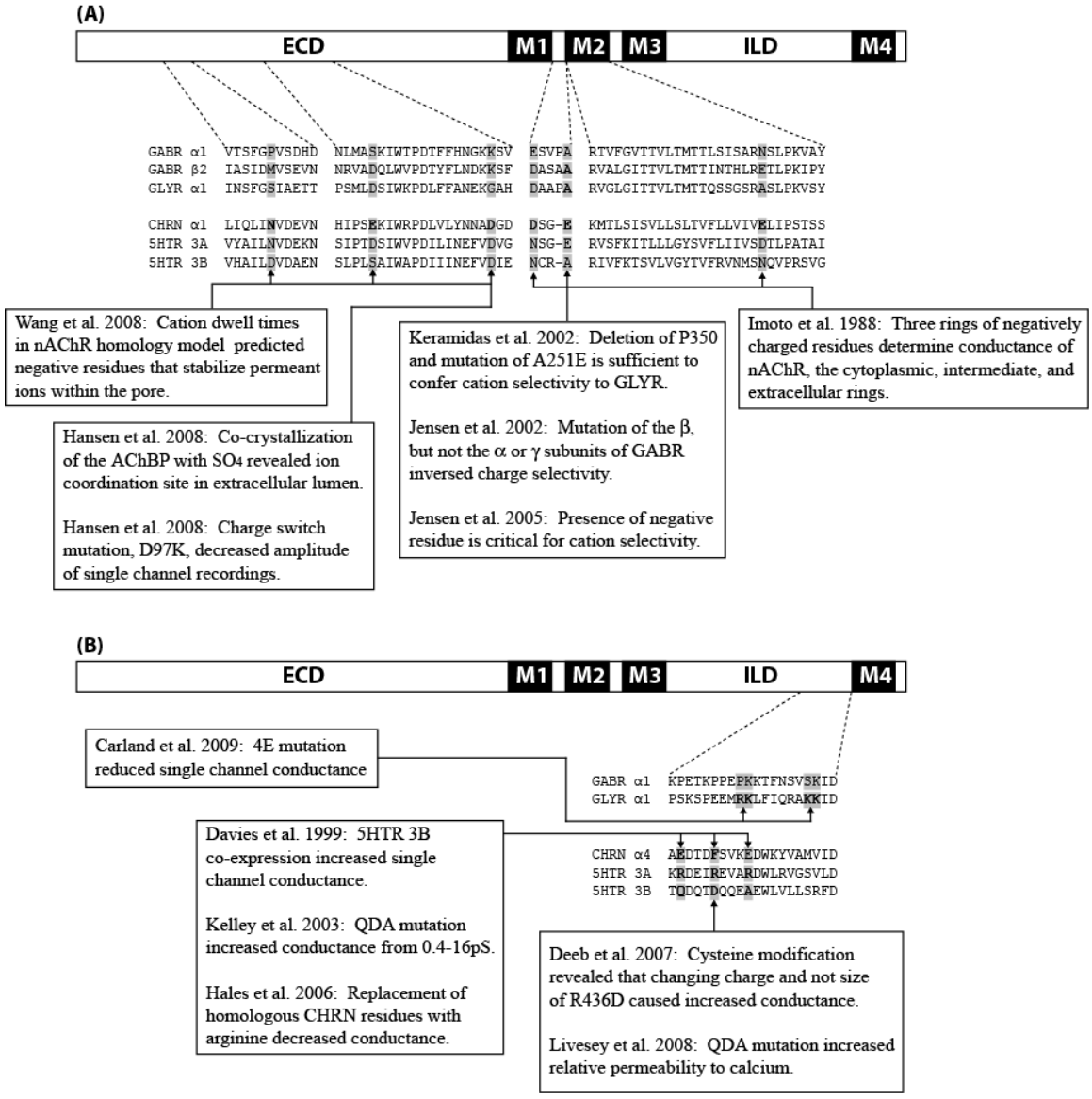

Figure 1.6: Ion permeation of pLGIC superfamily. Residues that have been shown to mediate correlates of ion permeation within (A) the extracellular domain (ECD) and transmembrane domains (M1-M4) and within (B) the intracellular loop domain (ILD) are highlighted. Bold residues indication positions that have been experimentally investigated; grey background highlights residues that are homologous to these positions. *The style of this figure was adapted from (Martin and Olsen 2000).*

1.3.3C: Trafficking and Phosphorylation

The intracellular loop domain is known to play a role in receptor activity through control of surface expression (Brandon, Bedford et al. 1999; Connolly, Kittler et al. 1999; Nymann-Andersen, Sawyer et al. 2002; Jovanovic, Thomas et al. 2004; Peran, Hooper et al. 2006; Chen and Olsen 2007; Michels and Moss 2007; Mizokami, Kanematsu et al. 2007; Tretter, Jacob et al. 2008; Mukherjee J. 2010). This domain is also the substrate for interactions with kinases and phosphatases that covalently modify the receptor to alter channel function (Leidenheimer, Browning et al. 1991; Smart 1997; Connolly, Kittler et al. 1999; Jovanovic, Thomas et al. 2004).

The surface expression, stability and targeting of $GABA_AR$s is a complex process controlled by many different proteins (Fig. 1.7). Briefly, I will outline the major players and highlight the role of the intracellular loop domain in receptor trafficking. $GABA_AR$ subunits are translated and the mature pentamer is assembled in the endoplasmic reticulum where the β and γ subunits bind the $GABA_AR$ associated protein (GABARAP; Nymann-Andersen, Wang et al. 2002; Fig. 1.7). GABARAP facilitates forward trafficking of the receptor through the Golgi apparatus to the cell surface (Chen and Olsen 2007; Michels and Moss 2007). Gephyrin binds GABARAP and targets receptors to inhibitory synapses where GABARAP is released from the receptor complex (Chen and Olsen 2007). Gephyrin gene deletion eliminates GlyR clustering but only decreases $GABA_AR$ clustering, suggesting that parallel mechanisms mediate synaptic targeting of the $GABA_AR$ (Kneussel, Brandstatter et al. 1999; Levi, Logan et al. 2004). Co-immunoprecipitation was used to identify the intracellular loop domain residues necessary for gephyrin binding in the $GABA_AR$ α1 and α2 subunits (Tretter, Jacob et al. 2008; Mukherjee J. 2010). Receptor endocytosis occurs in a clathrin-coated pit mediated by the adaptor protein 2 (AP2; Michels and Moss 2007).

The intracellular loop domains of the α6, β1-3, and γ1-3 subunits contain several phosphorylation sites (Fig. 1.8) for modification by protein kinase A (PKA), calcium/phospholipid dependent protein kinase (PKC), cGMP-dependent kinase (PKG), calcium/calmodulin dependent kinase II (CaMKII), and tyrosine kinase (SRC) (Martin and Olsen 2000; Jovanovic 2006). For example, RACK-1 facilitates PKC phosphorylation of β2(S409), which resides within the adaptor protein 2 (AP2) binding site; thus, phosphorylation at this position directly affects surface stability of the receptor by determining the rate of receptor recycling via AP2-mediated endocytosis in a clatherin-coated pit (Brandon, Bedford et al. 1999; Brandon, Delmas et al. 2000; Michels and Moss 2007). Furthermore, several subunits have splice variants of the intracellular loop domain; in particular, the long isoforms of the β2 and γ2 subunits both contain one additional phosphorylation sites (Olsen and Sieghart 2008). In my dissertation work I chose to use the short splice variant of both the β2 and γ2 subunits in order to avoid potential variability due to the additional phosphorylation sites. Phosphorylation of the β2 subunit controls surface stability by altering binding sites for integral trafficking proteins such as AP2 (Brandon, Bedford et al. 1999; Smith, McAinsh et al. 2008). In order to avoid potentially confounding effects from disruption of trafficking mechanisms, I chose to focus my study of the $GABA_AR$ intracellular loop domain on the α1 subunit as it has few known protein-protein interactions (Fig. 1.7) and has no phosphorylation sites (Fig. 1.8).

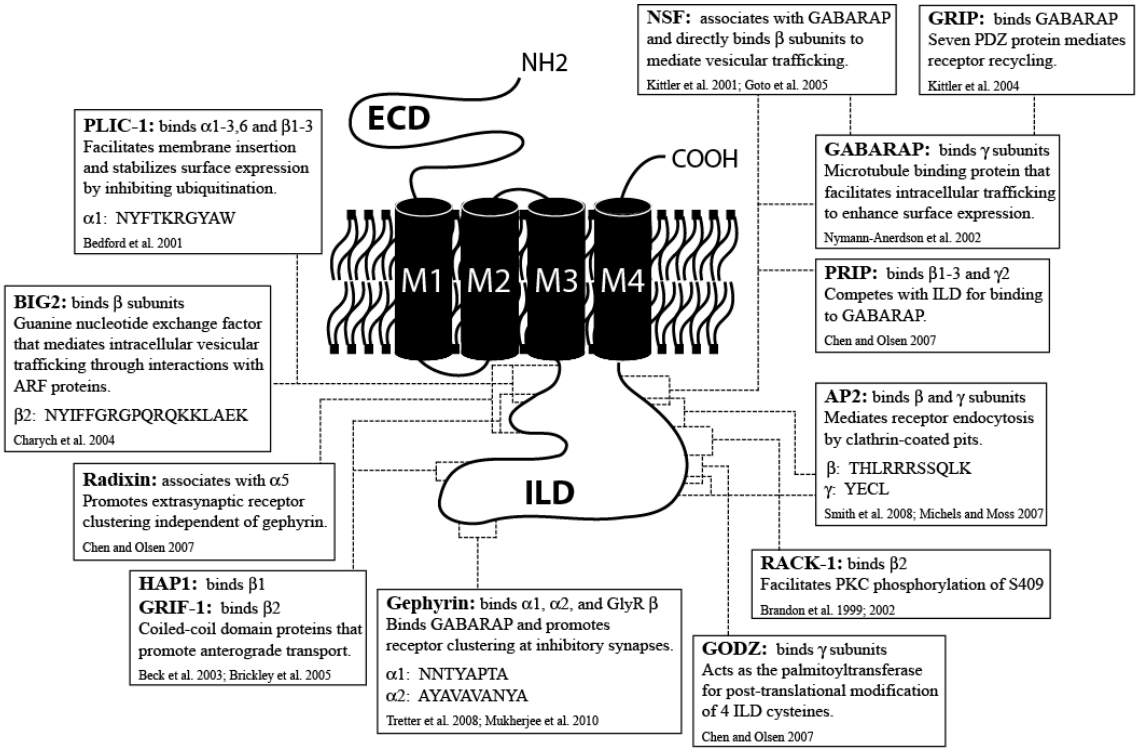

Abbreviations: AP2, adaptor protein 2; ARF, ADP-ribosylation factors; BIG2, brefeldin A-inhibited GDP/GTP exchange factor 2; GABARAP, GABAA receptor associated protein; GRIF-1, GABAA receptor interacting factor-1; GRIP, Glutamate receptor interacting protein 1; GODZ, Golgi-specific DHHC zinc finger protein; HAP1, Huntingtin associated protein 1; NSF, N ethylamaleimide-sensitive factor; PDZ, postsynaptic density protein, disc large, zonula occludens-1; Plic-1, protein linking IAP and cytoskeleton; PKC, protein kinase C; PRIP, phospholipase C-related, catalytically inactive protein; RACK-1, receptor of activated protein kinase C 1.

Figure 1.7: Known protein interactions with the $GABA_AR$ intracellular loop domain. Schematic depicts the general membrane topology of the extracellular domain (ECD), transmembrane domains (M1-M4), amd intracellular loop domain (ILD) for a single $GABA_AR$ subunit. The approximate binding sites for modulatory proteins are indicated. The β and γ subunits interact with many proteins that are integral to receptor trafficking and surface expression.

Figure 1.8: Phosphorylation of the intracellular loop domain. The *multialign* function in the Bioinformatics toolbox for Matlab was used to generate alignments of primary amino acid sequences. Round brackets (#) give the sequence number and square brackets [#] represent the number of residues that are not shown in the main alignment. Experimentally confirmed phosphorylation sites are shown highlighted in grey with the modified residue in bold (Martin and Olsen, 2000). The long splice variants of both the β2 and γ2 subunits contain an additional phosphorylation site.

1.3.4: Clinical Target

We know that the $GABA_AR$ is expressed ubiquitously in the central nervous system and proper $GABA_AR$ function is necessary to maintain the homeostatic balance between excitatory and inhibitory inputs. Changes in GABAergic signaling mediated by pharmacological agents or genetic predispositions can alter the level of inhibition to tip this balance. In particular, deficits in $GABA_AR$ function are linked to many diseases of the central nervous system, such as epilepsy (Baulac, Huberfeld et al. 2001; Harkin, Bowser et al. 2002; Maljevic, Krampfl et al. 2006; Kang, Shen et al. 2009; Ding, Feng et al. 2010; Macdonald, Kang et al. 2010), schizophrenia (Lo, Lau et al. 2004; Lo, Xu et al. 2007), and autism spectrum disorders (DeLorey, Handforth et al. 1998; Adusei, Pacey et al. 2010) which makes the $GABA_AR$ an important clinical target (Table 1.2). Similarly, therapeutics that modulate the $GABA_AR$ are used clinically to induce anesthesia, change mood, and control levels of excitability (Pritchett, Sontheimer et al. 1988; Pritchett, Sontheimer et al. 1989; Franks and Lieb 1994; Krasowski and Harrison 1999; Martin and Olsen 2000; Franks 2008). Therefore, a complete understanding of the function of the $GABA_AR$ is vital to the study and treatment of many neuronal conditions.

1.3.4A: Modulation

The goal of anesthesia is to safely and reversibly cause loss of consciousness to facilitate the comfort of medical procedures for the patient and the ease of surgery for the professional (Franks 2008). There are several types of anesthetics, including inhaled and intravenous agents, as well as alcohols (Martin and Olsen 2000). General anesthetics potentiate GABAergic currents (some even directly activate the receptor at high concentrations) to enhance inhibitory tone and induce a hypnotic state (Franks 2008). Anesthetic drugs modulate the open probability of single channel responses but do not directly affect the amplitude of conductances (Franks and Lieb 1994) to prolong the duration of IPSCs (Krasowski and Harrison 1999; Martin and Olsen 2000). In experiments presented in Chapter 5 I used three general anesthetics to manipulate the open

probability of the channel; the intravenous anesthetics propofol and etomidate and the inhaled anesthetic isoflurane were co-applied with GABA to allosterically increase channel open probability.

Benzodiazepines are intravenous agents used clinically to induce anesthesia and to treat anxiety conditions and panic disorders (Martin and Olsen 2000). The $GABA_AR$ was originally identified in brain membranes as the benzodiazepine receptor; radioligand binding studies showed that benzodiazepine binding was concentrated in synaptosomal membrane fractions (Mohler and Okada 1977; Martin and Olsen 2000). GABA agonists enhance benzodiazepine binding, which pointed to the existence of a mutal receptor (Tallman, Thomas et al. 1978). In particular, the γ2 subunit is necessary for modulation by benzodiazepines (Pritchett, Sontheimer et al. 1989); receptors containing the α1 subunit have a high affinity for benzodiazepines, but both the α4 and α6 subunits are insensitive to benzodiazepines (Olsen and Sieghart 2008).

The effective dose of most general anesthetics is less than 2-fold lower than the lethal dose (Franks 2008). Hence, much work has been dedicated to identifying the sites of action of allosteric modulators of the $GABA_AR$ in order to facilitate better drug design. Cutoff experiments identified that the alcohol modulatory pocket of $GABA_AR$ could only accommodate heptanol, whereas, GlyR was modulated by decanol indicating a larger alcohol binding site (Martin and Olsen 2000). The benzodiazepine binding site, identified with the substituted cysteine accessibility method, resides at the extracellular interface of the α and γ subunits (Teissere and Czajkowski 2001); Fig. 1.1A). Point mutation experiments identified the location of the general anesthetic binding pocket at the top of the interface of the four transmembrane domain segments (Krasowski and Harrison 1999; Martin and Olsen 2000; Franks 2008). Through mutagenesis the $GABA_AR$ α subunit has been shown to control modulation by volatile anesthetics, whereas, the β subunit determines the action of both volatile and intravenous

anesthetics (Franks 2008). Recently, crystal structures were solved of GLIC in complex with propofol and desflurane, which confirmed the general location of the anesthetic binding pocket (Nury, Van Renterghem et al. 2011). In sum, allosteric modulators of the $GABA_AR$ provide powerful tools both in the laboratory and in the clinic. A better understanding of the mechanisms of action and of the structure of the $GABA_AR$ will aid in the proper implementation of current drugs and the design of novel compounds.

1.3.4B: Dysfunction

In this section I will describe specific deficits in GABAergic function that have been shown to play a role in three diseases: autism spectrum disorders, epilepsy (seizures in general) and depressive conditions (schizophrenia and bipolar disorder).

Many genes that are linked to autism spectrum disorders encode cellular adhesion molecules, which help form synapses and determine the excitatory or inhibitory fate of new synapses (Smith and Sadee 2011). Autism spectrum disorders are characterized by delayed synaptic maturation and decreased $GABA_AR$ expression; lending many related disorders, such as Fragile X Syndrome, Rett syndrome, Angelman syndrome, and Turner syndrome, to confer increased seizure susceptibility (Hampson, Adusei et al. 2011). A murine model of Fragile X, created by knockout of the FMR1 gene, exhibited decreased expression of the $GABA_AR$ α1 subunit in infancy and the β2 subunit in adulthood (Adusei, Pacey et al. 2010). Angelman syndrome is caused by deletion of chromosome section 15q11-13, which contains the α5, β3, and γ3 genes of the $GABA_AR$ (McKernan and Whiting 1996). Knockout of the β3 subunit in mice induces a seizure phenotype typical of Angelman syndrome (DeLorey, Handforth et al. 1998) (Table 2.1). Furthermore, phosphorylation of the β3 subunit enhances seizure-induced receptor endocytosis (Terunuma, Xu et al. 2008).

Several mutations of $GABA_AR$ subunits have been linked to varying forms of epilepsy (Table 1.2). An epileptic seizure is a transient episode of abnormally excessive or synchronous neural activity (Fisher, van Emde Boas et al. 2005). In general, N-terminal mutations of the $GABA_AR$ associated with epilepsy have been shown to alter the kinetics of GABAergic currents, whereas C-terminal mutations cause decreased macroscopic currents through changes in receptor surface expression (Macdonald, Kang et al. 2010). For example, the γ2(K289M) in the M2-3 linker causes a $GABA_AR$ gating impairment to decrease inhibitory tone (Baulac, Huberfeld et al. 2001). The α1(A322D) point mutation in M3 disrupts membrane insertion and folding of the subunit and the α1(S326fs328X) frame shift mutations introduces a premature truncation; both of which eventually lead to a decrease in surface expression and decreased GABAergic currents (Maljevic, Krampfl et al. 2006; Gallagher, Ding et al. 2007; Ding, Feng et al. 2010). Two mutations in the γ2 intracellular loop domain introduce premature truncation condons, γ2(Q390X) and γ2(W429X); both also lead to decreased surface expression (Harkin, Bowser et al. 2002; Sun, Zhang et al. 2008). The γ2(Q390X) truncation in particular is retained in the endoplasmic reticulum and enacts a dominant-negative effect on WT receptors to even decrease the magnitude of currents in heterozygous conditions (Kang, Shen et al. 2009).

Genetic mutations within the $GABA_AR$ intracellular loop domain in particular have been correlated with schizophrenia and other depressive disorders. Genetic predisposition and environmental risk factors are currently the best indicators for the onset of schizophrenia. Cortical inhibition deficits in patients with schizophrenia, through loss of interneurons (Daskalakis, Fitzgerald et al. 2007) and decreased GABA synthesis (Straub, Lipska et al. 2007; Gonzalez-Burgos, Hashimoto et al. 2011), point to flawed $GABA_AR$ activity in disease pathogenesis. Changes in receptor expression have also been correlated with schizophrenia; specifically, levels of α1 mRNA have been shown to be decreased in pyramidal cells of the prefrontal cortex (Glausier and Lewis 2011). A single nucleotide polymorphism in the β2 gene

associated with schizophrenia decreases expression of the long isoform of the subunit (Lo, Lau et al. 2004; Zhao, Xu et al. 2006; Lo, Xu et al. 2007). Importantly, the intracellular loop domain of the β2L splice variant is 38 residues longer than β2S and contains a CaMKII phosphorylation site (Fig. 1.8). Alternate splicing of exon 10 of the GABRB2 gene, which encodes the intracellular loop domain, yields four variants of the β2 subunit. Real-time PCR of post-mortem tissue from patients with schizophrenia and bipolar disorder showed altered expression ratios of these splice variants compared to normal control patients (Zhao, Xu et al. 2009). GABAergic deficits have also been linked to major depressive disorder (Croarkin, Levinson et al. 2011); specifically an intracellular loop domain mutation α6(P385S) has been linked to neuroticism (Sen, Villafuerte et al. 2004). This position within the α6 intracellular loop domain has also been shown to reduce the anxiolytic effects of GABAergic therapeutics (Iwata, Cowley et al. 1999; Hoffman, Balyasnikova et al. 2002).

Taken together, these deficits of $GABA_AR$ activity emphasize the necessity for proper subunit expression and function to maintain the homeostatic balance between excitatory and inhibitory signaling. Furthermore, deficits caused by mutation or altered expression of the intracellular loop domain highlight the importance of this domain for normal brain function.

Gene	Mutation	Disorder	Effect	Reference
GABRA1	A322D	Epilepsy: JME	↓α1 surface expression	Maljevic et al. 2006
GABRA1	S326fs328X	Epilepsy: CAE	↓α1 surface expression	Macdonald et al. 2010
GABRB2	SNP	SCZ, BD	β2 splice variant expression	Zhao et al. 2009
GABRB3	Deletion	ASD: Angelman	No α5, β3 or γ3 expression	Hampson et al. 2011
GABRG2	K289M	Epilepsy: GEFS+	Impaired channel gating	Baulac et al. 2001
GABRG2	Q390X	Epilepsy: FS, SMEI	↓γ2 surface expression	Kang et al. 2009
GABRG2	W429X	Epilepsy: FS, GEFS+	↓γ2 surface expression	Sun et al. 2008
FMR1	Deletion	ASD: FXS	↓α1 and β2 expression	Adusei et al. 2010

Table 1.2: Genetic mutations known to affect expression or function of the $GABA_AR$. Dysfunction of the $GABA_AR$ has been linked to many forms of epilepsy, depression and autism.

Abbreviations: *ASD, autism spectrum disorders; BD, bipolar disorder; CAE, childhood absence epilepsy; FS, febrile seizure; fs, frameshift; FXS, fragile X syndrome; GEFS+, generalized epilepsy plus febrile seizure; JME, juvenile myoclonic epilepsy; SCZ, schizophrenia; SMEI, severe myoclonic epilepsy of infancy.*

1.4: Conclusion

The $GABA_AR$ plays a pivotal role in inhibitory neurotransmission and is essential for proper brain function. A complete understanding of the mechanisms that govern $GABA_AR$ activity is critical to study normal neural signaling and to address the clinical concerns regarding modulation of the receptor for treatment of disease and to induce the hypnotic state necessary for modern surgery. Much is presently known about the $GABA_AR$ through direct study and comparison with homologous proteins of the pLGIC superfamily. However, there are still several critical knowledge gaps, especially concerning the role of the intracellular loop domain. The high degree of primary sequence variability within pLGIC intracellular loop domains makes it difficult to use homology to drive predictions. Furthermore, there is no known structure of the $GABA_AR$ in order to ascertain functional relationships. Therefore, direct analysis is necessary to characterize the function of intracellular loop domain residues. In my dissertation studies, I have paired empirical and theoretical approaches to begin to fill these gaps in our understanding of $GABA_AR$ function. My work is focused on the most common arrangement of the $GABA_AR$, the synaptic $\alpha1\beta2\gamma2$ complex. I chose to investigate the α1 intracellular loop domain as it has no phosphorylation sites and is not involved in primary trafficking pathways. Therefore, mutagenesis within the α1 intracellular loop domain is not predicted to interfere with receptor assembly or surface expression. If the intracellular loop domain establishes the architecture of the intracellular vestibule then deletion of the α1 intracellular loop domain will alter the geometry of the pore to change ion permeation. Furthermore, if the intracellular loop domain defines the intracellular portion of the pore then charge switch point mutations will perturb integral electrostatic interactions within the permeation pathway.

In Chapter 2 I will describe the methods and materials that I used to investigate my research questions. In Chapter 3 I used whole-cell voltage clamp electrophysiology and immunocytochemistry with confocal visualization of receptor surface expression to measure

changes induced by deletion of the C-terminus and intracellular loop domain regions of the α1 subunit. In Chapter 4 I investigated the role of specific charged residues within the α1 intracellular loop domain by using whole-cell and single channel voltage clamp electrophysiology and immunocytochemistry with luminescent quantification of surface expression to measure changes induced by charge switch point mutations. In Chapter 5 I measured the directionality of current flow through the $GABA_AR$, i.e. the rectification of the IV relationship, with whole-cell recordings and ion replacement solutions. In Chapter 6 I will describe my theoretical predictions of the secondary structure of the $GABA_AR$ α1 intracellular loop domain. Finally, in Chapter 7 I will discuss the overall findings, relevance, and future directions of my dissertation work. Results presented here will establish a role for the $GABA_AR$ α1 intracellular loop domain in channel function, identify specific charged residues that control channel gating and ion permeation and provide a structural backbone for future predictions of receptor function.

Chapter 2

Experimental Methods and Materials

2.1: Overview

The goal of the studies presented in this dissertation was to determine the function of the intracellular loop domain of the $GABA_AR$ α1 subunit. To achieve this goal, I used 5 main techniques: cell culture, site-directed mutagenesis, immunocytochemistry, voltage clamp electrophysiology and bioinformatics. Briefly, I will explain my rationale for selecting each of these techniques. Then, a more complete description of the use of each technique will follow in subsequent sections of this chapter.

I used cultured human embryonic kidney type 293 (HEK293) cells as an *in vitro* expression system to study $GABA_AR$ activity. The use of cultured cells provided 3 main benefits. First, HEK293 cells do not express most ligand-gated ion channels (Thomas and Smart, 2005), which allowed for full experimental control of $GABA_AR$ composition. Second, HEK293 cells are an immortalized cell line with high fidelity of gene expression across passages, which make cultured cells a very consistent experimental substrate. Third, HEK293 cells are 20-30 μm in diameter, which is ideal for single electrode voltage clamp electrophysiology.

Site-directed mutagenesis was used to introduce point-mutations, deletions and insertions in the cDNA encoding the primary amino acid sequence for the $GABA_AR$ α1 subunit. Perturbations made in the primary amino acid sequence, therefore, allowed for changes to be made to the mature protein. Through these changes, I was able to make functional comparisons between the native residue and the introduced residue at specific positions within the α1 intracellular loop domain.

Immunocytochemistry methods were used to label the $GABA_AR$ α1 subunit protein for quantification of receptor surface expression. Antibody labeling relies heavily on the specificity of the antibody-antigen interaction. Importantly, the cDNA encoding the extracellular domain of the α1 subunit remained unperturbed in all constructs. Therefore, I chose to use a primary antibody specific to an extracellular epitope of the α1 subunit. Protein domains are known to be modular and the extracellular, transmembrane, and intracellular loop domain of pLGICs have been shown to retain function when combined as chimearas (Duret, Van Renterghem et al. 2011; Goyal, Salahudeen et al. 2011). Therefore, mutations within the intracellular loop domain were predicted to have no effect on the structure of the extracellular domain and the antibody-antigen interaction was assumed to be the same for intracellular loop domain type and mutant proteins. Thus, I was able to make comparisons across conditions without concern for antibody specificity, since I used the same primary antibody in all experiments.

Voltage clamp electrophysiology was used to record currents passed through membranes in the whole-cell and outside-out patch configurations. Patch clamp electrophysiology is a powerful measurement tool that permits full control of both the chemical and electrical components of the driving force on ion flux. The chemical gradient was experimentally controlled via the composition of intracellular and extracellular solutions. Cells were perfused with saline that established the extracellular concentration of permeant ion and also served to deliver pharmacologic agents to modulate receptor activity. In the whole-cell patch configuration the volume of solution within the pipette was infinitely greater than the volume of cytosol and, thus, served as the intracellular portion of the ion gradient. The chemical gradient established the theoretical reversal potential of the permeant ion. Voltage clamp mode provides direct control of the membrane potential which experimentally defined the electrical component of the driving force. Furthermore, single channel currents were recorded from patches in the outside-out

configuration to maintain the same experimental control over the chemical and electrical components of driving force.

Finally, I conducted bioinformatic analysis of the primary amino acid sequence of the $GABA_AR$ α1 intracellular loop domain in order to predict the secondary structure of the domain. Little is known about the functional contributions of the intracellular loop domain and even less is known about the structure of this domain. The link between function and structure is well established. The first structure solved with x-ray crystallography was of myoglobin, for which Max Perutz and Sir John Cowdery Kendrew shared the 1962 Nobel Prize in Chemistry (Kendrew, Bodo et al. 1958). To date, structures of four classes of globin proteins have been solved (Kakar, Hoffman et al. 2010). Myoglobin, hemoglobin, cytoglobin, and neuroglobin are found in genomes of prokaryotes and eukaryotes, including vertebrates, invertebrates, fungi and plants; globin sequences from *H. sapiens* share only ~50% homology, but have conserved secondary structures and share reversible oxygen binding function (Hardison 1998). The globin proteins are a classic example of how function is conserved through evolutions. Thus, proteins that share sequence homology are predicted to have similar structure and similar function (Baker and Sali 2001; Lee, Redfern et al. 2007).

Knowledge of either structure OR function may be used to inform the other. Therefore, secondary structural predictions provide a powerful platform to make theoretical predictions. Structure prediction methods are either based solely on the primary amino acid sequence or based on homology to a known structure (Baker and Sali, 2001). There are benefits and drawbacks to each approach. Homology modeling provides the best predictions, but requires that the structure of a least one related protein is known. On the other hand, *de novo* methods do not require sequence conservation or homology to known structures, but the prediction error is greater. Therefore, I chose three different methods that used both types of predictions to determine the

secondary structure of the α1 intracellular loop domain. I used Chou-Fasman amino acid scales to predict secondary structure directly from the primary sequence (Chou and Fasman 1978) and I used the Jnet algorithm to predict secondary structure from sequence alignment homology (Cole et al., 2008). Lastly, I generated a structural homology model of the $GABA_AR$ α1 subunit using the SwissModel automated homology modeling server, which uses a combination of *ab initio* and database loop building to complete each model template (Schwede et al., 2003).

2.2: Cell Culture

2.2.1: HEK293 cells

The human embryonic kidney type 293 (HEK293) cultured cell heterologous expression system was used for all experiments. This immortalized cell line[†] was established by transfecting human embryonic kidney cells with fragments of adenovirus DNA (Graham, Smiley et al. 1977). HEK293 cells have since had a long-standing history as an expression system to study the function of ligand-gated ion channels (Pritchett, Sontheimer et al. 1988; Thomas and Smart 2005). HEK293 cells provide a stable expression environment for the study of a particular protein of interest with a high degree of fidelity across passages[††], easily withstanding subculturing[††]. Likewise, HEK293 cells are easy to transfect for robust protein expression under viral promoter systems. The HEK293 immortalized cell line in particular is ideal for the study of neuronal proteins including the $GABA_AR$ because it does not express most ligand-gated ion channels, but it has been shown to express many signaling pathways present in native CNS cells (Thomas and Smart 2005) and also contains the most common neurofilament proteins (Shaw, Morse et al. 2002). HEK293 cells are well suited for *in vitro* patch clamp electrophysiology because of their size and morphology (Thomas and Smart 2005).

HEK293 cells have been reported to endogenously express some $GABA_AR$ subunits, including the β3, γ3, and ε subunits, under specific conditions (Thomas and Smart 2005). The endogenous β3 subunit may form homomers that induce a tonic leak current in untransfected cells (Ueno, Zorumski et al. 1996; Wooltorton, Moss et al. 1997; Taylor, Thomas et al. 1999) and confer non-traditional pharmacology, as well as, surface expression to cells transfected with the α1 and γ2 subunits (Davies, Hoffmann et al. 2000). This finding, however, has been difficult to replicate and may be linked to high passage number or specific culture conditions (Fuchs, Zezula et al. 1995). To combat this possibility, HEK293 cells were never passaged more than 30 times. Furthermore, mRNA and expression studies have failed to identify the endogenous β3 subunit

(Shaw et al., 2002; Taylor et al., 1999; Wooltorton et al., 1997), which highlights the variability and low levels of endogenous expression. After transfection, powerful viral promoters drive expression of recombinant receptors to overwhelm any possible effects from endogenous proteins (Thomas and Smart, 2005). Nevertheless, we regularly assayed HEK293 cells for endogenous β subunit expression by only transfecting cells with the α and γ subunit, which are non-functional without a β subunit; GABAergic currents under these conditions indicated the presence of an endogenous β subunit. Therefore, in these studies I have used HEK293 cells to study the pharmacology and biophysical properties of the $GABA_AR$ with the understanding that any possible contamination effects from endogenous receptor subunits were negligible.

HEK293 cells were maintained at 37°C and 5% CO_2, in Eagle Minimum Essential Medium (MEM; Sigma; M2279) supplemented with 5% FBS (Hyclone; 45000-736), 40 μM *L*-glutamine (Sigma; G7513), 100 U/ml penicillin and 0.1 mM streptomycin (pen-strep; Sigma; G1146); supplemented media hereafter referred to as MEM+ . Cells were passaged regularly to prevent growth beyond a confluent[†††] monolayer. Details of culture procedures are provided below; for an overview see Figure 2.1.

† An immortalized cell line will grow and divide indefinitely *in vitro* as long as correct cell culture conditions are maintained. Immortalized cells have been transformed to alter their inherent properties and allow indefinite growth.

†† Passaging refers to the act of subculturing a cell line by dilution of the cell suspension and transfer into a new culture vessel. The passage number is an indication of how many times a batch of cells has been subcultured.

††† Confluency is determined by the percentage of coverage of the bottom of the culture vessel. Complete coverage of the culture vessel base is deemed 100% confluent.

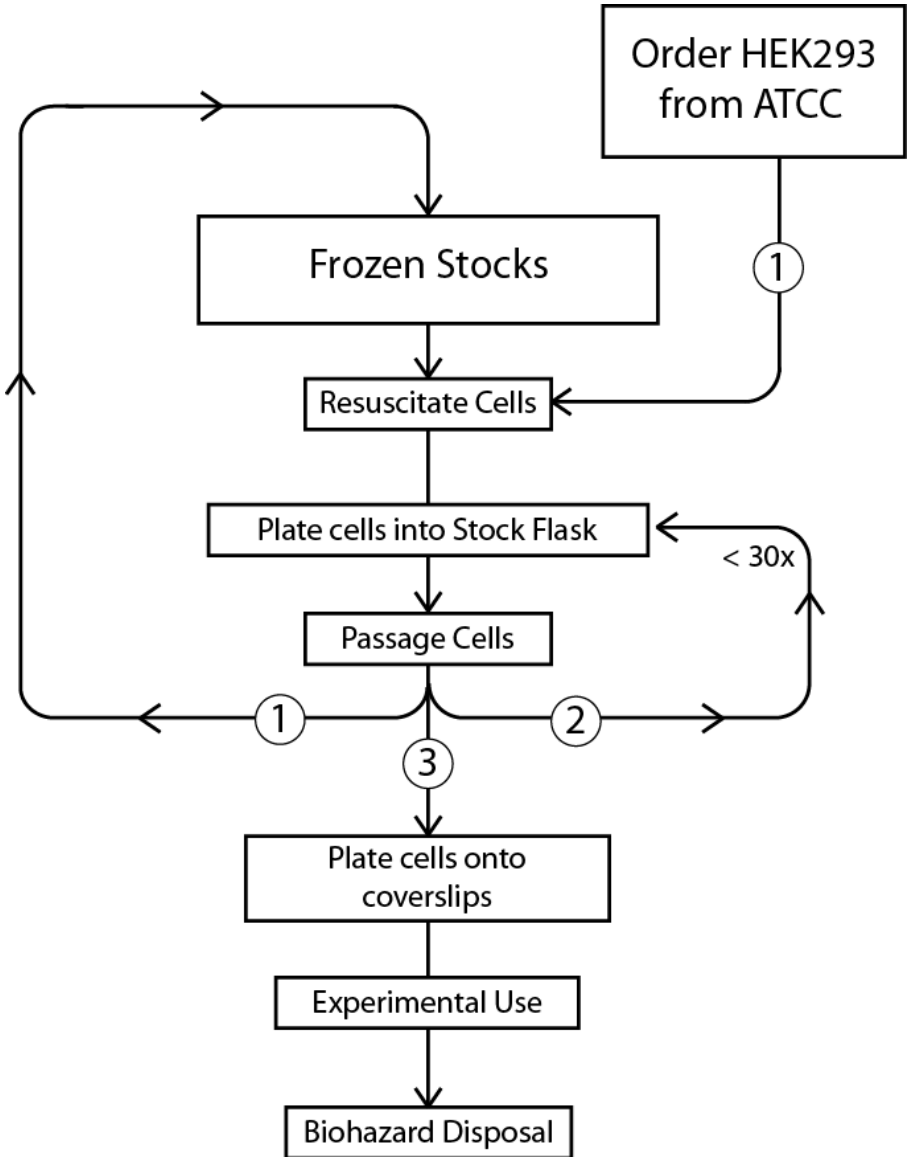

Figure 2.1: Passage and Care of HEK293 cells. Flowchart describing the cell culture paradigm for human embryonic kidney (HEK293) cells used in all experiments. The specific methods for freezing, resuscitation, and passage of cells are described in Section 2.1. (1) Upon receipt from American Type Culture Collection (ATCC), cells were grown up to generate frozen stocks for long term storage in liquid nitrogen. (2) Cells were passage weekly into a new flask, but not more than 30 times in order to maintain consistent fidelity of the expression system. (3) For experimental use, cells were plated onto glass coverslips that were coated with poly-D-lysine. Cells were transfected to induce expression of the $GABA_AR$. After experimental use, cells and coverslips were disposed of in biohazard sharps containers.

2.2.2: Resuscitation of cells

Frozen HEK293 cells were obtained from American Type Culture Collection (ATCC; CRL-1573). These commercially available cells have been maintained from the original line created in 1977 by Graham et al. Upon arrival, cells were quick-thawed, resuspended in MEM+, and transferred to a T25 flask (Becton, Dickinson &Co., Falcon; 353808). After 12 hours, the media was removed and replaced with fresh MEM+; then, the flask was fed in this manner on a weekly basis. Once confluent, cells were passaged into a new flask by trypsinization (trypsin; Sigma; T3924).

2.2.3: Preparation of Frozen Stocks

HEK293 cells were never subcultured more than 30 times in order to maintain fidelity of the expression system. Once cells were received from ATCC they were grown up in large volumes and stabilized in frozen aliquots for long term storage in liquid nitrogen to maintain low passage numbers. To generate frozen stocks, cells were passaged into a new T175 flask (Becton, Dickinson &Co., Falcon; 353028) and fed with fresh MEM+ weekly until confluent. Cells were split into two T175 flasks and once again fed weekly until confluent. This process was repeated for each flask to generate four T175 flasks. Once confluent, cells from all four flasks were trypsinized, resuspended and combined. Next, cells were counted with a hemocytometer, then pelleted and resuspend in freshly made freezing mix (10% FBS, 5% DMSO in MEM) as necessary to achieve ~$2x10^6$ cells/ml. Finally, aliquots were distributed into freezing vials (Corning; 430488) and flash frozen on dry ice for subsequent storage at -200°C in liquid nitrogen.

2.2.4: Passage and Plating

A stock T25 flask was maintained at all times to provide HEK293 cells for use in electrophysiology and immunocytochemistry experiments. HEK293 cells are of epithelial origin and will grow in a monolayer as long as there is available adherent surface. Growth beyond a monolayer will generate clumps of cells that can exhibit altered gene expression. Therefore, care was taken to passage cells before they arrived at 100% confluency. One week before experimental use, cells were plated onto poly-*D*-lysine (pDL; > 30,000 g/mol; Sigma, P7405) coated glass coverslips; pDL provided a charged surface for cell adhesion and the coverslip provided a means to transfer cells to the recording chamber. Once the stock flask reached 20 passages, new cells were resuscitated from frozen stocks to maintain a low passage number. Finally, the stock flask was discarded once a new flask had been established.

2.2.5: Vector Expression System

Wild type (WT) $GABA_AR$ complementary DNAs (cDNAs) for the human α1, β2, and γ2 subunits were harbored within the pCIS2 vector (We greatly appreciate the gift of cDNAs for the human α1, β2, and γ2s subunits from Dr. Neil L. Harrison, Ph.D., Columbia University, New York, NY). The pCIS2 vector induces overexpression of its open reading frame in HEK293 cells via a cytomegalovirus (CMV) promoter for expression in eukaryotic cells (Fig. 2.2).

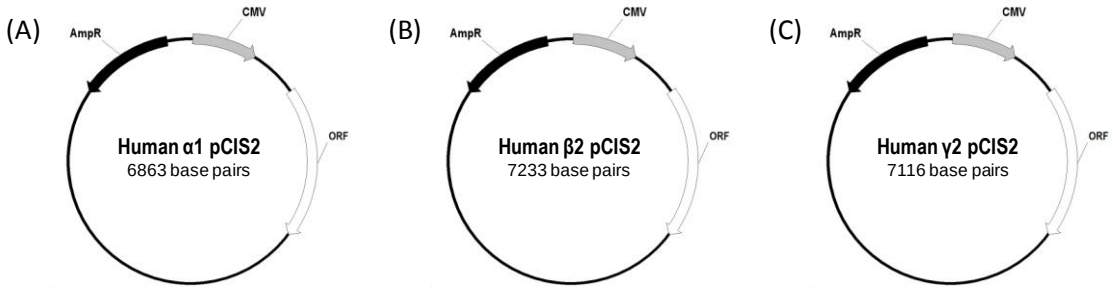

Figure 2.2: Vector maps of WT constructs. Expression vectors containing cDNA for (A) α1, (B) β2, and (C) γ2 subunits of the $GABA_AR$. Loci are shown for the cytomegalovirus promoter (CMV, gray), ampicillin resistance (AmpR, black), and open reading frame for each subunit (ORF, white).

2.2.6: Site-Directed Mutagenesis

Deletions and point mutations in the WT α1 subunit cDNA were introduced using the QuickChange® II site-directed mutagenesis kit (Stratagene) and confirmed by sequencing (Eurofins/MWG/Operon, Huntsville, AL). The QuickChange® kit uses a PCR-based method to introduce changes in double stranded DNA plasmids. To create a point mutation, I designed forward and reverse overlapping primers with the codon for the mutation in the center with 10-15 flanking base pairs complementary to the template cDNA. Deletion/insertion constructs were created using overlapping primers containing 10-15 base pairs complementary to the region of the template cDNA surrounding the desired deletion. Mutagenic codons were chosen to reflect the most conservative change from the template cDNA with the smallest possible percent of non-identical base pairs (%mismatch). Ideal primers had a length (N) of 25-45 base pairs and a melting temperature (T_m) greater than 78°C [Eq. 1], with a guanine and cytosine content (%GC) over 40%. Primers were designed with one or more guanine or cytosine bases at the 3' end in order for the polymerase to seat properly in the elongation step of the PCR. The custom oligomers were synthesized by Eurofins/MWG/Operon. For a complete list of primers see Table 2.1.

[Eq. 1] $$T_m = 81.5 + 0.41(\%GC) - {}^{675}/_{N} - \%mismatch$$

Template cDNA must be methylated, therefore we used a dam+ *E.coli* strain: XL1-Blue Supercompetent cells; after PCR, the parental methylated and hemimethylated DNA was digested with *DpnI* so that only mutated cDNA remained. Supercompetent cells were then transformed with the mutant plasmid DNA and selected using an agar plate containing the antibiotic ampicilin, for which only positively transformed cells expressed resistance. A single colony was used to spike a volume of broth subsequently purified by either MiniPrep or MaxiPrep (Qiagen, Valencia, CA). Transformed *E. coli* cells were grown up in 5 ml Luria Broth (LB) with

0.1 mg/ml ampicillin (LB/amp) and 500 µl of cells were saved and stored at 4 ℃ for later use. Plasmid DNA was then purified by spin column MiniPrep and sequenced by Eurofins/MWG/Operon. Once the desired mutation was confirmed, the retained cells were used to spike 200 ml of LB/amp for MaxiPrep DNA purification. A glycerol stock of each construct was made (200 µl of cells in LB/amp and 800 µl of 50% glycerol) and stored at -80℃. Finally, the concentration of purified plasmid DNA was determined using a SmartSpec^{TM} Plus Spectrophotometer (0.2-1 µg/µl; Bio-Rad Laboratories, Philadelphia, PA) and samples were stored at 4 ℃.

Construct	Forward Primer (5'→3')	T_m (°C)	Length
IL-BAC	gtaaactatttcact**AGCCAGCCCGCAGCA**attgaccgactg	76.7	48
IL-7K	gccacagtaaactatttcact**AAGAAGAAGAAGAAGAAGAAA**attgaccgactg	70.8	54
K312E	gccacagtaaactatttcact**GAG**agaggttatgcatgggatggc	72.9	45
R313E	cagtaaactatttcactaag**GAA**ggttatgcatgggatggc	69.7	41
D318K	cactaagagaggttatgcatgg**AAG**ggcaaaagtgtggttccag	73.1	44
K320E	ggttatgcatgggatggc**GAA**agtgtggttccagaaaagcc	73.7	41
E325K	gatggcaaaagtgtggttcca**AAG**aagccaaagaaagtaaagg	70.4	43
K326E	ggcaaaagtgtggttccagaa**GAG**ccaaagaaagtaaaggatcc	72.2	44
K328E	gtgtggttccagaaaagcca**GAG**aaagtaaaggatcctc	71.0	39
K329E	ggttccagaaaagccaaag**GAA**gtaaaggatcctcttattaag	69.5	43
K331E	ccagaaaagccaaagaaagta**GAG**gatcctcttattaag	67.9	39
D332K	gccaaagaaagtaaag**AAG**cctcttattaagaaaaacaacac	66.7	42
K336E	gtaaaggatcctcttatt**GAG**aaaaacaacacttacgctcc	68.7	41
K337E	gtaaaggatcctcttattaag**GAA**aacaacacttacgctcc	68.7	41
R354E	gctacacccctaatttggcc**GAA**ggcgacccgggcttagcc	78.7	41
D356K	ctaatttggccaggggc**AAG**ccgggcttagccaccattg	76.3	39
K364E	ccgggcttagccacgattgct**GAG**agtgcaaccatagaacc	75.7	41
E369K	ccattgctaaaagtgcaaccata**AAG**cctaaagaggtcaagccc	72.2	46
K371E	gtgcaaccatagaacct**GAG**gaggtcaagcccgaaacaaaacc	74.2	43
E372K	gcaaccatagaacctaaa**AAG**gtcaagcccgaaac	69.4	35
K374E	ccatagaacctaaagaggtc**GAG**cccgaaacaaaaccaccagaaccc	75.2	47
E376K	cctaaagaggtcaagccc**AAG**acaaaaccaccagaacccaag	73.5	42
K378E	gaggtcaagcccgaaaca**GAG**ccaccagaacccaagaaaacc	75.4	42
E381K	gcccgaaacaaaaccacca**AAG**cccaagaaaacctttaacag	71.5	42
K383E	gaaacaaaaccaccagaaccc**GAG**aaaacctttaacagtgtcagc	72.0	45
K384E	caaaaccaccagaacccaag**GAG**acctttaacagtgtcagc	72.7	41
K391E	cctttaacagtgtcagc**GAG**attgaccgactgtcaagaatagcc	73.1	44

Table 2.1: Mutagenic primers. Forward primers are shown for each deletion and point mutation that was introduced into the $GABA_AR$ α1 subunit. Reverse primers were the reverse complement oligomer. Mutagenic codons are in capital letters and bolded. The WT α1 subunit served as the template cDNA for all constructs. Melting temperatures (T_m) were calculated with [Eq. 1].

2.2.6: Calcium Phosphate Transfection

Forty eight to seventy two hours after plating onto pDL-coated glass coverslips, once the monolayer had grown to ~70% confluency, HEK293 cells were co-transfected with cDNAs for the $GABA_AR$ α1, β2 and γ2s subunits, as well as AAV-GFP, via a calcium phosphate method (Chen and Okayama 1987). The transfection solution contained 270 mM $CaCl_2$, 50 mM Bis(2-hydroxyethyl)-2-aminoethanesulfonic acid, 280 mM NaCl, and 1.5 mM $NaHPO_4$. The pH of the solution has been shown to greatly impact the efficiency of calcium phosphate precipitation of cDNA (Chen and Okayama, 1987); therefore the transfection solution was carefully adjusted and maintained at a pH of 6.95. Equal parts of each cDNA, for a total of 10 μg, were added to the transfection solution. Calcium phosphate precipitation of cDNA was allowed to progress for 30-45 min; then the transfection reaction was added to cell media. The transfection reaction is toxic to cells; therefore, the media was replaced with fresh MEM+ after 18-20 hours. Robust expression of the $GABA_AR$ subunits was evident 24-72 hours after transfection.

2.3: Surface Expression

The surface expression of the $GABA_AR$ was measured via immunocytochemistry labeling of the α1 subunit protein; followed by confocal visualization or luminescent quantification of labeling (Hague, Uberti et al. 2004). The $GABA_AR$ α1 subunit was the focus of these dissertation studies, but I only labeled for the α1 subunit because both the α and β subunits are necessary for GABA-gated currents (Amin and Weiss 1993; Boileau, Evers et al. 1999; Martin and Olsen 2000). Furthermore, the α1 subunit is not expressed on the cell surface as a homo-pentamer (Peran, Hooper et al. 2006). Therefore, labeling of the α1 subunit gave an accurate estimation of the location of the functional heteromeric complex. The primary antibody used in all experiments was a mouse anti-α chain monoclonal antibody specific to the N-terminus of the α1 subunit (Millipore, MAB339). I chose an extracellular epitope for two reasons. First, this allowed me to label only the proteins on the cell surface. Second, all mutagenesis undertaken in this dissertation work was within the intracellular loop domain and therefore did not directly change the epitope. Different secondary antibodies were used for each quantification method according to the needs of the assay. For confocal visualization, I used two distinct donkey anti-mouse antibodies that were conjugated to different fluorophores: FITC and Rhodamine (Jackson ImmunoResearch Laboratories, Inc., 715-095-150 and 715-025-150). For the luminescent assay, I used a sheep anti-mouse secondary antibody conjugated to horseradish peroxidase (HRP; GE Healthcare, NA931V). For an overview of immunocytochemical methods see Figure 2.3.

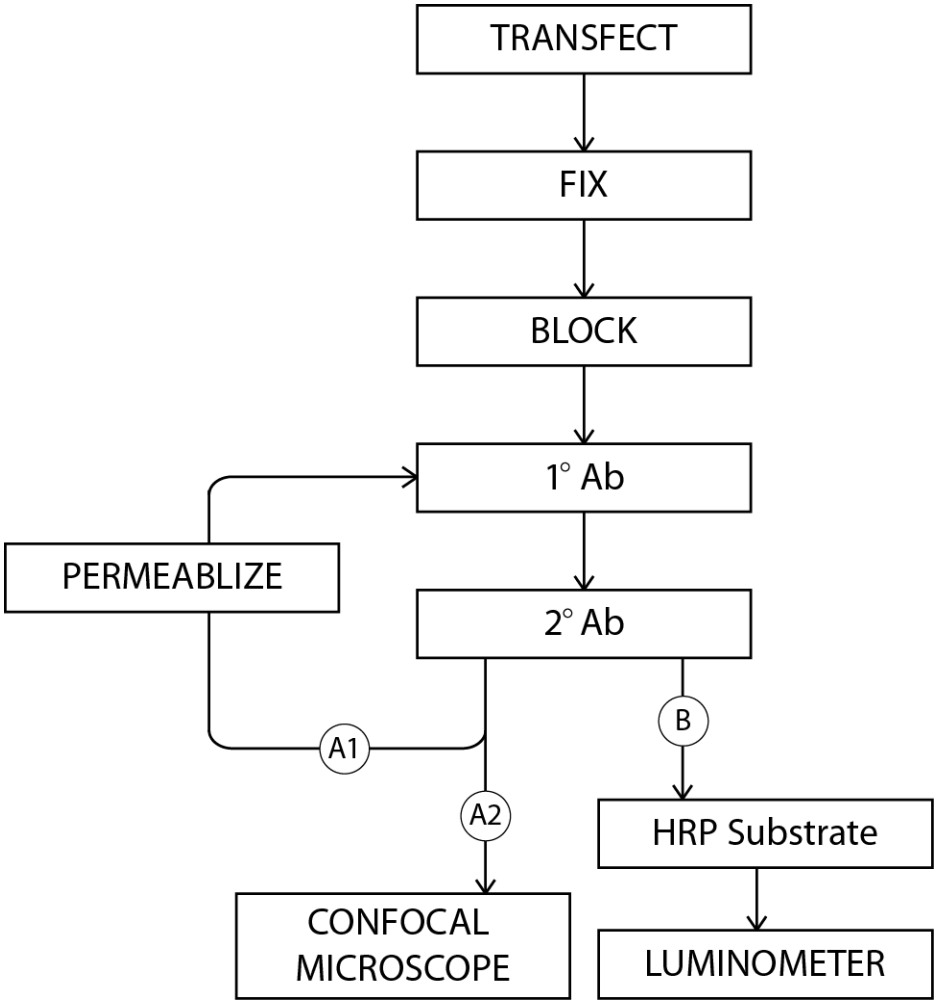

Figure 2.3: Immunocytochemistry protocols. Flowcharts depicting the procedures that were used to assess surface expression of the $GABA_AR$ with (A) confocal microscopy and (B) luminometer quantification of antibody labeling. HEK293 cells were transfected using the calcium phosphate method (Chen 1987), fixed with paraformaldehyde, then surface proteins were blocked, labeled with primary antibodies (1° Ab) specific to an extracellular epitope of the α1 subunit, followed by secondary antibodies (2° Ab) that were conjugated according to the needs of each assay. (A) Cells prepared for confocal analysis of protein localization underwent a second round of antibody labeling in (1) permeablizing conditions with a distinct secondary antibody before (2) transfer to the confocal microscope. All steps were at room temperature, 22 °C. All incubations lasted 1 hour and cells were washed three times for 5 min between each incubation step.

2.3.1: Confocal Microscopy

To prepare specimens for confocal visualization of receptor surface expression, HEK293 cells were plated onto pDL-coated glass coverslips and transfected as described in Section 2.2.6. After 48 hours to allow for $GABA_AR$ expression, cells were immuno-labeled with each incubation step at room temperature for 1 hour. Cells were rinsed three times with Trizma-buffered saline (TBS, Sigma), fixed with 4% paraformaldehyde in TBS, rinsed again, then incubated in 10% normal donkey serum (Sigma, D9663) in TBS (NS/TBS). Surface proteins were labeled in non-permeablizing conditions with a 1:500 dilution of the primary antibody in 2.5% NS/TBS followed by a 1:300 dilution of the secondary antibody conjugated to FITC in 2.5% NS/TBS. A second blocking step in 10% NS/TBS with 0.1% TritonX-100 was necessary to permeablize cell membranes. Proteins throughout the entire cell were then able to be labeled with a 1:500 dilution of the primary antibody in 2.5% NS/TBS followed by a 1:300 dilution of the secondary antibody conjugated to Rhodamine in 2.5% NS/TBS. Cells were then washed three times for 5 min each with TBS. Finally, coverslips were mounted onto glass slides using Vectashield mounting medium with DAPI (Vector Laboratories; H-1500). A drop of mounting medium was placed onto a glass slide and the coverslip containing labeled cells was inverted and placed onto the medium. Excess medium around the coverslip was aspirated off and the edges were sealed with clear nail polish.

Images were recorded using a Zeiss LSM510 microscope equipped with a 488nm Argon laser for FITC excitation and a 543 nm HeNe laser for Rhodamine excitation. For a schematic of the confocal microscope, including excitation and emission wavelengths for each fluorophore, see Figure 2.4. A z-stack was generated for each cell which was then compressed into one plane using ImageBrowser software (Zeiss). (A z-stack is a series of two dimensional images that progress vertically through the specimen in the z plane of Cartesian space.) In this way I accounted for total cell fluorescence. I analyzed images with ImageJ software (NIH) by outlining

individual cells and measuring the Integrated Density value for each fluorophore. This measure is a sum of the brightness of each pixel within the selection area. I also generated a Surface Plot for each cell to display the pixel intensity in three dimensions. Integrated density values for the surface fluorophore were divided by the sum of integrated density values for both fluorophores to determine the ratio of total α1 labeling that was on the cell surface. This measure was used to quantitatively compare the surface expression between WT and mutant α1 subunits.

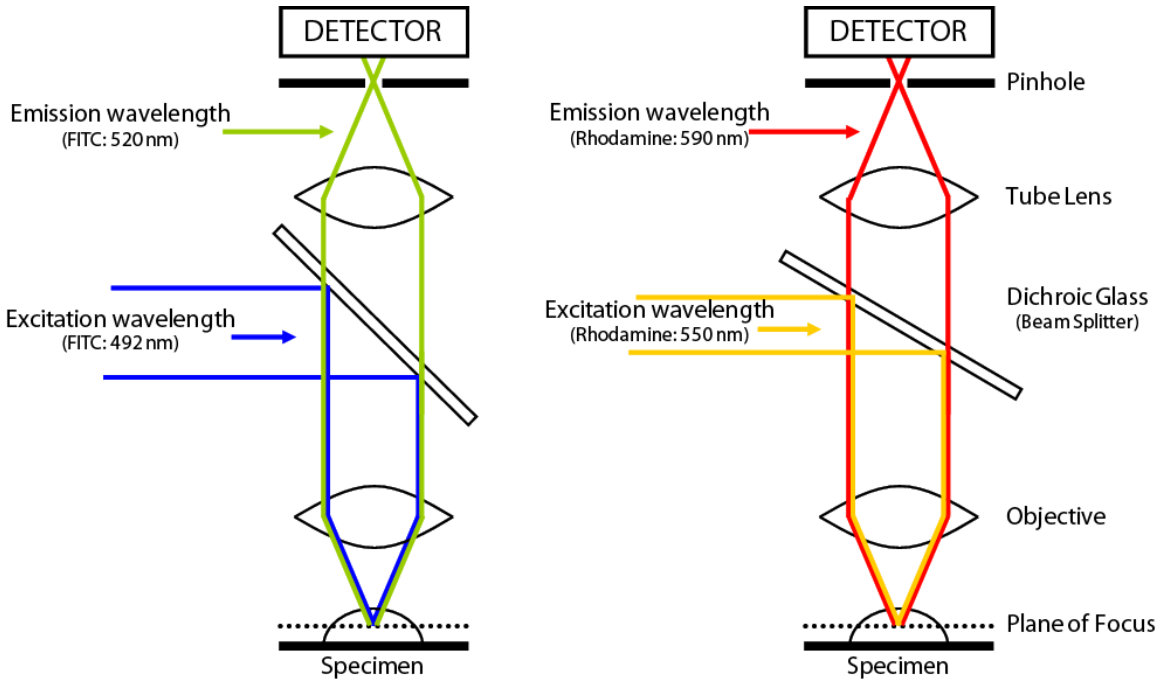

Figure 2.4: The Confocal Microscope. Schematic depicts the light path within the confocal microscope, indicating the excitation and emission wavelengths for FITC and Rhodamine respectively. The beam splitter is composed of dichroic glass which selectively passes and reflects precise wavelengths of light according to is orientation. The objective lens determines the focal plane within the specimen and the tube lens focuses light through a pinhole to be read by the detector at high resolution.

2.3.2: Luminescence Assay

HEK293 cells were plated in triplicate for each condition onto 35 mM CellBIND-treated dishes (Corning; CLS3294) and transfected with the calcium phosphate method, described in Section 2.2.6, although the transfection reaction was left on the cells for 72 hours to increase the number of transfected cells. Cells were then rinsed three times with phosphate-buffered saline plus calcium (PBS-Ca^{2+}; GIBCO), fixed with 4% paraformaldehyde in PBS-Ca^{2+} for 1 hour, rinsed again, then incubated with blocking buffer (2% nonfat milk in PBS-Ca^{2+}, pH 7.4) for 1 hour. Cells were then incubated in blocking buffer with a 1:1000 dilution of the primary antibody followed by a 1:2000 dilution of the HRP-congugated secondary antibody for 1 hour each. Next, cells were rinsed two times with blocking buffer and once with PBS-Ca^{2+}, and then incubated with SuperSignal® WestPico Chemiluminescent Substrate (Thermo Scientific) for 15 s. Enzymatic breakdown of the substrate by HRP emits light. The amount of luminescence was determined in arbitrary relative light units using a TD20/20 luminometer (Turner Designs Instrument).

In order to determine if experimental conditions were within the limits of the luminescence assay I first measured the amount of background staining in mock-transfected cells (expressing GFP to verify transfection success) and then I measured the surface expression of WT receptors under conditions to vary the amount of primary antibody and the amount of receptor protein. First, mock-transfected cells were labeled with primary antibody at a 1:1000 dilution and secondary antibody at a 1:2000 dilution as described previously. There was a 20-fold difference in the luminescent output from mock-transfected cells and cells expressing the WT receptor (Fig. 2.5A). Therefore, positive labeling resulted in luminescence that was well above the background signal. Second, WT transfected cells were labeled with increasing amounts of primary antibody from 1:10,000 to 1:100 (Fig. 2.5A). Primary antibody dilutions of 1:100 and 1:1000 yielded significantly more luminescence than 1:10,000 (Students t-test, $p < 0.05$).

However, there was no significant increase in labeling that was gained by increasing the amount of primary antibody from 1:1000 to 1:100 (Students t-test, $p > 0.05$). Next, I measured surfaced expression across a range of transfection conditions; 3, 10, and 30 µg of total cDNA, in equal parts of the cDNAs for the α1, β2, and γ2 subunits and GFP, were used in the transfection reaction (Fig. 2.5B). Increasing the amount of cDNA beyond 3 µg yielded significantly more luminescence (Students t-test, $p < 0.05$). However, there was no significant increase in labeling by increasing the amount of cDNA from 10 to 30 µg (Students t-test, $p > 0.05$). In sum, a 1:1000 dilution provided sufficient primary antibody in excess to label surface proteins translated from 10 µg of transfected cDNA.

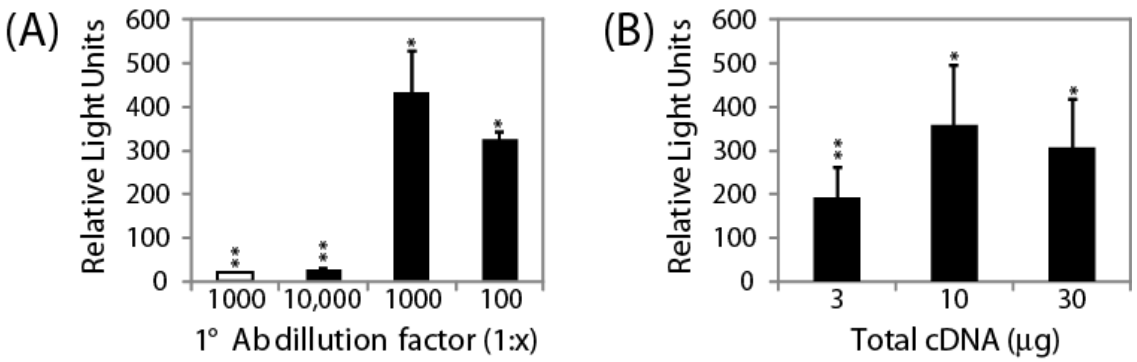

Figure 2.5: Immunocytochemistry controls. The TD20/20 luminometer was used to read HRP-luminol breakdown from fixed cells surface-labeled with ms anti-α1 subunit primary antibodies (1° Ab) and anti-ms-HRP secondary antibodies (2° Ab). In order to determine the maximal range of the luminometer assay we varied both the (A) 1° Ab dilution (n = 3) and (B) the total amount of cDNA that was used to transfect HEK293 cells (n = 6). The 1° Ab labeled WT (black) surface receptors in excess at a 1:1000 dilution. Labeling with 1:10,000 1° Ab did not produce a luminescence signal above the background signal, shown with mock transfected cells expressing only GFP (white, n = 12). Cells transfected with 10 µg of cDNA produced a protein yield that was labeled in excess by 1° Ab at 1:1000 and 2° Ab at 1:2000. Students t-test $p < 0.05$ for significant differences from *1:10,000 and **1:1000 or *3 µg and **10 µg.

2.4: Electrophysiology

The amplitude of whole cell currents (*I*) is dependent on the amplitude of single channel currents (*i*), the number of receptors on the cell surface (*n*) and the open probability of channels (P_O) and is defined by [Eq. 2].

[Eq. 2] $$I = i * n * P_O$$

In Section 2.3, I described how changes in surface expression (*n*) were assessed via immunocytochemistry with confocal imagery and luminescent quantification of labeling (Hague, Uberti et al. 2004). In this section I will describe how whole-cell and single channel currents were determined to functionally measure $GABA_AR$ activity.

In vitro voltage clamp electrophysiology was used to assay the function of the WT $GABA_AR$ and of mutant receptors that lack the intracellular loop domain and harbor charge switch point mutations. Whole-cell recordings were used to study the properties of receptor gating and ion permeation with pharmacologic agents and manipulation of the driving force on permeant ions. Excised patch recordings allowed for rapid solution exchange in order to discretely assess the time course of desensitization. Finally, single channel recordings permitted direct analysis of current amplitude and channel open probability.

2.41: Solutions

The standard intracellular solution (I1) contained 120 mM KCl, 2 mM $MgCl_2$, 10 mM EGTA, and 10 mM HEPES and was adjusted to pH 7.2 with NaOH. Cells were perfused with the standard extracellular solution (E2) that contained 160 mM NaCl, 10 mM HEPES, 6 mM *D*-glucose, 3 mM KCl, 1 mM $MgCl_2$, and 1.5 mM $CaCl_2$ and was adjusted to pH 7.4 with HCl (Table 2.2). The standard physiology solutions (I1:E1) established a nearly symmetrical chloride gradient with a theoretical reversal potential of -7.75 mV (Table 2.3). Changes in ion permeation were addressed using ion replacement solutions, where Na^+ and Cl^- were replaced with N-methyl-*D*-glucamine (NMDG) and gluconate, respectively. The low chloride intracellular saline (I2) contained 68 mM KCl, 48 mM potassium gluconate, 2 mM $MgCl_2$, 10 mM EGTA, and 10 mM HEPES and was adjusted to pH 7.2 with NaOH. The low chloride extracellular saline (E2) contained 5 mM NaCl, 155 mM sodium gluconate, 10 mM HEPES, 6 mM *D*-glucose, 3 mM KCl, 1 mM $MgCl_2$, and 1.5 mM $CaCl_2$ The low sodium extracellular saline (E3) contained 14 mM NaCl, 146 mM NMDG, 10 mM HEPES, 6 mM *D*-glucose, 3 mM KCl, 1 mM $MgCl_2$, 1.5 mM $CaCl_2$; both the E2 and E3 solutions were adjusted to pH 7.4 with HCl. For a side by side comparison of physiological solutions, see Table 2.2 and for specific recipes see Appendix A.

Solute	I1	I2	E1	E2	E3
NaCl	-	-	160 mM	5 mM	14 mM
KCl	120 mM	68 mM	3 mM	3 mM	3 mM
NMDG	-	-	-	-	146 mM
Na gluconate	-	-	-	155 mM	-
K gluconate	-	48 mM	-	-	-
$MgCl_2$	2 mM	2 mM	1 mM	1 mM	1 mM
$CaCl_2$	-	-	1.5 mM	1.5 mM	1.5 mM
HEPES	10 mM	10 mM	10 mM	10 mM	10 mM
EGTA	10 mM	10 mM	-	-	-
D-glucose	-	-	6 mM	6 mM	6 mM
pH correction					
Cl	-	-	0.2 mM	0.2 mM	0.2 mM
NaOH	12.5 mM	12.5 mM	-	-	-
Final ion composition					
$[Cl^-]$	124 mM	72 mM	168 mM	13 mM	168 mM
$[Na^+]$	12.5 mM	12.5 mM	160 mM	160 mM	14 mM
$[K^+]$	120 mM	116 mM	3 mM	3 mM	3 mM

Table 2.2: Physiological Solutions. Intracellular (I) and extracellular (E) salines were made with standard salt levels (1), low chloride (2), and low sodium (3). The millimolar concentration of each reagent is listed for the electrophysiology salines used in this study, together with the final concentration of acid or base used to adjust intracellular solutions to a pH of 7.2 and extracellular solutions to a pH of 7.4. The bottom two rows list the final concentrations of monovalent anions and cations for each solution. Intracellular and extracellular solutions were adjusted to a final osmolarity of 315 and 325 mOsm respectively with sucrose or deionized water as necessary.

Conditions	Solutions	E_{Cl} (mV)	LJP (mV)
Standard	I1:E1	-7.75	+5.7
Low extracellular chloride	I1:E2	+57.0	-5.5
Low extracellular sodium	I1:E3	-7.75	+1.8
Low intracellular chloride	I2:E1	-21.6	+9.6

Table 2.3: Theoretical reversal potential and liquid junction potential values. Values for the theoretical reversal potential (E_{Cl}) were calculated with the Nernst Equation [Eq. 3]. Values for the liquid junction potential (LJP) were calculated with Clampex software (Molecular Devices). Theoretical values are shown for each combination of intracellular (I) and extracellular (E) salines that was used experimentally.

The $GABA_AR$ has been shown to be selectively permeable to monovalent anions, in particular, chloride (Keramidas, Moorhouse et al. 2004; Jensen, Schousboe et al. 2005). Therefore, decreasing the extracellular concentration of chloride [E2] was expected to shift the reversal potential of currents in the positive direction. Likewise, decreasing the intracellular concentration of chloride [I2] was expected to cause a negative shift in the reversal potential of currents through this anionic pore. If mutations switched the charge selectively of the pore to allow cation permeation, the low sodium extracellular saline [E3] was predicted to cause a negative shift in the reversal potential. Comparison of these ion replacement solutions was primarily used to investigate the charge selectivity of the $GABA_AR$ pore.

Theoretical reversal potentials (E_{Cl}) were calculated for each combination of intracellular and extracellular solutions with the Nernst equation, [Eq. 3], assuming membranes were permeable only to chloride (Table 2.3). Deviations from E_{Cl} indicated that changes in channel permeability or selectivity were caused by mutagenesis. Subscripts refer to the intracellular (i) and extracellular (o) concentrations of chloride ($[Cl]$). Temperature (T) was 295 K (22 °C), the universal gas constant (R) is 8.13 J/K*mol and Faraday's constant (F) is 9.65 x 10^6 C/mol.

[Eq. 3] $$E_{Cl} = \frac{RT}{F} * \ln\left([Cl]_i/[Cl]_0\right)$$

Liquid junction potential values caused by differences in the relative mobilities of ions within each saline were calculated in Clampex 9.2 (Molecular Devices, Sunnyvale, CA) (Table 2.3). Then, experimentally calculated reversal potential values were corrected *a posteriori* by subtracting the junction potential value.

2.4.2: Electrophysiology Circuitry

The primary function of ion channels is to allow the movement of ions across the cell membrane, or in other words, to pass current (*I*). The architecture and composition of the ion channel pore establishes the ability of the ion channel to pass current and determines the selectivity of the ion channel for specific ions. Each ion channel then has properties that both allow and restrict ion flow. Barriers to ion flow are termed resistors and pathways for ion flow are described as conductors. Resistance (*R*) and conductance (*g*) are inversely related. In the context of the whole-cell, ion channels behave as variable resistors in parallel to one another, with additive conductances. Therefore, the sum of individual resistances (R_{mem}) determines the amount of current that may flow across the cell membrane (I_{mem}) when there is a potential difference (ΔV_{mem}) across the membrane, according to Ohm's Law [Eq. 4].

[Eq. 4] $$\Delta V_{mem} = I_{mem} R_{mem}$$

In the whole-cell patch configuration, the micropipette is continuous with the cell membrane; therefore, the resistance of the electrode and the cell membrane are in series (R_{series}). In voltage clamp electrophysiology the membrane potential (V_{mem}) is driven to equal a command potential (V_{cmd}). The amount of transmembrane current that is necessary to maintain V_{cmd} is equal and opposite to I_{mem} (Fig. 2.6). Thus, the electrophysiology circuitry is able to detect the transmembrane current that is elicited by each experimental condition. Importantly, electrophysiology circuitry must be able to accurately measure experimental I_{mem} without distorting the signal. Two factors that must be considered in order to preserve the accuracy of electrophysiological recordings are the time course of changes in potential and the fidelity of voltage clamp.

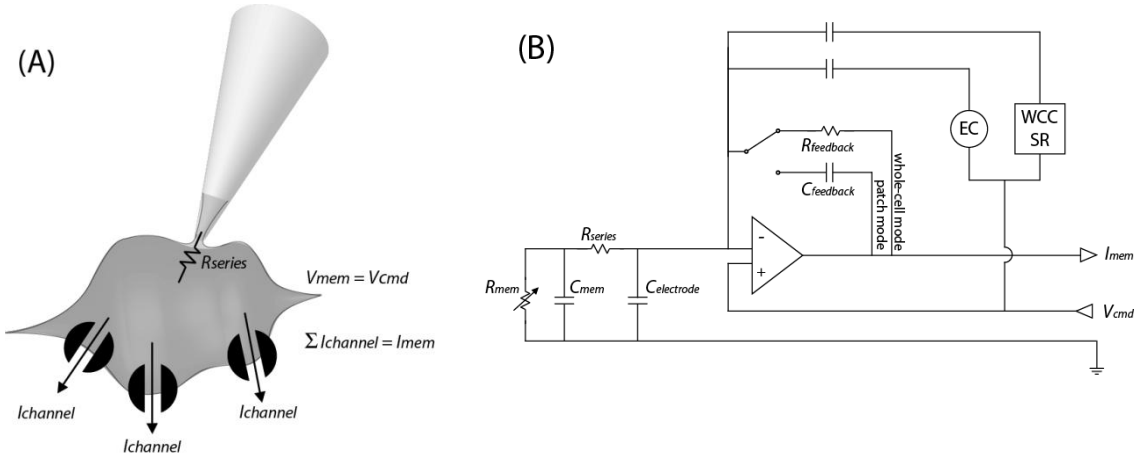

Figure 2.6: Electrophsiology circuitry. (A) Cartoon (not drawn to scale) depicting the whole-cell patch configuration, including the micropipette (white) and a single HEK293 cell (gray) expressing ion channels (black). Series resistance (R_{series}) is established by the initial resistance of the electrode and quality of the seal. In voltage-clamp mode, the membrane potential (V_{mem}) is driven to equal the command potential (V_{cmd}); the amount of current that is necessary to maintain V_{cmd} is equal and opposite to the transmembrane current of the membrane (I_{mem}), which is the sum of currents passed through each ion channel ($I_{channel}$). (B) Circuit diagram of whole-cell voltage clamp patch configuration showing the compensation loops used to correct for electrode capacitance (EC), whole-cell capacitance (WCC), and series resistance (SR) in order to ensure that $V_{mem} = V_{cmd}$. In the whole-cell mode, a resistive feedback loop ($R_{feedback}$) is applied to accommodate large currents and prevent charging of the membrane. A capacitative feedback loop ($C_{feedback}$) is used in the patch mode to record single channel currents.

First, V_{mem} does not change instantaneously in response to changes in V_{cmd}, but changes with a time course determined by cell capacitance and access resistance as defined by [Eq. 5].

[Eq. 5a] $$V_{mem} = V_{cmd}\left(1 - e^{-t/\tau}\right)$$

[Eq. 5b] $$\tau = R_{series}C_{mem}$$

Capacitance (C) is a property of the cell membrane (C_{mem}) based on its ability to separate charges. The strength of a capacitor is determined by the area of the conductors and the distance between them; the thinness of biological membranes makes the cell membrane an excellent capacitor. Lipid bilayers have an average capacitance of 1 μF/cm^2; therefore, the amount of whole-cell capacitance increases with cell size. Likewise, capacitance measures may be used to estimate cell size. The amount of charge stored in a capacitor is also established by potential energy; therefore, with constant voltage clamp there are no capacitative effects. However, a change in V_{cmd} will cause a rearrangement of charges to accompany the new potential. The time that it takes to "charge" or "discharge" the membrane in response to a voltage step is reflected by transient capacitative currents in physiological recordings when $V_{mem} \neq V_{cmd}$. Hence, capacitative currents have the ability to distort recordings with voltage steps.

I determined resistance and capacitance values from three electrodes before and after patch formation: $R_{electrode}$ = 6.13 ± 0.13 mΩ, R_{series} = 13.7 ± 4.06 mΩ, and C_{mem} = 19.9 ± 1.04 pF (n = 3; mean ± standard error of the mean (SEM)). Assuming 1 μF/cm^2, cells had an average diameter of 25.8 ± 1.24 μm. From [Eq. 5b], I determined that τ = 0.30 ± 0.12 ms. Therefore, the time that it would take for V_{mem} to equal 95% of V_{cmd} was calculated from [Eq. 5a] as t = 0.90 ± 0.36 ms (n = 3; mean ± SEM). The most rapid change in V_{cmd} that I applied in my dissertation work was at 5 ms intervals, more than five times slower than the theoretical limit of the membrane. Nonetheless, whole-cell capacitance may be electronically compensated by

applying current to negate capacitative transients (Fig. 2.6). Current voltage relationships determined with the 5 ms voltage step ramp protocol were not significantly different when determined with or without whole-cell capacitance compensation in regards to the reversal potential or the degree of current rectification (Fig. 2.7). Therefore, the effect of cell capacitance did not hinder my data collection and no whole-cell capacitance compensation was applied to limit the pre-processing of raw data.

The electrode also serves to separate charges between the intracellular and extracellular solutions and therefore contributes capacitance ($C_{electrode}$) to the whole-cell circuit. The effects of $C_{electrode}$ may be addressed mechanically by increasing the distance between charges and/or decreasing the effective surface area of the capacitor. Altering the geometry of the micropipette with different puller programing, using thick-walled glass to manufacture micropipettes, and coating the tip of the micropipette with an insulating material such as sylgard will increase charge separation to decrease capacitance. Reducing the amount of contact between the micropipette and bath solution will also decrease capacitance by decreasing the surface area of the capacitor. In order to eliminate the effects of $C_{electrode}$ from single channel records micropipettes were fabricated with thick-walled borosilicate glass and coated with sylgard. Electronic compensation of $C_{electrode}$ was achieved before patch formation by applying current that is equal and opposite to effectively subtract the capacitative transient (Fig. 2.6).

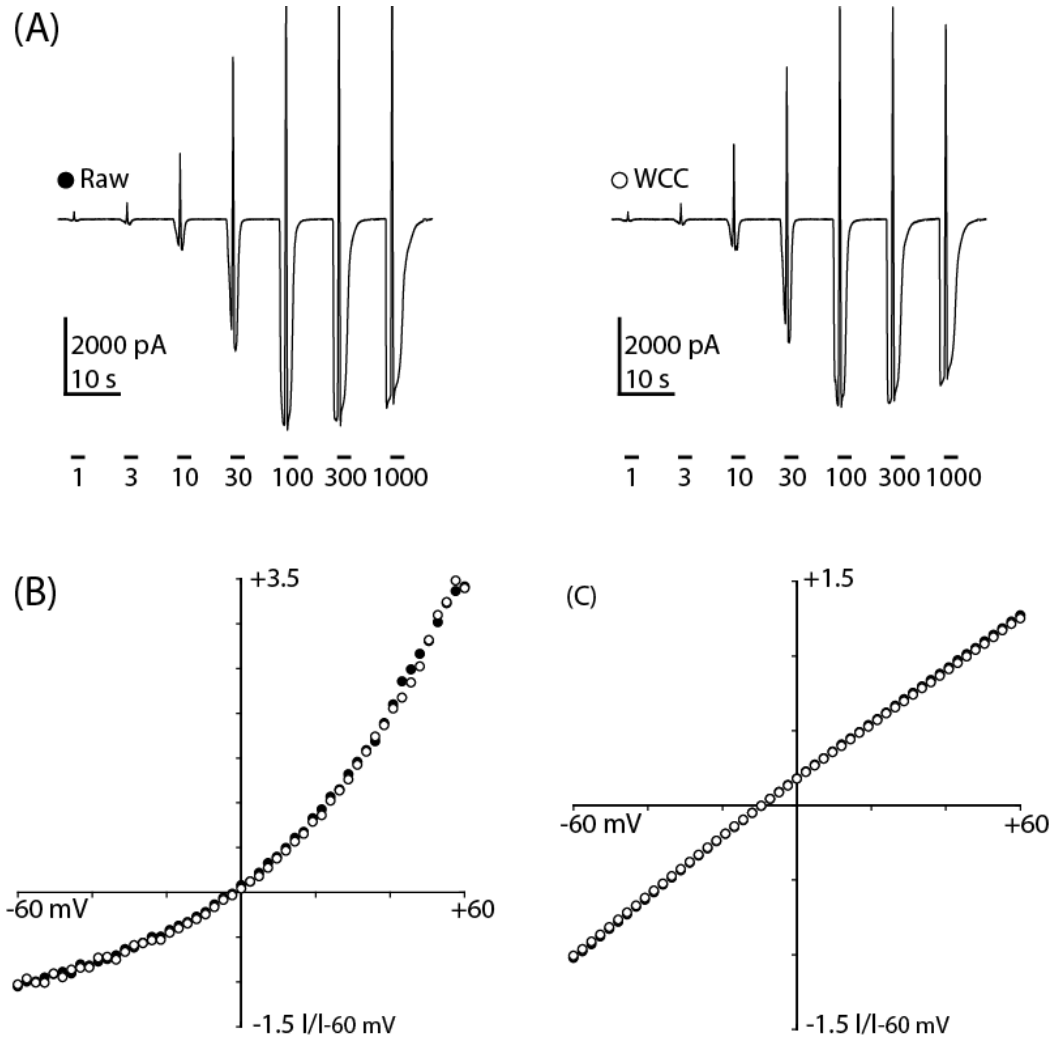

Figure 2.7: Whole-cell capacitance. (A) Representative traces determined from the same patch without (Raw) and with whole-cell capacitance (WCC). Bars indicate the duration of GABA application and are labeled with the concentration (μM). Representative IV relationships from the same patch are shown that were gathered without (black) and with WCC (white) from currents elicited by (B) 10 μM and (C) 1 mM GABA. Electronic compensation did not significantly alter the reversal potential or rectification profile (paired t-test, $p > 0.05$, $n = 4$).

Second, the goal of the voltage clamp electrophysiology circuitry is to ensure that $V_{mem} = V_{cmd}$ (Fig. 2.6). However, according to Ohms' law [Eq, 4] there is a potential drop that occurs when current flows through a resistor. When ion channels are in the active conducting state, equal and opposite current is passed through the micropipette to compensate for transmembrane current and maintain the command potential. A voltage drop will occur across R_{series} and the membrane potential experienced by the cell will, therefore, deviate from the theoretical command potential resulting in a loss of voltage-clamp. Large currents will thus cause a more pronounced loss of clamp. Furthermore, R_{series} is influenced by the quality of the seal; a "leaky" patch will increase R_{series} and the voltage drop will be greater.

Theoretically, if a 2 MΩ electrode yields a 5 MΩ series resistance and the cell is passing 1 nA of transmembrane current with a command potential of -60 mV the actual membrane potential is -55 mV [Eq. 4]. This difference in driving force translates to less than a 10% difference in current magnitude. The amplitude of currents elicited by 0.3-1000 μM GABA were not significantly different at holding potentials of -60 mV or -55 mV (n=34; paired t-test). Nonetheless, this highlights the importance of low resistance electrodes and high resistance seals before achieving the whole-cell configuration in order to maintain low R_{series} and therefore, maintain the voltage clamp.

2.4.3: The Electrophysiology Rig

The necessary components of the electrophysiology setup or "rig" include a proper environment to maintain the recording material, a means of visualizing the preparation, a stable platform for recording, and an electronic means for data acquisition and storage (Sherman-Gold, Finkel et al. 1993). I used an Axiovert 200 inverted microscope (Zeiss) equipped with 10X and 40X objectives, a HAL100 halogen lamp and HBO100 FluoArc fluorescence source, and LD condenser for phase contrast visualization (Fig. 2.8). HEK293 cells were co-transfected with GFP which served as a binary indicator of transfection success. The fluorescent source along with a HQ GFP filter set allowed for visualization of GFP expression in positively transfected cells, which were then targeted for experimental use. The microscope was mounted on a Micro-g anti-vibration table (Technical Manufacturing Corp., 63-563) to eliminate mechanical noise (Fig. 2.8). Likewise, micromanipulators for positioning the perfusion head (Scientifica Ltd., LBM-7) and maneuvering the electrode (Sutter, MP-225) were stably mounted to the microscope (Fig. 2.8). Transmembrane currents were recorded with a MultiClamp 700B amplifier (Molecular Devices) in conjunction with a CV-7B voltage clamp headstage (Axon Instruments). Data was acquired with pClamp 9.2 software (Molecular Devices) and digitized with the DigiData 1322A interface (Molecular Devices) for electronic storage (Dell, Inspiron 6400-POS); see Section 2.4.6 for details of data acquisition. A 3 ml syringe (Becton, Dickinson & Co., 309585) continuous with the electrode holder, and therefore interior of the micropipette, was used to apply negative or positive pressure as necessary to achieve the proper patch configuration.

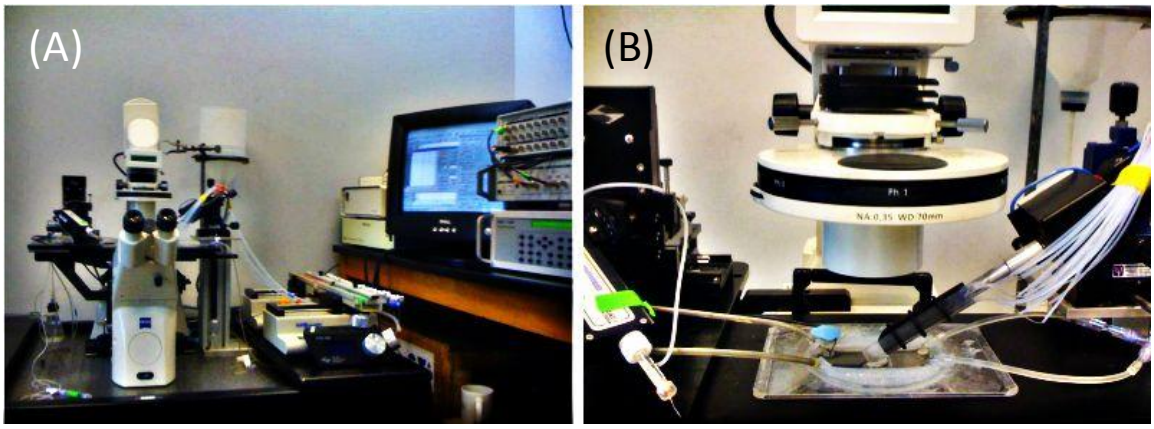

Figure 2.8: The Electrophysiology Rig and Perfusion System. (A) Setup and components of the rig and perfusion system are shown. [From Left to Right] The inverted microscope resided on an anti-vibration table to eliminate mechanical noise. Likewise, the electrode micromanipulator and perfusion head were stably mounted onto the microscope. Two 10-channel pumps delivered solutions to the perfusion head via PTFE tubing. The micromanipulator allowed for fine control of the electrode via the 3-axis controller. The rapid solution changer, amplifier, and digitizer were stacked to the right of the microscope and the computer monitor was positioned to prevent radiative noise. (B) A close-up view of the microscope stage shows orientation of electrode holder (left) and perfusion head (right). The bath dish was constructed by hand to provide a water-tight platform for coverslip isolation and drug delivery.

2.4.4: Achieving the patch configurations

Positive pressure was applied before the micropipette was lowered into the bath solution in order to keep the electrode tip clear of debris and to eliminate diffusion effects, thus preventing contamination of the intracellular solution. A 5 mV square wave was applied to assist in patch formation. Using coarse, then fine control, the electrode was positioned over the outer third portion of a GFP-positive HEK293 cell. The electrode was then lowered until contact was made with the cell, as evidenced by a jump in the baseline of the square waveform (~10% change in series resistance). Negative pressure was applied until a cell-attached configuration was achieved, marked by $R_{series} > 1$ GΩ. In order to transition into the whole-cell configuration, sharp negative pressure was given to "break in" to the cell. This transition was marked by a dramatic increase in the duration of the capacitative transients of the square wave. At this point an outside-out configuration could be attained by slowly pulling the electrode back on the diagonal axis with fine control. The size of capacitative transients decreased as the amount of membrane continuous with the electrode was decreased until a small membrane patch was excised off of the main cell body.

2.4.5: The Perfusion System

The perfusion system consisted of a gravity-driven backflow and a pump-driven 20-channel capillary tube perfusion head (Fig. 2.8). All solutions were removed by vacuum into a waste container. The microscope stage was equipped with a mounting frame formatted to hold a standard 100 mM petri dish. The perfusion bath was constructed by hand within a petri dish to provide a water-tight platform for stabilizing coverslips and delivering solutions (Fig. 2.8B). The perfusion head was mounted on a rapid solution exchanger (RSC 160; BioLogic) and connected to two 10-channel infusion pumps (KD Scientific) that were used to apply extracellular saline containing different concentrations of agonists and modulators at a rate of 1.0 ml/min (Fig. 2.8).

The solution changer was driven by protocols written in pClamp 9.2 (Molecular Devices); for specific protocols see Appendix C. Each pump held ten 10 ml syringes (Becton, Dickinson & Co., 309604) that delivered solutions to the perfusion head via polytetrafluoroethylene (PTFE) tubing (BioChem valve Inc., 008T16-080-20) connected by 3-way stopcocks (Baxter, 2C6240). The perfusion head was constructed with thin-walled borosilicate glass capillary tubes (Science Products GmbH, GB100T-8P) connected to the PTFE tubing by polyethylene capillary tubing (ID 0.86 mM, OD 1.27 mM). The perfusion system was calibrated daily by adjusting the solution flow so that the application of GABA was equal from every channel. Calibration of the perfusion system was checked regularly by measuring currents elicited by 10 μM GABA from each tube (Fig. 2.9).

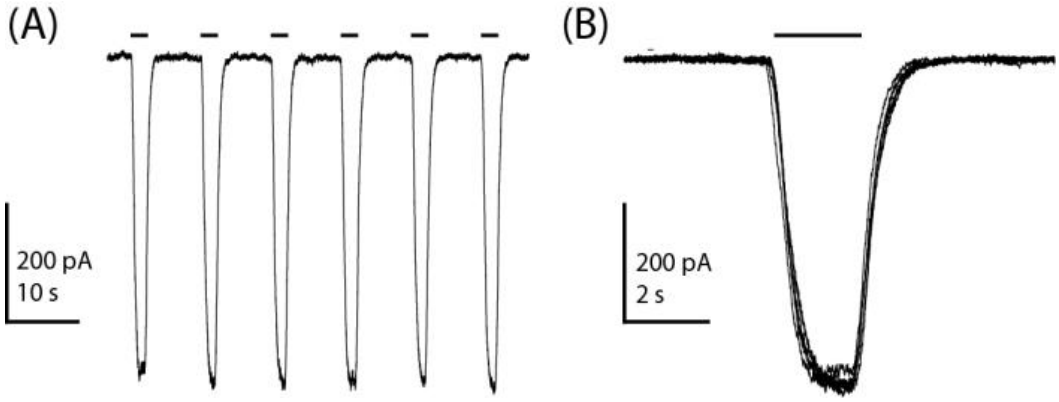

Figure 2.9: Perfusion system control. Calibration of the perfusion system was tested by applying the same concentration of agonist from every channel. Bars represent 2 s application of 10 μM GABA. The magnitude of currents did not vary more than 10% as shown (A) concatenated and (B) overlaid.

2.4.6: Whole-Cell Recordings

HEK293 cells transfected to express WT or mutant $GABA_A$Rs were characterized via whole-cell voltage clamp electrophysiology at room temperature, 22 °C, 36-72 hours after transfection. Patch pipettes for whole-cell recordings were fabricated from thin-walled borosilicate glass (TW150F-4, World Precision Instruments, Inc.) using a horizontal puller (P-97, Sutter Instrument Co.) to a final resistance of 2-5 MΩ; for specific puller program parameters see Appendix B.

Whole-cell currents were recorded in the acquisition mode of pClamp 9.2 software using a MultiClamp 700B amplifier, digitally filtered at 100 Hz using MultiClamp Commander software and digitized at 200 Hz using a DigiData 1322A interface (all Molecular Devices, Sunnyvale, CA); for specific parameters of data acquisition see Appendix C.

Data were gathered from at least 8 cells for each mutation from at least two independent transfections. To ensure consistency, several intracellular loop domain type responses were recorded from each batch of transfected cells. To generate the concentration-response relationship, each whole-cell patch was exposed to eight increasing concentrations of GABA for 2 s each with at least 8 s of washout time in between applications.

For more rapid solution exchange in order to assess the fast desensitization of channel gating, large (~10 pF; determined with MultiClamp Commander software) outside-out patches were pulled and positioned in the outflow of the solution changer, then 3 mM GABA was applied for 10 s and washed out for 20 s between sweeps.

To generate the current voltage (IV) relationship, a voltage ramp, from -60 mV to +60 mV and back to -60 mV (0.48 mV/ms for total ramp duration of 0.5 s), was applied within

the plateau response to each drug and after washout (Fig. 2.10D); for specific acquisition parameters of the ramp protocol see Appendix C. The baseline ramp was subtracted *a posteriori* to control for the basal response of the membrane. The timing of the voltage ramp was calibrated to occur within the plateau response to 2 s application of 10 µM and 1 mM GABA (Fig. 2.10). The up and down components of the voltage ramp were equivalent and the direction of the ramp did not alter the IV relationship (Fig. 2.11). Therefore for simplicity, each sweep was then normalized by its response at -60 mV and the up and down component of each ramp was averaged. Furthermore, I found that IV relationships were identical when determined from ramp data or by stepping the membrane potential to a different level for each trace (Fig. 2.12).

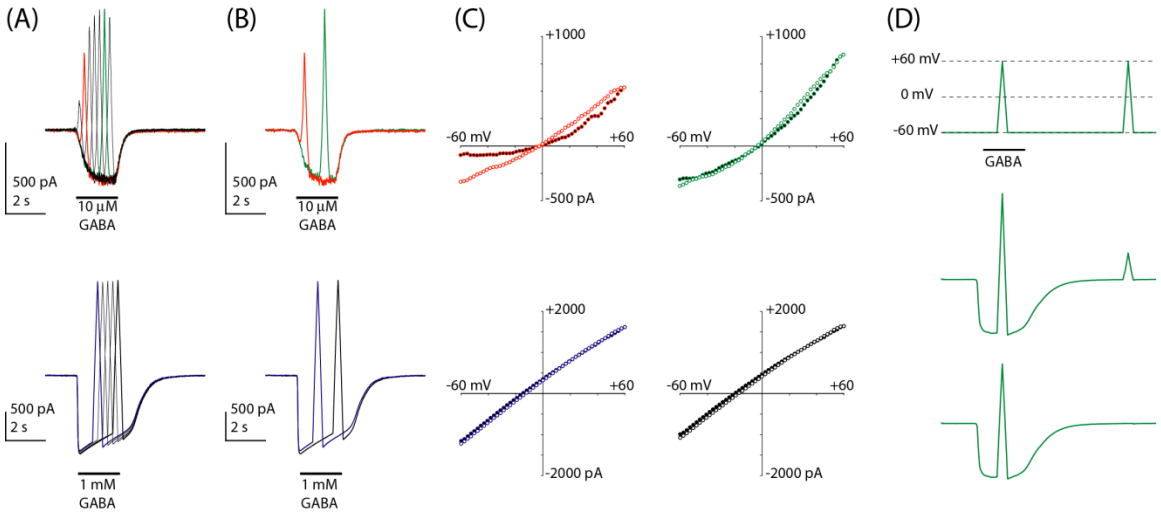

Figure 2.10: Ramp protocol. (A) The timing of the voltage ramp was optimized to occur within the steady state response to GABA at [upper panel] 10 µM and [lower panel] 1 mM. (B) Two sweeps are highlighted for each panel. (C) IV relationships generated from each sweep are shown with the up (black) and down (white) components of the ramp highlighted. There was no significant difference in reversal potential or rectification of the IV relationships generated from currents elicited by 1 mM GABA between the blue and black sweeps. However, the timing of the ramp greatly affected IV relationships from currents elicited by 10 µM GABA. Before steady state (red), the up and down components of the ramp showed significantly different rectification. At steady state (green), each component was equivalent. (D) The final timing of the ramp protocol is shown [upper panel] in relation to the 2 s application of GABA. An idealized current is shown [center panel] before and [lower panel] after baseline subtraction.

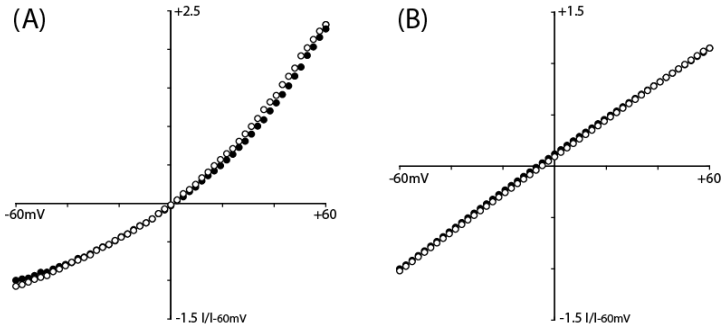

Figure 2.11.1: IV relationship is independent of ramp direction. IV relationships from currents elicited by (B) 10 μM and (C) 1 mM GABA. There were no significant differences between the up (black) and down (white) components of the ramp with respect to reversal potential or rectification index values (paired t-test, $p > 0.05$; $n = 34$).

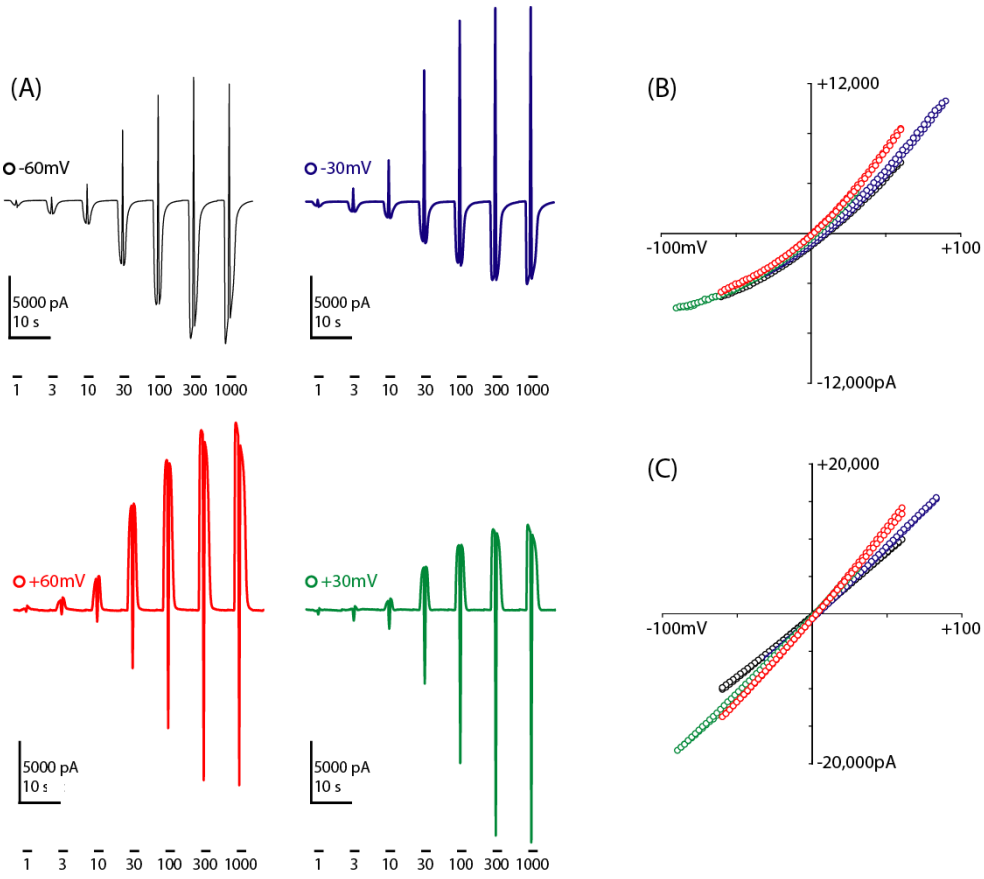

Figure 2.11.2: IV relationship is independent of ramp direction. (A) Representative traces gathered from the same patch at -60, -30, +30, and +60 mV holding potentials indicated next to each trace; ramp direction was up then down for negative holding potentials and inversed at positive holding potentials. Bars indicate the duration of GABA application and are labeled with the concentration (μM). IV relationships from currents elicited by (B) 10 μM and (C) 1 mM GABA. There were no significant differences in reversal potential or rectification index values at different holding potentials (Tukey's *post hoc*, $p > 0.05$; $n = 5$).

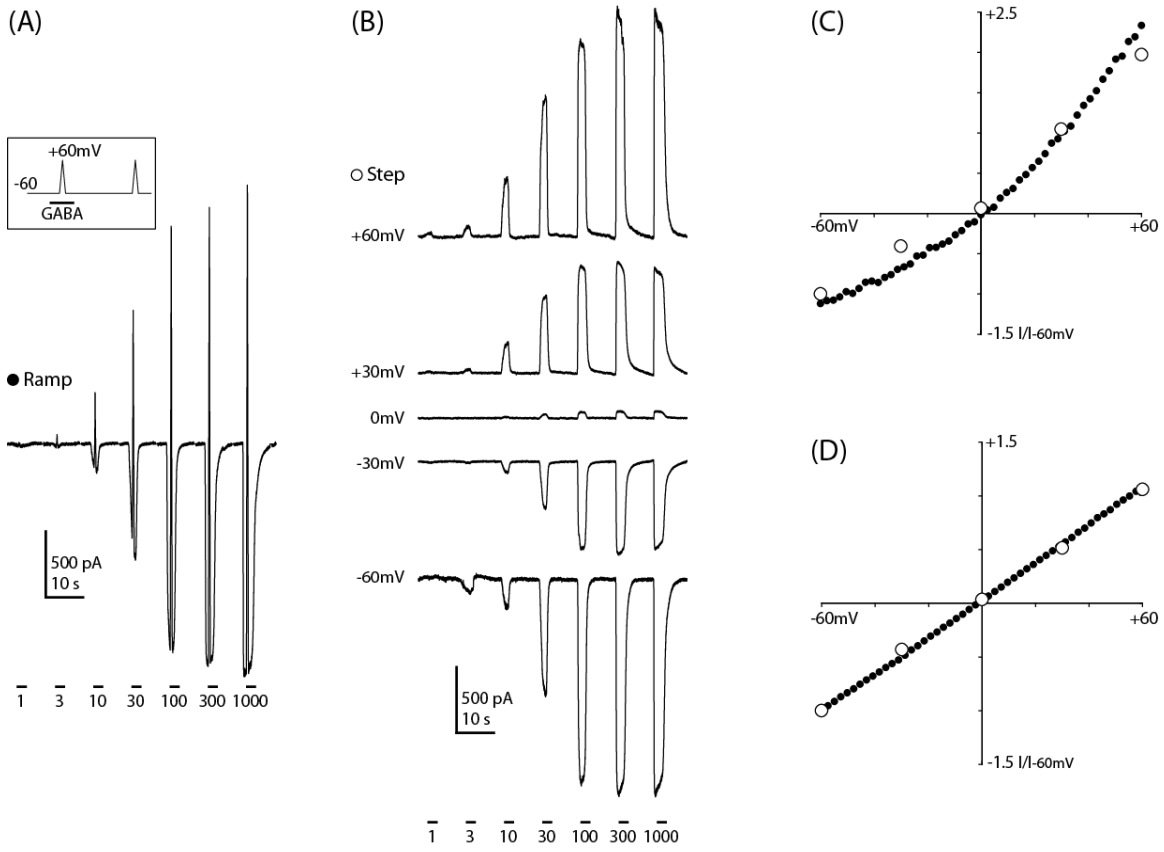

Figure 2.12: Ramp protocol verification. Representative traces gathered from the same patch (A) with application of the ramp protocol and (B) at varied holding potentials indicated next to each trace. Bars indicate the duration of GABA application and are labeled with the concentration (μM). (A) [Inset] shows the timing of ramp protocol with respect to 2 s GABA application. IV relationships from currents elicited by (C) 10 μM and (D) 1 mM GABA. There were no significant differences between data gathered with the ramp (black) or step (white) protocols with respect to reversal potential or rectification index values (paired t-test, $p > 0.05$, $n = 3$).

2.4.7: Whole-Cell Analysis

Analysis of recordings was carried out using MatLab (The Math Works, Inc.); for specific scripts see Appendix D. Peak currents (*I*) from GABA exposures spread over 3.5 logarithmic decades, were fit to the Hill equation, [Eq. 6], to determine the one-half maximum effective concentration (EC_{50}) of GABA, the maximum current amplitude (I_{max}) and the Hill coefficient (*nH*).

[Eq. 6] $$I = \frac{Imax*[GABA]^{nH}}{[GABA]^{nH}+EC_{50}{}^{nH}}$$

The desensitizing portion of currents elicited with saturating concentrations of GABA (1-3 mM) was defined as the time period from 200 ms after GABA onset to 200 ms before GABA was removed. Any traces still showing a rising phase during this time period were not included in this analysis. This segment was fit with an exponential equation, [Eq. 7a], to determine a weighted constant (*w*) for desensitization [Eq. 7b].

[Eq. 7a] $$y(t) = a * e^{b*t} + c * e^{d*t}$$

[Eq. 7b] $$w = \frac{a*b+c*d}{a+c}$$

Reversal potential (E_{rev}) values in normal and each ion replacement solution were calculated from the IV relationship by interpolating the membrane potential when $I = 0$ using the *interp1* Matlab function with *nearest neighbor* interpolation. When chloride was replaced with the larger anion gluconate, E_{rev} was used to calculate the relative permeability of gluconate (P_G/P_{Cl}) from the Goldman-Hodgkin-Katz (GHK) voltage equation, [Eq. 8], considering a pore permeable only to anions.

[Eq. 8] $$E_{rev} = \frac{RT}{F} * ln\left(\frac{\frac{P_G}{P_{Cl}}[G]_i+[Cl]_i}{\frac{P_G}{P_{Cl}}[G]_o+[Cl]_o}\right)$$

Rectification of the IV relationship was compared using a quantitative metric, the rectification index (*RI*) that was calculated by the following equation, [Eq. 9]. *RI* = 0 reflects an ohmic response, whereas *RI* < 0 reflects outward rectification and *RI* > 0 reflects inward rectification (Fig. 2.13).

[Eq. 9] $$RI = \frac{I_a}{I_b}$$

$$where \quad I_a = E_{rev} - 30mV \quad when \quad I_b = E_{rev} + 30mV$$

Rectification is theoretically predicted to occur in strong ionic gradients by the GHK current equation, [Eq. 10]. The constant field equation was also used to calculate the absolute permeability of chloride (*p*).

[Eq. 10] $$I_{Cl} = pz^2 \frac{EF}{\varphi} \frac{[Cl]_i - [Cl]_o e^{-zE/\varphi}}{1 - e^{-zE/\varphi}} \qquad where \quad \varphi = RT/F$$

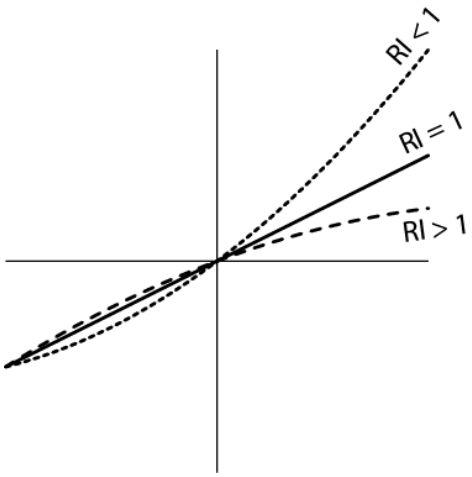

Figure 2.13: Rectification of currents. Rectification Index (RI) values are an indication of the directionality of current flow. The magnitude of inward and outward currents is equal under ohmic conditions (solid; RI = 1) exhibited by a linear IV relationship. IV relationships that exhibit inward (dashed; RI > 1) and outward rectification (dotted; RI < 1) are non-linear.

2.4.8: Single Channel Recordings

Single channel currents elicited from saturating GABA concentrations (3 mM) were recorded at -80 mV and filtered at 8 kHz with an Axopatch 200B amplifier (Molecular Devices) in the outside-out patch configuration. Data were digitized at 40 kHz using pClamp 9.2 and 10.0 (Molecular Devices). Patch pipettes were pulled from thick wall borosilicate glass (Warner Instruments, G150F-4) using a vertical puller (Narishige, PC-10). Pipette tips were coated with Sylgard-184 (Dow Corning) then fire polished to a final resistance of 8-12 MΩ ; for specific puller program parameters see Appendix B.

2.4.9: Single Channel Analysis

Recordings were low-pass filtered at 1kHz using QuB software (http://www.qub.buffalo.edu) and idealized using the segmental k-means (SKM) method (Qin 2004). Unitary current amplitudes were determined from a Gaussian fit of an all-points histogram (0.1 pA/bin) of single channel records that contained no overlapping openings. To determine burst open probability (P_O) clusters of bursts were first segmented by hand to eliminate bias from long-lived closed states. Using the critical time value determined by fitting a simple C-O-C model with the maximum interval likelihood (MIL) method (Qin, Auerbach et al. 1996) separate bursts were defined and then separated into segments using the ChpId preprocessing tool (Qin, Auerbach et al. 1997). Finally, the open probability of each segment was calculated from state dwell times determined with the statistics (Stat) tool. For specific use of QuB see Appendix E.

2.5: Statistical Analysis

Significant changes from the WT response induced by each construct were assessed using the statistics toolbox within MatLab (The Math Works, Inc., Natick, MA); for specific scripts see Appendix D. Each data metric was individually compared using the Student's t-test, paired or unpaired according to treatment (Student 1908; Student 1908). Multicomponent measurements were compared using Multivariate Analysis of Variance (MANOVA) with the Tukey and Dunnett *post hoc* analyses (Gordon 1997). The Tukey test makes all possible comparisons and was used to make assessments within WT responses, whereas, the Dunnett test compares all groups to a single control and therefore was used to compare mutant constructs to WT. Significance was held at $p < 0.05$ for all comparisons.

The standard error of the mean (s) for normalized means (X) was determined from the raw mean (μ) and standard error (σ) values using [Eq. 11a] for WT and [Eq. 11b] for mutants.

[Eq. 11a] $$s = X * \sqrt{2*(\sigma^2/\mu^2)}$$

[Eq. 11b] $$s = X * \sqrt{(\sigma^2/\mu^2)_{wt} + (\sigma^2/\mu^2)_{mut}}$$

2.6: Bioinformatics

To better understand secondary structure, in order to make predictions of possible functional relationships, I applied several bioinformatic analyses of the primary amino acid sequence of the $GABA_AR$ α1 subunit. Structure prediction methods are either based solely on the primary amino acid sequence or based on homology to a known structure (Baker and Sali, 2001). First, I generated amino acid sequence alignments to investigate the primary structure of $GABA_AR$ subunits. Next, I used the Chou-Fasman amino acid scales to predict the secondary structure of the α1 intracellular loop domain directly from the primary sequence (Chou and Fasman 1978) and I used the Jnet algorithm to predict secondary structure from sequence alignment homology (Cole et al., 2008). Lastly, I generated a structural homology model of the $GABA_AR$ α1 subunit using the SwissModel automated homology modeling server (Schewede et al., 2003).

2.6.1: Sequence alignment

Alignments of primary amino acid sequences were created using MatLab (The Math Works, Inc., Natick, MA) and provided useful insight into the conservation of pLGIC subunits and, in particular, subunits of the $GABA_AR$. The *multialign* function in the Bioinformatics toolbox for Matlab relies on progressive pairwise alignment of each sequence using the Gonnet scoring matrix (Gonnet, Cohen et al. 1992) followed by construction of a guide tree created with the neighbor-joining method (Saitou and Nei 1987; Studier and Keppler 1988). Phylogenetic trees were created using the *phytree* function in the Bioinformatics toolbox for Matlab, which assumes that all leaves are equidistant from the root. Patristic distances, relative values that are used to describe the amount of genetic change between sequences, were calculated from pairwise Blocks of Amino Acid Substitution Matrix (BLOMSUM) scores (Henikoff and Henikoff 1992).

2.6.2: Secondary structure prediction

I used the Chou-Fasman scales for predicting α helices and β strands within the ProtScale tool, accessible at <http://web.expasy.org/protscale/>, to predict the secondary structure of the α1 intracellular loop domain from its primary amino acid sequence (Gasteiger, Hoogland et al. 2005). Chou and Fasman (1978) analyzed the structures of 29 proteins to calculate the probability that each amino acid resides in an α-helix, a β-sheet, or a coil. The score for each position was determined as the mean value for that residue and the 5 flanking residues on either side; a score ≥ 0.9 for three or more consecutive residues was considered as a positive prediction.

I used the Jpred server, accessible at <http://www.compbio.dundee.ac.uk/jpred/>, to predict the secondary structure of the α1 intracellular loop domain alone and in context of the full length sequence. The Jpred server uses the Jnet algorithm to predict the propensity of each residue to exist in three secondary structure states: α helix, β strand, or coil (Cole, Barber et al. 2008). The Jnet algorithm uses a neural network process to first, run a Position-Specific-Iterated Basic Local Alignment Search Tool (PSI-BLAST) of the query sequence to generate a sequence alignment of homologous proteins (> 75% conservation), and then to generate a Hidden Markov Model (HMM) profile and a position-specific scoring matrix (PSSM) (Cole, Barber et al. 2008). Both methods are probabilistic and predict the propensity of each amino acid to exist in specific states (Delorenzi and Speed 2002). Finally, Jnet uses Lupas (1991) prediction of coils and also predicts the solvent accessibility of each residue. The Jpred server relies heavily on primary sequence homology, but a powerful advantage of this tool is the inclusion of a confidence score which integrates the results from each of the prediction applications.

2.6.3: Homology modeling

The homology model of the α1 subunit was generated using the SwissModel server, accessible at < http://swissmodel.expasy.org/> (Schwede, Kopp et al. 2003). There are presently several available homology modeling tools, including: Modeller v8.2 (Sali and Blundell, 1993), Nest v1.0 (Petrey et al., 2003), Buintracellular loop domainer v1.0 (Koehl and Delarue, 1995), SegMod/ENCAD v1.0 (Levitt, 1992) and Swiss-Model (Schwede et al., 2003). In a comparison study of these five methods, Dalton and Jackson (2007) identified no significant differences between the available freeware; each method was used to create models for proteins with known structures, then the root mean square deviation between the coordinates of the model and the structure was determined. The biggest difference between homology modeling methods is the approach that is used to model loops, sections of the protein that have no known structural homology. I chose to use the SwissModel server because it uses a combination of *ab initio* and database loop buildingto complete each models when there are discrepancies between the template coordinates and the query sequence (Schwede et al., 2003).

The sequence of the *H. sapiens* $GABA_AR$ α1 subunit (NP_000797) was uploaded into the workspace (Arnold, Bordoli et al. 2006) of the server and I specified the structure for the *T. californica* nAChR (PDB ID: 2BG9) as the template (Unwin, 2005). The 2BG9 structure does not provide a complete template as a portion of the intracellular loop domain was unresolved. Because the intracellular loop domain is greater than 10 residues long, *ab initio* loop buildingfailed and SwissModel used a rigid-body method to assemble a template from a loop library database. Rigid body assembly indicates that individual loop fragments retained their original conformation. In automated mode, the server then threaded the query sequence onto a merged template of chain C (δ subunit) of the 2BG9 template and the loop template. The quality of the model was then assessed to ensure that each amino acid resided within a favorable local energy environment (vanGunsteren, Billeter et al. 1996) and to assess the packing quality of the

model (Melo and Feytmans 1998). All models generated by the server are deposited into the open access SwissModel Repository (Kopp and Schwede 2004; Kopp and Schwede 2006; Kiefer, Arnold et al. 2009).

2.7: Conclusion

Data presented in Chapters 3, 4, and 5 was gathered with the experimental methods and materials described here to measure the contribution of the α1 intracellular loop domain to $GABA_AR$ function. HEK293 cells were used in all experiments as a consistent vehicle to express the $GABA_AR$. I used site-directed mutatgenesis to selectively delete the intracellular loop domain of the α1 subunit and to individually switch the charge of all the charged residues within the domain. Antibody labeling of the α1 subunit was used to measure the surface expression of the $GABA_AR$ and voltage clamp electrophysiology was used to characterize the function of WT and mutant receptors.

Chapter 3

The intracellular loop domain facilitates channel gating and hinders ion permeation

3.1: Overview

In this chapter I sought to address two hypotheses, that the intracellular loop domain of the $GABA_AR$ defines a portion of the permeation pathway and that this domain must be intact for proper channel activation to occur. To investigate these guiding questions, three deletion constructs of the $GABA_AR$ α1 subunit were characterized with whole-cell voltage clamp electrophysiology. Replacing the 80 residues of the α1 subunit intracellular loop domain with 7 linker residues decreased the apparent affinity for GABA but increased the maximal current magnitude. Intracellular loop domain deletion did not alter ion selectivity but replacing the domain with 7 positively charged lysine residues enhanced outward rectification. Finally, truncation of the α1 subunit severely impaired receptor surface expression, highlighting the portion of the C-terminus that is necessary for functional assembly and expression. These results define a novel role for the intracellular domain of the $GABA_AR$ α1 subunit in controlling ion permeation and channel gating.

3.2: Introduction

The traditional role of the intracellular loop domain of the $GABA_AR$ is as a substrate for protein-protein interactions that mediate the subcellular location of the ion channel. Previous studies of the $GABA_AR$ intracellular loop domain have predominantly focused on receptor surface stability and mobility (Brandon, Bedford et al. 1999; Connolly, Kittler et al. 1999; Peran, Hooper et al. 2006), phosphorylation (Leidenheimer, Browning et al. 1991; Smart 1997), and interactions with trafficking machinery (Chen and Olsen 2007; Michels and Moss 2007); see Section 1.3.3 for a specific discussion of these interactions. The structure of the *T. californica* nAChR (PDB: 2BG9) suggested that membrane associated α helices form an intracellular vestibule closed at the base with windows, formed by the five subunits, that provide a pathway for ion permeation (Unwin 2005; Fig 3.1A). If the $GABA_AR$ shares structural homology with the nAChR then charged residues within the intracellular loop domain may make electrostatic interactions with chloride ions to mediate ion permeations (Fig. 3.1C). Recent studies of other pLGICs identified specific charged residues within the intracellular loop domain that affect ion permeation and set conductance amplitudes, which supports this structural prediction (Davies, Pistis et al. 1999; Kelley, Dunlop et al. 2003; Hales, Dunlop et al. 2006; Deeb, Carland et al. 2007; Livesey, Cooper et al. 2008; Peters, Cooper et al. 2010); see Section 1.3.3 for a full discussion of ion permeation.

Mutagenesis studies in nAChR and GlyR, have uncovered a role for intracellular charged residues in determining channel conductance (Kelley, Dunlop et al. 2003; Hales, Dunlop et al. 2006; Deeb, Carland et al. 2007; Livesey, Cooper et al. 2008; Carland, Cooper et al. 2009; Peters, Cooper et al. 2010). This was first determined by comparing the $5\text{-}HT_{3A}$ and $5\text{-}HT_{3B}$ subunits that have a ~40-fold difference in conductance to identify the intracellular loop domain residues which control this phenomenon (Davies, Pistis et al. 1999; Kelley, Dunlop et al. 2003). The lack of homology in the intracellular loop domain makes it difficult to extrapolate these findings

across the entire pLGIC family (Fig. 1.2) and the intracellular loop domain role in permeation has yet to be established for the $GABA_AR$. Furthermore, these studies have focused solely on the membrane associated stretch and have largely ignored the remaining portion of the domain. It also remains to be seen if the intracellular loop domain component of permeation is conserved within heteromeric $GABA_ARs$. The studies presented here will address this knowledge gap.

Recently, several structures have been resolved for prokaryotic homologs of the pLGIC superfamily (Bocquet, Nury et al. 2009; Hilf and Dutzler 2009; Corringer, Baaden et al. 2010) (Fig. 3.1B). Both prokaryotic homologs are ligand gated cation selective ion channels; the homolog from *Gloebacter violaceus* (GLIC) is proton gated (Bocquet et al., 2007) and the homolog from *Erwinia chrysanthemi* (ELIC) is gated by primary amines including GABA (Zimmermann and Dutzler 2011). Both channels have an extracellular domain comprised of β sheets in the sandwich conformation and four α helical transmembrane domains (Fig. 3B). The linker between M3 and M4 of each prokaryotic homolog is <10 residues. This finding has called into question the necessity of the intracellular loop domain for channel activation. Jansen et al. (2008) showed that replacing the $5\text{-}HT_{3A}R$ intracellular loop domain sequence with that of the GLIC receptor resulted in functional, surface expressing receptors in oocytes. However, this resulted in a 2-fold increase in serotonin EC_{50} and a 10-fold decrease in picrotoxin IC_{50} (Jansen, Bali et al. 2008). The $5\text{-}HT_{3A}R$-GLIC chimera also increased single channel conductance. Complete deletion of the $5\text{-}HT_{3A}R$ intracellular loop domain, however, resulted in non-functional receptors (Jansen, Bali et al. 2008). These results suggest that the intracellular loop domain must be intact for proper receptor function to occur.

Taken together there is a void in our understanding of ion permeation through the $GABA_AR$ and our understanding of the role of the intracellular loop domain in directly determining channel activity. To address this knowledge gap, I tested two primary hypotheses.

First, in agreement with the nAChR structure (Unwin 2005), I hypothesized that the central pore of the $GABA_AR$ extends beyond the membrane into the intracellular space of the cell where it is defined by residues of the intracellular loop domain. Accordingly, I hypothesized that charged residues within this domain electrostatically control ion permeation (Fig. 3.1C). Second, I hypothesized that the intracellular loop domain must be intact for channel activation. To test these hypotheses, I created and characterized deletion constructs of the $GABA_AR$ intracellular loop domain. If the intracellular loop domain defines the intracellular lumen of the pore, then deletion of this domain would alter the geometry of the pore ultimately affecting ion permeation (Fig. 3.1D). Furthermore, functional changes induced by domain deletion will highlight the aspects of channel activity that are controlled by the intracellular loop domain.

The intracellular loop domains of the β and γ subunits are known to make important interactions with trafficking and scaffold proteins such as AP2, GABARAP, gephyrin, BIG-2, and GRIP-1 (Connolly, Kittler et al. 1999; Nymann-Andersen, Sawyer et al. 2002; Jovanovic, Thomas et al. 2004; Chen and Olsen 2007); for details on specific interactions see section 1.3.3. Consequently, in this study I chose to modify only the α1 subunit leaving the β2 and γ2 subunits intact to establish a role for the intracellular loop domain in controlling $GABA_AR$ activity, not its involvement in trafficking and signaling pathways.

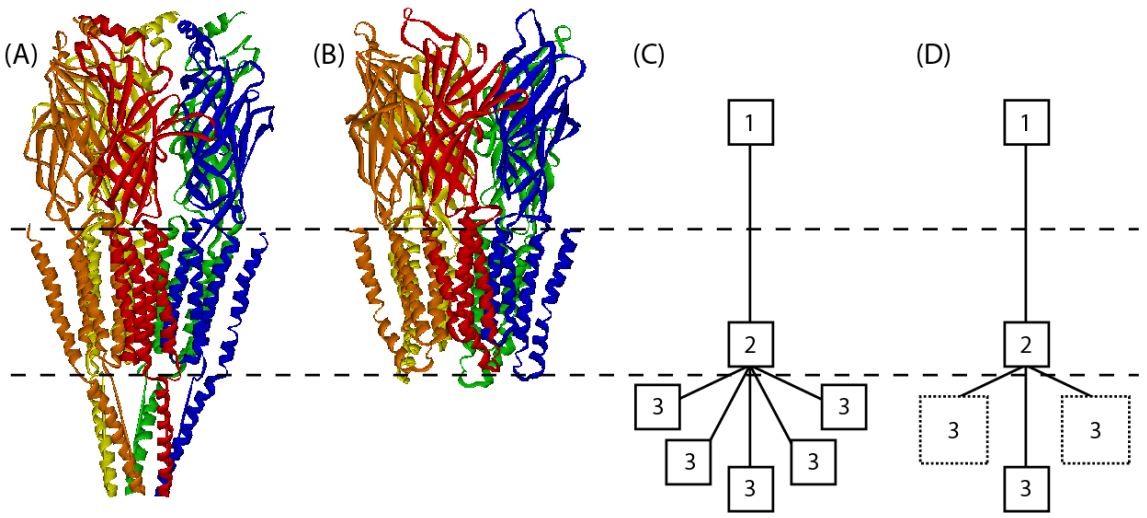

Figure 3.1: Putative ion sensor sites. (A) Structure of the nAChR from *T. californica*, (PDB: 2BG9) and (B) pLGIC from *G. violaceus*, (PDB: 3EAM). Schematic diagrams highlight the locations of putative ion sensors sites within the pore for (C) WT and (D) α1 intracellular loop domain deletion constructs. Ion sensor sites are known to be located within (1) the extracellular vestibule (Hansen, Wang et al. 2008) and (2) the selectivity filter (Jensen, Schousboe et al. 2005) and are hypothesized to be provided by (3) intracellular loop domain residues. Dashed lines represent the approximate boundary of the membrane. Large intracellular windows cause by α1 intracellular loop domain deletion may not provide the energetic stability of an ion sensor site as represented by dotted boxes.

3.3: Results

3.3.1: Deletion of the GABA$_A$R α1 intracellular loop domain and C-terminus

In order to measure the function of the $GABA_AR$ in the presence and absence of the intracellular loop domain, I replaced 80 α1 residues with 7 residues to retain channel function; Jensen et al. (2008) showed that complete deletion of the intracellular loop domain abolished function. First, I replaced the α1 intracellular loop domain with the intracellular heptapeptide from GLIC (IL-BAC; Fig. 3.2). Second, I replaced the α1 intracellular loop domain with seven lysine residues to investigate the effect of charge on ion permeation and channel activation (IL-7K; Fig. 3.2). To detect gross changes from wild type (WT) receptor function, GABA concentration-response relationships were constructed for WT, IL-BAC and IL-7K using whole-cell voltage clamp electrophysiology (Fig. 3.3). EC_{50} was increased for IL-BAC (144 ± 26.0 μM), and IL-7K (660 ± 172 μM) compared to WT (51.9 ± 8.11 μM) (mean ± standard error of the mean (SEM), Fig. 3.3B, Fig. 3.4D, Table 3.1). There were no changes induced in Hill slope, but both deletion constructs significantly increased current magnitude (Student's t-test, $p<0.05$, Fig. 3.3, Table 3.1).

Characterization of IL-BAC and IL-7K suggested that channels can function without a complete intracellular loop domain, albeit in a modified fashion. To investigate if this was true for the C-terminal domain in general I characterized a truncation construct of the α1 subunit (IL-stop). The IL-stop construct was created by introducing a premature stop codon to delete the final 66 residues of the α1 subunit, which included the final third of the intracellular loop domain and all of M4 (Fig. 3.2). IL-stop caused a 100-fold decrease in current magnitude, but no change in Hill slope or GABA EC_{50} compared to WT (Fig. 3.3; Table 3.1).

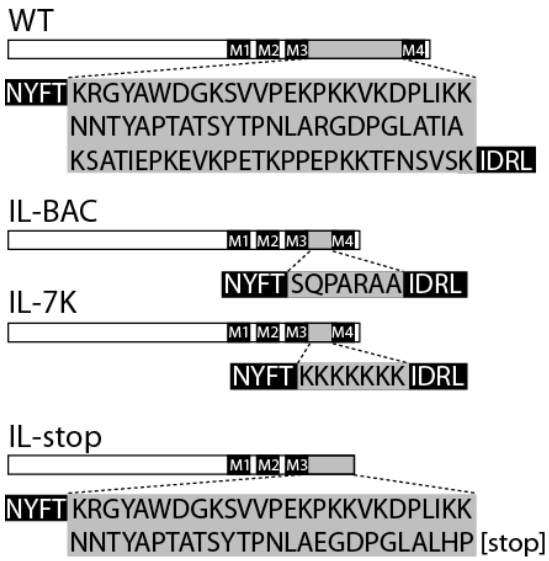

Figure 3.2: Deletion constructs. Schematics of wild type (WT) α1 intracellular loop domain sequence and three deletion constructs: IL-BAC, IL-7K, and IL-stop. Substituted residues are highlighted in gray. The location of the transmembrane domains (M1-M4) is indicated with white letters on a black background.

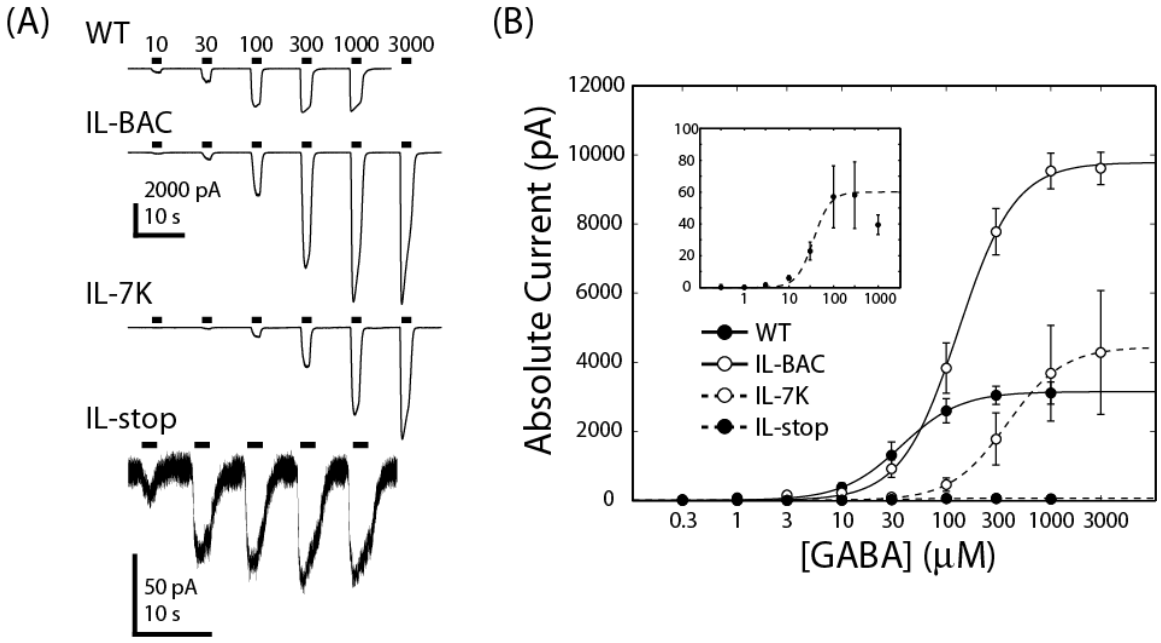

Figure 3.3: C-terminal deletions decreased apparent affinity and altered magnitude of whole-cell currents. (A) Representative whole-cell current traces for WT, IL-BAC, IL-7K, and IL-stop constructs. Bars indicate the duration of GABA application and are labeled with the concentration (μM). Note difference scale bars. (B) Hill equation fit of peak current data shows significant shifts in GABA apparent affinity and significant changes in current magnitude caused by deletion of the α1 ILD. [INSET] shows concentration response for IL-stop to highlight the significant decrease in current magnitude; error bars denote SEM; n = 6.

Construct	EC_{50} (μM)	nH	I_{max} (pA)	N
WT	51.9 ± 8.11	1.95 ± 0.07	-3283 ± 291.1	6
IL-BAC	144 ± 26.0*	1.81 ± 0.11	-9808 ± 462.2*	6
IL-7K	660 ± 172*	1.44 ± 0.13	-6252 ± 1210*	5
IL-stop	29.2 ± 7.17	3.02 ± 2.23	-75.75 ± 12.0*	7

Table 3.1: Hill fit parameters for deletion and truncation constructs. Maximal current (I_{max}), GABA apparent affinity (EC_{50}), and Hill coefficient (nH) values were determined from fitting peak current values to the Hill equation [Eq. 6]. Significant differences from WT were held at $p < 0.05$ (*) for Dunnett's *post hoc* comparison after ANOVA; means depicted ± SEM.

Construct	E_{rev} (mV)	RI.m	RI.b	N
WT	-9.55 ± 1.46	0.37 ± 0.03	0.67 ± 0.0	6
IL-BAC	-11.2 ± 1.25	0.46 ± 0.02	0.56 ± 0.02	6
IL-7K	-7.77 ± 0.61	0.41 ± 0.06	0.46 ± 0.02*	5

Table 3.2: IV relationship metrics for deletion constructs. Reversal potential (E_{rev}) values and metrics of the rectification profile, the slope (RI.m) and intercept (RI.b). Significant differences from WT were held at $p < 0.05$ (*) for Dunnett's *post hoc* comparison after ANOVA; means depicted ± SEM.

3.3.2: Deletion of intracellular loop domain did not alter ion selectivity

To investigate if deletion of the α1 intracellular loop domain altered charge selectivity or permeability of the $GABA_AR$ IV relationships were determined for WT, IL-BAC and IL-7K (Fig. 3.4) using the voltage ramp protocol described in Section 2.3.6. Neither IL-BAC (-11.2 ± 1.25 mV; n=6) nor IL-7K (-7.77 ± 0.61 mV; n=5) yielded a significant shift in reversal potential compared to WT (-9.55 ± 1.46 mV; n=6; Dunnett *post hoc*, $p>0.05$; Fig. 3.4C, E). I also measured the impact of intracellular loop domain deletion on the direction of current flow by constructing a rectification profile for each IV relationship (Fig. 3.4C-F) as described in Section 2.3.7. IL-BAC was not different from WT (Fig. 3.4D, Table 3.2), but IL-7K significantly decreased the intercept of the rectification profile by ~1.5-fold compared to WT (Dunnett *post hoc*, $p < 0.05$, Fig. 3.4F, Table 3.2).

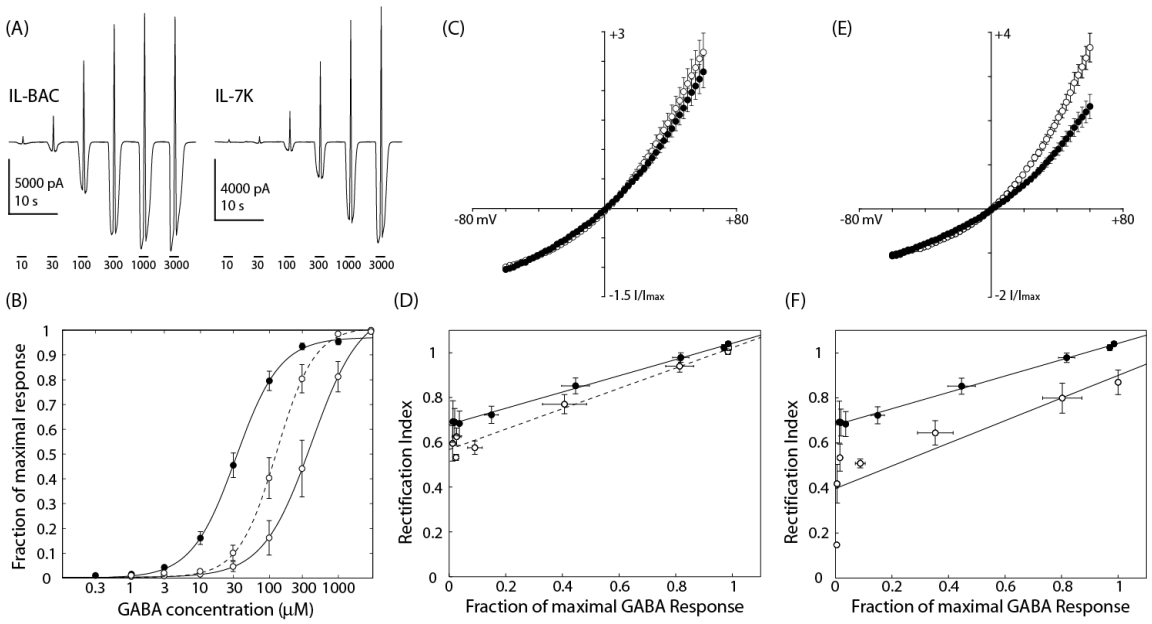

Figure 3.4: Deletion of the α1 intracellular loop domain enhanced outward rectification. (A) Representative currents from IL-BAC and IL-7K. Bars indicate the duration of GABA application and are labeled with concentration (μM). (B) Hill equation fit of normalized peak currents for WT (solid circles, solid line), IL-BAC (open circles, dashed line), and IL-7K (open circles, solid line) highlight significant shifts in GABA apparent affinity. IV relationships from currents elicited by EC_{10} GABA concentrations for (C) IL-BAC (open circles) and (E) IL-7K (open circles) compared to WT (solid circles). Rectification profiles for (D) IL-BAC (open circles, dashed line) and (F) IL-7K (open circles, solid line) compared to WT (solid circles, solid line). Data points depict mean ± SEM; n = 6.

3.3.3: Truncation of the α1 subunit decreased surface expression

A decrease in whole-cell current magnitude may be caused by changes in the number of receptors on the cell surface, a decrease in single channel current, or a decrease in the open probability of the channel, [Eq. 2]. To investigate the cause of the decrease in current amplitude that was induced by IL-stop, I measured the surface expression of the receptor protein from confocal images. HEK293 cells transfected to express WT or IL-stop were immuno-labeled in non-permeablizing and permeablizing conditions with discrete fluorophores in order to label only the receptors on the cell surface and then label the total receptor population, respectively, as described in Section 2.2 (Fig. 3.3). Qualitatively, the WT receptor was predominantly expressed on the surface of the cell, whereas the surface expression of IL-stop was reduced and there was an abundance of protein labeled in the interior of the cell (Fig. 3.3, Fig. 3.4). In order to quantify the degree of surface expression, I calculated a surface ratio comparing the fluorescent signal from surface labeling to the sum of fluorescence from both fluorophores. The IL-stop construct significantly decreased the surface ratio of the α1 receptor (0.22 ± 0.04) compared to WT (0.46 ± 0.05; Student's t-test, $p < 0.001$; $n = 4$, Fig. 3.4C).

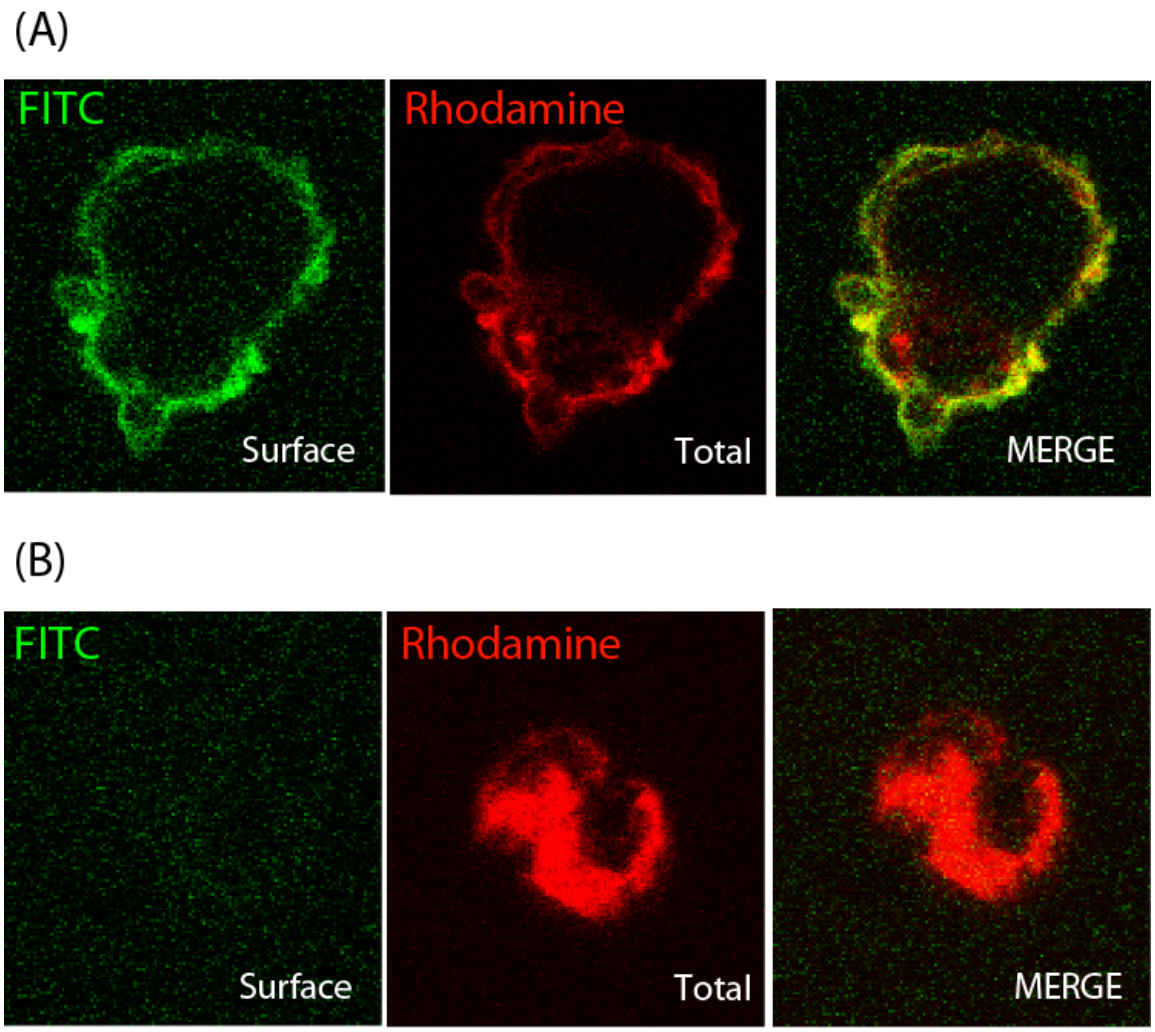

Figure 3.5: Truncation of the intracellular loop domain decreased surface expression. The panels show confocal images of transfected HEK293 cells that were labeled in non-permeablizing and permeablizing conditions with FITC (green) and Rhodamine (red) conjugated secondary antibodies, respectively, to highlight the surface and total expression of the α1 subunit. (A) The WT α1 subunit was expressed almost exclusively on the cell surface as shown by FITC labeling and co-localization of signals in the merged image. (B) The IL-stop construct eliminated surface expression of the α1 subunit with no FITC labeling.

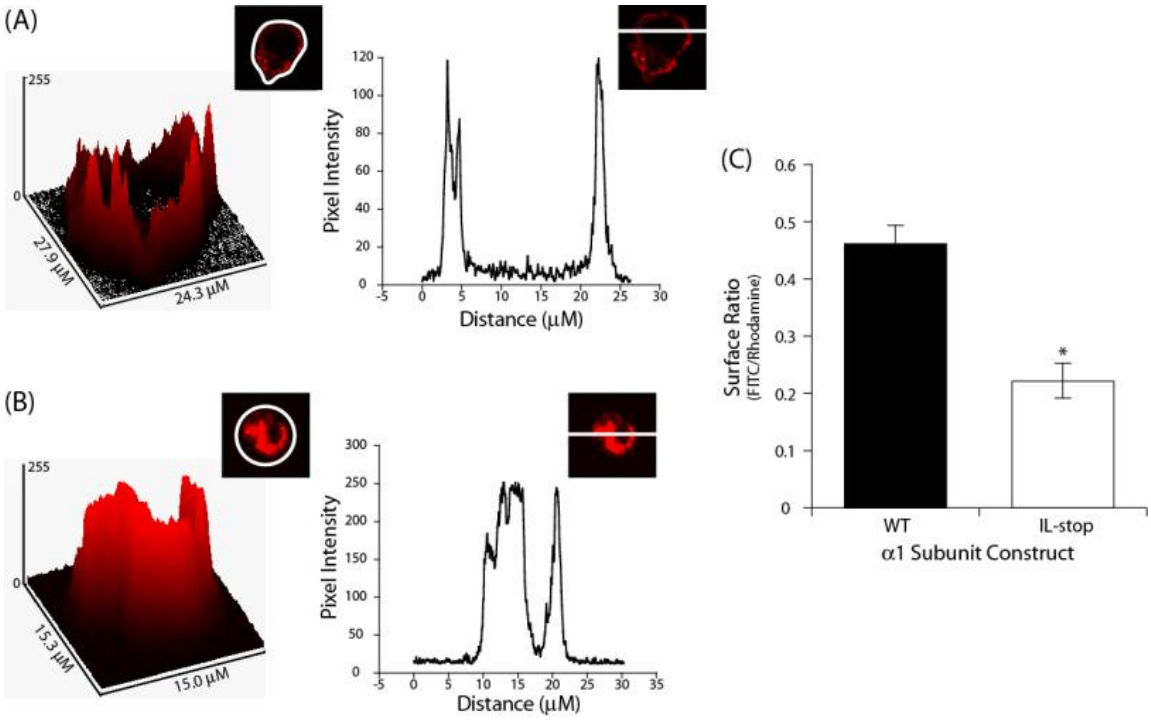

Figure 3.6: Quantification of confocal images. Images were analyzed with ImageJ software to determine the integrated density value for each fluorophore. Surface plots for the Rhodamine fluorophore are shown for (A) WT and (B) IL-stop. White lines indicate the area of integration for each plot. (C) Bar graph depicts the surface ratio for each construct, which was determined by dividing the sum of integrated density values for FITC by those for Rhodamine. The surface ratio of IL-stop (n = 4) was significantly decreased from WT (n = 3); Student's t-test, $p < 0.001$.

3.4: Discussion

3.4.1: The intracellular loop domain controls current magnitude

Deletion of the α1 intracellular loop domain was predicted to alter the intracellular geometry of the pore to alter ion permeation (Fig. 3.1). Indeed, both intracellular loop domain deletion constructs, IL-BAC and IL-7K, significantly increased macroscopic current amplitude (Fig. 3.3). One way that this finding can be explained is if the intact intracellular windows function to retard current flow. If this is the case, introduction of positively charged lysine residues in the IL-7K construct provided a stronger attractive electrostatic force with chloride ions than the mostly neutral bacterial heptapeptide in the IL-BAC construct to slow permeation. This assumption is consistent with the differing degrees of current enhancement that were observed for each intracellular loop domain deletion construct (Fig. 3.3). Further experiments, described in Chapter 4, will investigate the contribution of individual $GABA_AR$ α1 intracellular loop domain charged residues to the permeation pathway in order to identify the specific residues which control current magnitude in the intact receptor.

3.4.2: The intracellular loop domain controls channel gating

The IL-BAC and IL-7K deletion constructs also exhibited decreased GABA apparent affinity as evidenced by large shifts in EC_{50} (Fig. 3.3). The GABA binding pocket is located within the extracellular domain at the interface between α and β subunits (Boileau, Evers et al. 1999). Separate protein domains are known to be able to fold independently; in particular, the extracellular domain and transmembrane domain of GLIC and GlyR α1, respectively, have been shown to retain their function when combined as a chimera (Duret, Van Renterghem et al. 2011) and the intracellular loop domain of $5\text{-}HT_{3A}$ was successfully inserted between M3 and M4 of GLIC to confer the surface expression pattern of the eukaryotic receptor (Goyal, Salahudeen et al. 2011). Therefore, it is not unreasonable to assume that intracellular loop domain deletions did not perturb the GABA binding site and the observed changes in apparent affinity reflect a gating

impairment. This is an interesting conclusion because the major correlates of channel gating reside within the "hinge" region where several highly conserved loops of the extracellular domain interact with the top of the transmembrane domain and the M2-3 linker to translate the energy of ligand binding to open the channel gate; reviewed in (Kash, Trudell et al. 2004) and (Xiu, Hanek et al. 2005). However, experiments using chimera constructs to define the regions that control differences between subunits suggest a role for the C-terminus in channel gating. Akk and Steinback (2000) showed that the difference in closing rate between the embryonic and adult subunits of the muscle AChR is controlled by the C-terminus of the protein, including the intracellular loop domain and M4. Fisher (2004) showed that the difference in open duration of single channel currents conferred by the $GABA_AR$ α1 verses α6 subunits is controlled by the region of the protein including the M3 and intracellular loop domains. Taken together, our findings and those of others (Akk and Steinbach 2000; Fisher 2004) support the hypothesis that the tertiary structure of the intracellular loop domain must be intact in order for GABA binding to elicit proper channel gating. Data presented in Chapter 4 will further investigate this role and identify specific residues within the α1 intracellular loop domain that control channel gating.

3.4.3: The intracellular loop domain controls ion permeation but not charge selectivity

IV relationships for the IL-BAC and IL-7K deletion constructs showed no significant shift in the reversal potential compared to WT, suggesting that the α1 intracellular loop domain is not involved in charge selection (Fig. 3.4). This agrees with the present notion that the selectivity filter of $GABA_ARs$ resides outside the intracellular loop domain at the base of the transmembrane domain within the M1-2 linker (Jensen, Timmermann et al. 2002; Jensen, Pedersen et al. 2005; Jensen, Schousboe et al. 2005). The IL-7K construct did, however, have a significantly different IV relationship from WT, exhibiting enhanced outward rectification (Fig. 3.4). Rectification is a property of ionic pores that pass current preferentially in one direction and may be caused by changes in ion selectivity (Moorhouse, Keramidas et al. 2002), asymmetric pore geometry

(Kienker, DeGrado et al. 1994; Andriotis, Menon et al. 2001; Mokrab, Bavro et al. 2007; Kovarik, Zhou et al. 2009), and electrostatic barriers to ion permeation such as ion binding sites (Bormann, Hamill et al. 1987; Imoto, Busch et al. 1988; Moorhouse, Keramidas et al. 2002). IV relationships showed that intracellular loop domain replacement did not alter ion selectivity (Fig. 3.3). Both deletion constructs were predicted to alter the geometry of the pore, but only the IL-7K construct specifically introduced positive charge to the putative pore domain. Therefore, it is intriguing to surmise that the IL-7K construct induced outward rectification by altering the electrostatic landscape of the permeation pathway, providing further evidence for the hypothesis that intracellular loop domain residues mediate ion permeation. In Chapter 5, I will specifically investigate the asymmetry of currents through the $GABA_AR$ and use rectification as a tool to identify charged residues that define intracellular loop domain ion sensor sites of the permeation pathway. In particular, the IL-7K construct both exhibited a shift in EC_{50} and altered ion permeation. One potential mechanism to explain these findings is that IL-7K perturbed electrostatic interactions between permeant ions and the pore that serve as integral gating elements; the chloride-dependence of channel gating will be explored further, also in Chapter 5.

The intracellular windows predicted by the nAChR structure (Unwin, 2005) effectively split the permeation pathway into five paths (Mokrab, Bavro et al. 2007), which establishes an asymmetric pore geometry perpendicular to the membrane (Fig. 3.1A, Fig. 3.1C). However, the five windows are putatively oriented symmetrically around the central axis of the ion channel pore (Unwin 2005). Removal of bulk, following intracellular loop domain deletion, likely resulted in the appearance of large, non-selective windows that may not provide the energetic stability of an ion sensor site (Fig. 3.1D). If we consider this, then α1 intracellular loop domain deletion actually created a more asymmetric permeation pathway. Through the study of carbon nanotubes as a simple model of biological pores, current rectification is known to be observed through pores with asymmetric geometries (Andriotis, Menon et al. 2001; Kovarik, Zhou et al.

2009). Therefore, the IL-BAC deletion construct would have been predicted to also induce a change in current rectification. On the other hand, the transmembrane domain section of the pore is defined by an α helix, a structure that is known to inherently behave as a dipole to establish an asymmetric electrostatic landscape (Kienker et al., 1994). Therefore, the M2 α helical segment of the $GABA_AR$ pore may be the primary mediator of current rectification in WT receptors. In order to differentiate the cause of rectification, I hypothesized that deletion of the intracellular loop domain of all subunits of the αβ heteromer would either ablate rectification if the intracellular loop domain caused the asymmetry of current flow or rectification would be unaffected if mediated by transmembrane domain structures. To test this hypothesis I replaced the intracellular loop domain of the β2 subunit with the bacterial heptapeptide. However, preliminary results from α1β2(IL-BAC) and α1(IL-BAC)β2(IL-BAC) yielded no perceivable currents (n = 10; *data not shown*). Although this experiment was unable to delineate between the intracellular loop domain and the transmembrane domain, the causes of rectification of GABAergic currents and the influence of intracellular loop domain residues in mediating asymmetric current flow will be investigated further in Chapter 5.

3.4.4: Which domains are necessary for surface expression?

Removal of the intracellular loop domain from all five subunits of the pentamer has been reported to impair HEK293 cell expression (personal communication with J. A. Peters, University of Dundee) and deletion of the $GABA_AR$ β2 intracellular loop domain has been shown to decrease receptor surface expression (Terunuma, Xu et al. 2008). This highlights the necessity for the β subunit to remain intact for proper cell surface expression. I have chosen to focus my study of the $GABA_AR$ intracellular loop domain on the α1 subunit in order to avoid such potentially confounding effects from changes in surface expression. The α1 intracellular loop domain has been shown to restrict the lateral mobility of the $GABA_AR$ in HEK293 cells, but studies have shown that this domain plays no role in the surface expression or assembly of the heteromer complex (Peran, Hicks et al. 2001; Peran, Hooper et al. 2006; Jansen, Bali et al. 2008). Although mere deletion of the α1 intracellular loop domain yielded constructs with robust currents, truncation of the α1 subunit, which eliminated a portion of the intracellular loop domain and all of M4, caused a striking decrease in whole-cell current magnitude (Fig. 3.2). Confocal images showed that the IL-stop construct caused internalization of the α1 subunit (Fig. 3.5; Fig. 3.6). Several mutations of the α1 subunit, associated with inherited epilepsies, incur premature truncation codons and are known to impair receptor surface expression through endoplasmic reticulum associated degradation of the polypeptide (Cossette et al., 2002; MacDonald et al., 2010; Maljevic et al., 2006). In this light, M4 must be intact for proper subunit folding and incorporation into the mature receptor complex at the cell surface. Furthermore, a conserved aspartate residue at the interface of the intracellular loop domain and M4 has been shown to be necessary for subunit assembly (Terunuma, Xu et al. 2008). Therefore, M4 and the homologous residue α1(D393) were preserved in all subsequent constructs.

3.5: Conclusion

Taken together, the results of my deletion experiments established an important role for the $GABA_AR$ α1 intracellular loop domain architecture in controlling the function of the ion channel. To further investigate this functional role, in Chapter 4, I measured the effect of specific charged residues of the α1 intracellular loop domain to pin-point the subdomains of the intracellular loop domain that mediate channel gating and identify the residues which serve as ion sensor sites within the permeation pathway. In Chapter 5 I investigated the phenomenon of rectification further to understand the asymmetry of current flow through the $GABA_AR$.

Chapter 4

Functional subdomains of the α1 intracellular loop domain

4.1: Overview

A mutagenic charge switch screen of the $GABA_AR$ α1 subunit was used to investigate the functional role of specific intracellular loop domain residues. Whole-cell and single channel voltage clamp electrophysiology was used to measure concentration-response relationships and IV relationships for WT and mutant receptors in symmetrical and ion gradient conditions. Point mutations induced changes in receptor activity in a subdomain-dependent fashion. Charge switch mutations near M3 decreased the relative agonist efficacy of the channel indicative of a gating impairment and mutations near M4 enhanced receptor desensitization. Positions throughout the intracellular loop domain were shown to control anion permeation by positively shifting the reversal potential in low extracellular chloride conditions. In sum, these data provided the first evidence of an intracellular anion selectivity filter and identified functional subdomains of the intracellular loop domain of the $GABA_AR$ α1 subunit that control channel gating.

4.2: Introduction

As shown in the previous chapter, deletion of the α1 intracellular loop domain increased GABA EC_{50} and maximal current amplitude. In this chapter, I investigated the role that specific residues of the intracellular loop domain of the $GABA_AR$ α1 subunit play in mediating these aspects of channel activity with a mutagenic screen. If charged residues of the intracellular loop domain serve as ion sensor sites within the permeation pathway, then switching the charge will disrupt integral electrostatic interactions to hinder channel function.

To test this hypothesis, I conducted a mutagenic screen of all amino acids harboring ionizable side chains within the intracellular loop domain of the $GABA_AR$ α1 subunit. I chose to focus on residues with side chain pKa values that predict ionization at a neutral biological pH ~7. Lysine and arginine are predicted to carry a positive charge with side chain pKa values of 10.53 and 12.48; glutamate and aspartate are predicted to carry a negative charge with side chain pKa values of 4.25 and 3.65 (Nelson and Cox, 2005). Positions were mutated† in a point-wise fashion: acidic residues to lysine and basic residues to glutamate. This mutation scheme allowed for charge switches to be made with the most conservative change in side chain bulk possible using naturally occurring amino acids. Of the 80 α1 intracellular loop domain residues, 17 are positively charged and 8 are negatively charged for a total of 25 point mutations (Fig. 4.1).

† I devised the experiments and designed primers for the charge switch point mutations constructs. Mutagenesis was carried out by me and three lab technicians: Alison Abuin, Shannon Bell, and Riley Perszyk.

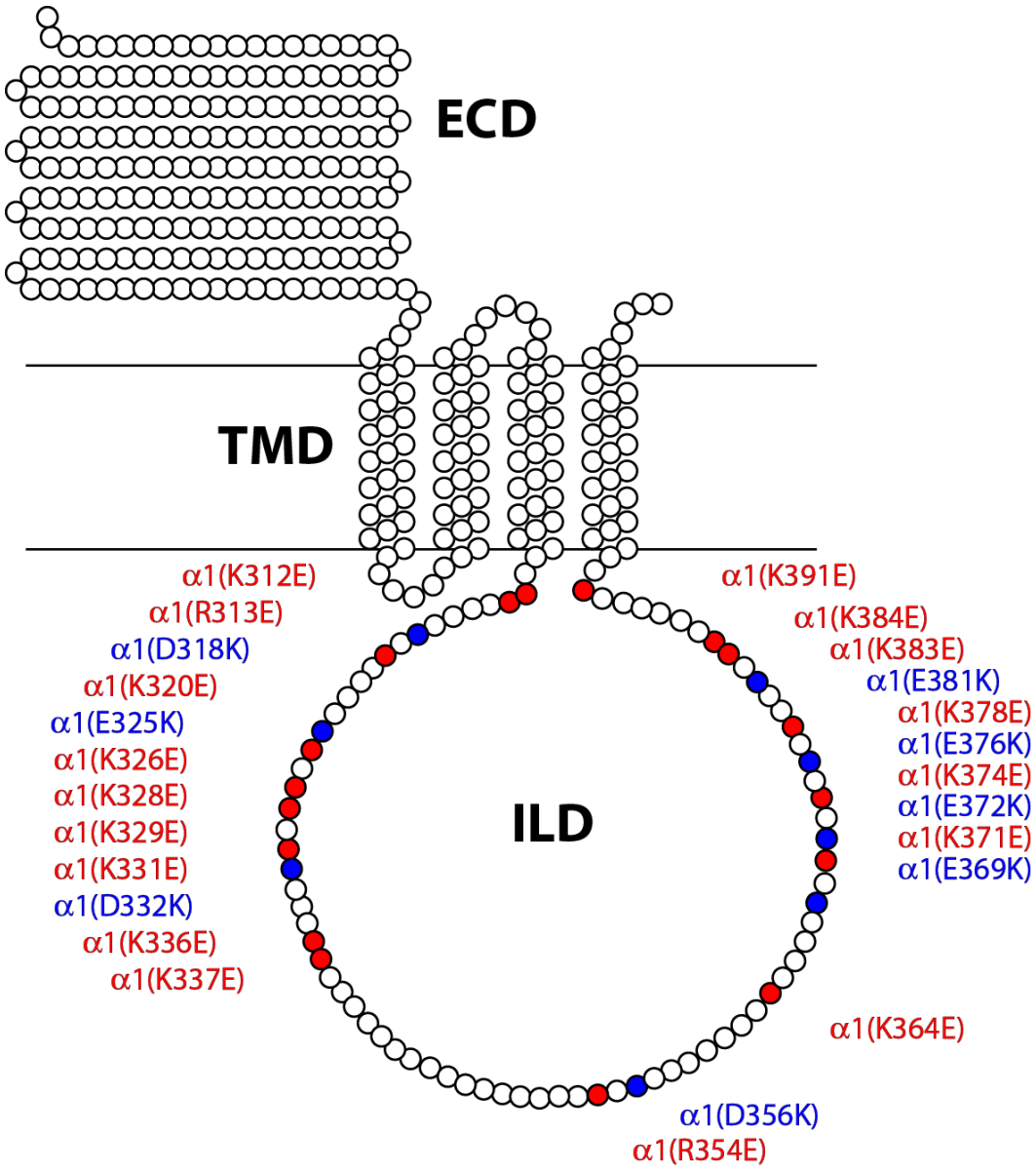

Figure 4.1: Charge switch mutations. Schematic of the $GABA_AR$ α1 subunit shows the arrangement of subunit domains including the extracellular domain (ECD), transmembrane domain (TMD), and intracellular loop domain (ILD). Each circle represents an amino acid position and the horizontal lines show the boundary of the membrane. Basic to glutamate (red) and acidic to lysine (blue) charge switch mutations were introduced point-wise into the WT α1 sequence.

4.3: Results

4.3.1: Charged residues of the α1 intracellular loop domain control ion permeation

Concentration-response relationships and IV relationships for WT and each point mutation were determined in symmetrical chloride and under ion gradient conditions using whole-cell voltage clamp electrophysiology. If mutations altered the magnitude of macroscopic currents, then subsequent experiments investigated channel conductance with single channel recordings and surface expression with immunocytochemistry. Changes in cation selectivity were revealed by significant shifts in reversal potential caused by decreasing extracellular sodium; likewise, changes in anion permeability were revealed by replacing extracellular chloride with the large anion gluconate. In this manner, I was able to detect changes in channel permeability incurred by mutagenesis.

I measured the GABA concentration-response relationship for each charge switch point mutation and compared the EC_{50}, I_{max}, and nH values of the Hill fit [Eq. 6] for each mutation to wild type (WT); for details of data acquisition and analysis see Section 2.3. Most of these mutations did not significantly alter the apparent affinity of the receptor for GABA, the maximal response to GABA or the Hill coefficient for the GABA concentration response relationship (Fig. 4.1, Table 4.1). This provided evidence that point mutations within the α1 intracellular loop domain did not alter the global structure or function of the receptor. Therefore, significant changes induced by mutagenesis indicated specific roles for each position.

Figure 4.2: Concentration-response relationships for charge switch mutations.

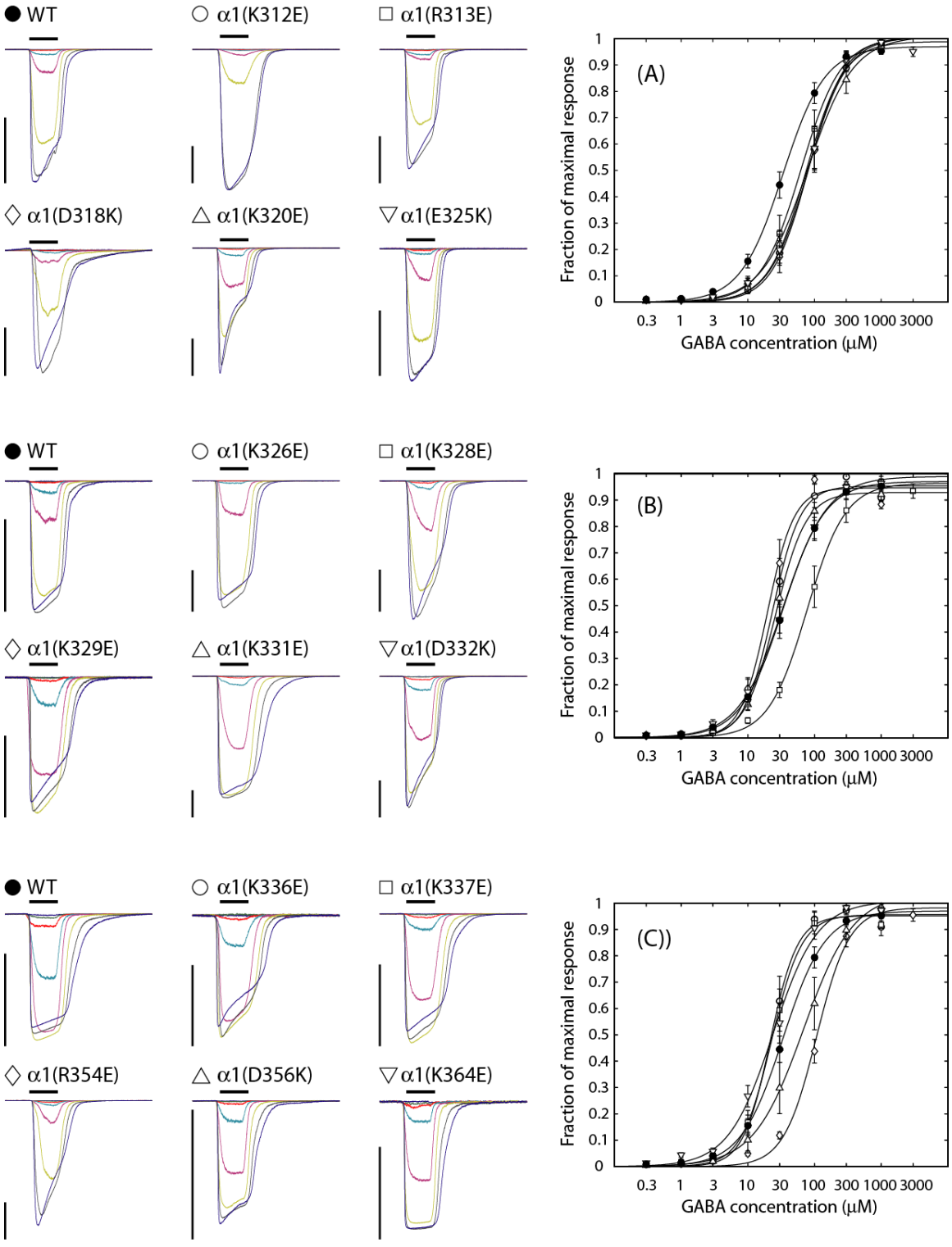

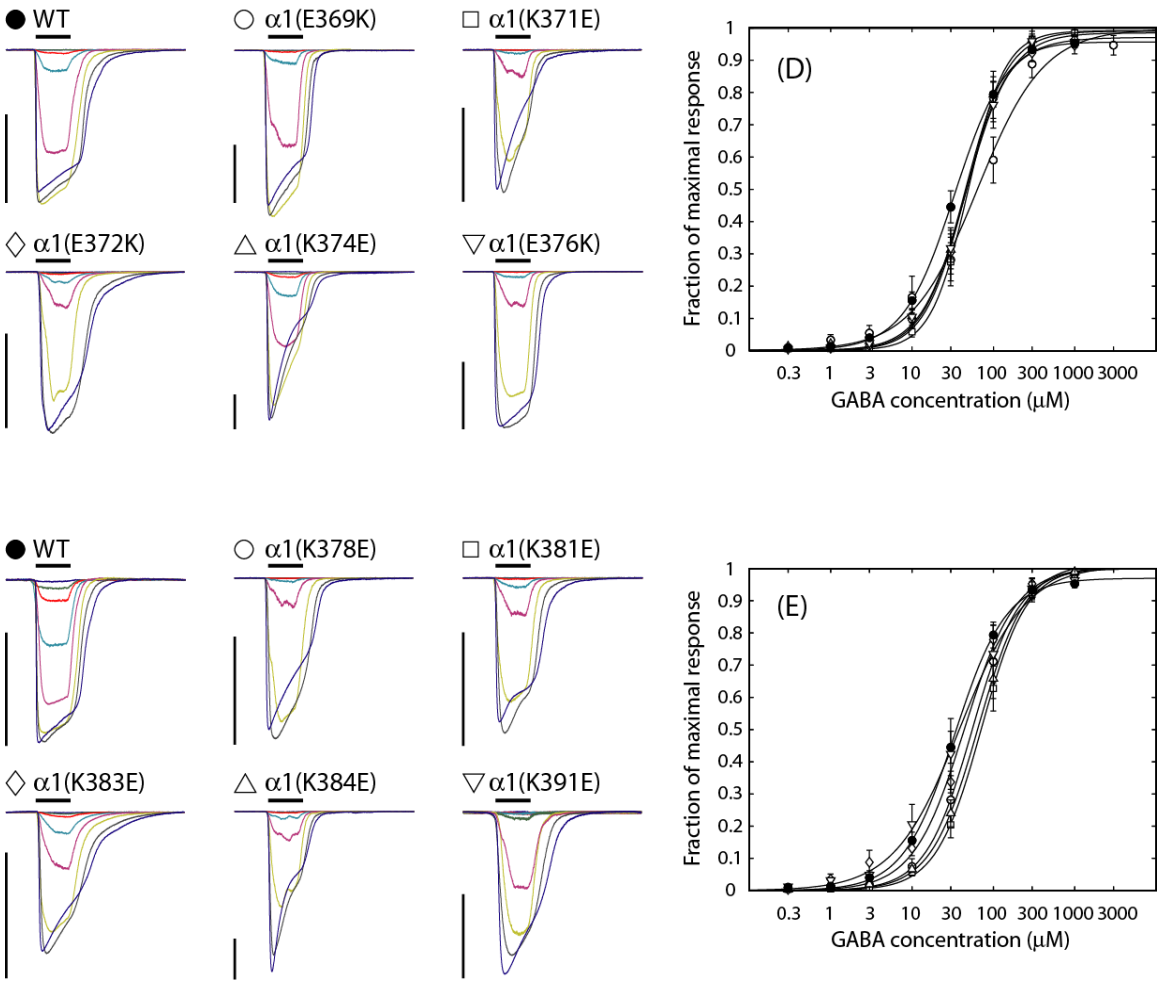

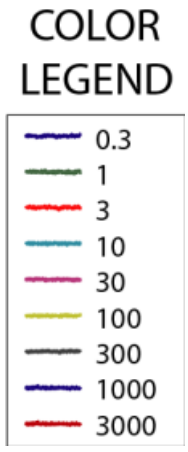

Figure 4.2: Concentration-response relationships for charge switch mutations. Representative traces are shown for each mutant construct with five different representative traces for WT. Horizontal bars depict 2 s application of increasing concentrations of GABA: 0.3 (navy), 1 (green), 3 (red), 10 (teal), 30 (pink), 100 (yellow), 300 (black), 1000 (blue), and 3000 (rust) μM; see Color Legend [left] for specific hues. Vertical bars represent 2000 pA for all current traces. Hill fits of normalized peak currents are shown to the right of each group of mutants (white) with corresponding symbols: circle, square, diamond, up triangle, down triangle. Mutants were numerically divided into five groups of five (A-E) for easy comparison to WT traces (black circle); see Table 4.1 for Hill fit values and sample sizes (n). All of the significant shifts in GABA EC_{50} caused by charge switches were located in the first three groups (A-C). Qualitatively, mutations in the last two groups (D-E) exhibited faster desensitization.

Construct (N)	Imax (nA)	EC_{50} (μM)	nH	Construct (N)	Imax (nA)	EC_{50} (μM)	nH
WT (34)	3.3 ± 0.3	53.0 ± 8.3	2.0 ± 0.1	R354E (8)	4.7 ± 0.7	109 ± 18.5†	1.8 ± 0.1
K312E (11)	3.4 ± 0.7	108 ± 30†	2.1 ± 0.4	D356K (10)	3.5 ± 0.8	92.7 ± 24.7	2.0 ± 0.1
R313E (12)	2.8 ± 0.5	78.9 ± 17	2.0 ± 0.1	K364E (10)	3.6 ± 0.7	30.7 ± 7.32	1.6 ± 0.1
D318K (10)	6.3 ± 0.8†‡	105 ± 24†	2.2 ± 0.2	E369K (11)	4.2 ±0. 7	88.9 ± 22.8	1.6± 0.2
K320E (10)	5.5 ± 0.9†	117 ± 31†‡	1.2 ± 0.2	K371E (4)	4.1 ± 0.8	53.2 ± 10.9	1.9 ± 0.2
E325K (8)	3.8 ± 0.6	89.2 ± 17	2.0 ± 0.1	E372K (11)	4.8 ± 1.1	65.2 ± 17.7	2.0 ± 0.1
K326E (10)	5.9 ± 0.1†	30.3 ± 6.6	2.6 ± 0.2	K374E (16)	5.7 ± 0.6†	51.5 ± 8.90	1.8 ± 0.1
K328E (10)	6.7 ± 0.1†‡	104 ± 23†	1.9 ± 0.2	E376K (9)	4.3 ± 0.4	59.7 ± 13.7	1.9 ± 0.1
K329E (10)	3.8 ± 0.9	20.2 ± 3.9	2.9 ± 0.2	K378E (10)	6.1 ± 1.2†	66.1 ± 10.6	2.0 ± 0.2
K331E (12)	5.3 ± 1.2	38.1 ± 5.7	2.2 ± 0.2	E381K (10)	3.5 ± 0.5	83.7 ± 13.2	1.8 ± 0.1
D332K (10)	4.5 ± 1.2	144 ± 26†‡	1.6 ± 0.2	K383E (11)	4.1 ± 0.6	50.5 ± 7.41	1.5± 0.2
K336E (8)	5.0 ± 1.3†	27.5 ± 6.1	3.8 ± 1.3	K384E (10)	6.0 ± 0.9†	74.8 ± 15.3	1.8 ± 0.1
K337E (11)	3.5 ± 0.9	29.6 ± 6.9	2.5 ± 0.2	K391E (9)	3.4 ± 0.6	59.3 ± 17.6	1.7 ± 0.1

Table 4.1: Hit fit parameters of charge switch mutations. The indicated lysine or arginine residues were mutated to glutamate. The indicated glutamate or aspartate residues were mutated to lysine. Maximal current (I_{max}), GABA apparent affinity (EC_{50}), and Hill coefficient (nH) values were determined from fitting peak current values to the Hill equation [Eq.7]. Significant differences from WT were held at $p < 0.05$ for Tukey (†) and Dunnett *post hoc* (‡) comparisons after MANOVA; means depicted ± SEM.

4.3.1A: Point mutations increased whole-cell current magnitude

Eight charge switch mutations, α1(D318K), α1(K320E), α1(K328E), α1(K329E), α1(K336E), α1(K374E), α1(K378E), and α1(K384E), significantly increased the magnitude of whole-cell currents ($p < 0.05$, Fig. 4.2, Table 4.1). The largest shifts in I_{max} were induced by the α1(K328E) mutation near M3 and the α1(K378E) mutation near M4, which caused a ~2-fold increase in I_{max} (Table 4.1).

Whole-cell current magnitude is an inherently variable metric that can be influenced by the number of receptors on the surface of the cells, the magnitude of single channel currents and the open probability of the ion channel [Eq. 2]. In order to verify the functional significance of these increases and determine the component of channel activity responsible, I quantified the surface expression and the amplitude of single channel currents for WT, α1(K328E), and α1(K378E) containing receptors.

4.3.1B: The α1(K378E) mutation increased surface expression

Surface expression of the $GABA_AR$ α1 subunit in transfected HEK293 cells was determined via luminescent quantification of immunocytochemical labeling; for specific methods see Section 2.2. The primary antibody was specific to an extracellular epitope of the α1 subunit; therefore, the same antibody could be used for WT and mutant subunits allowing for direct comparison of immunolabeling. The α1(K328E) mutation did not significantly alter the degree of surface labeling, but the α1(K378E) mutation nearly doubled the amount of surface labeling (Fig. 4.3).

4.3.1C: The α1(K378E) mutation decreased single channel conductance

I recorded currents passed through single channels containing the α1(K328E) and α1(K378E) mutations from membrane patches in the outside-out configuration and compared the responses to WT currents. The α1(K328E) mutation did not significantly alter the single channel amplitude of the $GABA_AR$ (Fig. 4.4, Table 4.2). Channels harboring the α1(K378E) mutation exhibited a ~30% decrease in unitary current amplitude (Fig. 4.4, Table 4.2). Neither mutation significantly altered the open probability of bursts of events (Student's t-test, $p > 0.05$; Table 4.2). In order to verify the difference in current amplitude between WT and α1(K378E), single channel currents were recorded from outside-out patches at membrane holding potentials between -80 and +60 mV. The α1(K378E) mutation caused a decrease in chord conductance and a modest negative shift in reversal potential compared to WT (Fig. 4.5, Table 4.2).

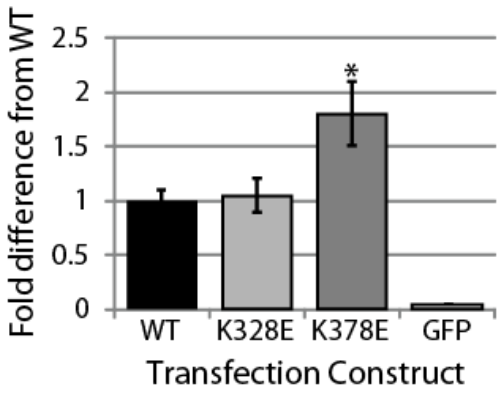

Figure 4.3: Surface expression of charge switch mutations. The TD20/20 luminometer was used to read HRP-luminol breakdown from fixed transfected HEK293 cells surface-labeled withK328E) (light gray, n = 6) and α1(K378E) (dark gray, n = 12) mutations were assessed for changes in surface expression compared to WT (black, n = 12). The α1(K378E) mutation produced a significant increase over WT; Students t-test, *p < 0.05. Mock transfected cells expressing only GFP (white, n = 12) showed that there was a negligible amount of background staining.

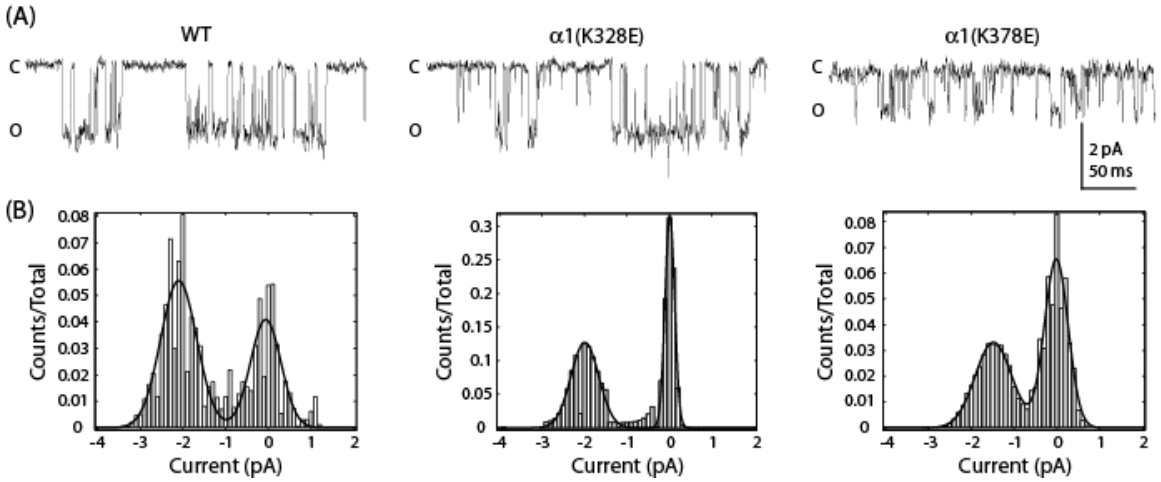

Figure 4.4: The α1(K378E) mutation decreased amplitude of single channel currents. (A) Single channel currents from outside-out patches containing WT, α1(K328E), and α1(K378E) receptors elicited with bath application of 3mM GABA. After analysis, a 60 Hz notch filter was applied for better visualization of openings. Open and closed levels are denoted by O and C respectively. (B) All-points histogram of current amplitudes with 0.01 pA/bin. Current amplitudes were fit with Gaussian functions to determine open and closed distributions; n = 3.

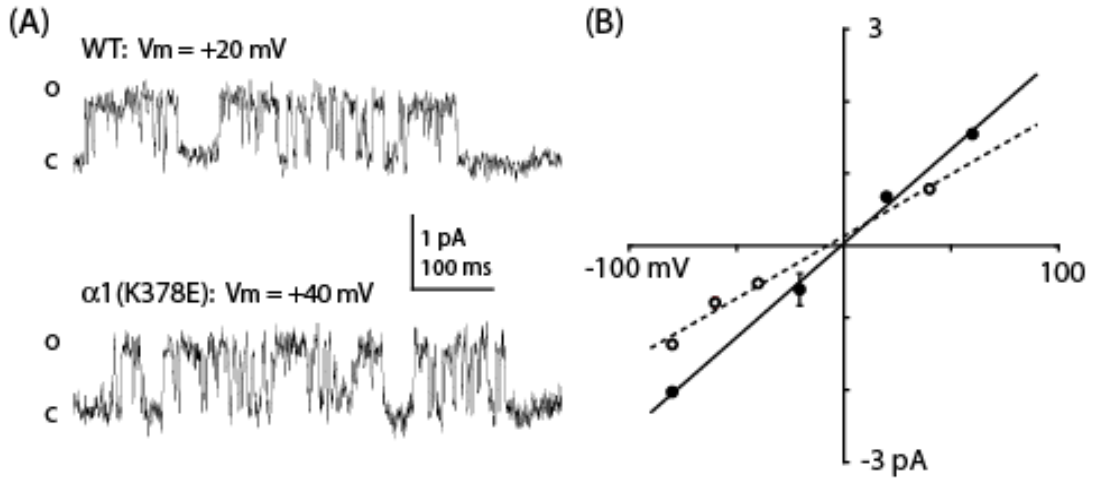

Figure 4.5: The α1(K378E) mutation decreased chord conductance. (A) Single channel currents from outside-out patches containing WT and α1(K378E) receptors at membrane holding potentials of +20 and +40 mV. Open and closed levels are denoted by O and C respectively. Traces show that the amplitude of currents is equivalent although the driving force on the ion is unequal. (B) IV relationship of WT (solid) and α1(K378E) (dashed) single channel currents. The α1(K378E) mutation decreased the chord conductance as shown by the change in slope of the IV relationship. Data points depict mean ± SEM; n=3.

Construct	WT	K328E	K378E
Unitary current (pA)	-2.03 ± 0.007	-1.97 ± 0.029	-1.37 ± 0.057*
Burst P_{open}	0.79 ± 0.017	0.86 ± 0.003	0.75 ± 0.006
Chord conductance (pS)	26.1 ± 5.09	N.D.	17.2 ± 5.82
Reversal Potential (mV)	-1.20 ± 10.2	N.D.	-7.45 ± 19.4

Table 4.2: Single channel properties of charge switch mutations. Single channel recordings were gathered from outside-out patches in extracellular saline containing 3 mM GABA. Mutants were compared to WT by the Students t-test with significance held at $p < 0.05$ (*). N = 3; means depicted ± 95% confidence interval of fit. Chord conductance and reversal potential values were not determined (N.D.) for α1(K328E).

4.3.1D: Ion replacement solutions confirmed anion selectivity of the WT pore

In order to determine the relative permeability of sodium and chloride in WT receptors, I replaced extracellular Na^+ and Cl^- ions with large impermeable ions of the same valence, N-methyl-*D*-glucamine and *D*-gluconate respectively; see Table 2.2 for composition of physiology solutions. Because the electrophoretic mobility of extracellular salines was not constant, junction potential values were calculated for each intracellular and extracellular saline combination and reversal potential values were corrected *a posteriori* (Table 2.3). In order to calculate the relative shift in reversal potential caused by ion replacement, I determined IV relationships from each whole-cell patch in symmetrical conditions (I1:E1) vs. low extracellular chloride (I1:E2) OR symmetrical conditions vs. low extracellular sodium (I1:E3). Thus, relative shifts in reversal potential were calculated within patch between symmetrical and low chloride conditions (E_{CS}), as well as, between symmetrical and low sodium conditions (E_{NS}). Calculation of IV relationships under ion concentration gradient conditions has been used to identify determinants of charge selectivity within the pLGIC superfamily (Fatima-Shad and Barry 1993; Jensen, Pedersen et al. 2005).

WT receptor containing cells had an experimentally determined reversal potential of -9.32 ± 0.93 mV in I1:E1 (n = 34; Fig. 4.6, Fig. 4.7, Table 4.3), which did not deviate from the theoretical reversal potential E_{Cl} = -7.75 mV. Decreasing extracellular chloride concentration positively shifted the reversal potential (E_{CS} = +41.3 ± 2.66 mV), which verified that the WT $GABA_AR$ was an anion permeable channel (n = 17; paired t-test $p < 0.05$; Fig. 4.6). However, the measured reversal potential value deviated from the theoretical shift in reversal potential (E_{Cl} = +65.7 mV) from I1:E1 to I1:E2 conditions (calculated assuming the pore was only permeable to chloride). Previous studies have reported a ~10% relative permeability of gluconate in $GABA_ARs$ (Fatima-Shad and Barry 1993; Jensen, Pedersen et al. 2005). Likewise, our experimental deviation may be caused by an equivalent relative permeability to gluconate

($P_G/P_{Cl} = 0.13 \pm 0.02$). Decreasing extracellular sodium did not significantly shift the reversal potential ($E_{NS} = +2.02 \pm 0.49$ mV), which confirmed that the cation permeability of the channel was negligible (n = 17; paired t-test $p > 0.05$; Fig. 4.7).

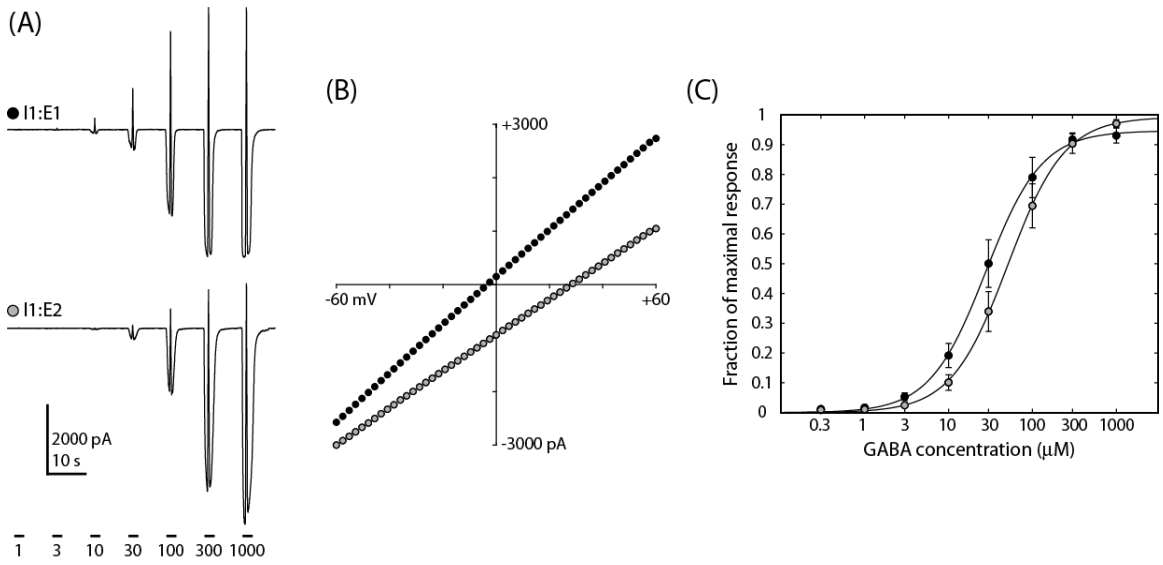

Figure 4.6: $GABA_AR$ ion channel is anion permeable. (A) Representative traces for WT receptors in symmetrical chloride (I1:E1) and in low extracellular chloride (I1:E2) conditions. Bars indicate the duration of GABA application and are labeled with the concentration (µM). (B) IV relationships determined in I1:E1 (black) and I1:E2 (gray) solutions. Mean data points are shown; n = 17. The reversal potential was significantly more positive in I1:E2 as expected for an anion permeable pore; paired t-test, $p > 0.05$. (C) Hill fit of normalized peak currents at -60 mV in I1:E1 (black) and I1:E2 (gray) solutions. Data points denote mean ± SEM; n = 17. The concentration-response relationship was shifted to the right in I1:E2, but there were no significant differences in EC_{50}, nH, or I_{max} between the I1:E1 and I1:E2 salines; paired t-test, $p < 0.05$.

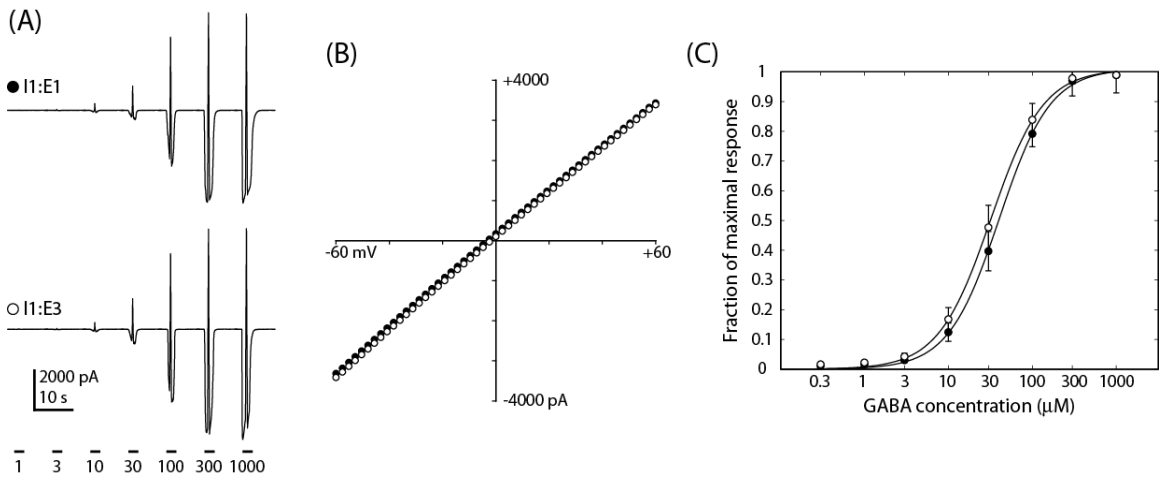

Figure 4.7: $GABA_AR$ ion channel is cation impermeable. (A) Representative traces for WT receptors in symmetrical chloride (I1:E1) and in low extracellular sodium (I1:E3) saline conditions. Bars indicate the duration of GABA application and are labeled with the concentration (μM). (B) IV relationships determined in I1:E1 (black) and I1:E3 (white) solutions. Mean data points are shown; n = 17. (C) Hill fit of normalized peak currents at -60 mV in I1:E1 (black) and I1:E3 (white) solutions. Data points denote mean ± SEM; n = 17. There were no significant differences in reversal potential, EC_{50}, nH, or I_{max} between the I1:E1 and I1:E3 conditions; paired t-test, $p > 0.05$.

4.3.1E: Intracellular loop domain charge switch point mutations did not alter charge selectivity

If charged residues lining the pore lumen make important electrostatic interactions with permeant ions, then switching the charge of such residues should perturb the selective permeability of the pore causing a shift in reversal potential. For example, an increase in the relative permeability of the channel to sodium (P_{Na}/P_{Cl}) will cause a negative relative shift in current reversal when the extracellular concentration of sodium is decreased. Of the 25 charge-switches made, none caused a significant negative shift in E_{NS} compared to WT (Dunnett *post hoc,* $p > 0.05$; Fig. 4.8, Fig. 4.10, Table 4.4). In fact, none of the mutations were significantly different from WT in regards to relative sodium permeability (Dunnett *post hoc,* $p > 0.05$).

4.3.1F: Charge switch point mutations shifted the relative reversal of anions

Eight charge-switch mutations, α1(K312E), α1(K320E), α1(D332K), α1(D356K), α1(K364E), α1(E369K), α1(K378E) and, α1(E381K), significantly increased E_{CS}, (Fig. 4.9, Fig. 4.10, Table 4.4). Three of these residues were located in a 20-residue span continuous with M3 and five of these residues were located in a 25-residue span near M4. In particular, the measured reversal potential shifts for the α1(K312E) mutation ($E_{CS} = +54.3 \pm 5.32$ mV) and the α1(K378E) mutation ($E_{CS} = +52.0 \pm 2.61$ mV) approached the theoretical value ($E_{Cl} = +65.7$ mV) predicted assuming the ion channel solely fluxes chloride ions (Fig. 4.9, Fig. 4.10, Table 4.4). Therefore, these significant changes in current reversal may be caused by largely eliminating the relative permeability of the ion channel to gluconate in receptors harboring the α1(K312E) mutation ($P_G/P_{Cl} = 0.027 \pm 0.014$) and the α1(K378E) mutation ($P_G/P_{Cl} = 0.028 \pm 0.011$) compared to WT receptors ($P_G/P_{Cl} = 0.13 \pm 0.02$).

Figure 4.8: Point mutations did not change charge selectivity of the pore.

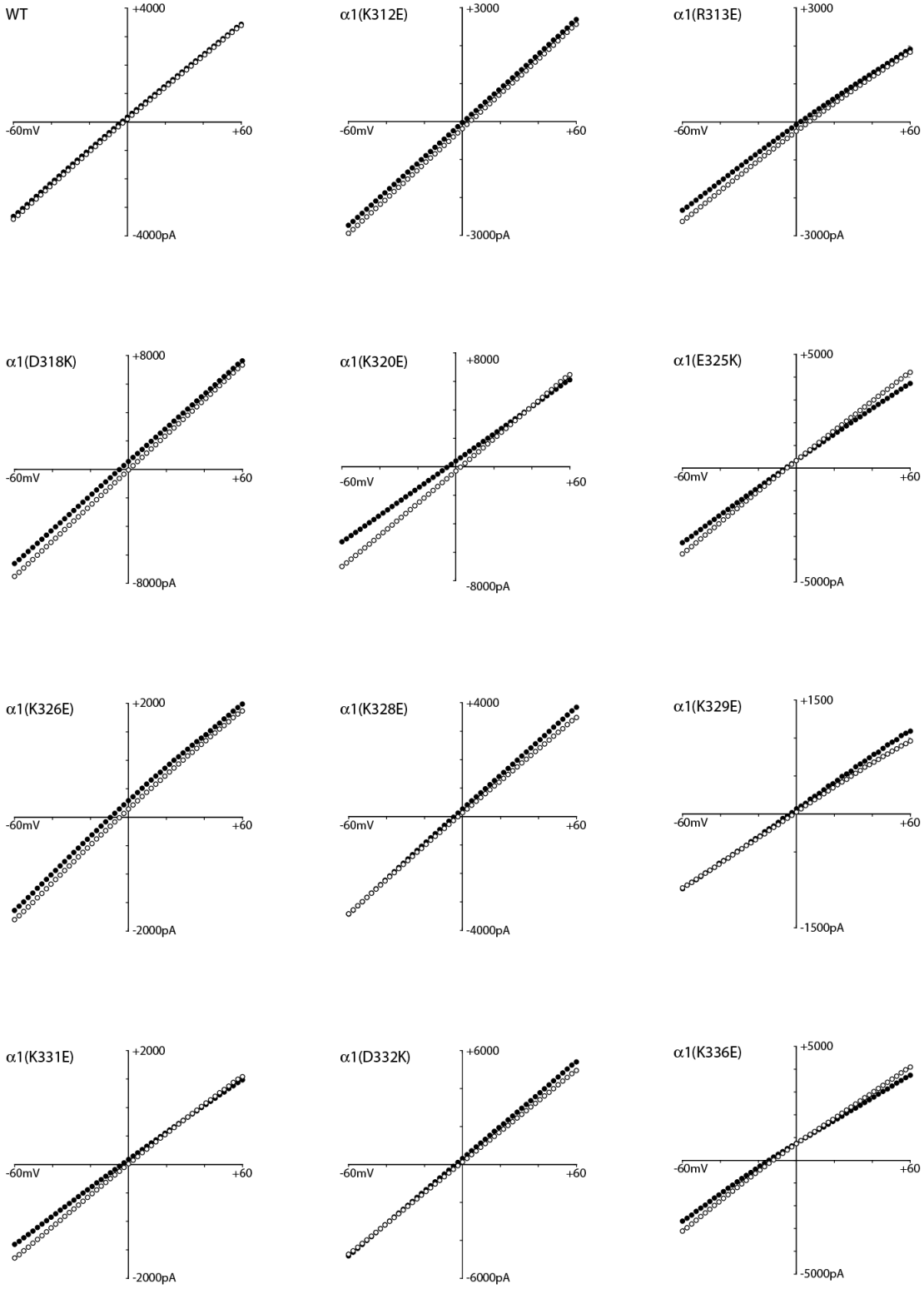

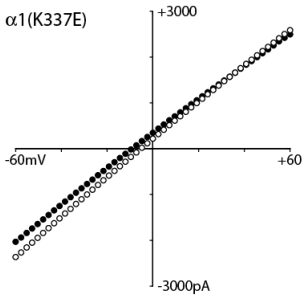
α1(K337E)
+3000
-60mV
+60
-3000pA

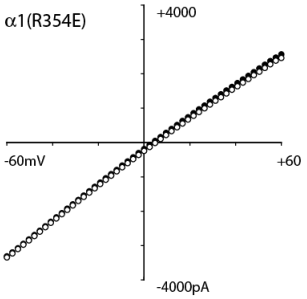
α1(R354E)
+4000
-60mV
+60
-4000pA

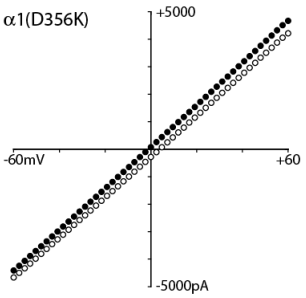
α1(D356K)
+5000
-60mV
+60
-5000pA

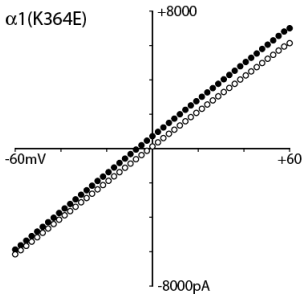
α1(K364E)
+8000
-60mV
+60
-8000pA

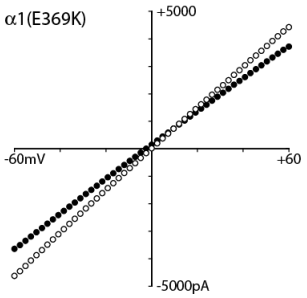
α1(E369K)
+5000
-60mV
+60
-5000pA

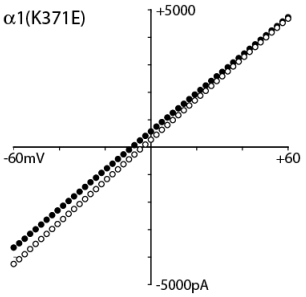
α1(K371E)
+5000
-60mV
+60
-5000pA

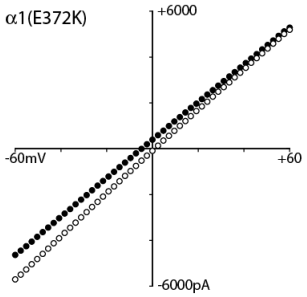
α1(E372K)
+6000
-60mV
+60
-6000pA

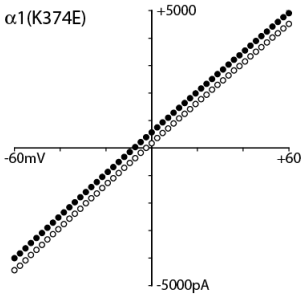
α1(K374E)
+5000
-60mV
+60
-5000pA

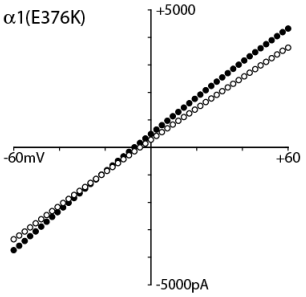
α1(E376K)
+5000
-60mV
+60
-5000pA

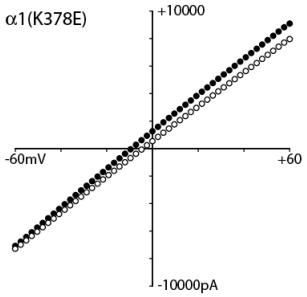
α1(K378E)
+10000
-60mV
+60
-10000pA

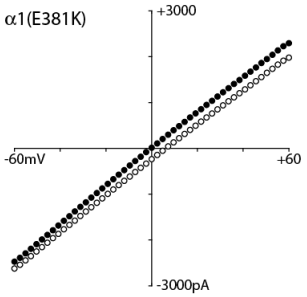
α1(E381K)
+3000
-60mV
+60
-3000pA

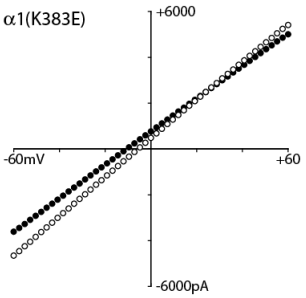
α1(K383E)
+6000
-60mV
+60
-6000pA

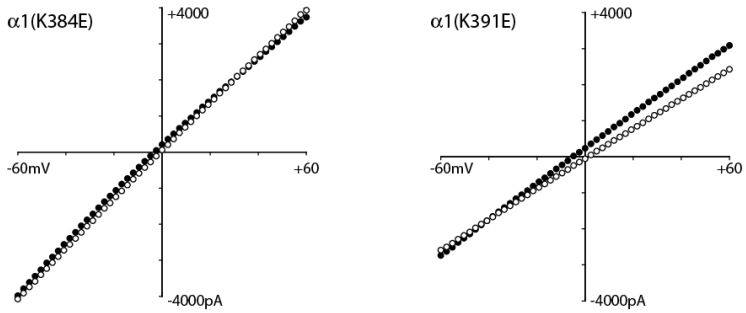

Figure 4.8: Point mutations did not change charge selectivity of the pore. IV relationships were determined for WT and each charge switch mutation in symmetrical conditions (black) and in low extracellular sodium conditions (white). There were no significant changes induced by decreasing the sodium concentration; likewise, there were no significant changes induced by charge switch mutations (all tests, $p > 0.05$). Circles depict mean current values; for specific reversal potential values and sample sizes see Table 4.4.

Figure 4.9: Mutations decreased relative anion permeability.

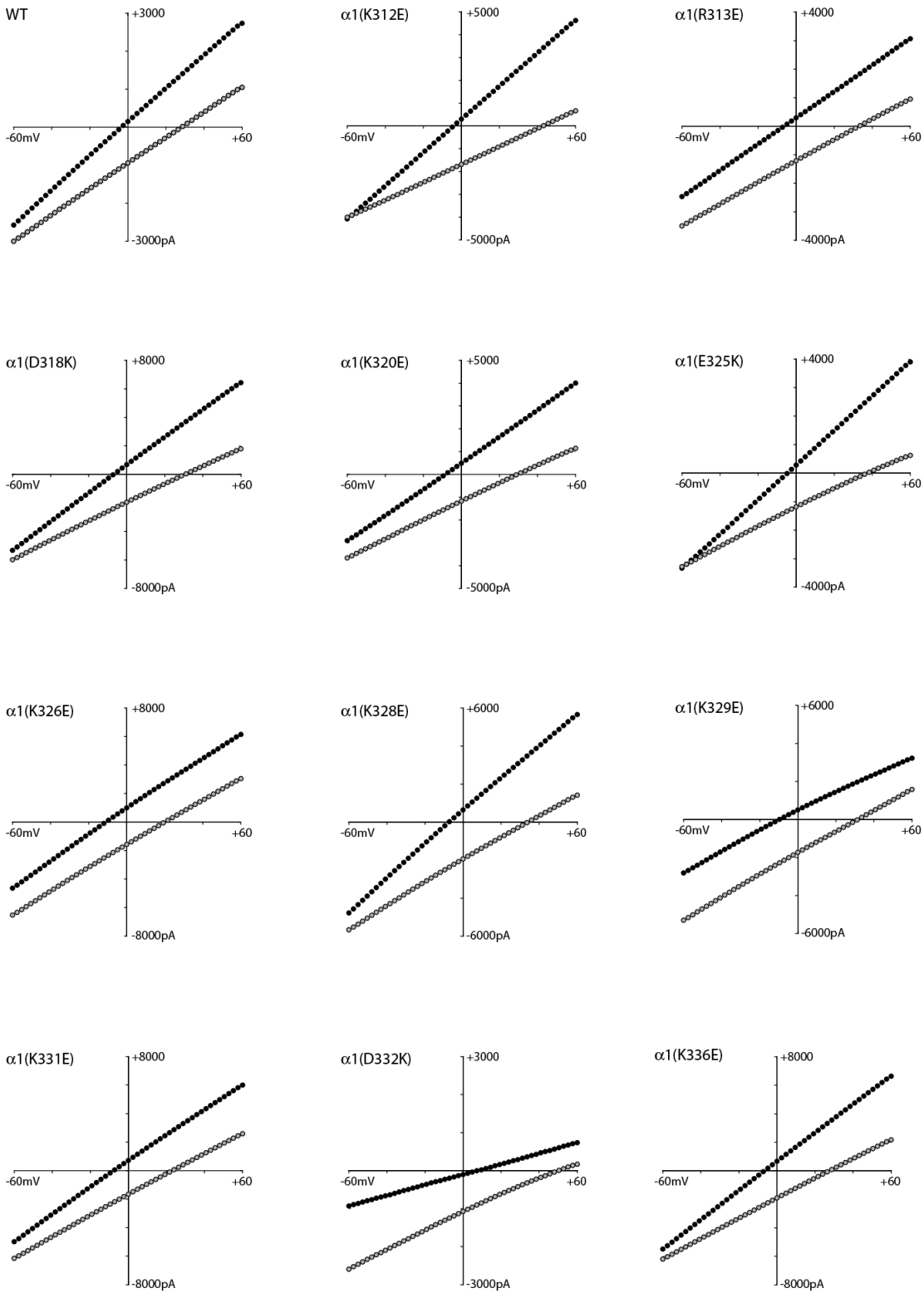

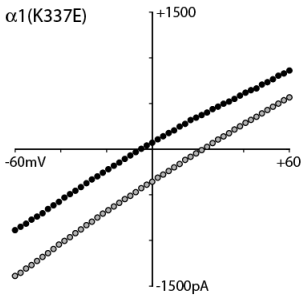
α1(K337E)
+1500
-60mV
+60
-1500pA

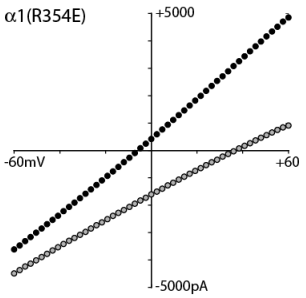
α1(R354E)
+5000
-60mV
+60
-5000pA

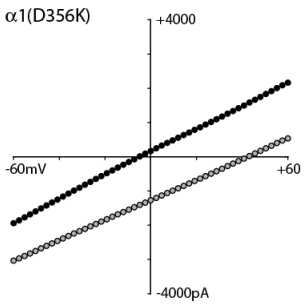
α1(D356K)
+4000
-60mV
+60
-4000pA

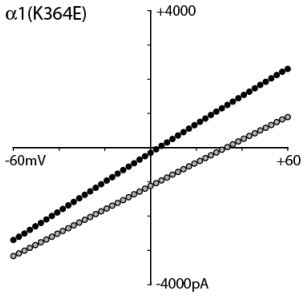
α1(K364E)
+4000
-60mV
+60
-4000pA

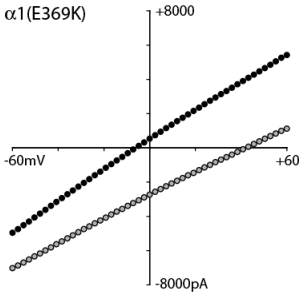
α1(E369K)
+8000
-60mV
+60
-8000pA

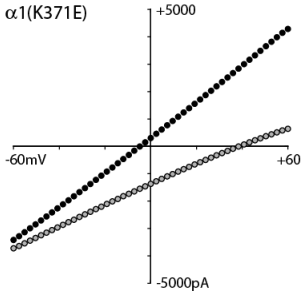
α1(K371E)
+5000
-60mV
+60
-5000pA

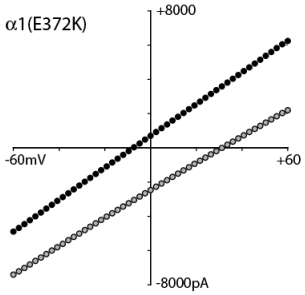
α1(E372K)
+8000
-60mV
+60
-8000pA

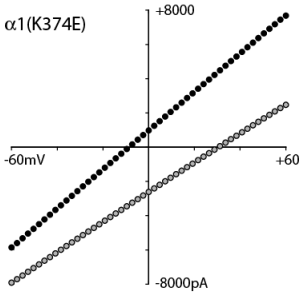
α1(K374E)
+8000
-60mV
+60
-8000pA

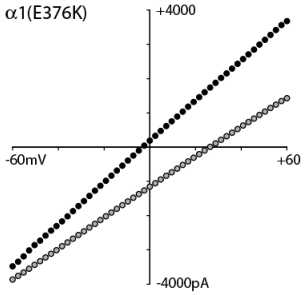
α1(E376K)
+4000
-60mV
+60
-4000pA

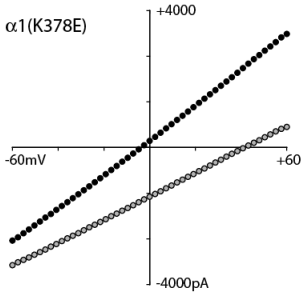
α1(K378E)
+4000
-60mV
+60
-4000pA

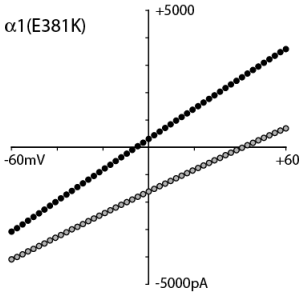
α1(E381K)
+5000
-60mV
+60
-5000pA

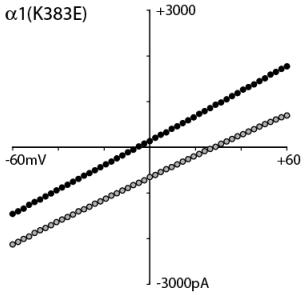
α1(K383E)
+3000
-60mV
+60
-3000pA

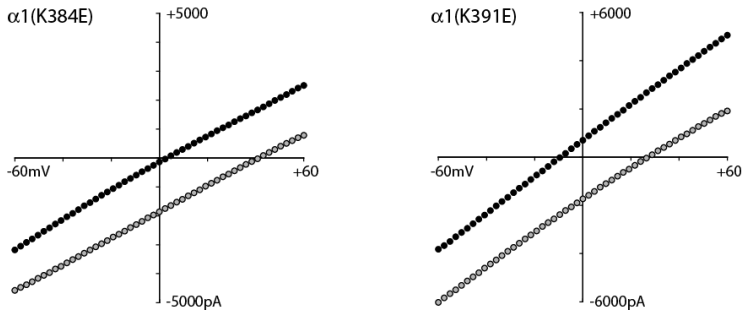

Figure 4.9: Mutations decreased relative anion permeability. IV relationships were determined for WT and each charge switch mutation in symmetrical chloride conditions (black) and in low extracellular chloride conditions (gray). Decreasing the extracellular chloride concentration significantly shifted the reversal potential as predicted for an anion permeable pore (Students t-test, $p < 0.05$). Six mutations significantly increased the reversal potential compared to WT (Students t-test, $p < 0.05$). Circles depict mean current values; for specific reversal potential values and sample sizes see Table 4.4.

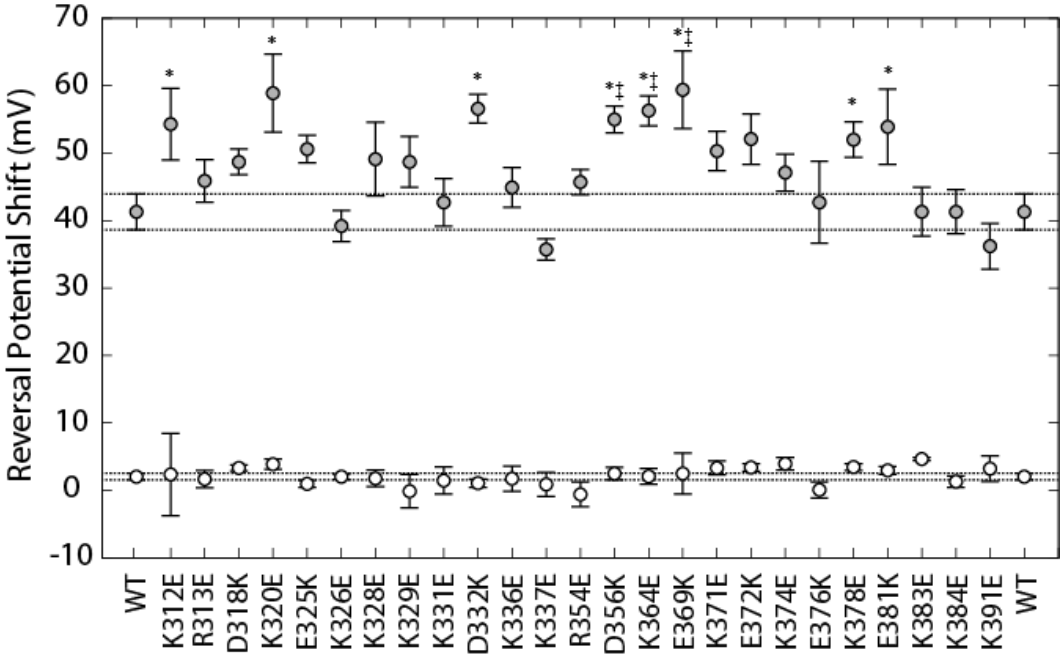

Figure 4.10: Mutations induced a subdomain dependent shift in anion permeability. Relative shifts in current reversal from symmetrical conditions (I1:E1) caused by decreasing extracellular chloride (E2; gray) or extracellular sodium (E3; white). Mean values are shown ± SEM. Dotted lines represent the SEM margins for WT, n = 17; Mutations, n = 5; significance held at $p < 0.05$ for Dunnett *post hoc* test (‡) and Students t-test (*) comparing each mutation to WT.

Construct	E_S (mV)	N	Construct	E_S (mV)	N
WT	-9.32 ± 0.93	34	R354E	-4.04 ± 2.65	9
K312E	-2.65 ± 2.28	10	D356K	-7.49 ± 0.98	10
R313E	-2.76 ± 2.39	12	K364E	-3.85 ± 5.46	10
D318K	-8.63 ± 1.48	10	E369K	-5.34 ± 1.85	11
K320E	-3.25 ± 3.77	9	K371E	-4.91 ± 2.88	11
E325K	-7.51 ± 1.78	8	E372K	-8.64 ± 0.75	11
K326E	-10.7 ± 1.57	10	K374E	-10.6 ± 1.22	16
K328E	-7.07 ± 2.04	10	E376K	-7.55 ± 1.60	10
K329E	-11.8 ± 1.76	10	K378E	-8.95 ± 1.95	11
K331E	-10.2 ± 1.27	14	E381K	-6.78 ± 1.46	10
D332K	-2.21 ± 3.32	9	K383E	-8.00 ± 1.77	11
K336E	-13.7 ± 1.74	10	K384E	-8.23 ± 1.66	10
K337E	-12.7 ± 1.08	11	K391E	-7.70 ± 2.38	9

Table 4.3: Reversal potential values for charge switch mutations. IV relationships were determined in symmetrical chloride (I1:E1) and the reversal potential (E_S) was interpolated. There were no significant differences in E_S from WT; means depicted ± SEM.

Construct	E_{NS} (mV)	N	E_{CS} (mV)	N	Construct	E_{NS} (mV)	N	E_{CS} (mV)	N
WT	2.02 ± 0.49	17	41.3 ± 2.66	17	R354E	-0.61± 1.83	4	45.7 ± 1.88	5
K312E	2.34 ± 6.10	5	54.3 ± 5.32*	4	D356K	2.47 ± 0.94	5	55.0 ± 1.99*‡	5
R313E	1.65 ± 1.29	6	45.9 ± 3.17	6	K364E	2.06 ± 1.18	5	56.3 ± 2.22*‡	4
D318K	3.31 ± 0.44	5	48.7 ± 1.91	5	E369K	2.48 ± 3.04	5	59.4 ± 5.76*‡	5
K320E	3.85 ± 0.75	5	58.9 ± 5.80*	4	K371E	3.32 ± 1.00	5	50.3 ± 2.93	6
E325K	0.94 ± 0.53	5	50.6 ± 2.07	3	E372K	3.39 ± 0.56	6	52.1 ± 3.74	5
K326E	2.00 ± 0.42	4	39.2 ± 2.31	5	K374E	3.92 ± 0.95	6	47.1 ± 2.76	10
K328E	1.76 ± 1.23	5	49.1 ± 5.48	4	E376K	0.05 ± 1.17	5	42.7 ± 6.07	5
K329E	-0.14 ± 2.50	5	48.7 ± 3.78	5	K378E	3.43 ± 0.48	6	52.0 ± 2.61*	5
K331E	1.42 ± 2.02	5	42.7 ± 3.54	9	E381K	2.95 ± 0.58	5	53.9 ± 5.57*	5
D332K	1.05 ± 0.62	5	56.6 ± 2.14*	5	K383E	4.63 ± 0.23	5	41.3 ± 3.62	6
K336E	1.72 ± 1.87	5	44.9 ± 2.94	5	K384E	1.28 ± 0.87	5	41.3 ± 3.26	5
K337E	0.86 ± 1.80	6	35.7 ± 1.58	5	K391E	3.21 ± 1.89	5	36.2 ± 3.39	4

Table 4.4: Relative shifts in reversal potential. The IV relationships were determined in a pair-wise fashion for normal and ion replacement solutions so that relative shifts in reversal potential induced by low sodium (E_{NS}) and low chloride (E_{CS}) extracellular solutions could be determined for each cell. Significant differences from WT were held at $p < 0.05$ for Students t-test (*) and Dunnett's post hoc (‡) comparisons after MANOVA; means depicted ± SEM.

4.3.2: Charged residues of the intracellular loop domain control channel gating

In Chapter 3 deletion of the intracellular loop domain was shown to significantly decrease the apparent affinity of the receptor for the full agonist GABA. Based on the modular nature of protein domains, it is highly unlikely that mutations within the intracellular loop domain altered ligand binding within the extracellular domain. Therefore, I hypothesized is that the intracellular loop domain, in fact, mediates channel gating. To test this hypothesis I calculated GABA EC_{50} values from a Hit fit of the concentration-relationship and compared the response of each charge switch mutation to WT. If a mutation significantly changed the GABA EC_{50}, then subsequent experiments investigated the relative efficacies of full and partial agonists to tease apart the contributions of binding and gating to the apparent affinity value. Additionally, I investigated the influence of desensitization on channel gating, by determining the time constant of desensitization for each construct.

4.3.2A: Charge switch point mutations decreased GABA apparent affinity

Six of the mutants, α1(K312E), α1(D318K), α1(K320E), α1(K328E), α1(D332K), and α1(R354E), showed a significant right shift in concentration response with a 2- to 3-fold increase in GABA EC_{50} (Fig. 4.2A-C, Table 4.1). All but one of the significant decreases in apparent affinity resulted from mutations located within a 20 residue span near M3. None of the charge switch mutations resulted in a significant increase in apparent affinity (all tests, $p > 0.05$).

A shift in EC_{50} can be caused by changes in receptor gating or a change in the local structure around the mutation that propagates throughout the subunit to alter the GABA binding site. According to David Colquhoun (1998), “Making this distinction between effects on binding and effects on conformation change is arguably the fundamental problem of modern molecular studies of receptors. It is not just a theoretical problem; this is how ion channels actually

behave." The $GABA_AR$ functions as both a ligand recognition receptor and an ion channel. The "affinity" of the receptor for an agonist and the "efficacy" of the agonist in activating the ion channel are intrinsically linked. This is why EC_{50} is termed "apparent affinity" because it may be skewed by both binding and gating effects. To determine the relative effects of the mutation on binding and gating, I constructed concentration-response relationships from the same whole-cell patch for both the partial agonist piperidine-4-sulfonic acid (P4S) and the full agonist GABA (Fig. 4.11). GABA and P4S are structurally similar (Fig. 4.11A) and bind at the same orthosteric site, but the partial agonist is less efficacious in gating the ion channel resulting in a reduction in the open probability of the receptor. Therefore, a decrease in relative agonist efficacy (I_{P4S}/I_{GABA}) is consistent with a reduction in gating efficiency; this concept is reviewed in Section 1.3.4.

4.3.2B: The α1(K312E) mutation caused a gating impairment

Cells expressing the α1(K312E) mutation yielded a ~2-fold increase in EC_{50} with no other significant changes in the GABA concentration response (Table 4.1). As expected, P4S exhibited decreased efficacy in both WT and mutant receptor containing cells. However, relative agonist efficacy for α1(K312E) was significantly decreased ($I_{P4S}/I_{GABA} = 0.08 \pm 0.035$) compared to WT ($I_{P4S}/I_{GABA} = 0.19 \pm 0.022$; Students t-test, $p < 0.05$; $n = 3$; Fig. 4.11). A decrease in relative agonist efficacy is consistent with the hypothesis that the α1(K312E) mutation exhibited decreased apparent affinity because of the importance of the native residue in receptor gating and NOT because the mutation altered ligand binding.

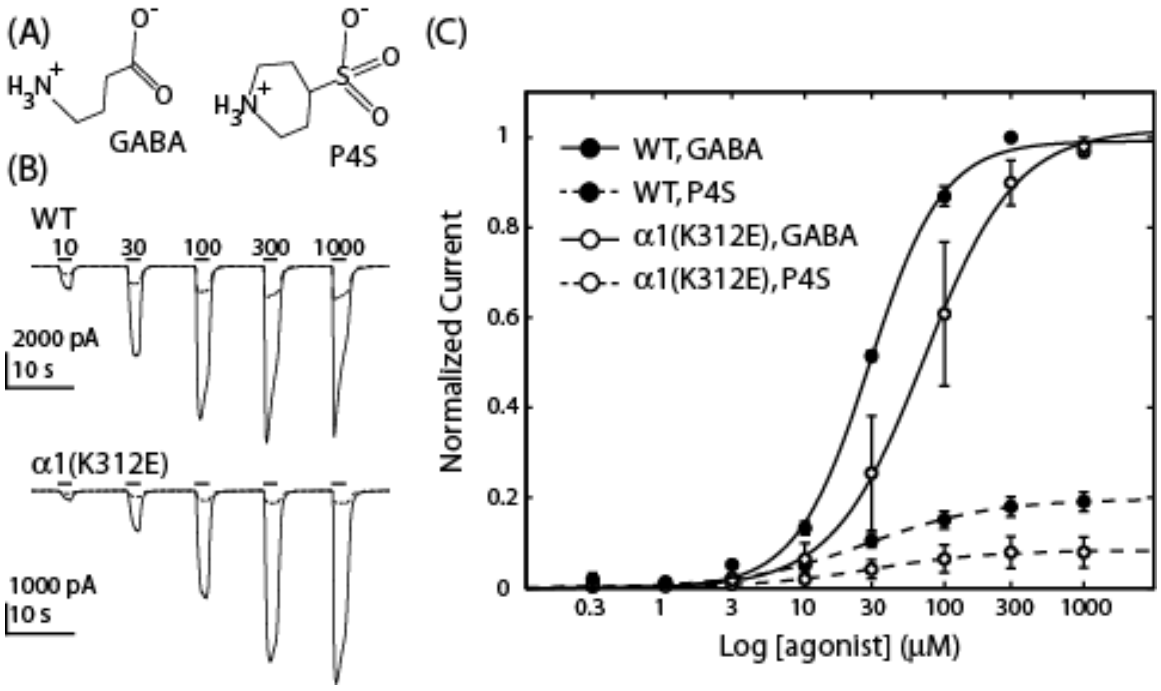

Figure 4.11: The α1(K312E) mutation decreased relative partial agonist efficacy. (A) Structural similarities between full and partial agonists, GABA and P4S respectively. (B) Averaged whole-cell current traces elicited with GABA (solid) and P4S (dashed) for WT and α1(K312E) receptor-containing cells; bars indicate agonist application with concentrations (μM). The same concentration range was used for full and partial agonists. (C) Hill equation fit of data normalized to the maximal GABA response showed a significant decrease in the relative agonist affinity ratio for the α1(K312E) mutation (open circles) compared to WT (solid circles); error bars denote SEM; n = 3 .

4.3.2C: Charge switch point mutations increased the speed of desensitization

Desensitization is characterized by channel closure during the prolonged application of agonist. To determine if charge-switch mutations induced changes in the desensitization component of gating, each macroscopic trace was fit with an exponential equation to determine a weighted time constant [Eq. 7] from currents elicited by maximally effective concentrations of GABA; for specific methods see Section 2.3.5. Seven mutations, α1(K320E), α1(K336E), α1(R354E), α1(K374E), α1(K378E), α1(K383E), and α1(K384E), had significantly enhanced desensitization compared to WT with up to a ~3-fold increase in the speed of desensitization induced by the α1(K384E) mutation (Fig. 4.12A).

Channel activation followed by the onset of desensitization occurs rapidly upon agonist binding; both transitions occur within 100 ms for the $GABA_AR$ α1 subunit (Lavoie et al., 1997; Picton and Fisher 2007). Slow solution exchange rates in the whole-cell patch configuration at the bottom of the perfusion chamber may confound calculation of desensitization rates. Channels that are first exposed to GABA solutions will activate and begin to desensitize before other channels have been exposed to GABA. In order to improve the temporal resolution of desensitization measurements, I used a rapid application technique to verify one of the mutants (Fig. 4.12B). Large (~10 pF) excised outside-out patches were pulled and lifted from the bottom of the dish to allow more rapid fluid exchange. The ratio of weighted time constants between WT and the α1(K378E) mutation remained constant at 2.5-fold when determined from both whole-cell and excised-patch traces. Therefore, calculation of desensitization rate from whole-cell currents was sufficient to detect changes incurred by mutagenesis.

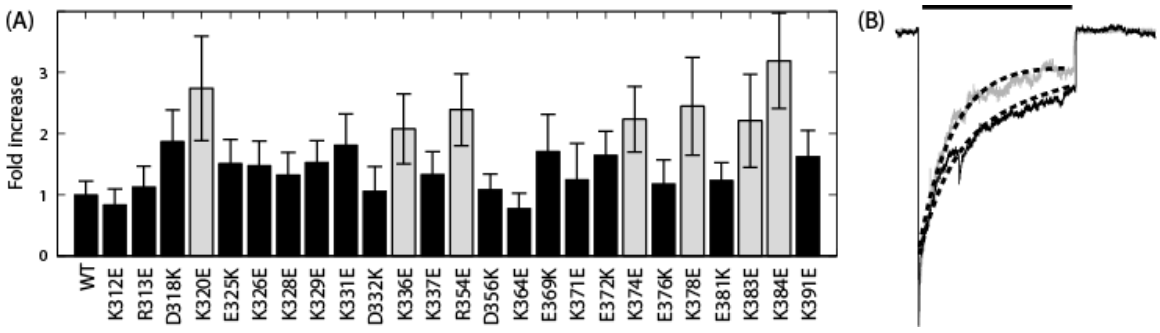

Figure 4.12: Charge switches increased speed of desensitization. (A) The rate of desensitization was determined from whole-cell currents elicited by maximal concentrations of GABA. The fold increase in weighted desensitization constant [Eq. 7] normalized to WT response, highlighted by dotted line, is shown for each charge switch point mutation. Gray bars indicate mutations which were significantly different from WT; Tukey *post hoc* test, $p < 0.05$; error bars denote SEM; WT, n = 30; Mutations, n = 8-17. (B) Scaled, representative currents elicited in excised outside-out macroscopic patches by 10 s application of 3 mM GABA from WT (black; n = 16) and α1(K378E) (gray; n = 3) receptor-containing patches. Dotted line depicts the exponential fit of averaged traces.

4.4: Discussion

4.4.1: Functional subdomains of the α1 intracellular loop domain

Using macroscopic and single channel voltage-clamp recording techniques, I have established a role for specific charged residues within the intracellular loop domain of the $GABA_AR$ α1 subunit in mediating channel gating by GABA, the time course of desensitization, the magnitude of channel conductance and anion permeation. Furthermore, the individual residues controlling each facet of channel activity are located within discrete subdomains of the intracellular loop domain, with respect to the primary amino acid sequence. These results, not only confirmed my hypothesis that the α1 intracellular loop domain plays a role in controlling channel gating and ion permeation, but also showed that these functions are segregated to specific regions of the domain.

4.4.1A: Defining the Subdomains of the ILD

The intracellular loop domains of pLGIC proteins have a higher degree of variability compared to the extracellular domain and the transmembrane domain, both in terms of side chain conservation and loop length. A primary amino acid sequence alignment of the intracellular loop domain of the three synaptic $GABA_AR$ α subunits highlights this variability, but also suggests some local conservation (Fig. 4.13). The first and last ~30 residues of the intracellular loop domain, i.e. those contiguous with M3 and M4, are regions of the α subunits that contain a large number of strongly conserved charged residues. I observed that charge-switch mutations close to M3 predominantly resulted in receptors with decreased GABA apparent affinity indicative of a gating impairment (Fig. 4.2, Fig. 4.14, Table 4.1); on the other hand, charge switch mutations close to M4 resulted in receptors with enhanced desensitization (Fig. 4.12, Fig. 4.14). Mutations within both charge rich regions caused a positive shift in reversal potential in low chloride extracellular saline, which suggests the existence of an intracellular anion selectivity filter (Fig. 4.9, Fig. 4.14). This led me to identify two functional subdomains of the domain: the M3

associated subdomain (M3A†) and the M4 associated subdomain (M4A†; Fig. 4.14, Fig. 4.15). Intriguingly, the proposed consensus sequence for gephyrin binding in the α1 and α2 subunits was located between M3A and M4A, within the center of the alignment (Tretter, Jacob et al. 2008; Mukherjee J. 2010), suggesting the existence of a third intracellular loop domain subdomain within α subunits that acts in a more "traditional" manner as a protein substrate to determine receptor localization (Fig. 4.14).

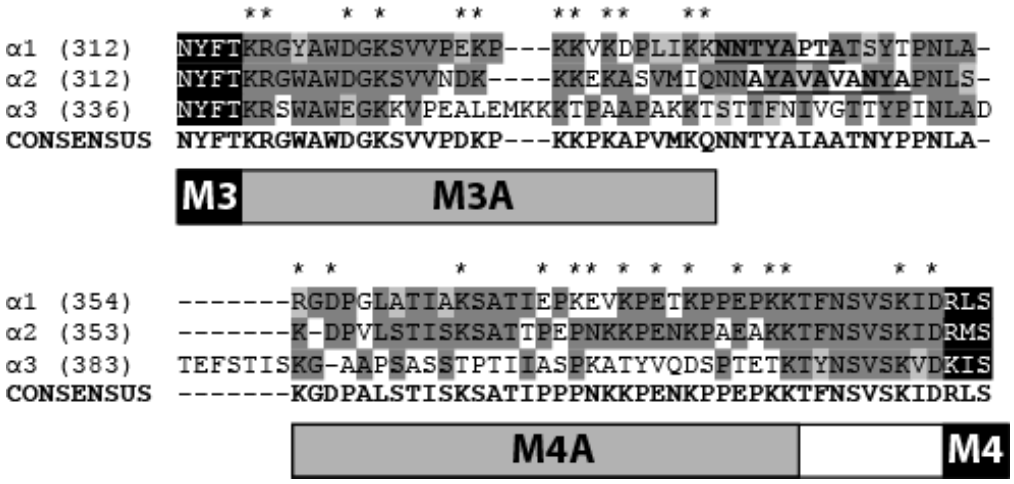

Figure 4.13: Sequence alignment of synaptic $GABA_AR$ α subunits. Round brackets (#) give the sequence number. Dark grey background shows residues with 100% identity to the consensus sequence and light grey background marks residues that share side-chain property conservation. The locations of charged residues within the α1 subunit are marked with an asterisk. Locations of transmembrane domains (M3 and M4) and membrane associated domains (M3A and M4A) are shown beneath the alignment.
Ascension number: *α1, NP_000797; α2, NP_000798; α3, NP_000799.*

† The M3A and M4A nomenclature for functional subdomains is meant to suggest that each subdomain is merely associated with the M3 and M4 transmembrane domains with no preconception of secondary structure.

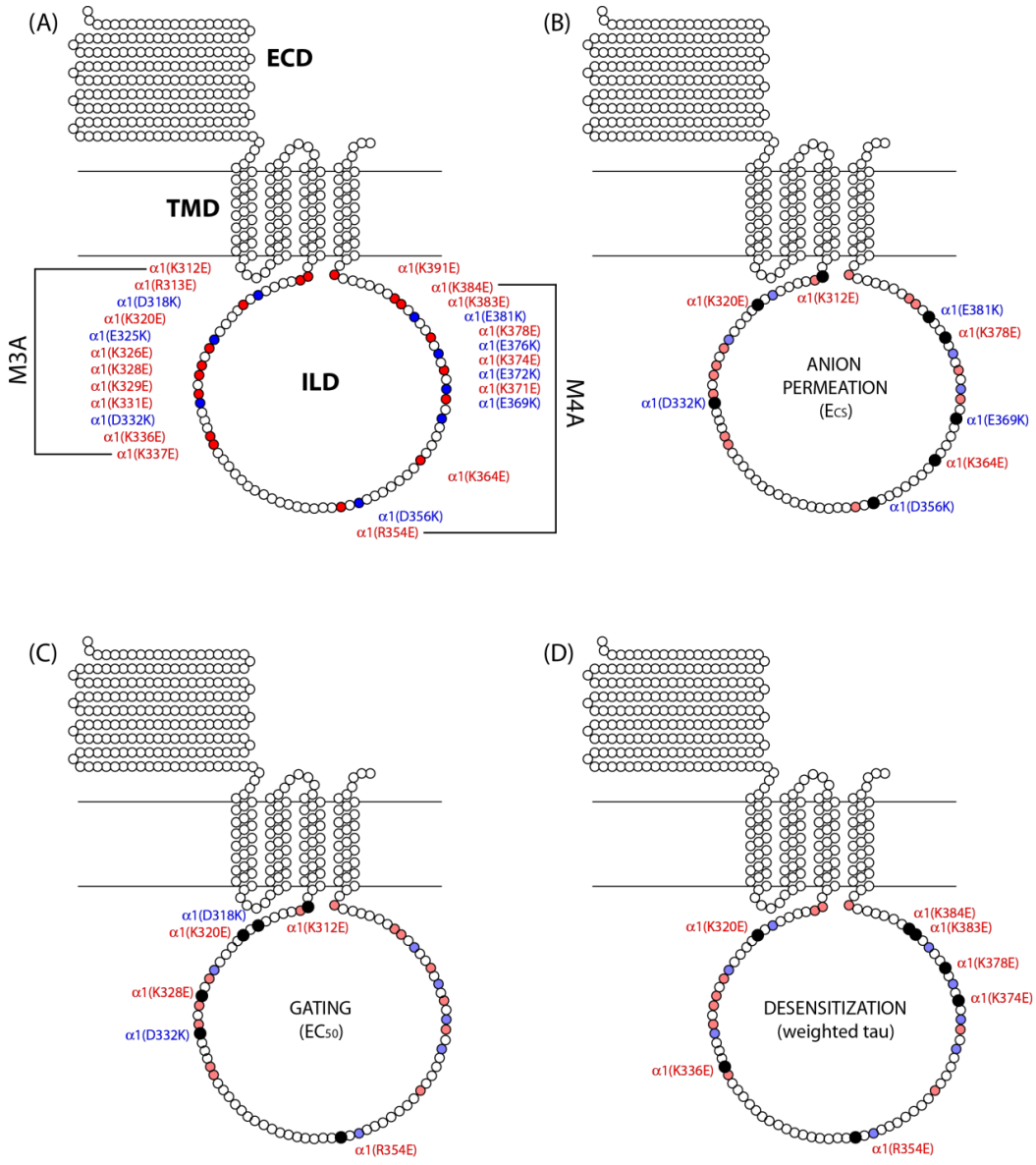

Figure 4.14: Subdomains of the α1 intracellular loop domain. (A) Schematic of the $GABA_AR$ α1 subunit shows the arrangement of the extracellular domain (ECD), transmembrane domain (TMD), and intracellular loop domain (ILD). Each circle represents an amino acid position and the horizontal lines show the boundary of the membrane. The positions of basic to glutamate (red) and acidic to lysine (blue) charge switch mutations are highlighted. Based on the proximity of functional changes induced by the point mutations I defined the M3 associated subdomain (M3A) to include residues from α1(K312) to α1(K337) and the M4 associated subdomain (M4A) to include residues from α1(R354) to α1(K384). Significant changes in (B) anion permeation, (C) channel gating and (D) desensitization are highlighted in black for each position.

4.4.1B: The M3A Subdomain

I defined M3A as the 25 residues between positions α1(K312) and α1(K337), containing twelve charged amino acids. Mutation of five of these charged residues caused a decrease in GABA apparent affinity (Fig. 4.2, Fig. 4.15C, Table 4.1). This observation may be due to a decrease in agonist affinity or impairment of the efficacy of the agonist; in terms of ion channel function this translates to either a binding or gating deficiency. The extracellular location of the GABA binding site (Section 1.3.3) and the modular nature of protein domains (Duret, Van Renterghem et al. 2011; Goyal, Salahudeen et al. 2011) strongly suggests that these mutations impaired receptor gating and NOT agonist binding. Functionally, the molecular movements that translate binding to gating are intrinsically linked and the two facets of channel activation are difficult to distinguish experimentally. The hypothesis that intracellular loop domain mutations decreased the apparent affinity for GABA via a gating impairment was experimentally supported by the observed reduction in relative partial agonist efficacy induced by the α1(K312E) mutation (Fig. 4.11). Both GABA and P4S bind at the same orthosteric site, therefore the relative agonist affinities for the receptor are predicted to be unaffected by a gating impairment (Colquhoun 1998). If a mutation impaired channel gating, then the efficacy of both agonists would be decreased; therefore relative agonist efficacy values would be different between the native and impaired receptor (Colquhoun 1998). Therefore, a decrease in I_{P4S}/I_{GABA} is consistent with the hypothesis that the α1(K312E) mutation exhibited decreased apparent affinity because of the importance of the native residue in receptor gating and not because the mutation altered ligand binding. Furthermore, this subdomain is continuous with M3, which has been shown to move during channel gating (Williams and Akabas 1999). One probable cause for the decrease in EC_{50} is that charged residues within M3A also undergo movement upon channel activation and by switching these charges we have impeded this movement. On the other hand, ions within the pore of voltage-gated potassium channels have been shown to stabilize the open, conducting state of the ion channel (Jensen, Borhani et al. 2010). A second cause for this observation is that

ion ion sensor electrostatic interactions, between permeant chloride ions and charged residues that define ion sensor sites of the permeation pathway, are integral gating elements. The chloride dependence of channel gating will be investigated in greater detail in Chapter 5.

4.4.1C: The M4A Subdomain

M4A was defined as the 30 residue span between α1(R354) and α1(K384) that contains twelve charged residues. Due to the C-terminal location of MA4 within the intracellular loop domain, this subdomain is predicted to be structurally homologous to the MA helix, which forms the intracellular windows in the nAChR (Unwin 2005); secondary structure predictions of the intracellular loop domain will be discussed in Chapter 6. Five mutations within the M4A subdomain significantly increased the speed of desensitization (Fig. 4.12). All of these residues are basic residues in the WT receptor: α1(R354), α1(K374), α1(K378), α1(K383), and α1(K384). The charge conservation of these residues suggests that intracellular control of desensitization is mediated by specific electrostatic interactions perhaps with permeant chloride ions. Again, this will be investigated in Chapter 5.

The mutation of charged residues near M4 has been shown to alter single channel conductance in homomeric 5-HT_{3A}R and α1 GlyR (Kelley, Dunlop et al. 2003; Carland, Cooper et al. 2009). This literature helped to inspire my primary hypothesis, that intracellular loop domain residues of the $GABA_A$R control ion permeation to set channel conductance. Indeed, the α1(K378E) mutation induced a significant decrease in single channel chord conductance (Fig. 4.4, Fig. 4.5, Table 4.2) which provides strong evidence that the M4A subdomain is the $GABA_A$R homolog of the MA stretch and also confirmed the hypothesis that intracellular residues of the α1 subunit interact with permeant ions.

4.4.2: Intracellular loop domain residues define an anion selectivity filter

To specifically identify residues that define the intracellular portion of the permeation pathway, I determined IV relationships for WT and each charge switch mutation in symmetrical and ion gradient conditions. None of the 25 charge switch mutations changed the cation permeability of the pore (Fig. 4.8). However, charge switch mutations from both membrane associated subdomains altered the anion permeability of the $GABA_AR$ (Fig. 4.9, Fig. 4.10)

Mutation of three M3A residues, α1(K312), α1(K320), and α1(D332), and five M4A residues, α1(D356), α1(K364), α1(E369), α1(K378), and α1(E381), induced a significant shift in the relative reversal potential caused by decreasing extracellular chloride (Fig. 4.9, Fig. 4.10, Table 4.4). Charge switch mutations at each of these positions caused positive shifts in E_{CS}, which approached the theoretical E_{Cl} value. Increased relative reversal potentials translated to a decreased permeability to gluconate that may reflect a decrease in the diameter of the intracellular pore entrance. Alternatively, point mutations may have electrostatically occluded the windows of the intracellular vestibule that are framed by the α1 subunit to impair gluconate permeation. These results are consistent with the hypothesis that intracellular residues of the $GABA_AR$ α1 subunit influence ion permeation. Previous studies have localized the charge selectivity filter of pLGICs to the M1-2 linker (Jensen, Timmermann et al. 2002; Keramidas, Moorhouse et al. 2002; Jensen, Pedersen et al. 2005). Results presented here provide the first evidence for an intracellular selectivity filter within the $GABA_AR$ that is able to discern between anionic species.

4.5: Conclusion

In this chapter, I have shown that charged residues of the $GABA_AR$ α1 subunit intracellular loop domain play a critical role in controlling channel gating and ion permeation. Furthermore, results suggest the existence of novel functional subdomains of the intracellular loop domain. I have shown that specific charged residues within both membrane-associated

subdomains control different facets of channel gating; M3A residues contribute to agonist dependent gating while M4A residues mediate the time course of receptor desensitization. Furthermore, positions within both subdomains were shown to line a novel portion of the pore lumen by influencing channel conductance and altering anion permeation. The $GABA_AR$ is defined by a diverse complement of subunits with unique properties and future studies will be necessary to determine if these intracellular loop domain contributions to channel function are subunit-specific. My findings have established a novel role for the M3-M4 intracellular loop in the α1 subunit of the $GABA_AR$. Importantly, these results, taken together with other recent advances (Davies, Pistis et al. 1999; Kelley, Dunlop et al. 2003; Hales, Dunlop et al. 2006; Deeb, Carland et al. 2007; Livesey, Cooper et al. 2008; Carland, Cooper et al. 2009; Peters, Cooper et al. 2010), suggest a critical role for intracellular loop domain charged residues in pLGIC function.

Chapter 5

The $GABA_AR$ exhibits outward rectification at low channel open probability

5.1: Overview

In this chapter, I have demonstrated that the outward rectification of currents flowing through $GABA_AR$ ion channels was inversely related to the channel open probability (P_O) and occurred independently of Goldman rectification. As a result, the potentiating effects of positive modulators were markedly less when chloride ions were flowing into the cell. These results showed that the direction of driving force on the permeant ion, as well as P_O, must be considered together in order to completely understand drug action on the $GABA_AR$. Finally, I used rectification as a tool to identify charged residues within the α1 intracellular loop domain that define ion sensor sites of the permeation pathway.

5.2: Introduction

Biological pores function as variable resistors with an intrinsic permeability to specific ions. The $GABA_AR$ has been shown to be permeable to the monovalent anion chloride; (Bormann, Hamill et al. 1987; Fatima-Shad and Barry 1993; Jensen, Timmermann et al. 2002; Jensen, Pedersen et al. 2005). When channels are active, the driving force on ions has two determining components: the potential energy across the membrane and the concentration gradient of the permeant ion. The equilibrium potential for any single ion is established by the chemical gradient and may be determined from the Nernst equation [Eq. 3]. The sum driving force on the ion depends on the potential difference between the membrane potential (V_{mem}) and the reversal potential of the ion (E_{Cl}). Therefore, the magnitude of currents (I) passed through a biological pore with a constant conductance ($g = 1/R$) may be calculated with Ohm's law [Eq. 4a]. This assumes a linear relationship between current and voltage. Rearrangement of Ohm's law highlights the separate components of the driving force [Eq. 4b].

[Eq. 3] $$E_{Cl} = \frac{RT}{F} * \ln\left([Cl]_i/[Cl]_0\right)$$

[Eq. 4a] $$V = IR$$

[Eq. 4b] $$I = g(V_{mem} - E_{Cl})$$

However, the permeability of biological pores is not always absolutely selective. Integration of the principles of Goldman (1943), Hodgkin and Katz (1949) allows for calculation of reversal potentials for non-selective membranes, calculation of the relative permeability of different ions through a single type of channel, and the calculation of the absolute permeability of a given ion. The Goldman-Hodgkin-Katz (GHK) voltage equation [Eq. 8] and the GHK current equation [Eq. 10] are based on two assumptions: permeation of individual ions is independent

and the electric field across the membrane is constant (Hille 2001). Goldman validated the constant field assumption by measuring the effect of direct current on the resistance and potential of artificial membranes (1943). In symmetrical conditions, the permeable membranes behaved linearly according to Ohm's law; however, rectification of currents was observed in asymmetric conditions (Goldman 1943). The GHK current equation predicts that the relationship between current and voltage will be non-linear in strong ionic gradients and is referred to as Goldman rectification.

[Eq. 8] $$E_{rev} = \frac{RT}{F} * ln\left(\frac{\frac{P_G}{P_{Cl}}[G]_i + [Cl]_i}{\frac{P_G}{P_{Cl}}[G]_o + [Cl]_o}\right)$$

[Eq. 10] $$I_{Cl} = p_{Cl} z^2 \frac{EF}{\varphi} \frac{[Cl]_i - [Cl]_o e^{-zE/\varphi}}{1 - e^{-zE/\varphi}} \quad where \quad \varphi = RT/F$$

It has become commonplace in recent years to study the pharmacology of the $GABA_AR$ using a symmetrical chloride gradient, to avoid Goldman rectification (1943) and a negative holding potential, to mimic the resting membrane potential of a neuron. This method results in a stable assay system in which the action of different drugs on receptor function can be accurately measured. However, these *in vitro* conditions reverse the direction of the driving force on chloride compared to *in vivo* conditions in the adult brain; GABA activation results in chloride efflux from the cell, not influx. The rationale for accepting such a functional difference stems from the fact that the ion channel has been reported to behave as a simple ohmic pore, conducting anions equally well in both directions across the membrane (Bormann, Hamill et al. 1987; Bormann 1988; Bormann 1988; Weiss, Barnes et al. 1988; Macdonald, Rogers et al. 1989). Channels gated by GABA have been shown to have up to four conducting states in outside-out patches with symmetrical chloride: 44, 30, 19, and 12 pS (Bormann, Hamill et al. 1987); current-voltage (IV) relationships generated from cultured chick cerebellar neurons (Weiss,

Barnes et al. 1988), cultured astrocytes (Bormann 1988) and cultured murine spinal neurons (Bormann, Hamill et al. 1987; Bormann 1988; Macdonald, Rogers et al. 1989) have been shown to vary linearly for all conducting states. In particular, the IV relationship for the main conductance state of the channel determined from single channel currents showed a linear response with a slope conductance of 20-30 pS (Bormann, Hamill et al. 1987; Weiss, Barnes et al. 1988; Macdonald, Rogers et al. 1989).

More recently, it has been reported that the $GABA_AR$ exhibits varying degrees of rectification (Weiss 1988; Pytel, Mercik et al. 2006; Pavlov, Savtchenko et al. 2009) that are not simply due to an asymmetry in the chloride concentration across the membrane as predicted by the constant field equation (Goldman 1943; Hodgkin and Katz 1949; Barker and Harrison 1988). Weiss and Barnes et al., (1988) recorded whole-cell and single channel currents from cultured chick cerebellar neurons; although the amplitude of outward whole-cell currents was greater than inward currents, the IV relationship determined from single channel currents was linear. Further investigation showed that the open probability (P_O) of single channel currents was, in fact, voltage dependent, which could cause the observed asymmetry of whole-cell currents (Weiss 1988). Intriguingly, desensitization has been shown to be caused by a change in channel open probability and not by affecting the amplitude or mean open time of bursts (Weiss 1988; Macdonald, Rogers et al. 1989); in the chick cerebellar neuron recordings, the voltage dependence of openings was ablated by desensitization (Weiss 1988). Furthermore, Pytel et al., (2006) showed that the rectification of currents through somatic patches from rat primary hippocampal neurons was linked to the GABA concentration; currents were outwardly rectifying at low concentrations and progressed through an ohmic stage to finally become inwardly rectifying at maximally effective concentrations of agonist. The authors also observed an increase in the speed of desensitization and faster paired-pulse recovery at positive potentials

(Pytel, Mercik et al. 2006), providing further evidence for the voltage dependence of channel gating. On the other hand, Baker and Harrison observed outward rectification of IPSCs recorded from cultured hippocampal neurons; however, the asymmetry of current flow was shown to be due to Goldman rectification because of asymmetric experimental conditions (1988).

To date, the characterization of current rectification through the $GABA_AR$ has been determined with primary tissue from a wide array of brain regions and organisms. Primary cultured cells are known to express many different combinations of $GABA_ARs$ according to the developmental stage as well as the brain region from which they are derived (McKernan and Whiting 1996; Olsen and Sieghart 2008). Therefore, the variability of findings regarding rectification of GABAergic currents may be due to heterogeneous receptor populations in primary tissues. To begin to clarify this inconsistency, I have used the HEK293 heterologous expression system to experimentally control the composition of the $GABA_AR$ and to investigate the rectification of currents through the $\alpha1\beta2\gamma2$ receptor. Due to the GABA concentration dependence of rectification and the observed changes in desensitization with membrane potential, I hypothesized that the direction of ion flux through the pore influences channel gating. To test this hypothesis, I characterized the IV relationship for the $\alpha1\beta2\gamma2$ receptor across the entire GABA concentration response and compared the rate of desensitization in outward and inward currents. The chloride gradient was manipulated in order to shift E_{Cl} and induce Goldman rectification. I hypothesized that the direction-dependent components of channel gating that mediated rectification are independent of Goldman rectification. Furthermore, in Chapter 4 I showed that charge switch mutations altered channel gating. If interactions between ions sensor structures of the pore and permeant ions are integral to channel gating, then decreasing the availability of charge carriers will impair gating.

Rectification of the IV relationship has been proposed for extrasynaptic receptors in steady-state, tonic conditions, but has never before been clearly linked as an intrinsic property of synaptic $GABA_A$Rs. Pavlov et al., (2009) showed that tonically active currents mediated by extrasynaptic receptors were outwardly rectifying from evoked IPSCs in hippocampal slice recordings. Furthermore, in a recombinant system, traditionally extrasynaptic (αβ) receptors exhibited outward rectification of currents elicited by maximally effective concentrations of GABA, whereas traditionally synaptic (αβγ) receptors displayed an ohmic response (Boileau, Li et al. 2003). Interestingly, the outward rectification of α4-containing receptors has been shown to be attenuated by the neurosteroid allopregnanolone (Shen, Gong et al. 2007), which is known to enhance the P_O of the ion channel (Akk, Covey et al. 2010). Extrasynaptic receptors, such as those containing the α4 subunit, are known to have less frequent openings with a shorter duration than synaptically targeted receptors (Farrant and Nusser 2005; Keramidas and Harrison 2008; Mortensen, Ebert et al. 2010). Due to the intrinsic difference in open probability between extrasynaptic and synaptic receptor types, I hypothesized that outward rectification of GABAergic currents is a general property of the $GABA_A$R linked to P_O. To test this hypothesis, I first compared the IV relationships for α1β2 and α1β2γ2 receptors. Then, I manipulated the P_O of the $GABA_A$R, pharmacologically and with mutagenesis, and determined IV relationships to measure the degree of rectification.

Rectification may be caused by changes in ion selectivity (Moorhouse, Keramidas et al. 2002) and electrostatic barriers to ion permeation such as ion binding sites (Bormann, Hamill et al. 1987; Imoto, Busch et al. 1988; Moorhouse, Keramidas et al. 2002). Due to these characteristics, rectification has been used as a tool to identify pore-lining residues (Imoto, Busch et al. 1988; Moorhouse, Keramidas et al. 2002) and to determine subunit stoichiometry of LGICs (Backus, Arigoni et al. 1993). Therefore, I used rectification as a tool to identify α1 intracellular

loop domain residues, which contribute to the ion permeation pathway. If the native residue defines an ion binding site, then charge switch mutation would perturb the electrostatic interaction with the permeant ion to alter the degree of rectification.

5.3: Results

5.3.1: Channel gating is voltage dependent

To test the first hypothesis, that $GABA_AR$ gating is voltage dependent, I used whole-cell voltage clamp electrophysiology to record inward and outward currents from α1β2γ2 receptors and compared the concentration-response relationship as well as the rate of desensitization. Then, I used a ramp protocol, described in section 2.3.6, to determine IV relationships across the entire GABA concentration-response for the α1β2γ2 receptor.

5.3.1A: Membrane potential determined current magnitude and the rate of desensitization

I observed striking differences in GABAergic currents when the direction of the driving force was reversed by changing the membrane holding potential (Fig. 5.1). Qualitatively, outward currents showed increased current magnitude at low GABA concentrations, 0.3-10 μM, and enhanced desensitization at high concentrations of GABA, 100-1000 μM, compared to inward currents (Fig. 5.1A). Interestingly, the maximal current magnitude was not significantly different at +60 mV (+1520 ± 120 pA) and at -60 mV (-1400 ± 140 pA) holding potentials (paired t-test, $p > 0.05$; $n = 3$; mean ± SEM). As a result, the concentration-response relationship of outward currents at +60 mV had slightly decreased EC_{50} (15.4 ± 3.90 μM) and nH values (1.10 ± 0.13) compared to inward currents at -60 mV (EC_{50} = 19.0 ± 4.80 μM; nH = 1.70 ± 0.06; n=3; mean ± SEM; Fig. 5.1B). Recordings from excised outside-out macroscopic patches showed a significant increase in the speed of desensitization at +60 mV (-1.1 ± 0.02 s^{-1}) compared to -60 mV (-0.56 ± 0.01 s^{-1}; $n = 10$; Students t-test, $p < 0.05$; mean ± SEM; Fig. 5.1C).

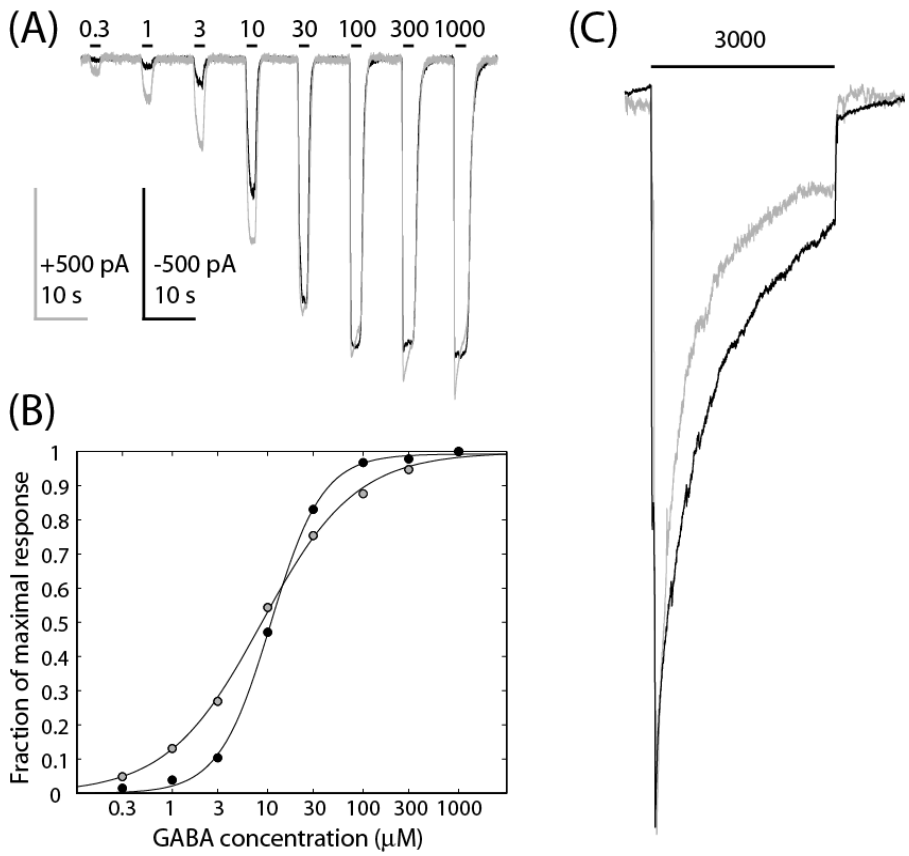

Figure 5.1: Desensitization was faster in outward currents. Inverting the membrane potential from -60 to +60 mV altered the GABA concentration response function, increased response magnitude and accelerated desensitization. (A) Representative traces from the same cell gathered at a holding potential of +60 mV (gray) and -60 mV (black). Bars indicate the duration of GABA application and are labeled with the concentration (µM). Outward currents elicited at +60 mV are shown inversed to highlight differences in kinetics and current magnitude. (B) Hill equation fit of normalized peak currents indicated a reduction in hill slope at +60 mV (gray) compared to -60 mV (black), indicative of increased desensitization. (C) Averaged currents elicited by a 10 s application of 3,000 µM GABA to macroscopic outside out patches held at +60 mV (gray) and -60 mV (black); n = 10. Currents are shown normalized by the peak value to highlight the increased speed of desensitization at the positive membrane potential.

5.3.1B: IV relationship was dependent on effective concentration of GABA

IV relationships for α1β2γ2 receptors revealed an obvious qualitative change in rectification with regards to the degree of channel activation by GABA (Fig. 5.2B). Rectification index (RI) values were determined at each GABA concentration. RI is defined as a ratio of current magnitudes at membrane potentials, centered about the reversal potential that was used to quantitatively compare the degree of current rectification under different conditions (Fig. 5.3). Goldman showed that rectification increased with changes in membrane potential (1943); likewise, the RI value for currents elicited by 30 μM GABA increased with the potential distance from the reversal potential (Fig. 5.3). Here, RI is fixed at Δ30 mV from the reversal potential [Eq. 10]. IV relationships from current responses to 0.3-30 μM GABA showed outward rectification and were associated with RI < 1, whereas RI ≈ 1 was observed for the more ohmic responses to 100-1000 μM GABA (Table 5.1). These two discrete populations, from currents elicited by low and high concentrations of GABA, had RI values that were significantly different from one another (Tukey's post hoc, $p < 0.05$; Table 5.1).

In light of the correlation between channel activation and rectification, I constructed a rectification profile for WT receptors to quantitatively assess the degree of rectification (Fig. 5.2C). When the RI for these responses was plotted against the degree of receptor activation (Table 5.1), I observed a linear correlation ($R^2 = 0.99$) with a slope of 0.38 ± 0.03 and an intercept of 0.67 ± 0.03 (n = 34).

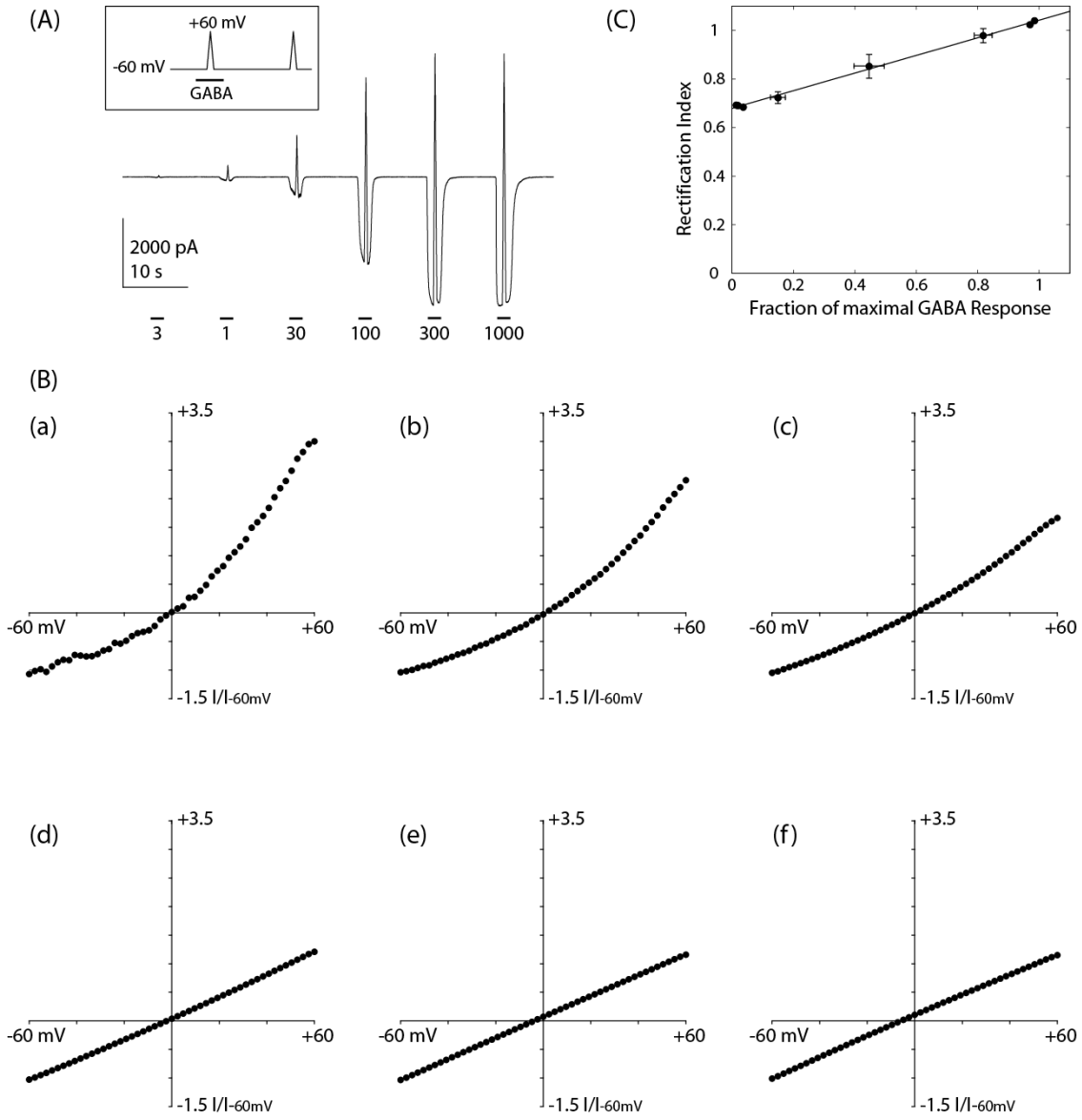

Figure 5.2: Rectification profile for α1β2γ2 $GABA_AR$. (A) Representative whole-cell current trace for α1β2γ2 receptors after baseline ramp was subtracted. Bars indicate the duration of GABA application and are labeled with the concentration (μM). [INSET] shows the timing of the voltage ramp in relation to the 2 s application of GABA. (B) IV relationships for currents elicited by (a) 3 μM, (b) 10 μM, (c) 30 μM, (d) 100 μM, (e) 300 μM, and (f) 1000 μM GABA. (C) Rectification profile for the α1β2γ2 $GABA_AR$. Peak currents normalized to the maximal response to GABA were plotted against RI values and the data points were best fit with a straight line: $y = m*x+b$, $R^2 = 0.99$. The slope (RI.m) and intercept (RI.b) of the fit were then used to compare each experimental condition. Data points depict mean ± SEM; n = 34.

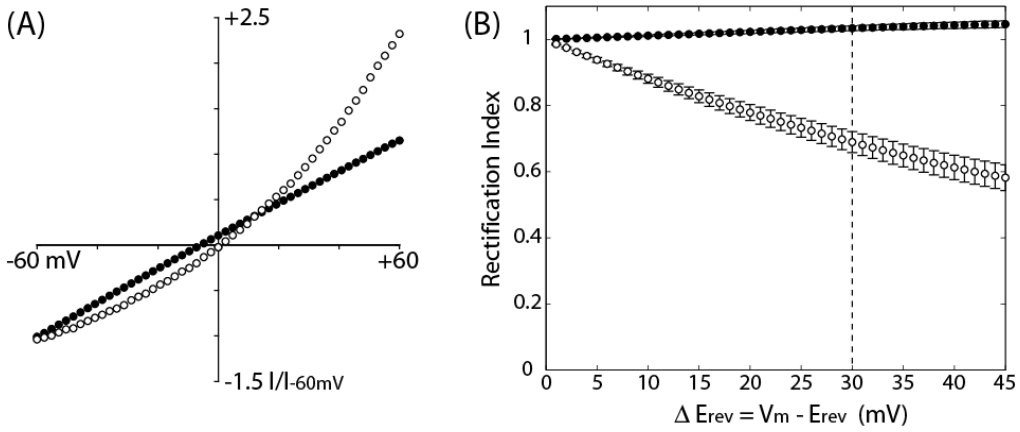

Figure 5.3: Rectification index values. In order to quantitatively compare the degree of rectification of each IV relationship we determined RI values as a ratio of the current magnitude Δ30 mV from the reversal potential [Eq. 10]. (A) IV relationships determined from currents elicited by 10 μM (white) and 1 mM (black) GABA. Currents are shown normalized by the magnitude of the inward current at -60 mV. (B) RI values for 10 μM (white) and 1 mM (black) GABA determined at increasing potential differences from the reversal potential. Data points depict mean ± SEM. The ohmic response at 1 mM GABA shows a nearly constant RI, whereas, the rectification of the response at 10 μM GABA caused a dynamic change in RI. Values determined at Δ30 mV were significantly different at 10 μM and 1 mM GABA (n = 34; Students t-test, $p < 0.05$).

[GABA] (μM)	3	10	30	100	300	1000
RI	0.68 ± 0.06‡	0.72 ± 0.04‡	0.85 ± 0.04	0.98 ± 0.02†	1.02 ± 0.01†	1.04 ± 0.01†
I/I_{max}	0.04 ± 0.01	0.15 ± 0.02	0.45 ± 0.05	0.82 ± 0.03	0.97 ± 0.01	0.99 ± 0.01

Table 5.1: Degree of rectification was positively correlated with degree of channel activation. Rectification index values (RI) were plotted against the degree of activation (I/I_{max}) to generate a rectification profile. The Tukey's *post hoc* test was used to compare all RI values to one another with significance held at $p < 0.05$ for differences from (†) 3 and (‡) 1000μM GABA. Means ± SEM, n = 34.

5.3.1C: Asymmetry of currents was independent of Goldman rectification

To test if current rectification through $GABA_A$Rs was dependent on the chemical force on permeant ions, I compared IV relationships in symmetrical chloride (I1:E1) and in solutions with decreased intracellular (I2) and extracellular (E2) chloride; for composition of solutions see Table 2.2. In decreased extracellular chloride conditions (I1:E2) the inward driving force on the permeant ion was decreased and the experimental reversal potential was shifted in the positive direction as would be predicted for an anion pore (Fig. 5.4A, Table 5.2). The reversal potential in I1:E2 was shifted ~20 mV from the theoretical E_{Cl} value, suggesting a relative permeability of gluconate of 0.13 ± 0.02, which agreed with previously reported values (Jensen, Pedersen et al. 2005). As predicted by the constant field equation, results showed that decreasing the intracellular concentration of chloride (I2:E1) specifically enhanced outward rectification (Fig. 5.4B). This resulted in a significantly decreased intercept of the rectification profile when compared to the symmetrical chloride condition (Students t-test, $p < 0.05$; $n = 8$; Table 5.2). On the contrary, the Goldman rectification that was predicted to occur in the I1:E2 condition was masked by the inherent outward rectification of the receptor and did not significantly shift the intercept (Fig. 5.4A, Table 5.2). Interestingly, the correlation between rectification and the degree of channel activation persisted in altered ionic gradients as shown by the slope values for each rectification profile, which were not statistically different from one another (Students t-test, $p > 0.05$; Fig. 5.4C, Table 5.2).

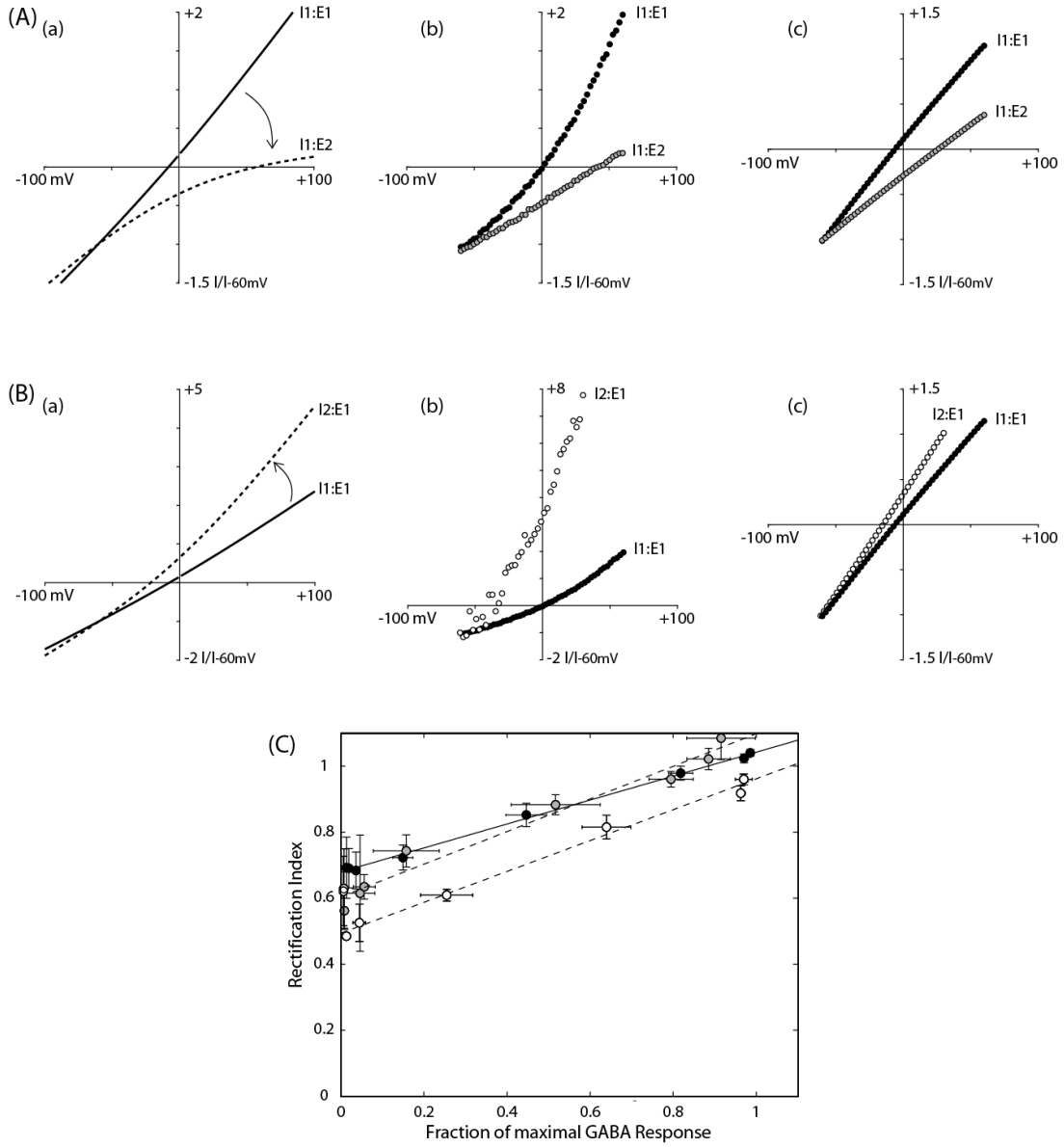

Figure 5.4: Goldman rectification. IV relationships were compared (A) in symmetrical chloride (I1:E1, black) and in low extracellular chloride (I1:E2, gray) OR (B) in symmetrical chloride (I1:E1, black) and in low intracellular chloride (I2:E1, white). (a) Theoretical IV relationships in ion replacement solutions as predicted by the constant field equation. For example, (A) shows that lowering the extracellular concentration of chloride causes a right shift in E_{Cl} and induces inward rectification; conversely, (B) shows that decreasing the intracellular concentration of chloride causes a left shift in E_{Cl} and enhances outward rectification. Experimentally determined IV relationships for WT $GABA_A$Rs generated from currents elicited by (b) 10 µM and (c) 1 mM GABA. Currents are shown normalized by the magnitude of the inward current at -60 mV. (C) Rectification profiles in symmetrical chloride (black, solid; n = 34), low extracellular chloride (gray, dashed; n = 6), and low intracellular chloride (white, dashed; n = 8).

Solutions	E_{Cl} (mV)	E_{rev} (mV)	P_{gluc}/P_{Cl}	RI.m	RI.b	N
I1:E1	-7.75	-9.32 ± 0.55	-	0.37 ± 0.03	0.67 ± 0.0	34
I1:E2	+57.0	40.5 ± 4.53	0.13 ± 0.02	0.43 ± 0.02	0.64 ± 0.04	6
I2:E1	-21.6	-22.3 ± 2.31	-	0.39 ± 0.04	0.56 ± 0.05*	8

Table 5.2: IV relationship metrics in altered ionic gradients. IV relationships were determined in symmetrical chloride (I1:E1) and in low extracellular chloride (I1:E2), in low intracellular chloride (I2:E1), and in low overall chloride (I2:E2) saline conditions. Values for calculated junction potentials and the raw and corrected reversal potential (E_{rev}) are given for each saline condition. Linear fit parameters of the rectification profile, the slope (RI.m) and intercept (RI.b), were significantly different from the I1:E1 condition; $p < 0.05$ for Students t-test (*); means depicted ± SEM.

5.3.1D: Chloride dependence of gating

Charged residues that face into the pore lumen serve as ion sensors and make important electrostatic interactions with ions to determine the rate and species of permeation. The results of the charge switch mutagenic screen, presented in Chapter 4, suggested that intracellular loop domain control of gating and desensitization are mediated through electrostatic interactions, which supports the hypothesis that ion-protein interactions within the pore are integral gating elements. To further test this hypothesis I determined GABA concentration-response relationships for WT receptors in symmetrical chloride and in chloride gradient conditions (Fig. 5.5). Whole-cell patches containing WT receptors had EC_{50} values that were 1.65-fold higher in I1:E2 compared to I1:E1 solutions (Fig. 5.5B); I also observed increases in I_{max} and the rate of desensitization in the low extracellular chloride condition (Fig. 5.5).

The theoretical reversal potential was positively shifted in decreased extracellular chloride conditions (E_{Cl} = +65.7 mV) compared to the symmetrical condition. Therefore, at a -60 mV holding potential, the driving force on the permeant ion was greater in I1:E2 and thus increased current magnitudes. In order to determine the effect of driving force on chloride-dependent desensitization, excised outside-out patches were held at membrane potentials that would deliver equivalent potential force in I1:E1 (-60 mV) and in I1:E2 (-20 mV) conditions (Fig. 5.5C). The rate of desensitization remained increased in low chloride conditions with equivalent electrochemical drive indicating that the difference was in fact chloride-dependent and not voltage-dependent (Fig. 5.5C).

To determine the chloride-dependence of EC_{50}, IV relationships were determined in I1:E1, I2:E1 and I1:E2 conditions and I constructed concentration-response relationships at membrane potentials (V_m) that would yield an equivalent driving force (Fig. 5.6). At $V_m = E_{rev}$ -50 mV, EC_{50} values were increased in I2:E1 (76.8 ± 12.2 μM) and I1:E2 (70.0 ± 22.9 μM) conditions compared to I1:E1 (45.1 ± 13.3 μM; n=17; mean ± SEM; Fig. 5.6).

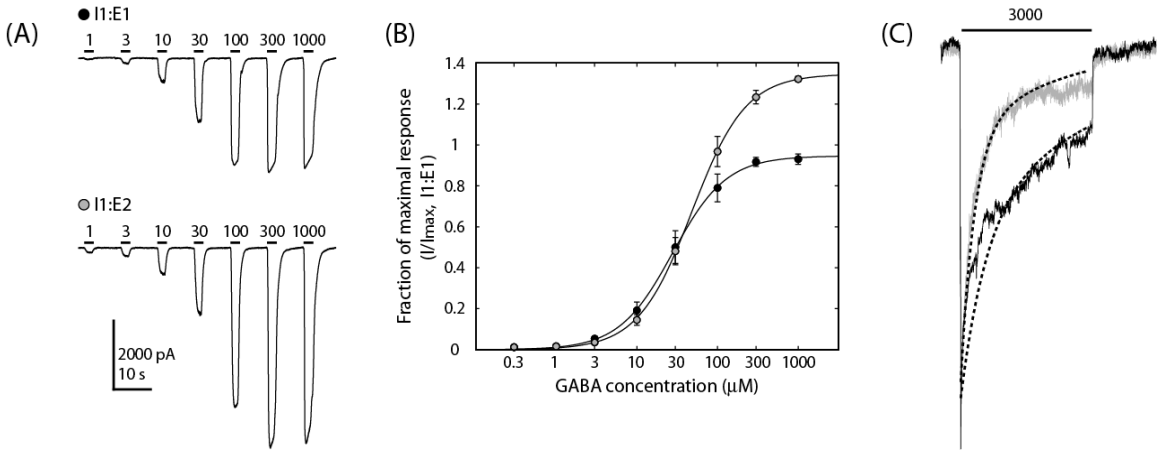

Figure 5.5: Chloride dependence of concentration-response relationship and desensitization. (A) Representative traces for WT receptors in symmetrical chloride (I1:E1) and in low extracellular chloride (I1:E2) saline conditions. Bars indicate the duration of GABA application and are labeled with the concentration (μM). (B) Hill fit of peak currents normalized to the maximal response to GABA for each whole-cell patch in the I1:E1 solutions. Data points depict mean ± SEM; n = 17. The magnitude of currents was increased in I1:E2 solutions and the apparent affinity for GABA were decreased. (C) Normalized, representative currents elicited in excised outside-out macroscopic patches by 10 s application of 3 mM GABA in I1:E1 (black; V_m = -60 mV; n = 16) and I1:E2 (gray; V_m = -20 mV; n = 10) solutions. Dotted line depicts the exponential fit of the average.

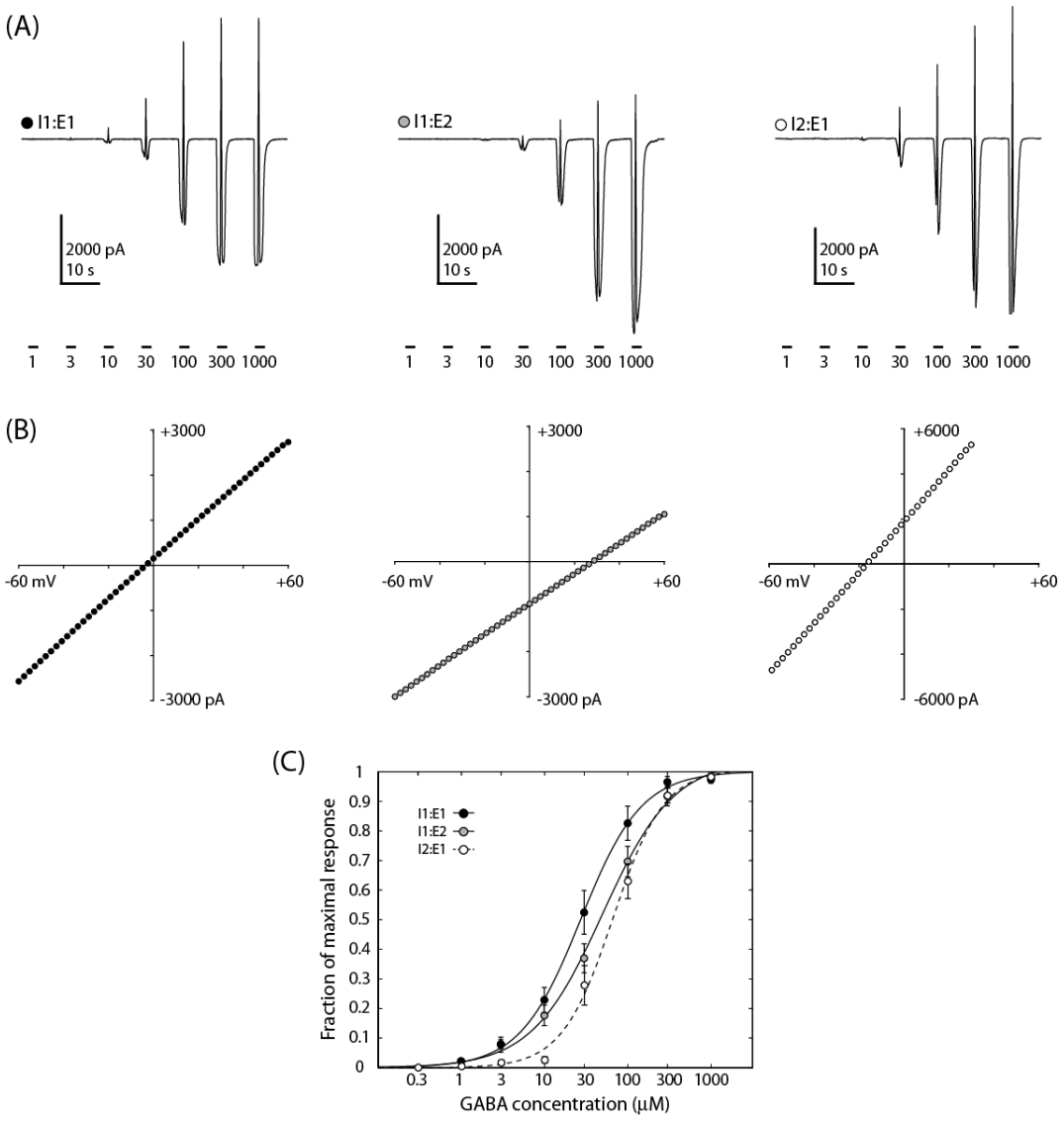

Figure 5.6: Chloride dependence of apparent affinity is independent of driving force. (A) Representative traces for WT receptors in symmetrical chloride (I1:E1; V_{mv}= -60 mV), in low extracellular chloride (I1:E2; V_m = -60 mV), and in low intracellular chloride (I2:E1; V_m = -90 mV) saline conditions. Traces were collected with the ramp protocol ±60 mV starting at the indicated V_m value. Bars show the duration of GABA application and are labeled with the concentration (μM). (B) IV relationships determined in I1:E1 (black), I1:E2 (gray), and I2:E1 (white) solutions. Mean data points are shown; n = 17. (C) Hill fit of normalized currents in I1:E1 (black), I1:E2 (gray), and I2:E1 (white) solutions under equivalent potential driving force ($V_m = E_{rev}$ - 50 mV). Data points denote mean ± SEM; n = 17.

5.3.2: Outward rectification of currents occurs at low P_O

Due to the strong correlation between RI and current magnitude and the enhanced outward rectification in the extrasynaptic receptor, I hypothesized that outward rectification would be more pronounced at low P_O. To test this hypothesis, I measured the IV relationship of three systems known to exhibit reduced P_O and also determined IV relationships in the presence of modulators that potentiate receptor activity to increase P_O. First, I compared the rectification of receptors containing only the α1 and β2 subunits to receptors also containing the γ2 subunit that is known to target receptors to the synapse and infers unique receptor activity (Boileau, Li et al. 2003). Second, I constructed a rectification profile from currents elicited by the partial agonist piperidine-4-sulfonic acid (P4S), which has decreased efficacy compared to the full agonist GABA (Mortensen, Kristiansen et al. 2004). Third, I characterized the IV relationship for receptors containing the α1(L277A) mutation that has been shown to have impaired gating resulting in reduced P_O (Colquhoun 1998; O'Shea and Harrison 2000; Hille 2001). Finally, I examined whether increasing P_O would decrease rectification. To test this hypothesis I co-applied GABA with the positive allosteric modulators, isoflurane, etomidate, and propofol, in order to fully characterize the relationship between rectification and channel open probability.

5.3.2A: Extrasynaptic receptors are outwardly rectifying

Strong rectification of the IV relationship has been proposed for extrasynaptic receptors in steady-state, tonic conditions, but has never before been clearly linked as an intrinsic property of synaptic $GABA_A$Rs. The most common synaptic arrangement of the $GABA_AR$ contains the α1, β2, and γ2 subunits; in contrast, receptors containing only the α1 and β2 subunits show extrasynaptic expression (McKernan and Whiting 1996; Martin and Olsen 2000). Therefore I chose to compare the rectification profiles of α1β2γ2 and α1β2 receptors (Fig. 5.7). The α1β2 complex exhibited significant two-fold decreases in both the GABA EC_{50} and I_{max} compared to α1β2γ2 receptors (Students t-test, $p < 0.05$), but there was no change in nH (Fig. 5.7D, Table 5.3).

Interestingly, the degree of rectification (RI) was not significantly different between the synaptic and extrasynaptic receptors at submaximal concentrations of GABA (≤ 100 μM; Students t-test, $p < 0.05$; Fig. 5.7B). Specifically, the α1β2γ2 and α1β2 complexes had RI values of 0.65 ± 0.06 (n = 5) and 0.64 ± 0.04 (n = 13) respectively, from currents elicited by 10 μM GABA. As previously shown (Boileau, Li et al. 2003), incorporation of the γ2 subunit significantly decreased the degree of rectification, with a characteristically ohmic IV relationship at maximally effective concentrations of GABA. At 1 mM GABA, the α1β2γ2 and α1β2 complexes had RI values of 1.03 ± 0.02 (n = 6) and 0.85 ± 0.03 (n = 14) respectively (Fig. 5.7C). Consequently, the rectification profiles for synaptic and extrasynaptic receptors were quantitatively and qualitatively different; the linear fit for α1β2 had a significantly decreased slope value of 0.25 ± 0.03 with no change in the intercept value of 0.60 ± 0.03 (Students t-test; Fig. 5.7E). For the first time, these results highlight the differences between synaptic and extrasynaptic receptor IV relationships in a recombinant system across the GABA concentration-response.

Construct	Agonist	E_{rev} (mV)	RI.m	RI.b	N
α1β2γ2	GABA	-9.32 ± 0.55	0.37 ± 0.03	0.67 ± 0.0	34
α1β2	GABA	-5.80 ± 1.44	0.25 ± 0.03*	0.60 ± 0.03	14
α1β2γ2	P4S	-4.92 ± 1.66	0.64 ± 0.29*	0.60 ± 0.09	7
α1(L277A) β2γ2	GABA	-3.77 ± 1.48	0.01 ± 0.10*	0.71 ± 0.07	8

Table 5.3: IV relationship metrics for low P_O conditions. Corrected reversal potential (E_{rev}) values and linear fit parameters of the rectification profile, the slope (RI.m) and intercept (RI.b). Significant differences from WT α1β2γ2 were held at $p < 0.05$ for Students t-test (*); means depicted ± SEM.

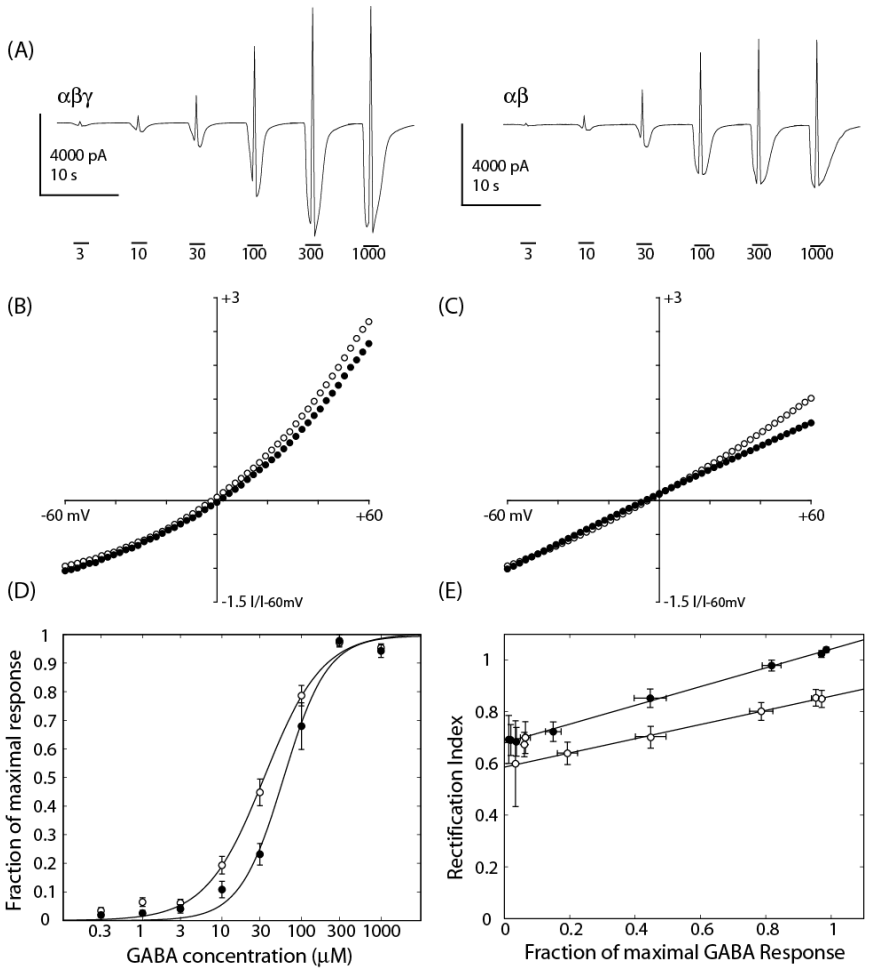

Figure 5.7: Incorporation of the γ subunit decreased outward rectification at maximally effective GABA concentrations. (A) Representative currents from WT α1β2γ2 and α1β2 receptors. Bars indicate the duration of GABA application and are labeled with concentration (μM). IV relationships determined from currents elicited by (B) 10 μM and (C) 1 mM GABA for α1β2 receptors (white) and α1β2γ2 (black). (D) Hill equation fit of normalized peak currents for α1β2γ2 (n = 5) and α1β2 (n = 14) highlights the differing GABA affinities for each receptor complex. (E) Rectification profile for α1β2γ2 (n = 6) and α1β2 (n = 14). The α1β2 receptors exhibit significantly enhanced outward rectification represented by a decreased slope of the rectification profile (Students t-test, $p < 0.05$). Data points depict mean ± SEM.

5.3.2B: Decreasing open probability enhanced rectification

Next, P_O of the α1β2γ2 WT receptor was decreased pharmacologically and with mutagenesis. The partial agonist P4S decreased I_{max} by ~70% compared to the full agonist GABA (Fig. 5.8, Table 5.3). P4S was active within the same concentration range with an apparent affinity of 41.8 ± 6.85 μM (Fig. 5.8C). At 1 mM P4S, there was significantly greater outward rectification (RI = 0.71 ± 0.05) than at the same concentration of GABA (RI = 1.02 ± 0.01, n = 7, Students t-test, $p < 0.05$; Fig. 5.8B). Furthermore, the slope of the rectification profile for P4S (0.85 ± 0.24) was significantly greater than for GABA (Students t-test, $p < 0.05$; Fig. 5.8D; Table 5.3).

The α1(L277A) mutation, within the M2-3 linker, is known to impair channel gating (O'Shea and Harrison 2000; see Section 1.3.3). Receptors harboring the α1(L277A) mutation exhibited a significant ~6.5 fold decrease in the GABA apparent affinity (EC_{50} = 281 ± 43.6 μM; n = 8, Students t-test, $p < 0.05$, Fig. 5.9C, Table 5.3); there were no changes in nH (1.34 ± 0.14) or I_{max} (-1908 ± 620.9 pA) for the α1(L277A) mutation compared to WT. The α1(L277A) mutation enhanced outward rectification across the receptor's entire response to GABA. Current responses activated by 10 mM GABA in cells expressing α1(L277A) containing receptors had a RI value of 0.58 ± 0.06 (Fig. 5.9B). When the RI of responses was plotted against the degree of activation, we found that the α1(L277A) mutation significantly altered the rectification profile with a slope of 0.01 ± 0.10 (Students t-test, $p < 0.05$; Table 5.3); the intercept was not statistically different from WT (Students t-test, $p > 0.05$; Fig. 5.9D, Table 5.3).

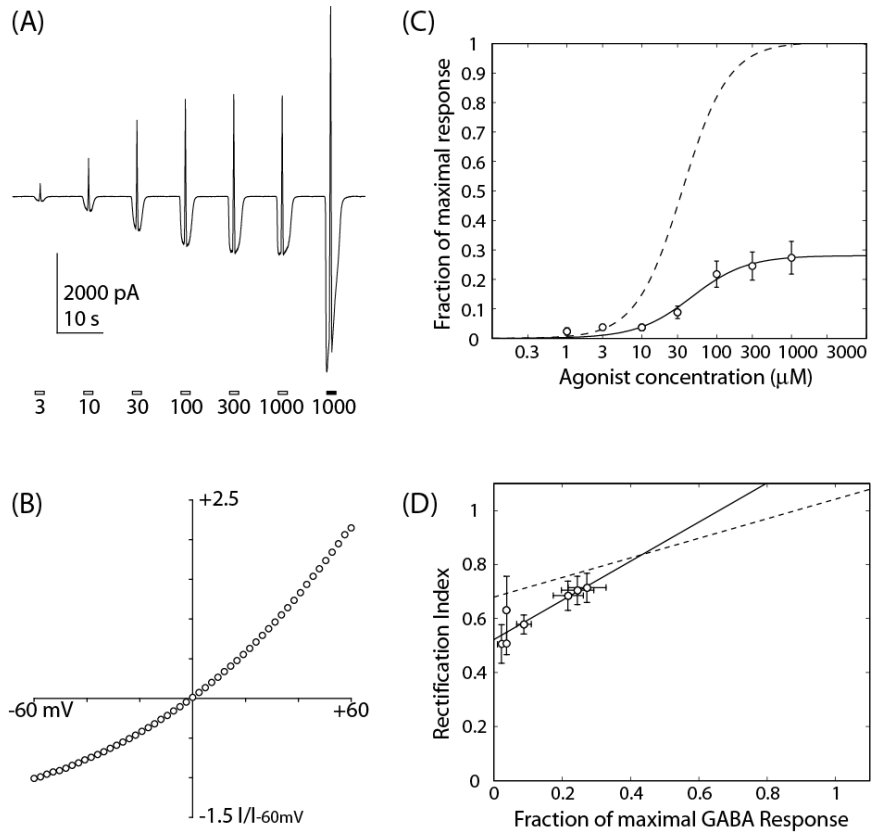

Figure 5.8: Outward rectification was enhanced at low P_O. (A) Representative currents elicited by the partial agonist P4S (white) and the maximal concentration of GABA (black). Bars depict application of agonist and are labeled with concentration (μM). IV relationship determined from maximally effective concentration of 1 mM P4S. (E) Hill equation fit of normalized peak currents shows the decreased efficacy of P4S (n = 7). The dotted line represents the Hill fit for currents elicited by the full agonist GABA. (D) The enhanced outward rectification observed with P4S yielded specific changes in the rectification profile of $GABA_A$Rs. The partial agonist significantly increased the slope and decreased the intercept of the profile (n = 7; Students t-test, $p < 0.05$). The dotted line represents the rectification profile for WT GABAergic IV relationships.

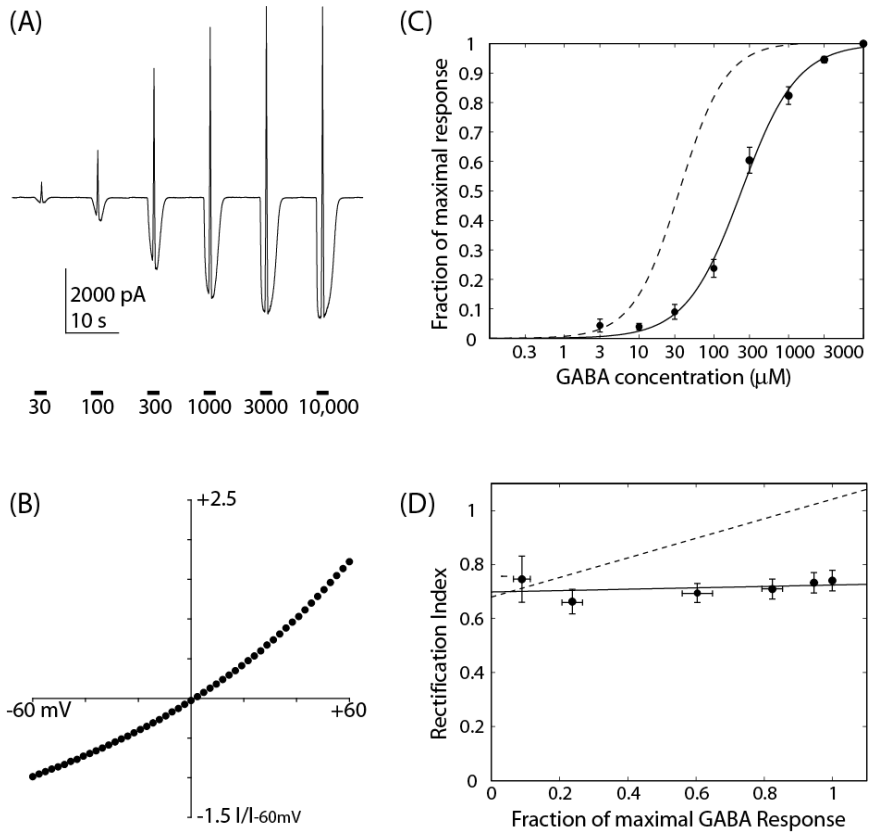

Figure 5.9: Impaired gating enhanced outward rectification. (A) Representative whole-cell current trace for α1(L277A) mutation. Bars indicate the duration of GABA application and are labeled with the concentration (μM). (B) IV relationship determined from a maximally effective concentration of 10 mM GABA. Currents are shown normalized by the magnitude of inward current at -60 mV. (C) Hill equation fit of normalized peak currents shows the significant shift in GABA apparent affinity caused by the gating mutation (n = 8). The dotted line represents the Hill fit for WT GABAergic currents. (D) The α1(L277A) mutation showed rectification independent of the degree of channel activation as represented by a profile slope near zero (n = 8). The dotted line represents the rectification profile for WT GABAergic IV relationships.

5.3.2C: $GABA_AR$ modulation by general anesthetics was voltage dependent

I determined the IV relationship of GABA responses in the presence of intravenous and inhaled general anesthetics (Fig. 5.10A). The positive allosteric modulators etomidate, propofol, and isoflurane enhanced current magnitude by 162 ± 15%, 148 ± 31%, and 137 ± 28% respectively, at a holding potential of -60 mV, and 66 ± 8%, 81 ± 11%, and 70 ± 14% respectively, at a holding potential of +60 mV. I found that all three drugs reduced the amount of outward rectification (Fig. 5.10). In addition, I observed that the effect on rectification increased with potentiation and was voltage dependent (Fig. 5.11). The rectification profile for these positive allosteric modulators had a slope of 0.37 ± 0.03 and an intercept of 0.62 ± 0.01 that was not statistically different from that of GABA (n = 8; Students t-test, $p > 0.05$; Fig. 5.10B).

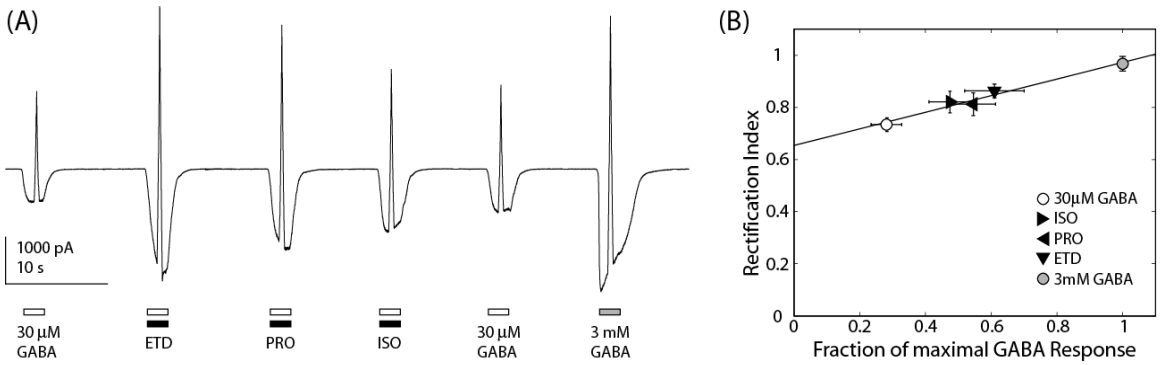

Figure 5.10: Rectification profile for positive allosteric modulators. (A) Representative trace elicited by 30 µM GABA plus co-application of 1 µM etomidate (ETD), 2 µM propofol (PRO) and 330 µM isoflurane (ISO). Peak currents were normalized to the maximal response of each cell to 3m M GABA. (B) Rectification profile for the positive modulators ISO (▶), ETD (◀), and PRO (▼), as well as GABA at 30 µM (○) and 3 mM (●). Data points depict mean ± SEM; n = 8.

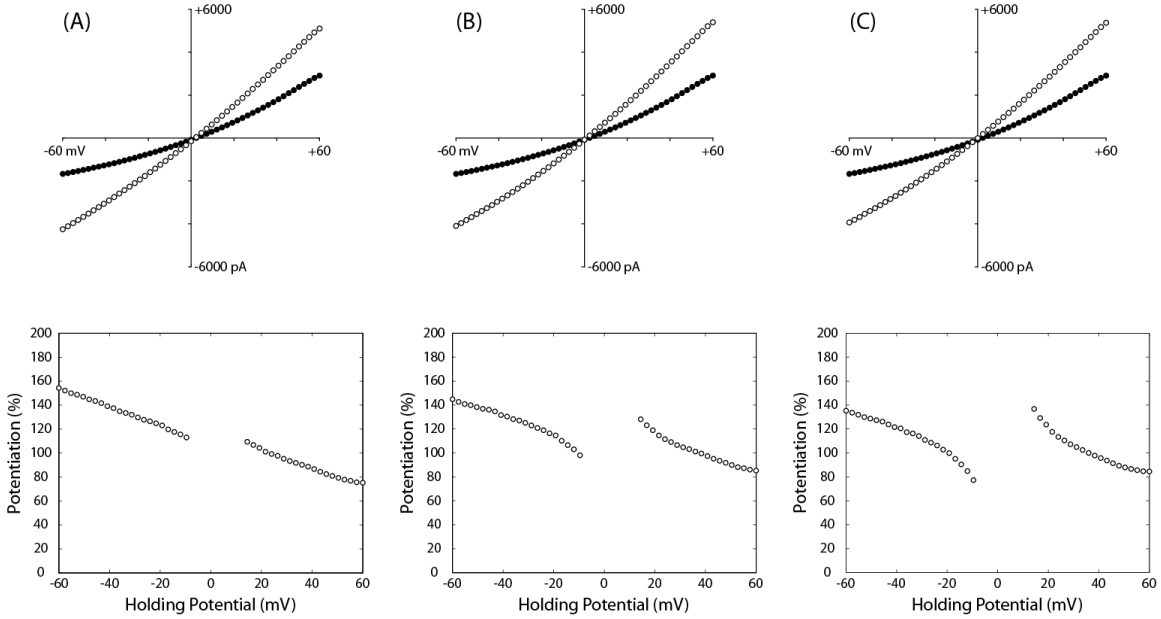

Figure 5.11: Degree of potentiation was voltage dependent. [Top panel] IV relationships for 30 µM GABA (black) and 30 µM GABA potentiated by (A) 1 µM etomidate, (B) 2 µM propofol, and (C) 330 µM isoflurane (white). [Bottom panel] The degree of potentiation for each modulator became asymptotic at the reversal potential and decreased as the membrane potential became more positive. To eliminate error, values determined from $I < \pm I_{RMS}$ were not included in the plot.

5.3.3: Rectification can be used as a tool to identify ion sensor sites

Rectification has been used as a tool to identify pore-lining residues in several pLGICs (Imoto, Busch et al. 1988; Backus, Arigoni et al. 1993). Therefore, I hypothesized that mutation of charged residues which faced into the pore would alter the electrostatic landscape of the permeation pathway to alter chloride permeability and hence, rectification. I constructed rectification profiles for each of the 25 charge switch point mutations that were characterized in Chapter 4 and compared the slope and intercept for each linear fit to WT α1β2γ2 receptor values (Table 5.4). Three mutations, α1(D318K), α1(D356K), and α1(K374E), significantly decreased the intercept (Students t-test, $p < 0.05$; Fig. 12-14; Table 5.4). The α1(D318K) mutation also significantly decreased the slope of the rectification profile (Students t-test, $p < 0.05$; Fig. 5.12; Table 5.4).

Construct	RI.m	RI.b	N	Construct	RI.m	RI.b	N
WT	0.38 ± 0.03	0.65 ± 0.03	31	R354E	0.29 ± 0.03	0.71 ± 0.04	9
K312E	0.35 ± 0.05	0.67 ± 0.05	10	D356K	0.60 ± 0.05*‡	0.44 ± 0.02*‡	9
R313E	0.44 ± 0.04	0.60 ± 0.05	10	K364E	0.37 ± 0.05	0.66 ± 0.04	9
D318K	0.52 ± 0.02	0.50 ± 0.02*	9	E369K	0.31 ± 0.04	0.69 ± 0.05	9
K320E	0.27 ± 0.06	0.71 ± 0.05	9	K371E	0.43 ± 0.06	0.55 ± 0.04	10
E325K	0.52 ± 0.03	0.52 ± 0.04	8	E372K	0.48 ± 0.02	0.57 ± 0.02	10
K326E	0.46 ± 0.03	0.63 ± 0.03	10	K374E	0.51 ± 0.02	0.53 ± 0.02*	11
K328E	0.38 ± 0.05	0.65 ± 0.03	10	E376K	0.49 ± 0.02	0.54 ± 0.02	5
K329E	0.48 ± 0.03	0.58 ± 0.02	8	K378E	0.42 ± 0.04	0.61 ± 0.03	10
K331E	0.38 ± 0.03	0.70 ± 0.03	14	E381K	0.33 ± 0.06	0.69 ± 0.06	19
D332K	0.48 ± 0.03	0.55 ± 0.02	7	K383E	0.50 ± 0.03	0.55 ± 0.02	8
K336E	0.35 ± 0.06	0.71 ± 0.06	10	K384E	0.46 ± 0.04	0.60 ± 0.01	9
K337E	0.46 ± 0.03	0.62 ± 0.02	10	K391E	0.36 ± 0.05	0.65 ± 0.05	8

Table 5.4: Rectification profile parameters for charge switch mutations. Linear fit parameters of the rectification profile, the slope (RI.m) and intercept (RI.b). Point mutations were significantly different from WT; $p < 0.05$ for Students t-test (*); $p < 0.05$ for Dunnett's *post hoc* (‡); means depicted ± SEM.

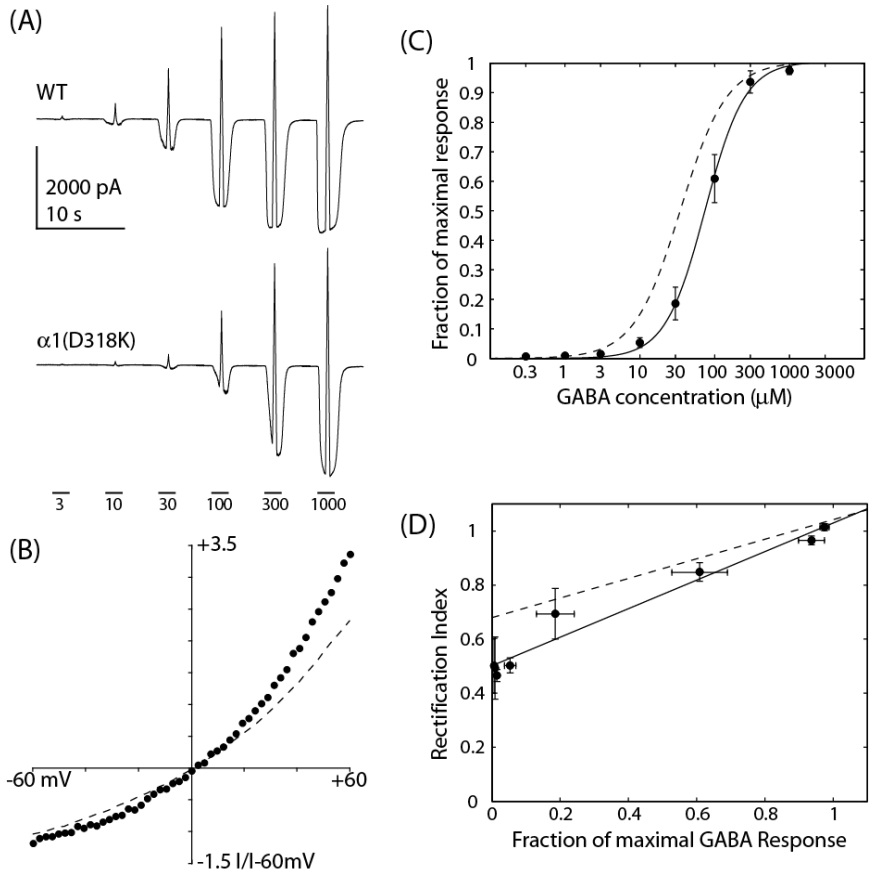

Figure 5.12: Rectification profile of α1(D318K). (A) Representative whole-cell current traces for α1(D318K) mutation. Bars indicate the duration of GABA application and are labeled with the concentration (μM). (B) IV relationship determined from a submaximally effective (EC_{10}) concentration of 10 μM GABA. Currents are shown normalized by the magnitude of inward current at -60 mV. (C) Hill equation fit of normalized peak currents shows that the charge switch mutation significantly decreased the apparent affinity for GABA ($n = 10$; pairwise comparison, $p < 0.05$). (D) The α1(D318K) mutation enhanced the degree of outward rectification at low P_O ($n = 10$). The dotted lines represent the WT GABAergic responses.

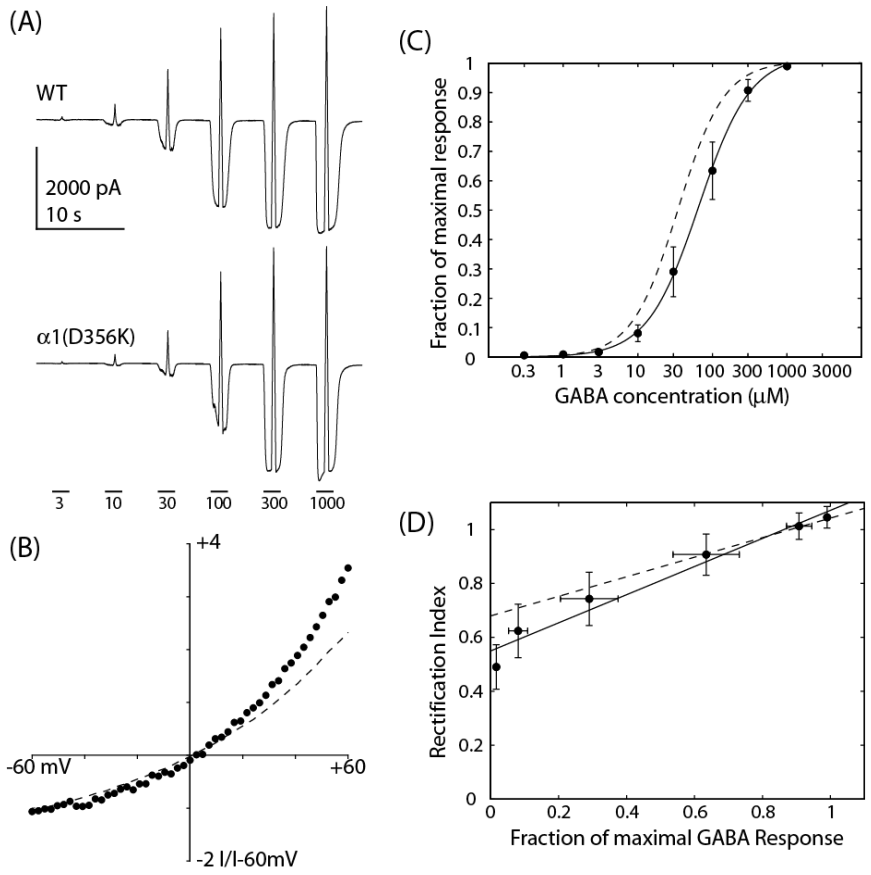

Figure 5.13: Rectification profile of α1(D356K). (A) Representative whole-cell current traces for WT and the α1(D356K) mutation. Bars indicate the duration of GABA application and are labeled with the concentration (μM). (B) IV relationship determined from a submaximally effective (EC_{10}) concentration of 10 μM GABA. Currents are shown normalized by the magnitude of inward current at -60 mV. (C) Hill equation fit of normalized peak currents shows that the charge switch mutation significantly decreased the apparent affinity for GABA ($n = 10$; pairwise comparison, $p < 0.05$). (D) The α1(D356K) mutation enhanced the degree of outward rectification at low P_O ($n = 10$). The dotted lines represent the WT GABAergic responses.

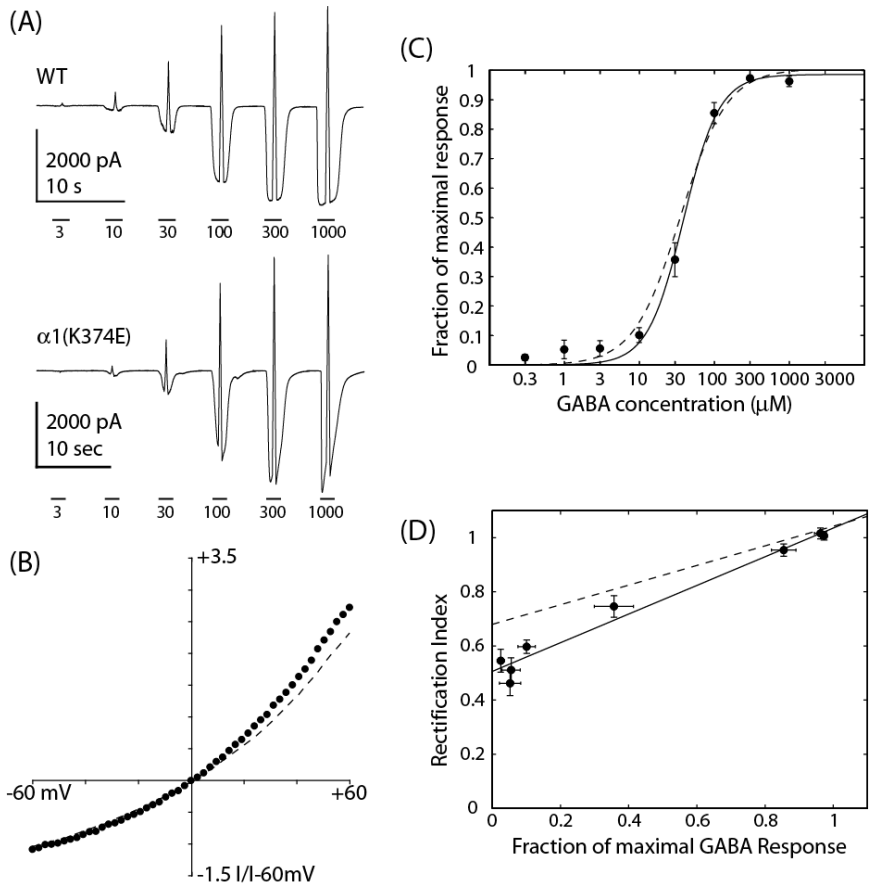

Figure 5.14: Rectification profile of α1(K374E). (A) Representative whole-cell current traces for WT and the α1(K374E) mutation. Bars indicate the duration of GABA application and are labeled with the concentration (μM). (B) IV relationship determined from a submaximally effective (EC_{10}) concentration of 10 μM GABA. Currents are shown normalized by the magnitude of inward current at -60 mV. (C) Hill equation fit of normalized peak currents shows that there was no change in the concentration-response induced by the charge switch mutation (n = 16). (D) The α1(K374E) mutation enhanced the degree of outward rectification at low P_O (n = 16). The dotted lines represent the WT GABAergic responses.

5.4: Discussion

5.4.1: Channel open probability is inversely related to degree of outward rectification

5.4.1A: Rectification is not limited to extrasynaptic $GABA_ARs$

The $GABA_AR$ has been shown to behave according to Ohm's law [Eq. 4] from single channel recordings of outside-out patches from spinal cord neurons in symmetrical chloride conditions (Bormann 1988; Macdonald, Rogers et al. 1989). However, more recently, GABA elicited currents from somatic patches of hippocampal neurons have revealed a non-linear IV relationship (Pytel, Mercik et al. 2006; Pavlov, Savtchenko et al. 2009). This suggested that rectification is subunit specific with differences in phasic versus tonic receptor sub-types; the most common synaptic receptor, mediating phasic signaling, is comprised of the α1, β2, and γ2 subunits, whereas extrasynaptic, tonic, receptors most often contain the δ and α4 or α6 subunits (McKernan and Whiting 1996; Martin and Olsen 2000). Changes in current rectification have also been observed through neuronal development providing further evidence for subunit specificity (Krishek and Smart 2001). Indeed, extrasynaptic α1β2 $GABA_ARs$ exhibit outward rectification that is attenuated by incorporation of the synaptic-targeting γ subunit (Boileau, Li et al. 2003). My results showed that, in fact, the degree of outward rectification at submaximal concentrations of GABA (≤ 100 μM) was not significantly different between α1β2γ2 and α1β2 containing receptors (Students t-test, $p > 0.05$); only RI values from currents elicited by 300 μM and 1 mM GABA were significantly more outwardly rectifying for the extrasynaptic receptor (Students t-test, $p < 0.05$; Fig. 5.5). It has been suggested that the amount of cDNA for the γ subunit must be in excess in order to force expression of the α1β2γ2 complex (Boileau, Li et al. 2003). I found that a 1:1:1 transfection ratio was sufficient to generate receptor complexes that incorporated the γ subunit adequately to eliminate the rectification effects of α1β2 receptors at maximal GABA (Fig. 5.5).

Single channel responses of extrasynaptic $GABA_AR$s exhibit a lower probability of being in the open state than their synaptic counterparts (Angelotti and Macdonald 1993; Fisher 2004; Farrant and Nusser 2005). Furthermore, neurosteroid application, which increases the duration of single channel openings (Akk, Covey et al. 2010), has been shown to reduce the magnitude of outward currents in α4-containing receptors to induce inward rectification (Shen, Gong et al. 2007). This change in the IV relationship induced by modulation of receptor kinetics led me to hypothesize that current rectification in the $GABA_AR$ is more generally linked to channel P_O and not limited to extrasynaptic receptors.

5.4.1B: P_O modulates degree of rectification

I determined IV relationships for the WT α1β2γ2 receptor under several different P_O conditions and found that rectification of current flow was inversely related to the degree of channel activation. When the magnitude of the current was increased by the application of a greater concentration of GABA or by a positive allosteric modulator, the degree of current rectification was reduced; responses became more "ohmic" (Fig. 5.2, 5.10). This did not occur when current amplitude was increased by simply changing the electrochemical driving force on the permeant ion, suggesting that rectification is linked to the direction of chloride flux and not caused by a direct action of membrane potential on the ion channel protein (as occurs with voltage-gated ion channels).

The link between the degree of channel activation and the amount of rectification was further emphasized in experiments where channel gating was hindered by using a partial agonist to activate the channel and by introducing a well-characterized deleterious gating mutation. In both cases, impaired channel gating, and thus decreased P_O, was associated with increased outward rectification (Fig. 5.8 Fig. 5.9). Taken together, all of these results demonstrate a robust

link between $GABA_AR$ channel P_O and current rectification. The possible causes of rectification are explored in Section 5.4.2.

5.4.1C: The efficacy of drugs that modulate P_O is voltage dependent

The $GABA_AR$ is the primary site of action for many clinically important therapeutics, including benzodiazepines and general anesthetics, which enhance channel activity by increasing P_O; pharmacologic modulation of the $GABA_AR$ is reviewed in Section 1.3.4. Results presented here showed an apparent voltage dependence of positive allosteric modulators of the $GABA_AR$. The magnitude of potentiation by general anesthetics was greater at negative potentials and decreased as the membrane potential became more positive (Fig. 5.11). The magnitude of current potentiation by allosteric modulators was attenuated at positive membrane potentials because the IV relationship became linear as P_O was increased. Therefore, the degree of enhancement caused by positive modulators was blunted at positive potentials. These findings suggest that experiments carried out with the common *in vitro* conditions (-60 mV holding potential in symmetrical chloride) will overestimate the effect of positive allosteric modulators at positive potentials, or when channel activation results in chloride influx. Interestingly, the potentiating effect of etomidate at -60 mV was 90% greater than at +60 mV, whereas, the effect of propofol was 83% greater and the effect of isoflurane was only 75% greater, suggesting a drug specific effect. Structures of GLIC crystallized in the presence of propofol and desflurane (similar to isoflurane) revealed the location of the general anesthetic binding site within the interface of the four transmembrane domain segments (Nury, Van Renterghem et al. 2011). Propofol was bound at the extracellular side of the cavity and desflurane was bound deep within the pocket (Nury, Van Renterghem et al. 2011). The gating mechanism predicted by comparison of the structures of GLIC and ELIC calculates a structural rearrangement of the anesthetic binding pocket in the open and closed conformations, respectively (Corringer, Baaden et al. 2010; Nury, Van Renterghem et al. 2011). Drugs which bind at different sites within the pocket are then predicted

to selectively affect channel gating. Likewise, the results presented here indicate that the orientation of the permeation pathway (the open conformation of the pore) is unique in the presence of each allosteric modulator to selectively determine the amplitude of inward and outward currents.

The action of $GABA_AR$ modulators has previously been shown to be voltage dependent; benzodiazepines have been shown to slow the rate of deactivation of GABAergic currents from cultured cerebellar granule cells at negative potentials, but not at positive potentials (Mellor and Randall 1998); inhibition of currents through α1β2γ2L receptors by amphiphiles was greater at positive potentials (Chisari, Shu et al. 2010); and the neurosteroid THP has been shown to decrease the magnitude of outward currents but not inward currents of α4β2δ receptors (Shen, Gong et al. 2007). My results showed that the magnitude of potentiation of α1β2γ2s receptors by intravenous and inhaled general anesthetics was dependent on the direction of chloride flux; etomidate, propofol, and isoflurane all selectively enhanced inward current magnitude.

5.4.2: Probable causes of rectification

From the work of Mokrab et al., (2007), who calculated the interaction energy between chloride ions and pore structures predicted by a homology model of the $GABA_AR$, outward rectification is expected when we look to the architecture of the pore lumen. The permeation pathway follows the central axis of the receptor structure through the extracellular and transmembrane domains, but is effectively split into five unequal paths by the intracellular loop domain (Mokrab, Bavro et al. 2007). Gage and Chung (1994) observed rectification of GABAergic single channel currents through membrane patches from hippocampal cultured neurons, that they surmised may be caused by parallel conducting pores with different voltage dependent open probabilities. Likewise, rectification has been shown to be caused by asymmetric pore geometry in many experiments using carbon nanotubes as simple models of ionic pores

(Andriotis, Menon et al. 2001; Kovarik, Zhou et al. 2009). For our purposes, the putative membrane associated α-helix of pLGICs forms an intracellular vestibule with lateral windows that set up five paths in the permeation pathway that function as parallel conducting pathways (Andriotis, Menon et al. 2001; Unwin 2005; Mokrab, Bavro et al. 2007). These windows form putative ion binding sites as entry/exit points of the pore (Unwin 2005; Peters, Cooper et al. 2010) (Fig. 3.1).

Chloride ions from the synaptic space must compete for a single binding site at the extracellular pore entrance. However, once within the pore, exit into the cell is energetically favorable with five putative ion sensors at the intracellular pore interface. On the other hand, chloride ions from the cytosol may bind to any of the intracellular ions sensors, BUT a bottle neck exists at the entry point to the transmembrane segment of the pore that may restrict access to the selectivity filter, located at the base of the transmembrane domain in the M1-2 linker (Jensen, Pedersen et al. 2005). The rates of chloride influx and chloride efflux are therefore predicted to be unequal.

The constant field equation predicts that rectification occurs under ionic gradient conditions where the chemical driving force on the permeant ion is much greater in one direction (Goldman 1943; Hodgkin and Katz 1949). Goldman rectification has been shown to occur in IPSCs recorded from cultured hippocampal neurons in asymmetrical chloride solutions that were calibrated to mimic physiological conditions (Barker and Harrison 1988). The $GABA_AR$ is known to conduct anions, therefore, outward rectification was predicted to occur when the equilibrium potential was negative and inward rectification was predicted to occur when the equilibrium potential was positive (Fig. 5.4). Under symmetrical conditions, the $GABA_AR$ was predicted to behave according to Ohm's law and exhibit a linear IV relationship (Fig. 5.4). From

the constant field equation [Eq. 10], it is clear that only two variables can account for outward rectification: the permeability of chloride (P_{Cl}) or the concentration of chloride.

5.4.2A: Goldman rectification

Experimentally, lowering the extracellular concentration of chloride caused a right shift in E_{Cl} and the IV relationship was more inwardly rectifying as predicted by the constant field equation (Fig. 5.4). Likewise, lowering the intracellular concentration of chloride shifted E_{Cl} to the left, and induced outward rectification that was greater than in the symmetrical chloride condition (Fig. 5.4). However, the degree of rectification in low P_O conditions was greater than predicted. Conversely, the linear response of the IV relationship at high P_O was less rectifying than predicted. These discrepancies occurred because the relationship between P_O and rectification (the slope of the rectification profile) persisted when E_{Cl} was shifted by changing the chloride gradient. (Table 5.3). Therefore, the observed outward rectification of GABAergic currents at low P_O was independent of Goldman rectification.

5.4.2B: Permeability of chloride

If the inward permeability of chloride was greater than the outward permeability then the magnitude of outward currents will be enhanced, resulting in outward rectification (Fig. 5.15). Likewise, if P_{Cl} is constant currents will behave according to Ohm's Law (Fig. 5.15). Calculation of chloride permeability from experimental current values, assuming that chloride concentration was constant, predicted that P_{Cl} varied with changes in membrane potential (Fig. 5.16). P_{Cl} increased as the membrane potential became more positive at low P_O, whereas, P_{Cl} was more constant at high P_O. Tangents to the P_{Cl}-potential relationship at ±60 mV revealed a striking disconnect (Fig. 5.16). Not only was P_{Cl} strongly voltage dependent, but it also appeared to be tending towards different inward and outward limits, emphasizing the asymmetry of chloride permeation.

5.4.2C: Local chloride concentration

Alternatively, if we assume that permeability is constant, the local extracellular concentration of chloride at the pore entrance must be greater than the bulk solute concentration OR the local intracellular concentration must be less than the bulk solute concentration to account for the enhanced inward drive on the ion at low P_O. Bormann et al. (1987) showed that increasing chloride concentration equally on both sides of the membrane increased channel conductance by increasing the number of charge carriers available. With this in mind, it is easy to envisage how gating elements could restrict anion access to parts of the pore, resulting in charge asymmetry and hence rectification.

The fenestrations of the intracellular vestibule are predicted to be no greater than the diameter of a hydrated ion (Unwin 2000; Unwin 2005). Hence, charged residues that line these windows will greatly influence the flux and local concentration of ions within the intracellular vestibule (Unwin 2000; Kelley, Dunlop et al. 2003; Unwin 2005). It is enticing to imagine that the molecular movements that occur with gating may alter the structure of the intracellular vestibule to effectively decrease the local intracellular concentration of chloride. The chemical drive on permeant ions would then be asymmetric resulting in outward rectification of currents at low P_O.

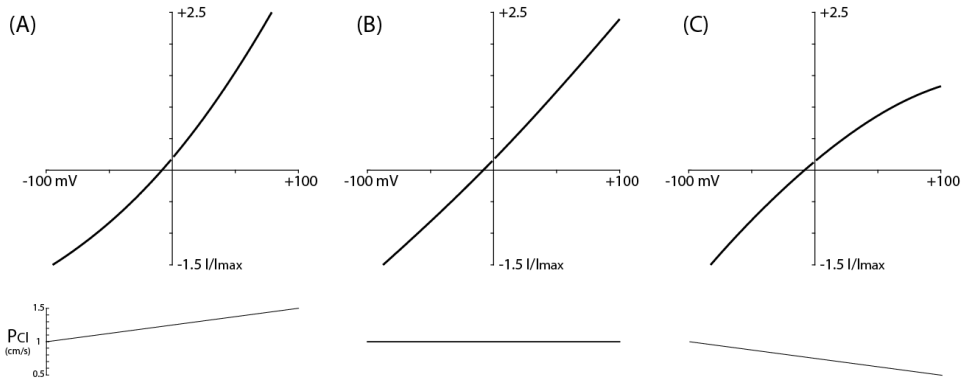

Figure 5.16: Theoretical IV relationships with non-constant chloride permeability. The constant field equation [Eq. 10] was used to predict the magnitude of currents with (A) increasing, (B) constant, and (C) decreasing permeability to chloride (P_{Cl}) with respect to the membrane potential. Bottom panels depict theoretical chloride permeabilities that were used to generate IV relationships. Intracellular and extracellular concentrations of chloride used for these predictions correlated to I1:E1 solutions. Notice that E_{rev} does not change although the directionality of current flow is significantly altered.

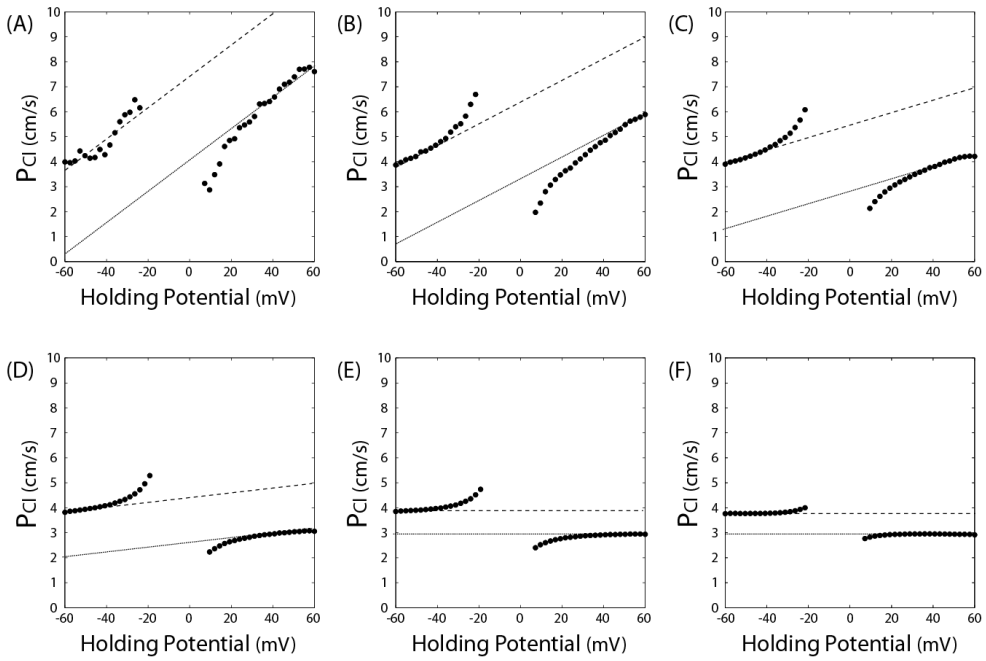

Figure 5.16: Chloride permeability was not constant at low open probability. The constant field equation was used to calculate the channel permeability to chloride (P_{Cl}) from currents elicited by (A) 3 µM, (B) 10 µM, (C) 30 µM, (D) 100 µM, (E) 300 µM, and (F) 1 mM GABA. To eliminate error, values determined from $I < \pm I_{RMS}$ were not included in the plot. Lines represent the trend of chloride efflux (dashed) and influx (dotted).

5.4.3: Gating elements

5.4.3A: Enhanced desensitization of outward currents masked rectification

Upon GABA application, the channel quickly transitions from the closed to the open state as the receptor binds its ligand and the ion channel gate is opened. At low P_O, the more frequent presence of gating elements within the pore may hinder ion permeation directionally generating an asymmetry similar to that observed in the I2:E1 condition. At high P_O, the ion channel behaved as a simple ohmic pore, with a linear relationship between the magnitude of current and the electrical driving force contributed by the membrane potential. With prolonged GABA application, the open channel transitions to a non-conducting desensitized state. I observed that desensitization of currents elicited by maximally effective concentrations of GABA was faster when chloride flux was inward, resulting in outward currents (Fig. 5.1). Thus, it is tempting to speculate that the asymmetric conditions that determine rectification were established by the directional movement of the primary channel gate. If the gate is able to move more easily in one direction over the other, then this asymmetry would be more evident at low P_O when the gate is moving. However, this asymmetry was masked by the enhanced desensitization of outward currents, which served to linearize the IV relationship. This leads me to predict that the separate closed-open and open-desensitized transitions must be mediated by different structures within the ion channel. If the primary channel gate and the desensitization gate were the same structure, then the decrease in P_O caused by desensitization would also correspond with an increase in outward rectification and not linearize the IV relationship as was observed. Importantly, many therapeutic agents modulate channel function by directly influencing the probability that the receptor will occupy one conformational state over another. These results show that state dependence, and hence drug action, is inherently voltage dependent.

5.4.3B: Chloride dependence

Molecular dynamic simulations of a potassium channel suggest that ions within the pore stabilize the open state of the channel to influence channel gating (Jensen, Borhani et al. 2010). I observed that concentration-response relationships constructed in the presence of low chloride extracellular and intracellular salines exhibited decreased apparent affinity compared to relationships determined in standard solutions (Fig. 4.5). I also observed a significant increase in whole-cell current magnitude and a significant increase in the speed of desensitization when extracellular chloride was decreased (Students t-test, $p < 0.05$, Fig. 4.4). The driving force on the permeant ion was greater at -60 mV under asymmetric conditions, which accounts for the enhancement of current magnitude. In order to test the effect of driving force on the other altered metrics, I determined IV relationships in altered ionic gradients and calculated the apparent affinity for GABA and the rate of desensitization under equivalent potential force (Fig. 4.4, Fig. 4.5). The relative increases in EC_{50} and desensitization persisted in commensurate driving force conditions; thus, the observed changes in $GABA_AR$ were mediated by a chloride-dependent mechanism. Furthermore, the chloride-dependence of apparent affinity persisted when the concentration of charge carriers was decreased on either side of the membrane suggesting that this phenomenon is mediated by structures within the pore lumen.

Gating is a complex phenomenon which involves many kinds of molecular movements and electrostatic interactions. Gating impairments that specifically alter P_O may be introduced through several mechanisms by: interfering with the energy transfer that propagates the energy of binding to open the channel gate and hindering the molecular movements that occur during gating. These data provide evidence that current rectification is inherently linked to the open probability of the channel. I have also shown that correlates of gating observable through apparent affinity and the time course of desensitization are chloride-dependent. Therefore, disruption of electrostatic interactions at important ion sensor sites within the pore represents a

new class of gating impairment. Hence, analysis of the rectification profile of ligand gated ion channels is a powerful tool that can be used to identify residues that are involved in gating through specific interactions with permeant ions.

5.4.4: Ion sensor sites within the permeation pathway

Three charge switch point mutations within the $GABA_AR$ α1 intracellular loop domain significantly enhanced outward rectification (Fig. 5.12-14, Table 5.4). Interestingly, each point mutation that enhanced outward rectification also induced changes in aspects of channel gating, either apparent affinity or desensitization (Chapter 4). These positions were therefore predicted to serve as ion sensor sites within the permeation pathway, and may mediate rectification by controlling the concentration of chloride ions within the intracellular vestibule. The mutations α1(D318K) and α1(D356K) both significantly decreased the intercept of the rectification profile and both right-shifted the GABA concentration-response relationships compared to WT (Fig. 4.14, Fig. 5.12; Fig. 5.13). The α1(D356K) mutation also significantly increased the slope of the rectification profile and shifted the relative anion permeability of the pore (Fig. 4.14, Fig. 5.13). The α1(K374E) mutation significantly decreased the intercept of the rectification profile and induced faster desensitization (Fig. 4.14, Fig. 5.14). These data support the hypothesis that charged residues of the permeation pathway are also involved in gating the ion channel through specific interactions with permeant ions.

5.4.5: P_O mediated rectification is a universal property of $GABA_ARs$

Finally, I will discuss some recent findings from the lab of Sheryl Smith, SUNY Downstate Medical Center, Brooklyn, NY, which provide further evidence that P_O mediated rectification is a property of both synaptic and extrasynaptic $GABA_ARs$. The canonical synaptic and extrasynaptic α subunits are α1-3 and α4-6, respectively (McKernan and Whiting 1996). Each of these α subunits confers distinct kinetics and pharmacology to the $GABA_AR$ (Lavoie,

Tingey et al. 1997; Picton and Fisher 2007; Mortensen, Ebert et al. 2010). Shen et al. (2007) have shown that the neurosteroid allopregnanolone increases the magnitude of inward currents and decreases the magnitude of outward currents through α4-containing $GABA_A$Rs; allopregnanolone was shown to induce inward rectification by specifically accelerating receptor desensitization in outward currents. In comparison, our results have shown that the speed of desensitization was faster in outward GABAergic currents through modulator naive α1-containing receptors (Fig. 5.1). The action of allopregnanolone did not change chloride selectivity and persisted in altered chloride gradients (Shen, Gong et al. 2007). Likewise, the relationship observed here between RI and P_O occurred independently of Goldman rectification (Fig. 5.4). Furthermore, allopregnanolone potentiation of inward currents was unaffected by GABA concentration, but allopregnanolone inhibition of outward currents was greater at high concentrations of GABA (Shen, Gong et al. 2007). This is consistent with the observation that allopregnanolone enhanced desensitization of outward currents and is a beautiful example of how drastically the directional dependence of desensitization can alter the shape of the IV relationship. Finally, through careful use of mutagenesis, the voltage-dependence of allopregnanolone modulation was shown to be mediated by an arginine residue within the α4 intracellular loop domain; charge neutralization at this site specifically ablated the effect of allopregnanolone on outward currents but preserved the enhancement of inward currents (Shen, Gong et al. 2007). This position, α4(R353), is homologous to the α1(D356) position; the α1(D356K) charge switch, introduced in this study, selectively enhanced the degree of outward rectification at low P_O, but was not different from WT at high P_O. If we assume that the asymmetry that establishes outward rectification persists at high P_O and is merely masked by desensitization, then α1(D356K) must also enhance desensitization of outward currents to overcome the greater degree of outward rectification present compared to WT. Thus, the effects of both the α1(D356K) and the α4(R353Q) mutations were voltage-dependent with respect to the open probability of the ion channel. It is tempting to surmise that modulation of α4 function through allopregnanolone

-mediated changes in P_O acts through same mechanism as the P_O dependent rectification that we have observed in α1-containing $GABA_A$Rs. In sum, these results provide compelling evidence that the α1(D356) position represents a conserved ion sensor site for $GABA_A$R α subunits.

5.5: Conclusion

These results have shown that the apparent voltage-dependence of the α1β2γ2 $GABA_A$R was inversely related to channel open probability. The relative magnitude of outward currents was greater than the magnitude of inward currents, in low P_O conditions, resulting in outward rectification. At high P_O, desensitization of outward currents was enhanced resulting in a linearization of the IV relationship. The different effects of gating and desensitization on the IV relationship suggest that these mechanisms were mediated by different channel structures. I have also shown that the degree of receptor enhancement by therapeutics was voltage dependent; in particular, potentiation was greater at negative membrane potentials. Therefore, in order to properly understand receptor activation and modulation, we must take both the channel open probability and the direction of ion flux into account. Finally, rectification was used as a tool to identify intracellular loop domain residues that define a portion of the permeation pathway.

Chapter Six

Secondary Structure of the ILD

6.1: Overview

To date, there is no known structure for the $GABA_AR$. Several structures have been resolved for homologous proteins which provide insight for some domains of the receptor, but structural information for the intracellular loop domain is incomplete. Therefore, I used bioinformatic analysis of the primary sequence to predict the secondary structure of the intracellular loop domain and generated a homology model of the $GABA_AR$ α1 subunit. Results predicted that the intracellular loop domain contains two α helices that are continuous with the flanking transmembrane domains and separated by a β sheet.

6.2: Introduction

Studying the evolutionary genomics of protein families provides much information for understanding a particular protein of interest. In this context, the primary and secondary structures of protein domains can be compared and similar biological functions may be inferred. The structure-function paradigm is a well-established theory that relies on the notion of "inheritance through homology" (Lee, Redfern et al. 2007). Homologous proteins within such families are believed to have diverged from a common evolutionary origin and therefore proteins with similar primary sequences will have similar structure and similar function.

Several structures of pLGICs and homologous proteins have been resolved and provide a backbone for making predictions of the structure for the $GABA_AR$ specifically (Unwin 1993; Brejc, van Dijk et al. 2001; Cromer, Morton et al. 2002; Unwin 2005; Bocquet, Nury et al. 2009; Hilf and Dutzler 2009; Corringer, Baaden et al. 2010). For a complete discussion of receptor structure see Section 1.3.2. In general, the extracellular domain of pLGICs is thought to contain an N-terminal α helix and is primarily comprised of β strands that form a β sandwich structure, the transmembrane domain is predicted to pass through the membrane in four α helical segments (M1-M4), and a partial structure has been resolved for the intracellular loop domain of the nAChR, which predicts a membrane associated α helix continuous with M4 (Fig. 1.4C). Although much is currently known about the function and structure of proteins within the pLGIC superfamily, there is a distinct lack of structural information for the intracellular loop domain and, therefore, it is difficult to make functional comparisons within this domain. Furthermore, the intracellular loop domain has the largest degree of amino acid sequence variability which makes it difficult to make comparisons through sequence alignments.

To begin to fill this knowledge gap, I first investigated the primary sequence homology and evolution of the $GABA_AR$ subunits by generating an amino acid sequence alignment and

phylogenetic comparison tree. Next, I predicted the secondary structure of the $GABA_AR$ α1 intracellular loop domain with bioinformatic analysis of the primary sequence. Finally, I generated a structural homology model for the $GABA_AR$ α1 subunit.

6.3: Results

6.3.1: Primary sequence alignments revealed conservation of three domains

Homology may be carried by orthologs, proteins which arise from speciation, or paralogs, proteins from gene duplication and subsequent differentiation (Lee, Redfern et al. 2007). An understanding of the origin of homologs can give insight into the function of structurally similar proteins because orthologs are likely to maintain the same function, whereas, paralogs are free to occupy a novel functional niche (Lee, Redfern et al. 2007). The functional $GABA_AR$ is a heteromeric protein that may be composed of a variety of subunits, which are paralogs and therefore may infer unique function to the receptor. Interestingly, the majority of $GABA_AR$ genes are found in clusters on four chromosomes within the *Homo sapiens* genome (Table 6.1). Furthermore, the relative orientation and grouping of genes indicate the order of gene duplications that arose to generate the unique paralogs. Phylogenic analysis of amino acid sequences revealed that the δ and π subunits are more similar to one another than the other subunits (Fig. 6.1) and the gene for each subunit resides on a chromosome without other $GABA_AR$ genes. The α3, θ, and ε genes are located in a cluster on the X chromosome. The θ subunit is most similar to the β subunits and ε is similar to the γ subunits. Moreover, the α5, β3, and γ3 genes are located in a cluster on chromosome 15 in the same order and relative orientation as the α3, θ, and ε genes. This parallel likely arose from a gene duplication event. A subsequent gene cluster duplication likely occurred to generate the position of the α1, β2, and γ2 genes on chromosome 5. Furthermore, an additional gene duplication event occurred to spawn the α6 gene.

This is perfect example of how paralogy generates novel functions; the α1 and α2 subunits have very similar primary sequences and similar functionality whereas the α4 and α6 subunits are alike one another, but very different from α1 and α2. In particular, α1 and α2 tend to assemble with the γ subunit and are targeted to the synapse; conversely, α4 and α6 are more

typically co-expressed with the δ subunit and are localized extrasynaptically (Connolly 2008). Therefore, gene duplication occurred within the gene cluster on chromosome 5 to generate two copies of the α1 subunit gene. Through paralogy, one copy of the gene diverged and gained new function to become the α6 subunit gene. Then, a gene cluster duplication occurred to generate the α2, α4, β1, and γ1 genes on chromosome 4. Phylogenetic evaluation of genes gives an indication of evolutionary lineage. The patristic distances calculated by the phylogenetic tree algorithm are relative values intended to describe the amount of genetic change between sequences. Interestingly, the relative distances and connectivity of the $GABA_AR$ suggest that the evolution of the α subunit genes are consistent with that which I inferred from chromosomal locations (Fig. 6.1).

Alignment of primary sequences for the $GABA_AR$ α, β, and γ subunit paralogs showed a high degree of conservation within the extracellular domain and transmembrane domain, but a striking degree of variability within the intracellular loop domain (Fig. 6.2), which makes this domain a prime target for studying the functional differences between subunit paralogs. The phylogeny of the $GABA_AR$ α, β, and γ subunits was different when the full length sequence or when only the intracellular loop domain sequence was used to construct the phylogenic tree (Fig. 6.3). For example, the β and γ subunits shared a node on the intracellular loop domain tree, but not when the full sequence was considered. This difference may indicate shared functionality, in particular, the ILDs of β and γ subunits are known to share a functional role in mediating receptor trafficking and surface stability (Chen and Olsen 2007; Michels and Moss 2007).

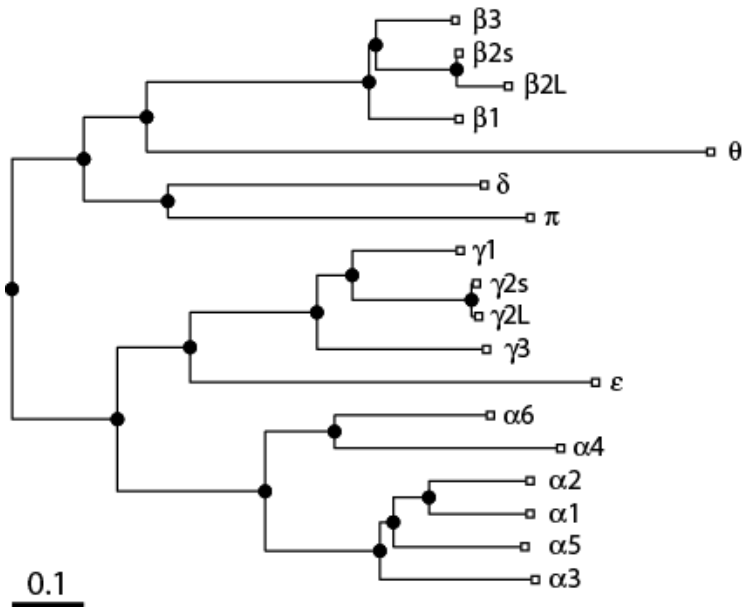

Figure 6.1: Phylogeny of $GABA_AR$ subunits. Tree was created using the *phytree* function in the Bioinformatics toolbox for Matlab. Calibration bar represents the patristic distance calculated from pairwise BLOMSUM scores.

Accession numbers: *α1, NP_000797; α2, NP_000798; α3, NP_000799; α4, NP_000800; α5, NP_000801; α6, NP_000802; β1, NP_000803; β2S, NP_000804; β2L, NP_068711; β3, NP_000805; γ1, NP_775807; γ2S, NP_000807; γ2L, NP_944494; γ3, NP_150092; δ, NP_000806; ε, NP_004952; θ, NP_061028; π, NP_055026.*

Gene	Location		Gene	Location	
GABRD	1p36.3	→	GABRP	5q35.1	→
GABRG1	4p12	←	GABRB2	5q34	←
GABRA2	4p12	←	GABRA6	5q34	→
GABRA4	4p12	←	GABRA1	5q34	→
GABRB1	4p12	→	GABRG2	5q34	→
GABRB3	15q13.2	←	GABRA3	Xq28	←
GABRA5	15q13.2	→	GABRE	Xq28	←
GABRG3	15q13.2	→	GABRAQ	Xq28	→

Table 6.1: Gene loci. Gene names for $GABA_AR$ subunits are: α (GABRA), β (GABRB), γ (GABRG), δ (GABRD), ε (GABRE), θ (GABRQ), π (GABRP). Genes are grouped by chromosome and listed in 5' to 3'order. The transcription direction of the gene is shown to indicate location on the forward (→) or reverse (←) DNA strand.

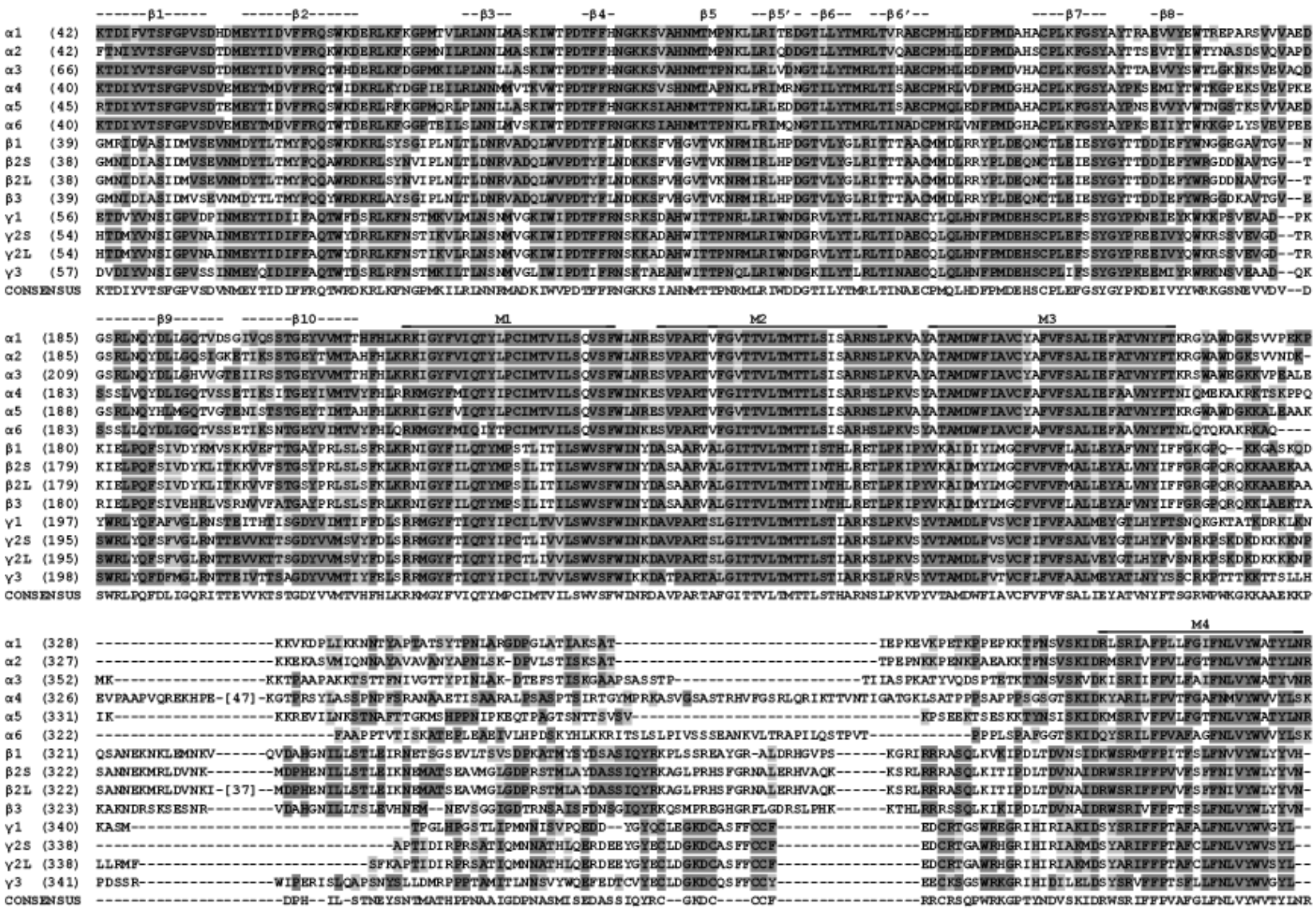
α1 (42) KTDIFVTSFGPVSDHDMEYTIDVFFRQSWKDERLKFKGPMTVLRLNNLMASKIWTPDTFFHNGKKSVAHNMTMPNKLLRITEDGTLLYTMRLTVRAECPMHLEDFPMDAHACPLKFGSYAYTRAEVVYEWTREPARSVVVAED
α2 (42) FTNIYVTSFGPVSDTDMEYTIDVFFRQKWKDERLKFKGPMNILRLNNLMASKIWTPDTFFHNGKKSVAHNMTMPNKLLRIQDDGTLLYTMRLTVQAECPMHLEDFPMDAHSCPLKFGSYAYTTSEVTYIWTYNASDSVQVAPD
α3 (66) KTDIYVTSFGPVSDTDMEYTIDVFFRQTWHDERLKFDGPMKILPLNNLLASKIWTPDTFFHNGKKSVAHNMTTPNKLLRLVDNGTLLYTMRLTIHAECPMHLEDFPMDVHACPLKFGSYAYTTAEVVYSWTLGKNKSVEVAQD
α4 (40) KTDIYVTSFGPVSDVEMEYTMDVFFRQTWIDKRLKYDGPIEILRLNNMMVTKVWTPDTFFRNGKKSVSHNMIAPNKLFRIMRNGTILYTMRLTISAECPMRLVDFPMDGHACPLKFGSYAYPKSEMIYTWTKGPEKSVEVPKE
α5 (45) RTDIYVTSFGPVSDTEMEYTIDVFFRQSWKDERLRFKGPMQRLPINNLLASKIWTPDTFFHNGKKSIAHNMTTPNKLLRLEDDGTLLYTMRLTISAECPMQLEDFPMDAHACPLKFGSYAYPNSEVVYVWTNGSTKSVVVAED
α6 (40) KTDIYVTSFGPVSDVEMEYTMDVFFRQTWTDERLKFGGPTEILSLNNLMVSKIWTPDTFFRNGKKSIAHNMTTPNKLFRIMQNGTILYTMRLTINADCPMRLVNFPMDGHACPLKFGSYAYPKSEIIYTWKKGPLYSVEVPEE
β1 (39) GMRIDVASIDMVSEVNMDYTLTMYFQQSWKDKRLSYSGIPLNLTLDNRVADQLWVPDTYFLNDKKSFVHGVTVKNRMIRLHPDGTVLYGLRITTTAACMMDLRRYPLDEQNCTLEIESYGYTTDDIEFYWNGGEGAVTGV--N
β2S (38) GMNIDIASIDMVSEVNMDYTLTMYFQQAWRDKRLSYNVIPLNLTLDNRVADQLWVPDTYFLNDKKSFVHGVTVKNRMIRLHPDGTVLYGLRITTTAACMMDLRRYPLDEQNCTLEIESYGYTTDDIEFYWRGDDNAVTGV--T
β2L (38) GMNIDIASIDMVSEVNMDYTLTMYFQQAWRDKRLSYNVIPLNLTLDNRVADQLWVPDTYFLNDKKSFVHGVTVKNRMIRLHPDGTVLYGLRITTTAACMMDLRRYPLDEQNCTLEIESYGYTTDDIEFYWRGDDNAVTGV--T
β3 (39) GMNIDIASIDMVSEVNMDYTLTMYFQQYWRDKRLAYSGIPLNLTLDNRVADQLWVPDTYFLNDKKSFVHGVTVKNRMIRLHPDGTVLYGLRITTTAACMMDLRRYPLDEQNCTLEIESYGYTTDDIEFYWRGGDKAVTGV--E
γ1 (56) ETDVYVNSIGPVDPINMEYTIDIIFAQTWFDSRLKFNSTMKVLMLNSMMVGKIWIPDTFFRNSRKSDAHWITTPNRLLRIWNDGRVLYTLRLTINAECYLQLHNFPMDEHSCPLEFSSYGYPKNEIEYKWKKPSVEVAD--PK
γ2S (54) HTDMYVNSIGPVNAINMEYTIDIFFAQTWYDRRLKFNSTIKVLRLNSMMVGKIWIPDTFFRNSKKADAHWITTPNRMLRIWNDGRVLYTLRLTIDAECQLQLHNFPMDEHSCPLEFSSYGYPREEIVYQWKRSSVEVGD--TR
γ2L (54) HTDMYVNSIGPVNAINMEYTIDIFFAQTWYDRRLKFNSTIKVLRLNSMMVGKIWIPDTFFRNSKKADAHWITTPNRMLRIWNDGRVLYTLRLTIDAECQLQLHNFPMDEHSCPLEFSSYGYPREEIVYQWKRSSVEVGD--TR
γ3 (57) DVDIYVNSIGPVSSINMEYQIDIFFAQTWTDSRLRFNSTMKILTLNSMMVGLIWIPDTIFRNSKTAEAHWITTPNQLLRIWNDGKILYTLRLTINAECQLQLHNFPMDEHSCPLIFSSYGYPKEEMIYRWRKNSVEAAD--QK
CONSENSUS KTDIYVTSFGPVSDVNMEYTIDIFFRQTWFDKRLKFNGPMKILRINNNRMADKIWVPDTFFRNGKKSIAHNMTTPNRMLRIWDDGTILYTMRLTINAECPMQLHDFPMDEHSCPLEFGSYGYPKDEIVYYWRKGSNEVVDV--D

α1 (185) GSRLNQYDLLGQTVDSGIVQSSTGEYVVMTTHFHLKRKIGYFVIQTYLPCIMTVILSQVSFWLNRESVPARTVFGVTTVLTMTTLSISARNSLPKVAYATAMDWFIAVCYAFVFSALIEFATVNYFTKRGYAWDGKSVVPEKP
α2 (185) GSRLNQYDLLGQSIGKETIKSSTGEYTVMTAHFHLKRKIGYFVIQTYLPCIMTVILSQVSFWLNRESVPARTVFGVTTVLTMTTLSISARNSLPKVAYATAMDWFIAVCYAFVFSALIEFATVNYFTKRGWAWDGKSVVNDK-
α3 (209) GSRLNQYDLLGHVVGTEIIRSSTGEYVVMTTHFHLKRKIGYFVIQTYLPCIMTVILSQVSFWLNRESVPARTVFGVTTVLTMTTLSISARNSLPKVAYATAMDWFIAVCYAFVFSALIEFATVNYFTKRSWAWEGKKVPEALE
α4 (183) SSSLVQYDLIGQTVSSETIKSITGEYIVMTVYFHLRRMGYFMIQTYIPCIMTVILSQVSFWINKESVPARTVFGITTVLTMTTLSISARHSLPKVSYATAMDWFIAVCFAFVFSALIEFAAVNYFTNIQMEKAKRKTSKPPQ
α5 (188) GSRLNQYHLMGQTVGTENISTSTGEYTIMTAHFHLKRKIGYFVIQTYLPCIMTVILSQVSFWLNRESVPARTVFGVTTVLTMTTLSISARNSLPKVAYATAMDWFIAVCYAFVFSALIEFATVNYFTKRGWAWDGKKALEAAK
α6 (183) SSSLLQYDLIGQTVSSETIKSNTGEYVIMTVYFHLQRMGYFMIQIYTPCIMTVILSQVSFWINKESVPARTVFGITTVLTMTTLSISARHSLPKVSYATAMDWFIAVCFAFVFSALIEFAAVNYFTNLQTQKAKRKAQ----
β1 (180) KIELPQFSIVDYKMVSKKVFFTTGAYPRLSLSFRLKRNIGYFILQTYMPSTLITILSWVSFWINYDASAARVALGITTVLTMTISTHLRETLPKIPYVKAIDIYIMGCFVFVFLALLEYAFVNYIFFGKGPQ--KKGASKQD
β2S (179) KIELPQFSIVDYKLITKKVVFSTGSYPRLSLSFKLKRNIGYFILQTYMPSILITILSWVSFWINYDASAARVALGITTVLTMTTINTHLRETLPKIPYVKAIDMYIMGCFVFVFMALLEYALVNYIFFGRGPQRQKKAAEKAA
β2L (179) KIELPQFSIVDYKLITKKVVFSTGSYPRLSLSFKLKRNIGYFILQTYMPSILITILSWVSFWINYDASAARVALGITTVLTMTTINTHLRETLPKIPYVKAIDMYIMGCFVFVFMALLEYALVNYIFFGRGPQRQKKAAEKAA
β3 (180) RIELPQFSIVEHRLVSRNVVFATGAYPRLSLSFRLKRNIGYFILQTYMPSILITILSWVSFWINYDASAARVALGITTVLTMTTINTHLRETLPKIPYVKAIDMYIMGCFVFVFLALLEYAFVNYIFFGRGPQRQKKLAEKTA
γ1 (197) YWRLYQFAFVGLRNSTEITHTISGDYVIMTIFFDLSRRMGYFTIQTYIPCILTVVLSWVSFWINKDAVPARTSLGITTVLTMTTLSTIARKSLPKVSYVTAMDLFVSVCFIFVFAALMEYGTLHYFTSNQKGKTATKDRKLKN
γ2S (195) SWRLYQFSFVGLRNTTEVVKTTSGDYVVMSVYFDLSRRMGYFTIQTYIPCTLIVVLSWVSFWINKDAVPARTSLGITTVLTMTTLSTIARKSLPKVSYVTAMDLFVSVCFIFVFSALVEYGTLHYFVSNRKPSKDKDKKKKNP
γ2L (195) SWRLYQFSFVGLRNTTEVVKTTSGDYVVMSVYFDLSRRMGYFTIQTYIPCTLIVVLSWVSFWINKDAVPARTSLGITTVLTMTTLSTIARKSLPKVSYVTAMDLFVSVCFIFVFSALVEYGTLHYFVSNRKPSKDKDKKKKNP
γ3 (198) SWRLYQFDFMGLRNTTEIVTTSAGDYVVMTIYFELSRRMGYFTIQTYIPCILTVVLSWVSFWIKKDATPARTALGITTVLTMTTLSTIARKSLPRVSYVTAMDLFVTVCFLFVFAALMEYATLNYYSSCRKPTTTKKTTSLLH
CONSENSUS SWRLPQFDLIGQRITTEVVKTSTGDYVVMTVHFHLKRRMGYFVIQTYMPCIMTVILSWVSFWINRDAVPARTAFGITTVLTMTTLSTHARNSLPKVPYVTAMDWFIAVCFVFVFSALIEYATVNYFTSGRWPWKGKKAAEKKP

α1 (328) ----------KKVKDPLIKKNNTYAPTATSYTPNLARGDPGLATIAKSAT----------IEPKEVKPETKPPEPKKTFNSVSKIDRLSRIAFPLLFGIFNLVYWATYLNR
α2 (327) ----------KKEKASVMIQNNAYAVAVANYAPNLSK-DPVLSTISKSAT----------TPEPNKKPENKPAEAKKTFNSVSKIDRMSRIVFPVLFGTFNLVYWATYLNR
α3 (352) MK----------KKTPAAPAKKTSTTFNIVGTTYPINLAK-DTEFSTISKGAAPSASSTP----------TIIASPKATYVQDSPTETKTYNSVSKVDKISRIIFPVLFAIFNLVYWATYVNR
α4 (326) EVPAAPVQREKHPE-[47]-KGTPRSYLASSPNPFSRANAAETISAARALPSASPTSIRTGYMPRKASVGSASTRHVFGSRLQRIKTTVNTIGATGKLSATPFPSAPPSGSGTSKIDKYARILFPVTFGAFNMVYWVVYLSK
α5 (331) IK----------KKREVILNKSTNAFTTGKMSHPPNIPKEQTPAGTSNTTSVSV----------KPSEEKTSESKKTYNSISKIDKMSRIVFPVLFGTFNLVYWATYLNR
α6 (322) ----------FAAPPTVTISKATEPLEAEIVLHPDSKYHLKKRITSLSLPIVSSSEANKVLTRAPILQSTPVT----------PPPLSPAFGGTSKIDQYSRILFPVAFAGFNLVYWVVYLSK
β1 (321) QSANEKNKLEMNKV------QVDAHGNILLSTLEIRNETSGSEVLTSVSDPKATMYSYDSASIQYRKPLSSREAYGR-ALDRHGVPS------KGRIRRRASQLKVKIPDLTDVNSIDKWSRMFFPITFSLFNVVYWLYYVH-
β2S (322) SANNEKMRLDVNK--------MDPHENILLSTLEIKNEMATSEAVMGLGDPRSTMLAYDASSIQYRKAGLPRHSFGRNALERHVAQK------KSRLRRRASQLKITIPDLTDVNAIDRWSRIFFPVVFSFFNIVYWLYYVN-
β2L (322) SANNEKMRLDVNKI-[37]--MDPHENILLSTLEIKNEMATSEAVMGLGDPRSTMLAYDASSIQYRKAGLPRHSFGRNALERHVAQK------KSRLRRRASQLKITIPDLTDVNAIDRWSRIFFPVVFSFFNIVYWLYYVN-
β3 (323) KAKNDRSKSESNR--------VDAHGNILLTSLEVHNEM--NEVSGGIGDTRNSAISFDNSGIQYRKQSMPREGHGRFLGDRSLPHK------KTHLRRRSSQLKIKIPDLTDVNAIDRWSRIVFPFTFSLFNLVYWLYYVN-
γ1 (340) KASM----------TPGLHPGSTLIPMNNISVPQEDD--YGYQCLEGKDCASFFCCF----------EDCRTGSWREGRIHIRIAKIDSYSRIFFPTAFALFNLVYWVGYL--
γ2S (338) ----------APTIDIRPRSATIQMNNATHLQERDEEYGYECLDGKDCASFFCCF----------EDCRTGAWRHGRIHIRIARMDSYARIFFPTAFCLFNLVYWVSYL--
γ2L (338) LLRMF----------SFKAPTIDIRPRSATIQMNNATHLQERDEEYGYECLDGKDCASFFCCF----------EDCRTGAWRHGRIHIRIARMDSYARIFFPTAFCLFNLVYWVSYL--
γ3 (341) PDSSR----------WIPERISLQAPSNYSLLDMRPPFTAMITLNNSVYWQEFEDTCVYECLDGKDCQSFFCCY----------EECKSGSWRKGRIHIDILELDSYSRVFFPTSFLLFNLVYWVGYL--
CONSENSUS ----------DPH--IL-STNEYSNTMATHPPNAAIGDPNASMISEDASSIQYRC--GKDC----CCF----------RRCRSQPWRKGPTYNDVSKIDRWSRIFFPVAFGLFNLVYWVTYLNR

M1
M2
M3
M4

Figure 6.2: Sequence alignment of $GABA_AR$ subunits. [Previous page] The *multialign* function in the Bioinformatics toolbox for Matlab was used to generate alignments of primary amino acid sequences of the $GABA_AR$ α, β, and γ subunits. The predicted secondary structure of the $GABA_AR$ is shown above the alignment for α helices (underlined) and β strands (dashed). The structure of the $GABA_AR$ extracellular domain was predicted by Cromer et al., (2005) from comparison to the AChBP structure (PDB: 1I9B) to define the residues within the β strands (β1-10). The location of the four transmembrane domains (M1-M4) was predicted by Bertaccini and Trudell (2002) from comparison of 10 topology predictions. Round brackets (#) give the sequence number and square brackets [#] represent the number of residues that are not shown in the main alignment. Dark grey background shows residues with 100% identity to the consensus sequence and light grey background marks residues that share side-chain property conservation. Notice the high degree of primary sequence conservation within the extracellular domain and transmembrane domain, whereas the intracellular loop domain exhibits the greatest degree of variability.

Accession numbers: *α1, NP_000797; α2, NP_000798; α3, NP_000799; α4, NP_000800; α5, NP_000801; α6, NP_000802; β1, NP_000803; β2S, NP_000804; β2L, NP_068711; β3, NP_000805; γ1, NP_775807; γ2S, NP_000807; γ2L, NP_944494; γ3, NP_150092.*

INSERTS:

α4	**[47]**	APLQNTNANLNMRKRTNALVHSESDVGNRTEVGNHSSKSSTVVQESS
β2L	**[37]**	FYKDIKQNGTQYRSLWDPTGNLSPTRRTTNYDFSLYT

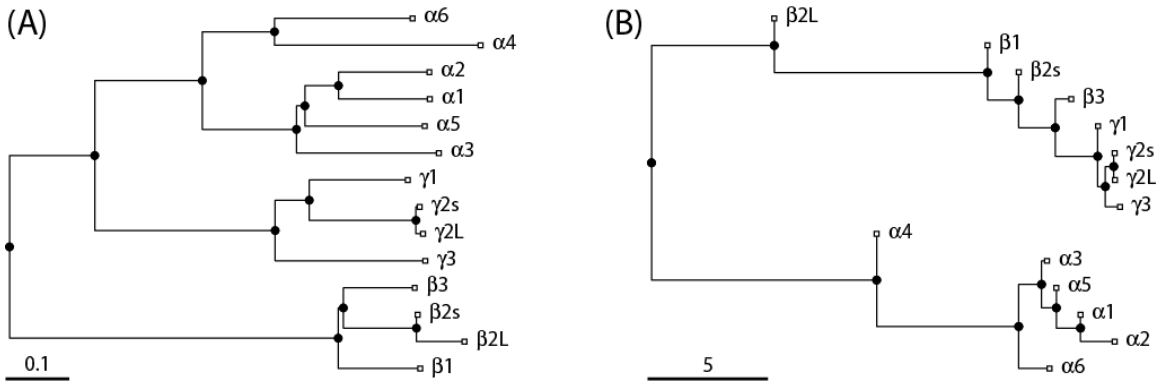

Figure 6.3: Evolutionary relatedness of $GABA_AR$ domains. Phylogenetic trees constructed from sequence alignments of (A) the full primary amino acid sequence and (B) only the intracellular loop domain residues for the α, β, and γ subunits of the $GABA_AR$. Calibration bars represent the patristic distance calculated from pairwise BLOMSUM scores. Notice the higher degree of genetic "distance" between the intracellular loop domain sequences. Interestingly, the intracellular loop domain sequences of β and γ subunits shared a node, whereas, γ was evolutionarily closer to the α subunits in regards to the full length sequence.

6.3.2: Secondary structures predicted from primary amino acid sequence

I used two methods to predict the secondary structure of the α1 ILD: the Chou-Fasman scale and the Jnet algorithm; for details of analysis see Section 2.5.2. First, I used the Chou-Fasman scale (1978) to predict the secondary structure of the α1 intracellular loop domain directly from the primary amino acid sequence (Fig. 6.4). This is a *de novo* prediction method that calculates the probability that each residue of the α1 intracellular loop domain resides within an α helix or a β strand. Separate amino acid scales were determined for each secondary structure type from comparison of 29 unique protein structures (Chou and Fasman 1978). Results showed a high probability (score ≥ 0.9) of α helices flanking the intracellular loop domain, near both M3 and M4 (Fig. 6.4). The interior ends of each helix were also predicted to be β strands that may be able to fold together as a β sheet (Fig. 6.4).

Second, I used the Jnet algorithm to predict the secondary structure of the α1 intracellular loop domain alone and in context of the full length sequence (Cole, Barber et al. 2008) (Fig. 6.5). This prediction method relies heavily on primary sequence homology; therefore, I determined a secondary structure prediction for the entire α1 subunit because the extracellular domain and transmembrane domain regions displayed a higher degree of primary sequence conservation (Fig. 6.2 and Fig. 6.5A). The Jnet algorithm successfully predicted the structure of the α1 subunit extracellular domain as predicted by Cromer et al., (2002) and the location of the transmembrane domain α helices as predicted by Bertaccini and Trudell (2002) (Fig. 6.5A). In the context of the full length sequence, the Jet algorithm predicted an eight residue α helix within the intracellular loop domain near M3 (Fig. 6.5A). A shorter three residue helix and a six residue β strand were predicted in the context of the intracellular loop domain primary sequence alone (Fig. 6.5B).

Both methods predicted that residues near M3 reside within an α helix and that residues in the center of the intracellular loop domain form a β sheet (Fig. 6.4 and Fig. 6.5). However,

only the *de novo* prediction derived from the Chou-Fasman scale determined that residues near M4 also form an α helix (Fig. 6.4). Based on the nAChR structure, it is encouraging to envision that the M4 membrane associated domain of the $GABA_AR$ intracellular loop domain is also α helical.

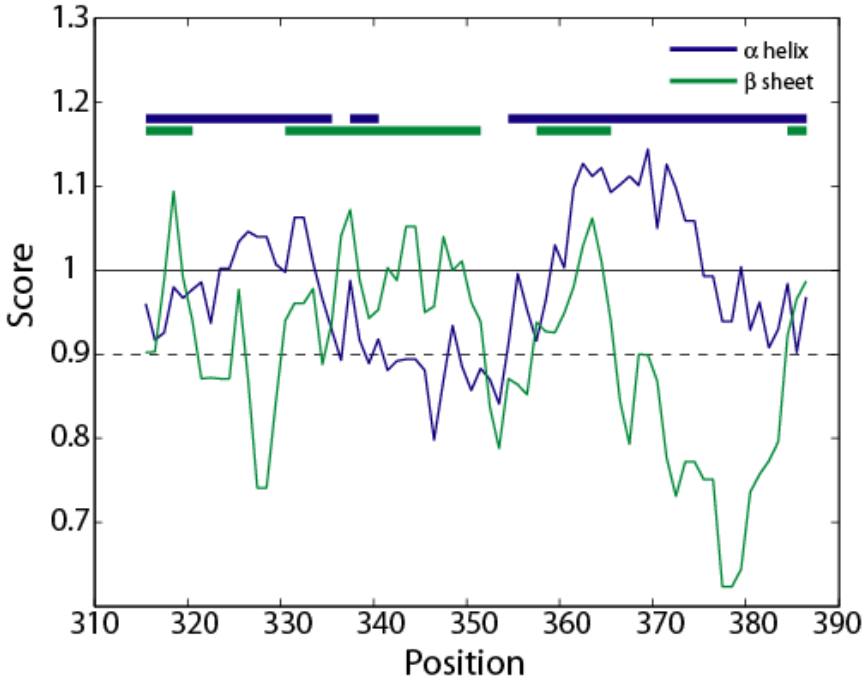

Figure 6.4: Chou-Fasman predictions of α1 intracellular loop domain. Prediction scores for α helix (blue) and β sheet (green) secondary structures calculated from the primary sequence of the α1 intracellular loop domain using the scoring matrix proposed by Chou and Fasman (1978). Dotted line marks the threshold score for positive prediction. Overlaid bars denote stretches of 3 or more residues that were positive for each secondary structure. Prediction shows a strong probability (score ≥ 0.9) of α helix domains associated with both M3 and M4.

(A)

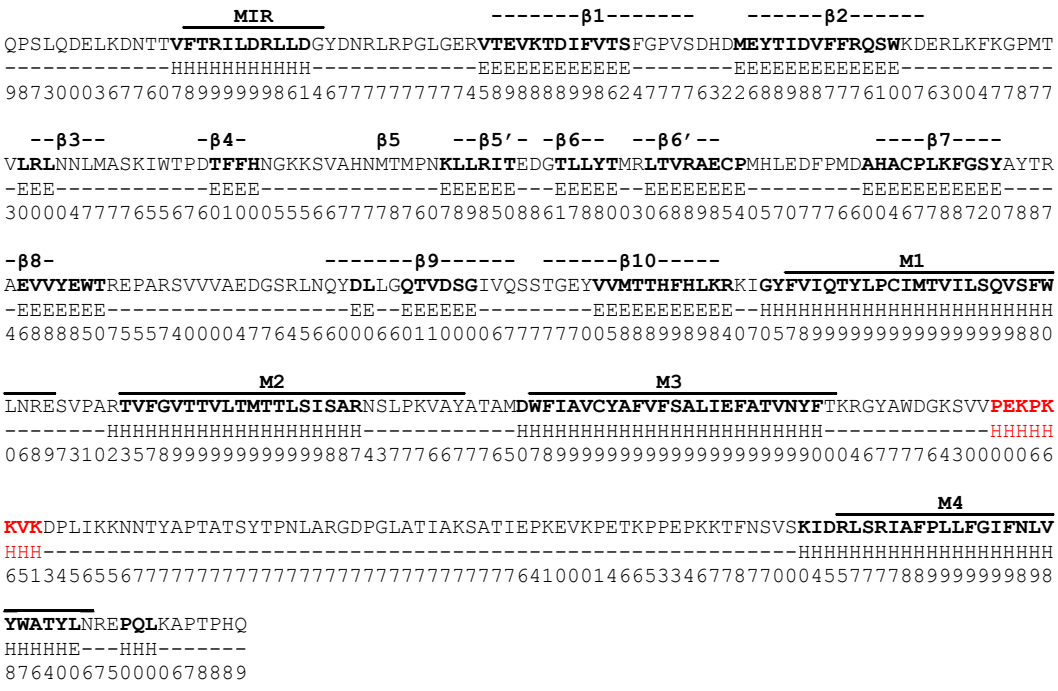

(B)

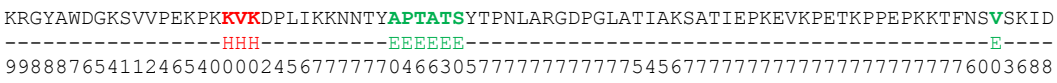

Figure 6.5: Jnet secondary structure prediction. Structure predictions were made with the (A) full length α1 sequence and (B) only the α1 intracellular loop domain as query sequences. Jnet predictions for α helices are denoted with [H] and predictions for β strands are denoted with [E]. The algorithm did not predict any coil [C] domains. The confidence score at each position is shown (9 is the highest and 0 is the lowest possible score). Predictions within the intracellular loop domain are highlighted for α helix (red) and β strand (green). The structure of the extracellular domain predicted by Cromer et al., (2002) and the location of the four α helical transmembrane domains (M1-M4) predicted by Bertaccini and Trudell (2002) are shown to highlight the validity of this method.

6.3.3: Homology model of the α1 subunit

Amino acid sequences vary on a faster evolutionary time scale than tertiary structures (Chothia and Lesk 1986). Therefore, only 30% primary sequence conservation is necessary to construct a viable homology model that may be used to predict functional relationships from structural similarities (Baker and Sali 2001; Lee, Redfern et al. 2007). Models created from *de novo* or *ab initio* methods, when insufficient sequence homology is present, are less accurate; but are still useful tools to predict possible protein structure and give insight into functional relationships (Baker and Sali, 2001).

As I've discussed previously, there is strong primary sequence conservation within the pLGIC superfamily for the extracellular domain and transmembrane domain; the intracellular loop domain, however, is highly variable (Fig. 1.2, Fig. 6.2). The most complete structure to date of a pLGIC is of the nAChR from *T. californica*. But, the nAChR structure only contained partial structural information for the intracellular loop domain (Unwin 2005). Therefore, the template for the intracellular loop domain had to be constructed with *de novo* or *ab initio* methods. *De novo* prediction methods begin with the primary structure of a peptide and perturb the structure until the free energy of the protein reaches a global minima (Baker and Sali 2001). *Ab initio* modeling is limited to small proteins because the process explores the conformational space to determine the best orientation (Dalton and Jackson 2007). These methods reside at the frontier of current modeling techniques and are, therefore, inherently variable. As more unique structures are resolved, prediction methods will improve and increase the resolution and accuracy of structural models.

I used the SwissModel homology modeling server to determine a homology model for the $GABA_AR$ α1 subunit based primarily on the nAChR structure (Fig. 6.6); for specific methods see section 2.5.3. To create a homology model, the SwissModel server undergoes an automated iterative process through the following steps: template selection, query-template sequence alignment, model building, and evaluation. I specified the nAChR structure (PDB: 2BG9) as the primary template. The nAChR from *T. californica* is comprised of four different subunit types with a δ-α-γ-α-β orientation about the pore. Sequence alignments showed a similar level of homology between the α1 subunit and the nAChR subunits with ~20% of identical residues and ~50% similar residues (Table 6.2). Based on the locations of the ligand binding sites, the $GABA_AR$ α1 subunit is most equivalent to the nAChR δ and γ subunits (Mokrab, Bavro et al. 2007). The SwissModel server chose chain C, the *δ* subunit, as the best fit (Fig. 6.6A). Gaps in the sequence alignment between the $GABA_AR$ α1 subunit and the nAChR *δ* subunit were designated as loops that necessitated additional template data. The biggest discrepancies in automated modeling methods are in the loop building process (Dalton and Jackson 2007). I chose to use the SwissModel server because it uses a combination of *ab initio* and database loop building to complete each models when there are discrepancies between the template and query sequence (Schwede, Kopp et al. 2003). Loops were segregated from the template-matching segments and an independent model was built for each; then, the individual segments were assembled as rigid bodies (Schwede, Kopp et al. 2003). Intracellular loop domain loop segments containing 10 or more residues were modeled with fragments from the UniProt database. Therefore, the SwissModel homology model template for the $GABA_AR$ α1 subunit was solely based on known protein structures, which made this method more reliable than a *de novo* loop building method. As the final step, the model was evaluated at every iteration until the lowest energy state was achieved (Bordoli, Kiefer et al. 2009).

The final homology model of the $GABA_AR$ α1 subunit generated in automated-mode closely resembled the nAChR δ subunit (Fig. 6.6). Due to the high degree of familial conservation within the extracellular domain and transmembrane domain, these two domains were nearly identical in the structure and the model (Fig. 6.6C). The $GABA_AR$ α1 model predicted that the intracellular loop domain was composed of two membrane associated α helices in line with the primary axis of the receptor (Fig. 6.6B). The membrane associated α helix continuous with M4 was predicted to be split by a β sheet (Fig. 6.6 and Fig. 6.7). Overlay of the $GABA_AR$ model and nAChR structure showed that the split helix of the model remained in line with the MA helix of the template (Fig. 6.6C). Based on the predictions of the $GABA_AR$ α1 model, I defined three structural subdomains of the intracellular loop domain: two membrane associated (MA) α helices and one β sheet (Fig. 6.8). I named the α helices MA3† and MA4† respectively to denote their proximity to the transmembrane domain segments; the MA domain continuous with M4 was split by the β sheet into two segments, that were designated MA4a and MA4b (Fig. 6.8).

Subunit	α		β		δ		γ	
	%ID	%SM	%ID	%SM	%ID	%SM	%ID	%SM
α1	19.9	51.5	21.0	57.0	20.8	52.3	20.6	51.5
β2s	17.4	53.4	22.5	55.1	19.6	55.8	19.1	52.1
γ2s	20.2	52.5	16.4	44.8	18.3	48.4	17.4	46.3

Table 6.2: Pairwise comparison of nAChR and $GABA_AR$ subunits. Amino acid sequences for *T. californica* nAChR (α, β, δ, γ) and *H. sapiens* $GABA_AR$ (α1, β2s, γ2s) were aligned in pairs with the Needleman-Wunsch algorithm (*nwalign*) in Matlab (The Math Works, Inc.). The percentages of identical (%ID) and similar (%SM) residues were calculated for each alignment.

† The nomenclature for structural subdomains is meant to be distinct from that of functional subdomains. MA3 and MA4 are α helices whereas M3A and M4A nomenclature suggests that each subdomain is merely associated with the M3 and M4 transmembrane domains with no preconception of secondary structure.

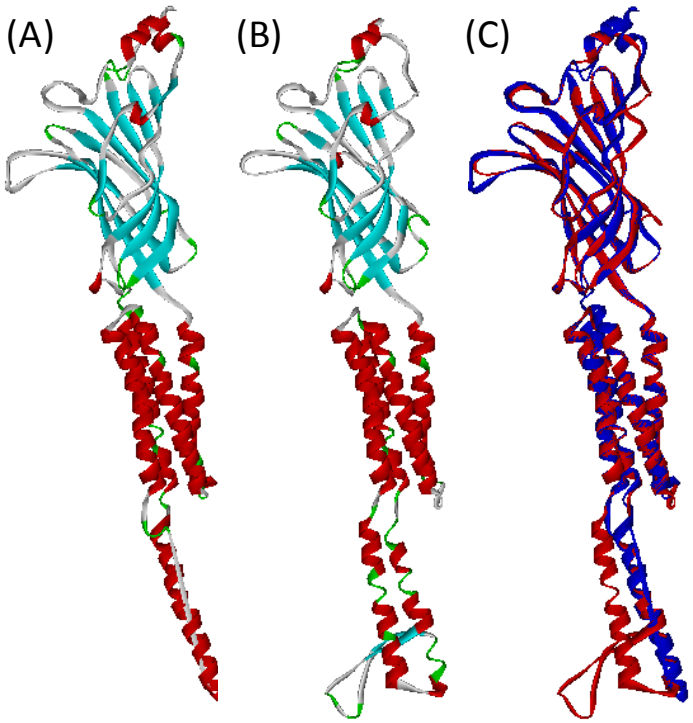

Figure 6.6: Homology model. (A) The *T. californica* nAChR structure (PDB: 2BG9C) was used as the template for generation of (B) the homology model of the $GABA_AR$ α1 subunit. Structures are shown colored according to secondary structure: α helices (red), β strands (cyan), turns (green), and loops (white). (C) Overlaid view of nAChR δ structure (blue) and $GABA_AR$ α1 model (red).

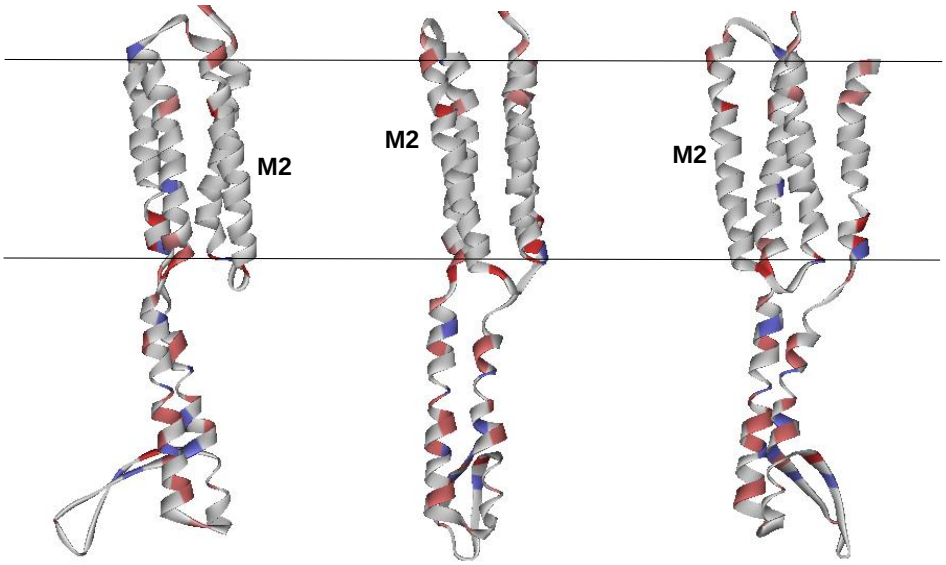

Figure 6.7: Rotated views of the putative intracellular loop domain structure. The extracellular domain is removed for simplicity. The second transmembrane domain (M2) is labeled for orientation and the horizontal lines represent the boundaries of the membrane. The structure is colored electrostatically by pKa with acidic residues (blue) and basic residues (red).

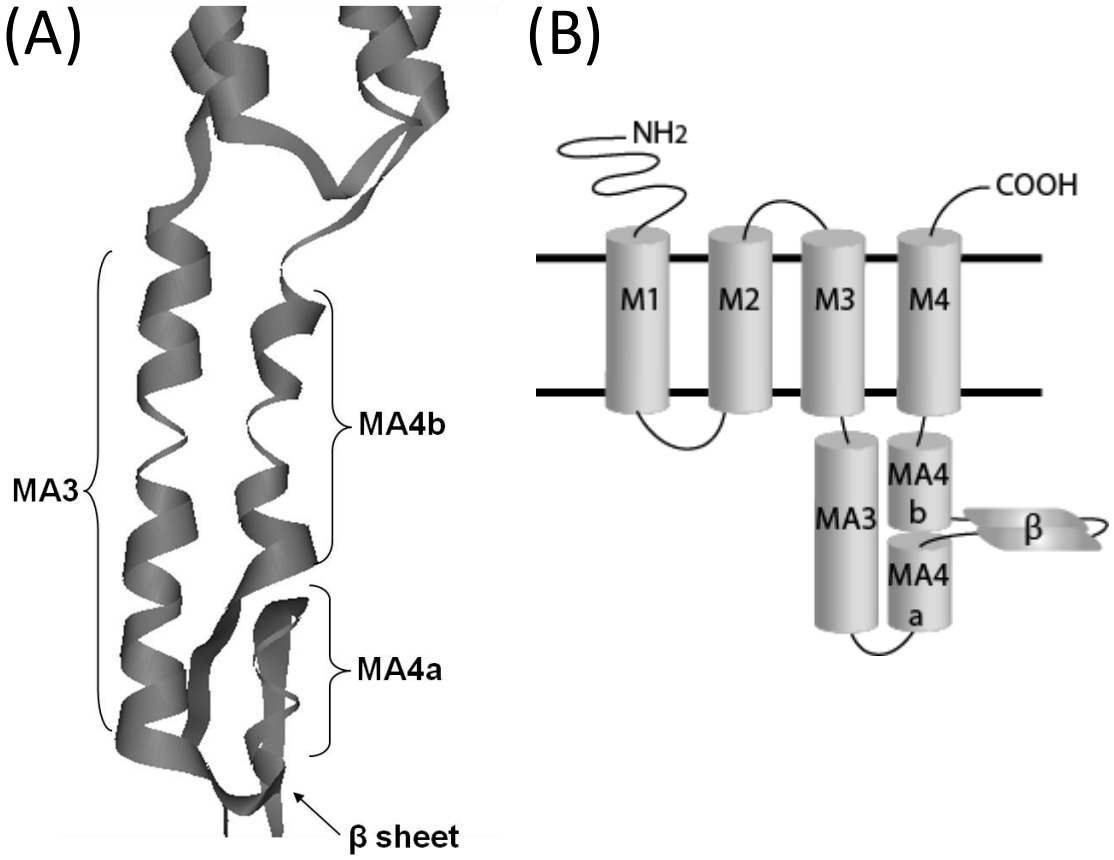

Figure 6.8: Structural subdomains of the intracellular loop domain. (A) Homology model predicted three distinct structural subdomains: two membrane associated α helices (MA3 and MA4) and one β sheet. (B) Schematic of membrane topology for the homology model of the $GABA_AR$ α1 subunit.

6.4: Discussion

Francois Jacob, who shared the 1965 Nobel Prize in Medicine, said, "Nature is a tinkerer, NOT an inventor." Most proteins will gain functions through addition of domains that are based on existing proteins and become larger over evolutionary time; unless there is a special pressure for spatial constraint, such as secretory proteins like the AChBP, which must remain small to allow for vesicular packaging (Fig. 1.4A). The modular nature of protein domains allows for insertions and deletions to occur over time to impart unique characteristics to related proteins. A domain is defined as a section of the protein with a unique function that has evolved separately and folds independently (Lee, Redfern et al. 2007).

The modular nature of pLGIC domains is highlighted in Figure 1.4 which compares the structure of the *T. californica* nAChR to two homologous proteins, the *L. stagnalis* AChBP and a prokaryotic precursor from *G. violaceus* (GLIC). The eukaryotic nAChR contains three protein domains (extracellular, transmembrane, and intracellular loop domains), but the prokaryotic GLIC receptor only contains two domains (extracellular and transmembrane domains). The AChBP is homologous to the extracellular domain of pLGICs and represents a perfect example of nature using an existing structure to perform a different function; the protein is secreted into the synaptic cleft to absorb neurotransmitter and determine the time course of chemical signaling (Brejc et al., 2001). Recently, a chimera comprised of the extracellular domain of GLIC and the transmembrane domain of GlyR α1 has been shown to be functionally gated by protons, as expected for GLIC, but with a chloride conductance, as expected for GlyR (Duret, Van Renterghem et al. 2011) highlighting the modular nature of pLGIC protein domains.

The extracellular domain, or domain homolog, within all three structures is strongly conserved as a β-sheet sandwich structure. Likewise, the transmembrane domain of both membrane bound proteins is conserved with four α-helices in the same transmembrane topology.

Interestingly, prokaryotic homologs to the pLGIC superfamily only contain a very short linker between M3 and M4 (Bocquet, Nury et al. 2009; Hilf and Dutzler 2009; Corringer, Baaden et al. 2010). On the other hand, the intracellular loop domain of eukaryotic pLGICs is a large, variable domain that is known to confer unique functionality; for example, the long isoforms of both the $GABA_AR$ β2 and γ2 subunits contain a unique phosphorylation site (Martin and Olsen, 2000). It is interesting to surmise that evolutionary pressures have promoted divergence of the intracellular loop domain in eukaryotic homologs. These characteristics also suggest that the inclusion and diversity of the intracellular loop domain confers an additional level of functional complexity to address the needs of higher organisms. An understanding of protein domains is a powerful tool that may be used to infer functional relationships between homologous proteins. As we gain knowledge of the structure of the intracellular loop domain, the field will be better able to make functional comparisons within this domain across the pLGIC superfamily.

To begin to fill this knowledge gap, I calculated the structure of the intracellular loop domain of the $GABA_AR$ α1 subunit by three different methods: *de novo* sequence prediction, sequence alignment prediction, and homology modeling with ridged assembly loop building (Fig. 6.9). Comparison of the results from each method highlighted areas of prediction convergence and also showed regions where predictions were more varied. All prediction methods calculated the existence of an α helix near M3; the Jnet algorithm predicted a very short helix with 3-8 residues, but both the Chou-Fasman prediction scale and homology model predicted a ~25 residue helix (Fig. 6.9). A second α helix was predicted to exist near M4; the Chou-Fasman scale predicted a 32 residue helix and the SwissModel server predicted a 13 residue helix, while the Jnet algorithm had no secondary structure prediction for this region of the intracellular loop domain (Fig. 6.9). The biggest discrepancy between the predictions was the putative location of a β sheet; but all three methods predicted at least one β strand near the center of the intracellular loop domain (Fig. 6.9).

Both the Chou-Fasman scale and the PSSM prediction within the Jnet algorithm used a sliding window to determine probability scores for each residue. Sliding window methods take the attributes of local residues into consideration; these methods are more conservative and have the potential to truncate the span of secondary structures. For example, a residue known to be within the center of an α helix will have a higher probability score than a residue on the edge of the structure, because it is surrounded by residues that also have a high probability of residing within an α helix. This shortcoming seemed to affect the Jnet prediction in particular, because it predicted the same structures within a similar span of the intracellular loop domain as the other methods, but the length of each predicted secondary structure was truncated in comparison. There are advantages and disadvantages to all prediction methods, which is why I chose to use multiple approaches.

To benefit from the power of multiple comparisons, I determined a consensus prediction based on all three methods (Fig. 6.9D). My final prediction for the secondary structure of the $GABA_AR$ α1 intracellular loop domain is that there are two membrane associated helices, MA3 and MA4 connected by a short β sheet. A second homology model was generated in the project mode of the SwissModel server. I manually adjusted the target-template alignment to assign the residues of MA4 (between α1(D365) and α1(K383)) to the membrane associated segment in the nAChR structure (Fig. 6.10). The resulting structure showed a broken α helix near M3 and a continuous α helix aligned with M4, with no β strand segment (Fig. 6.10A). Finally I generated a composite model with the N-terminus, M1-M3, and MA3 contributed by the automated-mode model and the C-terminus, MA4 through M4 contributed by the project-mode model (Fig. 6.10B) to best fit the consensus secondary structure predictions of the membrane associated α helices (Fig. 6.9D).

```
(A)   KRGYAWDGKSVVPEKPKKVKDPLIKKNNTYAPTATSYTPNLARGDPGLATIAKSATIEPKEVKPETKPPEPKKTFNSVSKID
      ----HHHHHHHHHHHHHHHHHHHH-HHHH--------------HHHHHHHHHHHHHHHHHHHHHHHHHHHHHHHH------
      ----EEEEE---------EEEEEEEEEEEEEEEEEEEEE-----EEEEEEEE-------------------EEE------

(B1)  KRGYAWDGKSVVPEKPKKVKDPLIKKNNTYAPTATSYTPNLARGDPGLATIAKSATIEPKEVKPETKPPEPKKTFNSVSKID
      ------------HHHHHHHH-------------------------------------------------------HHH
      ---------------------------------------------------------------------------------

(B2)  KRGYAWDGKSVVPEKPKKVKDPLIKKNNTYAPTATSYTPNLARGDPGLATIAKSATIEPKEVKPETKPPEPKKTFNSVSKID
      -----------------HHH-----------------------------------------------------------
      ------------------------------EEEEEE-----------------------------------------E----

(C)   KRGYAWDGKSVVPEKPKKVKDPLIKKNNTYAPTATSYTPNLARGDPGLATIAKSATIEPKEVKPETKPPEPKKTFNSVSKID
      ---HHHHHHHHHHHHHHHHHHHHHHHH--HHHHHHHHH----------------------HHHHHHHHHHHHH---------
      ----------------------------------------EEEEEEEEEEEEEEEEEEEE----------------------

                  MA3              -------β-------          MA4
(D)   KRGYAWDGKSVVPEKPKKVKDPLIKKNNTYAPTATSYTPNLARGDPGLATIAKSATIEPKEVKPETKPPEPKKTFNSVSKID
      ---HHHHHHHHHHHHHHHHHHHHHHHHH---------------HHHHHHHHHHHHHHHHHHHHHHHHHHHHHHHH------
      ----------------------------EEEEEEEEEEEEEE-------------------------------------
```

Figure 6.9: Summary of secondary structure predictions. The secondary structure of the $GABA_AR$ α1 subunit were determined by (A) the Chou-Fasman scale, (B) the Jnet algorithm for both (1) the full length sequence and (2) intracellular loop domain sequence only, and (C) the SwissModel server. Predictions for α helix (red, H), β strand (green, E), or both (blue) structures are highlighted. (D) The consensus prediction of secondary structure was determined by comparing the convergence of each prediction.

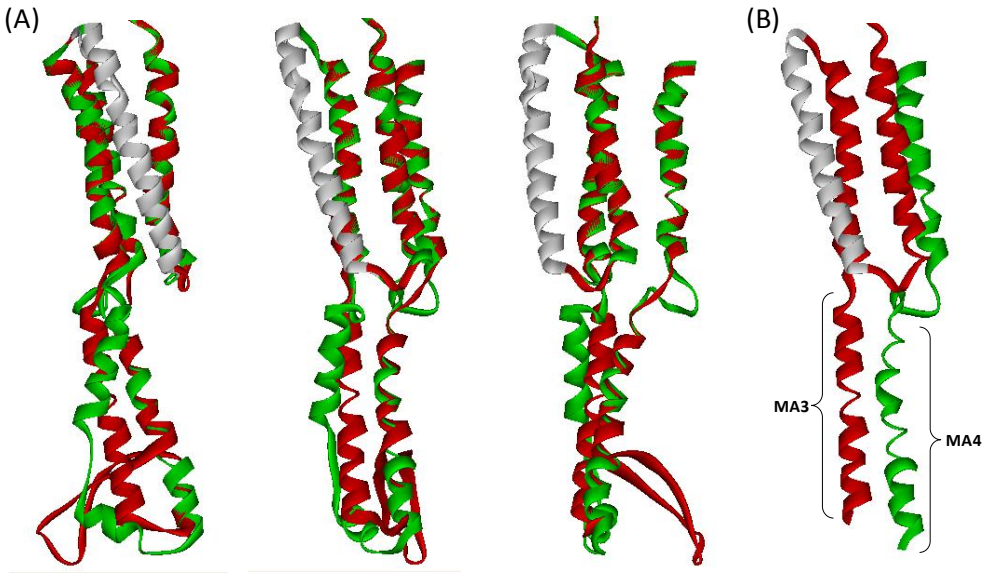

Figure. 6.10: Composite homology model. (A) Rotated views of two homology models generated for the $GABA_AR$ α1 subunit. The M2 segment is colored white for orientation. The two models are overlaid to highlight the differences in the intracellular loop domain predictions. The SwissModel prediction from automated-mode (red) shows a split α helix near M4 and the Swiss model prediction in project-mode (green) was aligned to force a continuous helix. (B) The final composite model shows two α helices in parallel as predicted by comparison of all methods (Fig. 6.9).

6.5: Conclusion

Based on the nAChR structure (Unwin 2005), the MA helices are predicted to line the intracellular windows of the pore. Specific charged residues of the MA helices are predicted to function as ion sensor sites of the permeation pathway and therefore would be expected to face into the aqueous space. Interestingly, the putative β sheet contained the gephyrin binding site (Mukherjee et al., 2010; Tretter et al., 2008). If the orientation of the β sheet is similar to that predicted by the initial homology model, this binding site would be very accessible, oriented away from the main bulk of the protein to limit steric hindrance to gephyrin binding. In conclusion, much can be learned via the structure-function paradigm. Moreover, by combining my experimental findings with theoretical predictions I have provided a structural backbone to support my data. In Chapter 7, I will discuss the similarities and differences between the functional and structural subdomains that have been identified here.

Chapter 7

Discussion

In this final chapter I will integrate the experimental findings reported in Chapters 3-6 to draw a complete picture of the function and structure of the intracellular loop domain of the α1 subunit. I will discuss the implications of my findings for $GABA_AR$ activity and discuss possible caveats to my results. Finally I will propose future directions for this work to continue to shed light on our understanding of the $GABA_AR$.

7.1: Subdomains of the $GABA_AR$ α1 intracellular loop domain

Data presented in Chapter 3 showed that deletion of the α1 intracellular loop domain enhanced the amplitude of macroscopic currents and decreased the apparent affinity of the receptor for GABA. In Chapters 4 and 5, point mutation identified the charged residues which control specific aspects of ion permeation, including relative anion selectivity and current amplitude and rectification, and channel gating, including apparent affinity and desensitization. Two functional subdomains of the $GABA_AR$ α1 intracellular loop domain (M3A and M4A) were identified based on groups of significant changes that were incurred by charge switch mutation (Fig. 7.1A). In Chapter 6, secondary structure predictions identified three structural subdomains of the intracellular loop domain, two α helices (MA3, MA4) and a β sheet (Fig. 7.1B). Overlay of the findings from charge switch mutagenesis onto the model reveals that the functional and structural subdomains overlap (Fig. 7.2). Hereafter I will use the structure nomenclature and refer to the subdomain near M3 as MA3 and the subdomain near M4 as MA4.

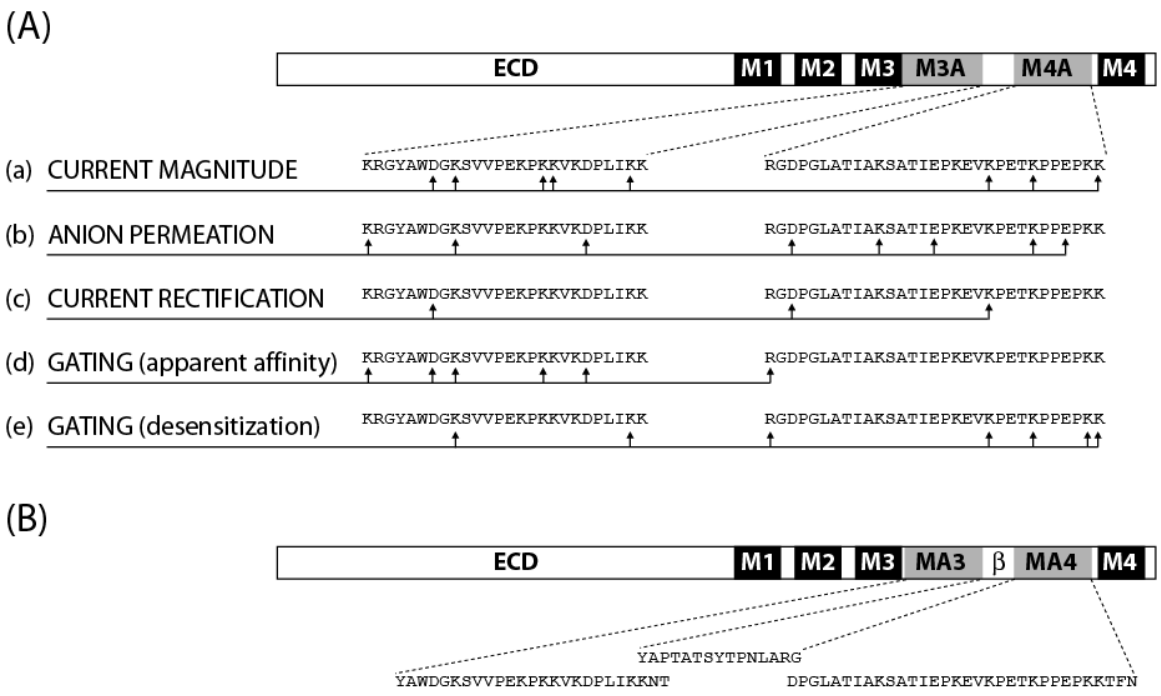

Figure 7.1: Functional and Structural Subdomains of the $GABA_AR$ α1 subunit. Schematic depicting the primary structure of the extracelluar domain (ECD), transmembrane domains (M1-M4), and the intracellular loop domain (ILD). The ILD residues predicted for each subdomain are indicated. (A) Charge switch point mutations that altered specific aspects of $GABA_AR$ function were segregated within two subdomains (M3A, M4A) of the intracellular loop domain. Residues that control the (a) macroscopic current magnitude, (b) relative anion permeability, (c) rectification, (d) apparent affinity and (e) desensitization of GABAergic currents are indicated. (B) Secondary structure predictions identified three subdomains, two α helices (MA3, MA4) split by a β strand (β).

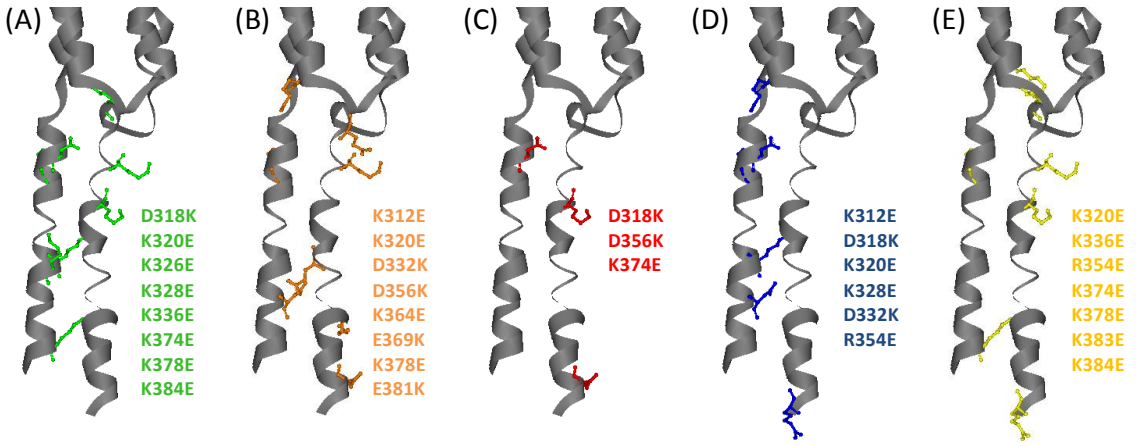

Figure 7.2: Location of integral charged residues. Residues that showed significant control of (A) macroscopic current magnitude (green), (B) relative anion permeability (orange), (C) rectification (red), (D) apparent affinity (blue) and (E) desensitization (yellow) are highlighted on the homology model structure. Mutations of the α1 intracellular loop domain that significantly altered each metric are listed in each panel. The orientation of the structure is such that the viewer is looking from inside the intracellular lumen towards the putative MA domains of the α1 subunit.

7.2: Permeation Pathway

Previous studies have shown that charged residues within the intracellular membrane associated stretch near M4 control channel conductance in the 5-HT_3R, nAChR, and GlyR members of the pLGIC superfamily (Davies, Pistis et al. 1999; Kelley, Dunlop et al. 2003; Hales, Dunlop et al. 2006; Livesey, Cooper et al. 2008; Carland, Cooper et al. 2009). Results presented here provide the first evidence that residues within the intracellular loop domain control the amplitude of currents through the $GABA_A$R. Eight mutations, α1(D318K), α1(K320E), α1(K328E), α1(K329E), α1(K336E), α1(K374E), α1(K378E), and α1(K384E), increased the maximal amplitude of macroscopic currents (Fig. 7.1Aa, Fig. 7.2A). The previous studies have focused on intracellular residues near M4 (Kelley, Dunlop et al. 2003; Hales, Dunlop et al. 2006; Carland, Cooper et al. 2009), but this data provides the first evidence that intracellular loop domain residues near M3 contribute to ion permeation. Furthermore, the α1(K378E) mutation decreased the amplitude of single channel currents by ~30%. However, this mutation significantly increased the surface expression of the α1 subunit which masked the decrease in conductance from macroscopic analysis (Chapter 4). Additional charged residues within the intracellular loop domain may control single channel conductance, but were false negatives in this study due to the nature of whole-cell currents. Future experiments are necessary to fully characterize the single channel conductance of charge switch point mutations within the α1 subunit, as well as, the other $GABA_A$R subunits. In sum, results presented in this dissertation show that charged residues within BOTH membrane associated subdomains are critical determinants of current magnitude through the $GABA_A$R.

Charge switch mutations within the $GABA_A$R α1 intracellular loop domain did not switch the charge selectivity of the pore but eight mutations shifted the relative permeability of anions, α1(K312E), α1(K320E), α1(D332K), α1(D356K), α1(K364E), α1(E369K), α1(K378E) and, α1(E381K) (Fig. 7.1Ab, Fig. 7.1B). These residues positively shifted the reversal of GABAergic

currents in experimental conditions where the extracellular concentration of chloride was reduced by replacing the anion with gluconate. Gluconate has a 5.85 Å diameter and has been previously reported to permeate GABA-gated channels ~10% as effectively as the smaller chloride ion, which has a 3.60 Å diameter (Robinson and Stokes 1965; Fatima-Shad and Barry 1993; Jensen, Pedersen et al. 2005). In these studies, the WT receptor exhibited a relative gluconate permeability of 13%. Significant shifts in reversal potential caused by point mutations ablated the channel's permeability to gluconate (Chapter 4). These residues reside within BOTH of the membrane associated subdomains (Fig. 7.1B). According to the nAChR structure, membrane associate helices (homologous to MA4) are predicted to line the windows of the intracellular vestibule (Unwin 2005). It is not unreasonable to surmise that charge switch mutations decreased the effective diameter of intracellular windows to prevent gluconate permeation. In this light, results suggest that residues within both MA3 and MA4 interact with permeant ions to define the effective diameter of the pore AND both MA3 and MA4 are then predicted to line the windows of the intracellular vestibule.

I also used analysis of the rectification profile of the $GABA_AR$ as a tool to identify pore lining residues. In particular, α1(D318K), α1(D356K) and α1(K374E) enhanced outward rectification of the IV relationship (Fig. 7.1Ac, Fig. 7.2C). Until a structure is resolved for the $GABA_AR$ with x-ray crystallography we must rely on homology modeling to predict functional relationships. The results of direct analysis of intracellular loop domain residues, presented in this dissertation, provide empirical data to inform future model building. The charged residues that control current amplitude, anion permeation and current rectification (Fig. 7.1A) are predicted to electrostatically define the permeation pathway and therefore must be accessible to ions within the pore lumen.

7.3: Gating elements

Data presented in Chapter 3 showed that deletion of the intracellular loop domain of the $GABA_AR$ α1 subunit decreased the apparent affinity of the receptor, which was most likely caused by a gating impairment NOT a change in ligand binding. Comparison of structures in the open and closed conformations indicated a "twist deformation" mechanism of channel gating (Corringer, Baaden et al. 2010; Fig. 7.3). Residues within the pre-M1 segment, M2-3 linker, and loops 2 and 7 at the interface of the extracellular domain and transmembrane domain (O'Shea and Harrison 2000; Kash, Jenkins et al. 2003; Kash, Trudell et al. 2004; Xiu, Hanek et al. 2005; Keramidas, Kash et al. 2006; Mercado and Czajkowski 2006) translate the energy of ligand binding to open the channel gate. Furthermore, chimera experiments have localized the differences in gating between subunits to the C-terminus (Akk and Steinbach 2000; Fisher 2004). These results narrow the findings of Fisher (2004), Akk and Steinback (2000) and suggest that the intracellular loop domain confers the subtle differences in gating between homologous subunits.

Results presented in Chapter 4 identified specific residues that contribute to intracellular control of gating. Interestingly the different components of gating were segregated within discrete subdomains of the intracellular loop domain. The apparent affinity component of gating was mediated by residues within the MA3 sudomain (Fig. 7.1Ad, Fig. 7.2D). Six charge switch mutations decreased the apparent affinity of the receptor for GABA: α1(K312E), α1(D318K), α1(K320E), α1(K328E), α1(D332K), and α1(R354E). One potential explanation for this finding is that the MA3 subdomain moves to allow channel gating. Residues within the M3 transmembrane segment are more accessible to covalent modification after GABA application which suggests that M3 moves during gating (Williams and Akabas 1999). Results presented here suggest that MA3 may also move to gate the channel.

As I have discussed throughout this dissertation, ligand binding and channel gating are intrinsically linked. The $GABA_AR$ protein performs dual functions to both detect and respond to a chemical signal. It is very difficult to define the separate components of $GABA_AR$ function experimentally. The three separate domains of pLGIC subunits are modular and retain individual functionality when combined in chimera constructs (Duret, Van Renterghem et al. 2011; Goyal, Salahudeen et al. 2011). Therefore, deletion of the intracellular loop domain (or point mutations within the intracellular loop domain) was not predicted to alter the orthosteric binding site within the extracellular domain. I have shown through secondary measures that changes in EC_{50} values were caused by changes in gating not binding. In particular the α1(K312E) mutation decreased the relative agonist efficacy of the receptor indicative of a gating impairment (Chapter 4). But, without direct binding data it is difficult to fully identify a cause. However, even binding assays are hampered by the interconnected nature of binding and gating. Ligand binding induces a conformation change in the protein to elicit channel gating that immediately alters agonist affinity (Colquhoun 1998). Thus, a gating impairment will also alter experimental measures of ligand affinity, i.e. binding assays, because the ligand will have a different affinity for each conformation state (Colquhoun 1998). Jones and Westbrook (1995) proposed that desensitization segregates the channel into agonist bound states that must transition through an open state before unbinding. Changes in gating will shift the probability for the receptor to occupy different kinetic states and have the potential to "trap the agonist" in the bound state. Therefore, binding affinity values would also be confounded by gating mutations.

The desensitization component of gating was predominantly controlled by residues within the MA4 subdomain (Fig. 7.1Ae, Fig. 7.2E). Seven charge switch mutations enhanced desensitization: α1(K320E), α1(K336E), α1(R354E), α1(K374E), α1(K378E), α1(K383E), and α1(K384E). Taken together, these results suggest that the main channel gate and the desensitization gate are unique structures. It is not unreasonable to surmise that the MA4 α helix

serves as the desensitization gate. Upon prolong application of agonist the $GABA_AR$ transitions into the non-conducting desensitized state. Expansion of the gating model proposed by Corringer et al., (2010) to include the intracellular loop domain shows how a "twist" conformation change could open and close the windows of the intracellular vestibule to control ion flow (Fig. 7.3). It is easy to envision how translocation of M3 twists MA3 to open the windows of the intracellular vestibule along with the main channel gate within M2 (Fig. 7.3B). Then if agonist binding persists, the membrane associated α helix near M4 (MA4) twists further to close the windows (Fig. 7.3B). In this scheme, the extracellular and transmembrane domains would remain in an active-like conformation while the channel is in the desensitized, non-conducting state (Fig. 7.3). This agrees with kinetic models of receptor activity which predict that the channel transitions from desensitization back through an open state before ligand unbinding can occur (Jones and Westbrook 1995).

The α1(R354E) mutation significantly increased both EC_{50} and the rate of desensitization (Chapter 4). This residue is predicted to reside at the base of MA4, furthest from the membrane (Chapter 6). The homology model predicts that the two membrane associated α helices are in parallel and run along the central axis of the receptor. Therefore, it is interesting to suppose that the α1(R354) position serves as a pivot to allow all of the structural rearrangements necessary to open and close the intracellular windows of the pore (Fig. 7.3).

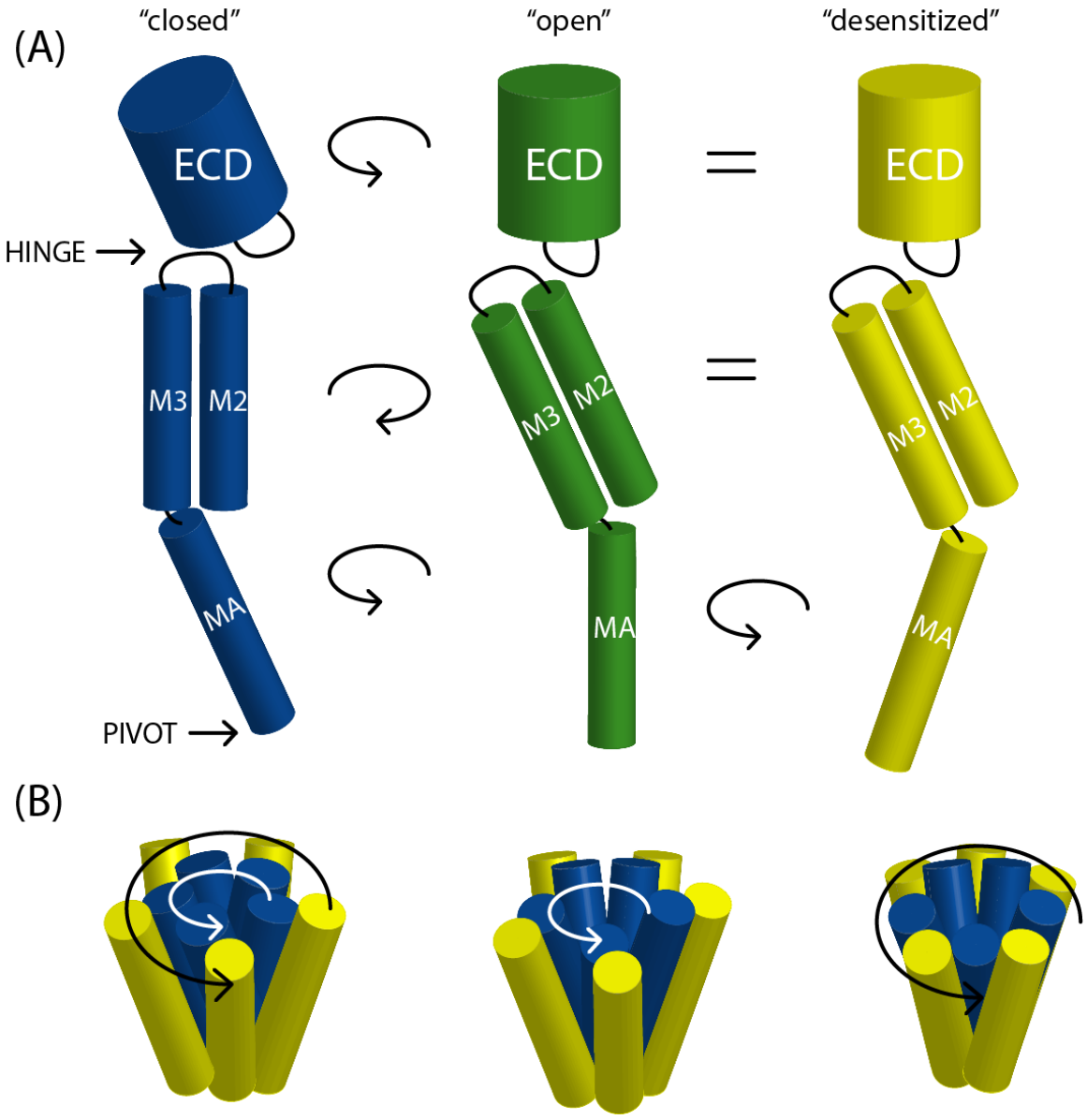

Figure 7.3: A putative desensitization gate. The resolved structures of prokaryotic pLGIC homologs suggest a twist deformation gating mechanism. (A) Schematic of the orientation of the extracellular domain (ECD) and α helices of the transmembrane domain (TMD: M2, M3) and intracellular loop domain (ILD: MA) of one subunit in conducting (open) and non-conducting states (closed, desensitized). Ligand binding within the ECD twists the TMD counter-clockwise about the central axis to open the pore. If the ILD serves as the desensitization gate, then the MA helix may twist closed while the orientation of ECD and TMD is unperturbed. (B) Putative orientation of the ILD in conducting and non-conducting states. The intracellular windows are closed in the resting and desensitized states to prevent ion flow. MA3 (blue) twists clockwise to open intracellular windows in conducting state and allow ion flow through the pore. MA4 (yellow) twists further to close intracellular windows to prevent ion flux in the desensitized receptor. *Adapted from Corringer et al. (2010) to include the ILD.*

The significant changes in apparent affinity and desensitization caused by charge switch mutagenesis suggest that intracellular loop domain control of channel gating is mediated through electrostatic interactions. Data presented in Chapter 5 showed that channel gating is, in fact, chloride dependent. The apparent affinity of the receptor for GABA was decreased and desensitization was enhanced in low chloride conditions. The reversal potential is shifted when the concentration of permeant ions is not symmetrical; therefore, I measured desensitization and calculated the concentration-response relationship under equivalent electrochemical driving force (Chapter 5). Furthermore, channel gating was altered when either the intracellular or extracellular chloride concentration was decreased. This suggests that the chloride dependence of $GABA_AR$ gating is controlled by structures within the pore.

The windows of the intracellular vestibule are predicted to be the same size as a hydrated ion (Unwin 2005). Charged residues that line the windows are therefore predicted to coordinate the appropriate ion to facilitation permeation (Fig. 7.4). Charge switch mutations did not only disrupt ion permeation, but also changed channel gating. Taken together, the interaction between chloride ions and charged residues of the intracellular loop domain is predicted to be an integral gating element. In particular, all of the MA4 residues that control desensitization are basic. It is easy to picture how positively charged side chains could coordinate an anion within the window to stabilize the open conformation (Fig. 7.4A). If we hold this to be true, then in the low chloride condition, no ion is present in the window and the repulsive force from like charges promotes rearrangement of the α helices to twist closed and stagger the charges (Fig. 7.4B). Likewise, charge switch point mutations would disrupt this electrostatic interaction and eliminate anion coordination to promote closure of the windows (Fig. 7.4C).

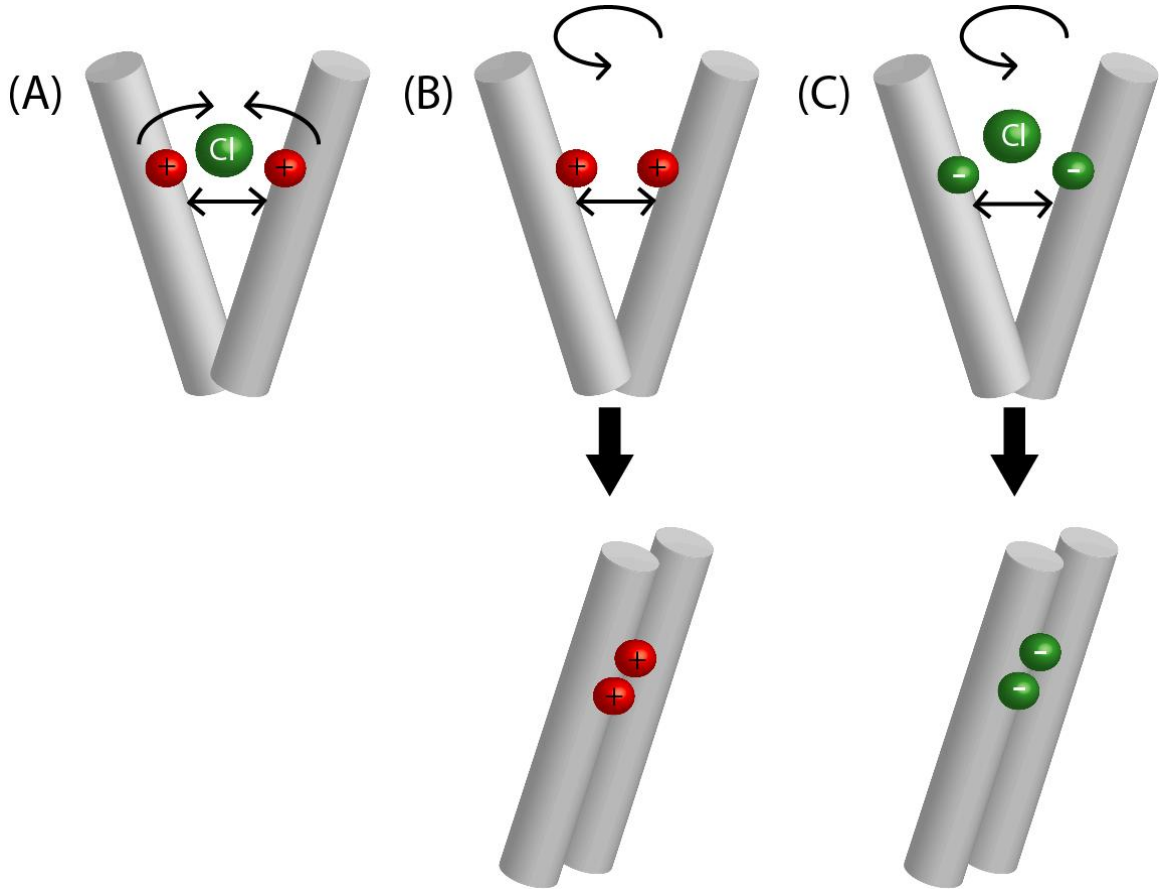

Figure 7.4: Chloride ions stabilize the open state. Schematic of the putative intracellular entrances to the permeation pathway in (A) normal conditions, (B) low chloride conditions, and (C) with charge switch mutation of the ion sensor. Charged residues at conserved positions along the membrane associate helix domain of the intracellular loop domain may serve as ion sensors to coordinate permeant chloride ions and stabilize the open, conduction conformation of the ion channel. In the absence of chloride (B) or when the ion sensor has been mutated (C) repellent charges will close the intracellular windows via a rearrangement of the intracellular vestibule.

7.4: Conclusion

Further work is necessary to investigate the contribution of the intracellular loop domain of each $GABA_AR$ subunit to channel activity. The windows of the intracellular vestibule reside at subunit interfaces; therefore, each side is contributed by a different subunit in the heteromeric receptor. Analysis of the interaction energy between chloride ions and the pore within a homology model of the $GABA_AR$ predicted that the intracellular windows establish very different paths to ion permeation (Mokrab, Bavro et al. 2007). Each subunit is known to confer unique kinetics (Lavoie, Tingey et al. 1997; Fisher 2004; Picton and Fisher 2007), pharmacology (Pritchett, Sontheimer et al. 1989; Franks and Lieb 1994; Krasowski and Harrison 1999; Franks 2008), and expression (McKernan and Whiting 1996; Essrich, Lorez et al. 1998; Connolly 2008) to the $GABA_AR$. Likewise, the function of the intracellular loop domain within each subunit is predicted to be unique.

To data, no structure has been solved for the $GABA_AR$. However, structures of homologous proteins provide a template for homology modeling. Direct study of protein domains, such as in the experiments presented here, is necessary to inform future model building and refinement of structures for the $GABA_AR$. Structure predictions through homology modeling or direct analysis of amino acid sequence supply a powerful platform to make predictions of protein function. As more structures are resolved, modeling and prediction techniques will continue to improve. Further work is necessary to solve the structure of the $GABA_AR$ in order to confirm predictions based on functional measures.

Studies presented in this dissertation have identified subdomains of the $GABA_AR$ α1 intracellular loop domain that control unique aspects of channel function and possess defined

secondary structure. Structure predictions forecast that the intracellular loop domain is composed of two membrane associated α helices, MA3 and MA4, which are separated by a β strand. Empirical results show that charged residues within the α1 intracellular loop domain control ion permeation and channel gating. Residues within both MA3 and MA4 control current amplitude and anion permeation, while residues within MA3 determine agonist dependent channel gating and residues within MA4 mediate the rate of desensitization. Taken together, this work is critical to define the role of the intracellular loop domain in $GABA_AR$ function and thereby expand our knowledge of inhibitory neurotransmission.

Appendix A: Solution Recipes

I1: Standard Intracellular Saline

Final Concentration	Volume	Stock Concentration
120 mM KCl	24 ml	1 M KCl
2 mM $MgCl_2$	800 µl	0.5 M $MgCl_2$
10 mM EGTA	20 ml	100 mM EGTA
10 mM HEPES	2 ml	1 M HEPES
pH 7.2 with 5 M NaOH; osmolarity to 315 mOsm*; Total volume to 200 mL MilliQ water		

I2: Low Chloride Intracellular Saline

Final Concentration	Volume	Stock Concentration
68 mM KCl	13.6 ml	1 M KCl
48 mM potassium gluconate	9.6 ml	1 M K gluconate
2 mM $MgCl_2$	800 µl	0.5 M $MgCl_2$
10 mM EGTA	20 ml	100 mM EGTA
10 mM HEPES	2 ml	1 M HEPES
pH 7.2 with 5 M NaOH; osmolarity to 315 mOsm*; Total volume to 200 mL MilliQ water		

*Adjust osmolarity with sucrose or MilliQ water accordingly.

E1. Standard Extracellular Saline

Final Concentration	Amount	Stock Concentration
160 mM NaCl	37.75 g	-
10 mM HEPES	9.5 g	-
6 mM *D*-glucose	4 g	-
3 mM KCl	12 ml	1 M KCl
1 mM $MgCl_2$	4 ml	1 M $MgCl_2$
1.5 mM $CaCl_2$	6 ml	1 M $CaCl_2$
pH 7.4 with 6 M HCl; osmolarity to 325 mOsm*; Total volume to 4 L MilliQ water		

E2: Low Chloride Extracellular Saline

Final Concentration	Amount	Stock Concentration
5 mM NaCl	1.17g	-
155 mM sodium gluconate	135 g	-
10 mM HEPES	9.5 g	-
6 mM *D*-glucose	4 g	-
3 mM KCl	12 ml	1 M KCl
1 mM $MgCl_2$	4 ml	1 M $MgCl_2$
1.5 mM $CaCl_2$	6 ml	1 M $CaCl_2$
pH 7.4 with 6 M HCl; osmolarity to 325 mOsm*; Total volume to 4 L MilliQ water		

E3: Low Sodium Extracellular Saline

Final Concentration	Amount	Stock Concentration
14 mM NaCl	3.27 g	-
146 mM N-methyl-*D*-glucamine	114 g	-
10 mM HEPES	9.5 g	-
6 mM *D*-glucose	4 g	-
3 mM KCl	12 ml	1 M KCl
1 mM $MgCl_2$	4 ml	1 M $MgCl_2$
1.5 mM $CaCl_2$	6 ml	1 M $CaCl_2$
pH 7.4 with 6 M HCl; osmolarity to 325 mOsm*; Total volume to 4 L MilliQ water		

*Adjust osmolarity with sucrose or MilliQ water accordingly.

Appendix B: Pipette Programs

I. Whole-cell recordings

Sutter P-97	Heat	Pull	Velocity	Time
Ramp test				
Pressure=500	ramp +10	5	15	80
	ramp +10	5	15	80
	ramp +10	5	15	80
	ramp	5	55	80
Resistance: 2-5 MΩ				

II. Single channel recordings

Narishige PC-10		
"Step 2"	heater 1	79.8
	heater 2	43.4
Sylgard & Fire Polish		
Resistance: 8-12 MΩ		

Appendix C: pClamp Parameters for Data Acquisition

DRCup_1-10_10s

Parameters to generate the concentration response relationship from solutions in tubes 1-10.

Trial: 1
Sweeps: 8
Duration: 10.24 s
Sampling Rate: 200 Hz
Samples: 2048

Wave 1: analog waveform, epochs
Analog out: Cmd 1

Type	Step	Step	Step
level	1	2	1
Δlevel	0	1	0
interval	200	400	hold
time	1 s	2 s	7.24 s

IVramp_1-10_10s

Parameters used to generate the IV relationship across the concentration response relationship from solutions in tubes 1-10.

Trial: 1
Sweeps: 8
Duration: 10.24 s
Sampling Rate: 200 Hz
Samples: 2048

Wave 1: analog waveform, epochs
Analog out: Cmd 1

Type	Step	Step	Step
level	1	2	1
Δlevel	0	1	0
interval	200	400	hold
time	1 s	2 s	7.24 s

Wave 0: analog waveform, epochs
Analog out: Cmd 1

Type	Off	Ramp	Ramp	Off	Ramp	Ramp	Off
level	0	120	0	0	120	0	0
Δlevel	0	0	0	0	0	0	0
interval	500	50	50	1100	50	50	hold
time	2.5 s	0.25 s	0.25 s	5.5 s	0.25 s	0.25 s	1.24 s

Appendix D: Matlab Scripts

[1] norm_drc
Fit concentration response data to Hill Equation

[2] DZ
Fit portion of trace to determine desensitization tau

[3] norm_iv1
Subtract baseline ramp and extract IV relationship
Interpolate reversal potential values

[4] RI
Determine rectification index values and rectification profile

[5] norm_iv2
Subtract baseline ramp and extract IV relationship for paired data set
Interpolate reversal potential values and determine relative shift in reversal potential

[6] Statistics

[7] Sequence Alignments

[1] norm_drc

```
g=fittype('a*x+b');
A=dir('*.abf');
for z=1:length(A)
for n=1:8
    %load files
    D(:,n)=import_abf2(A(z).name,n);
    %leak subtraction
    T=[0:.005:10.235]';
    ydata=[D(1:81,n); D(end-81:end,n)];
    xdata=[T(1:81,1); T(end-81:end,1)];
    nm=fit(xdata,ydata,g,'Startpoint',[1,1]);
    y=nm.a*T(:,1)+nm.b;
    Dnew(n,:)=D(:,n)-y;
    S(z,n,:)=Dnew(n,:);
end
%plot each trace
figure;plot(T,squeeze(S(z,:,:)));
end
%plot average trace
figure;plot(T,squeeze(mean(S,1)),'k');

%generate DRC and graph
for s=1:z;
for n=1:8;
    Smin(s,n)=min(S(s,n,:));     %I
end
    Speak(s,1)=min(Smin(s,:));      %Imax
    Sp(s,:)=Smin(s,:)./Speak(s,1);  %I/Imax
end

%define Concentration [0.3,1,3,10,30,100,300,1000]
str=input('Concentration range []: ');
Conc=str;
Clog=log10(Conc);

%define the Hill Equation as a fit type
ec=fittype('m*(x^h/(x^h+e^h))');  %x is defined below as t, it is the
log10 of GABA concentration
opts2=fitoptions(ec);           %e=EC50; h=hill slope; m=Imax
opts2.Lower=[0 0 0];  %[e h m]
opts2.Upper=[5000 5000 10000];
opts2.Startpoint=[20 1.7 0];

for s=1:z;
Sdrc=fit(Conc',Sp(s,:)',ec,opts2);
S_EC(s,1)=Sdrc.e; %EC50
S_EC(s,2)=Sdrc.h; %hill slope
S_EC(s,3)=Sdrc.m*Speak(s,:); %Imax
end
Sp_mean=mean(Sp,1);Sp_sem=std(Sp)/sqrt(z);
```

```
t=logspace(-1,4,100);
T=log10(t);

Sdrc=fit(Conc',Sp_mean',ec,opts2);
YS=Sdrc.m*(t.^Sdrc.h./(t.^Sdrc.h+Sdrc.e^Sdrc.h));

%plot concentration response with data points and errorbars
figure;plot(T,YS,'k','LineWidth',1);hold on;
errorbar(Clog,Sp_mean,Sp_sem,'ko','LineWidth',1,
'MarkerFaceColor','k');
    set(gca, 'XTick',Clog);
    set(gca, 'XTickLabel',Conc);
    set(gca, 'XLim',[-1 3.5]);
```

[2] DZ

```
g=fittype('a*x+b');
A=dir('*.abf');
q=length(A);
S=NaN(q,8,2048);
D=NaN(2048,8); Dnew=NaN(8,2048);
for z=1:q
for n=1:8
    %load files
    R=import_abf(A(z).name,n,0.005);
    %leak subtraction
    D(:,n)=R(:,2);
    T=R(:,1);
    ydata=[D(1:81,n); D(end-81:end,n)];
    xdata=[T(1:81,1); T(end-81:end,1)];
    nm=fit(xdata,ydata,g,'Startpoint',[1,1]);
    y=nm.a*T(:,1)+nm.b;
    Dnew(n,:)=D(:,n)-y;
    S(z,n,:)=Dnew(n,:);
end
end

%normalize each trace to Imax of trace
Smin=NaN(q,8);Speak=NaN(q,1);
SP=NaN(q,8,2048);Sp=NaN(q,8,2048);
Sm=squeeze(mean(S,1));
for s=1:q;
for n=1:8;
    Smin(s,n)=min(S(s,n,:));      %I
    SP(s,n,:)=S(s,n,:)./3.3026e+003;  %I/I_WT

    M(1,n)=min(Sm(n,:));
    SM(n,:)=Sm(n,:)./-M(1,n);
end
    Speak(s,1)=min(Smin(s,:));       %Imax
    Sp(s,:,:)=S(s,:,:)./-Speak(s,1);  %All/Imax
end
SPm=squeeze(mean(SP,1));
Spm=squeeze(mean(Sp,1));
```

```
%select portion to fit
%200ms after GABA onset to 200ms before GABA off
Sd=Sp(:,:,500:700);
t=T(1:201,:);
Dz=NaN(s,3);

str=input(sweep #?);
n=str;


for s=1:q;
    %fit with exp2 'a*exp(b*x)+c*exp(d*x)'
    DD=dfit(t,squeeze(Sd(s,n,:)));
    %determine weighted tau '(a*b+c*d)/(a+c)'
    Dz(s,1)=DD.b;Dz(s,2)=DD.d;
    Dz(s,3)=((DD.a*DD.b)+(DD.c*DD.d))/(DD.a+DD.c);
end

Sm=squeeze(mean(Sd(:,n,:),1));
DD_mean=dfit(t,Sm);
((DD_mean.a*DD_mean.b)+(DD_mean.c*DD_mean.d))/(DD_mean.a+DD_mean.c)
figure;plot(T,SPm(n,:),'k');
figure;plot(T,SM(n,:),'k');
```

```
function cf_=dfit(t,Sdd_11)
%CREATEFIT    Create plot of datasets and fits
%   CREATEFIT(T,SDD_11)
%   Creates a plot, similar to the plot in the main curve fitting
%   window, using the data that you provide as input.  You can
%   apply this function to the same data you used with cftool
%   or with different data.  You may want to edit the function to
%   customize the code and this help message.
%
%   Number of datasets:  1
%   Number of fits:  1


% Data from dataset "Sdd_11 vs. t":
%    X = t:
%    Y = Sdd_11:
%    Unweighted
%
% This function was automatically generated on 27-Apr-2010 15:56:34

% Set up figure to receive datasets and fits
f_ = figure;
figure(f_);
set(f_,'Units','Pixels','Position',[617 109 680 484]);
legh_ = []; legt_ = {};   % handles and text for legend
xlim_ = [Inf -Inf];       % limits of x axis
ax_ = axes;
set(ax_,'Units','normalized','OuterPosition',[0 0 1 1]);
set(ax_,'Box','on');
axes(ax_); hold on;


% --- Plot data originally in dataset "Sdd_11 vs. t"
t = t(:);
Sdd_11 = Sdd_11(:);
h_ = line(t,Sdd_11,'Parent',ax_,'Color',[0.333333 1 0.666667],...
    'LineStyle','none', 'LineWidth',1,...
    'Marker','.', 'MarkerSize',12);
xlim_(1) = min(xlim_(1),min(t));
xlim_(2) = max(xlim_(2),max(t));
legh_(end+1) = h_;
legt_{end+1} = 'Sdd_11 vs. t';

% Nudge axis limits beyond data limits
if all(isfinite(xlim_))
    xlim_ = xlim_ + [-1 1] * 0.01 * diff(xlim_);
    set(ax_,'XLim',xlim_)
else
    set(ax_, 'XLim',[-0.01, 1.01]);
end


% --- Create fit "fit 4"
ok_ = isfinite(t) & isfinite(Sdd_11);
if ~all( ok_ )
    warning( 'GenerateMFile:IgnoringNansAndInfs', ...
        'Ignoring NaNs and Infs in data' );
```

```
end
st_ = [-0.6424073644000492 -0.95636415432561961 -0.01947664708425649
1.1707375832684273 ];
ft_ = fittype('exp2');

% Fit this model using new data
cf_ = fit(t(ok_),Sdd_11(ok_),ft_,'Startpoint',st_);

% Or use coefficients from the original fit:
if 0
    cv_ = { -0.64765014429525702, -0.93449372685018117, -
0.013637918394817023, 1.4002926067615225};
    cf_ = cfit(ft_,cv_{:});
end

% Plot this fit
h_ = plot(cf_,'fit',0.95);
legend off;  % turn off legend from plot method call
set(h_(1),'Color',[0.333333 0.333333 0.333333],...
    'LineStyle','-', 'LineWidth',2,...
    'Marker','none', 'MarkerSize',6);
legh_(end+1) = h_(1);
legt_{end+1} = 'fit 4';

% Done plotting data and fits.  Now finish up loose ends.
hold off;
leginfo_ = {'Orientation', 'vertical'};
h_ = legend(ax_,legh_,legt_,leginfo_{:}); % create and reposition
legend
set(h_,'Units','normalized');
t_ = get(h_,'Position');
t_(1:2) = [-0.0237745,0.87252];
set(h_,'Interpreter','none','Position',t_);
xlabel(ax_,'');               % remove x label
ylabel(ax_,'');               % remove y label
```

[3] norm_iv1

```
g=fittype('a*x+b');
A=dir('*.abf');
q=length(A);
Snew=NaN(q,8,2048);
D=NaN(2048,8); Dnew=NaN(8,2048);
for z=1:q
for n=1:8
    R=import_abf(A(z).name,n,0.005);
    %leak subtraction
    D(:,n)=R(:,2);
    T=R(:,1);
    ydata=[D(1:81,n); D(end-81:end,n)];
    xdata=[T(1:81,1); T(end-81:end,1)];
    nm=fit(xdata,ydata,g,'Startpoint',[1,1]);
    y=nm.a*T(:,1)+nm.b;
    Dnew(n,:)=D(:,n)-y;
    Snew(z,n,:)=Dnew(n,:);
    %subtract baseline IV
    Snew(z,n,533:633)=Snew(z,n,533:633)-Snew(z,n,1733:1833);
    Snew(z,n,1733:1833)=Snew(z,n,1733:1833)-Snew(z,n,1733:1833);
end
end

%select iv portion of trace
S=NaN(q,8,101);
for a=1:q
for n=1:8;
    S(a,n,:)=Snew(a,n,533:633);
end
end

%normalize
Smin=NaN(a,8);Speak=NaN(a,1);
SP=NaN(a,8,101);Sp=NaN(a,8,101);
for s=1:a;
for n=1:8;
    Smin(s,n)=min(S(s,n,:));      %I
    SP(s,n,:)=S(s,n,:)./-Smin(s,n);  %I/I_slosh
end
    Speak(s,1)=min(Smin(s,:));      %Imax
    Sp(s,:,:)=S(s,:,:)./-Speak(s,1);  %All/Imax
end

Sp_mean=mean(Sp,1); Sp_sem=std(Sp)/sqrt(size(Sp,1));
SP_mean=mean(SP,1); SP_sem=std(SP)/sqrt(size(SP,1));
```

```
[butter_b butter_a]=butter(2,10/100,'low');     %filtering at 10Hz
                                    %10/100=0.1 ratio to the Nyquist

Vu=(-60:2.4:60);Vd=(57.6:-2.4:-60);
V=[Vu Vd];
Vd=(60:-2.4:-60);


%determine Reversal Potential for traces filtered at 10Hz
Su=NaN(a,8,51);Sd=NaN(a,8,51);Ts=NaN(a,8,51);
YSu=NaN(a,8,51);YSd=NaN(a,8,51);
RevSu=NaN(a,8);RevSd=NaN(a,8);RevS=NaN(a,8);
RI_S=NaN(a,8);
for n=1:8;
    for z=1:a;
    Su(z,n,:)=Sp(z,n,1:51);Sd(z,n,:)=Sp(z,n,51:101);
    YSu(z,n,:)=filtfilt(butter_b,butter_a,squeeze(Su(z,n,:)));
    YSd(z,n,:)=filtfilt(butter_b,butter_a,squeeze(Sd(z,n,:)));
    RevSu(z,n)=interp1(squeeze(YSu(z,n,:)),Vu,0);
    RevSd(z,n)=interp1(squeeze(YSd(z,n,:)),Vd,0);
    RevS(z,n)=(RevSu(z,n)+RevSd(z,n))/2;
if ((((YSu(z,n,1)+YSd(z,n,51))/2)<0)&&(YSu(z,n,51)>0));
    RI_S(z,n)=abs((YSu(z,n,1)+YSd(z,n,51))/2)/YSu(z,n,51);
end
    end
end

%average UP/DOWN
for n=1:8;
    for z=1:a;
    Su(z,n,:)=SP(z,n,1:51);Sd(z,n,:)=SP(z,n,51:101);
    T=squeeze(Sd(z,n,:)); Tq=fliplr(T'); Ts(z,n,:)=Tq';
    end
end
SA=(Su+Ts)/2;
SA_mean=squeeze(mean(SA,1));

%plot IV relationships
for n=1:8;
      figure;plot(Vu,SA_mean(n,:),'ko','LineWidth',1,'MarkerFaceColor',
      'k','MarkerSize',5);
end
```

[4] RI

```
%applied after norm_iv1

a=size(Snew,1);
S=NaN(a,8,101);
Smin=NaN(a,8);SP=NaN(a,8,101);Sp=NaN(a,8,101);
for s=1:a;
for n=1:8;
    S(s,n,:)=Snew(s,n,533:633);
    Smin(s,n)=S(s,n,1);     %I
    SP(s,n,:)=S(s,n,:)./-Smin(s,n);  %I/I_slosh
end
end

%Erev
[butter_b butter_a]=butter(2,10/100,'low');    %filtering at 10Hz
                                               %10/100=0.1 ratio to the
Nyquist
Su=NaN(a,8,51);Sd=NaN(a,8,51);Ts=NaN(a,8,51);
YS=NaN(a,8,51);RevS=NaN(a,8);
Ru=NaN(a,8);Rd=NaN(a,8);
RIu=NaN(a,8);RId=NaN(a,8);ri=NaN(a,8);

for n=1:8;
    for z=1:a;
    Su(z,n,:)=SP(z,n,1:51);Sd(z,n,:)=SP(z,n,51:101);
    T=squeeze(Sd(z,n,:)); Tq=fliplr(T'); Ts(z,n,:)=Tq';
    end
end
SA=(Su+Ts)/2;
SA_mean=mean(SA,1);
SA_sem=std(SA)/sqrt(size(SA,1));
%determine Reversal Potential for traces filtered at 10Hz

for n=1:8;
    for z=1:a;
    YS(z,n,:)=filtfilt(butter_b,butter_a,squeeze(SA(z,n,:)));
    RevS(z,n)=interp1(squeeze(YS(z,n,:)),Vu,0);
    Ru(z,n)=RevS(z,n)+30;Rd(z,n)=RevS(z,n)-30;
    RIu(z,n)=interp1(Vu,squeeze(YS(z,n,:)),Ru(z,n));
    RId(z,n)=interp1(Vu,squeeze(YS(z,n,:)),Rd(z,n));
    ri(z,n)=-RId(z,n)/RIu(z,n);
    end
end
```

```
%determine percent max
Sm=NaN(a,8);Spk=NaN(a,1);Spp=NaN(a,8);
for s=1:z;
for n=1:8;
    Sm(s,n)=min(Snew(s,n,:));     %I
end
    Spk(s,1)=min(Sm(s,:));      %Imax
    Spp(s,:)=Sm(s,:)./Spk(s,1);  %I/Imax
end


%linear fit of rectification f(x) = p1*x + p2
ec=fittype('p1*x + p2');
opts2=fitoptions(ec);
opts2.Lower=[-2 0];
opts2.Upper=[2 3];
opts2.Startpoint=[0.5 0.5];

for z=1:a;
    X=squeeze(Spp(z,:,:));Y=squeeze(ri(z,:,:));
    f=fit(X',Y',ec,opts2);
    F(z,1)=f.p1;F(z,2)=f.p2;
end
%to exclude NaN values by hand define a and b range
%X=squeeze(Spp(z,a:b,:));Y=squeeze(ri(z,a:b,:)); f=fit(X',Y',ec,opts2);
F(z,1)=f.p1;F(z,2)=f.p2;

X=squeeze(nanmean(Spp,1));Y=squeeze(nanmean(ri,1));
Xm=squeeze(nanstd(Spp,1)/sqrt(a));Ym=squeeze(nanstd(ri,1)/sqrt(a));
M=(0:0.2:1.2);m=mean(F,1);
L=m(1)*M+m(2);
figure;plot(M,L,'k');hold on;
errorbar(X,Y,Ym,'ko');herrorbar(X,Y,Xm,'ko');xlim([0 1.05]);
ylim([0 1.1]);
figure;errorbar(Vu,squeeze(SA_mean(:,8,:)),squeeze(SA_sem(:,8,:)),'ko')
;axis square; ylim([-1.5 1.5]);
figure;errorbar(Vu,squeeze(SA_mean(:,4,:)),squeeze(SA_sem(:,4,:)),'ko')
;axis square; ylim([-2 3]);

str2=input('SAVE AS:   '_RI');
save(str2);
```

[5] norm_iv2

```
%load pairwise files in format "V_S1_..., V_N1_...OR V_S11_...,
V_C11_..."

g=fittype('a*x+b');
A=dir('*.abf');
q=length(A);
Snew=NaN(q,8,2048);
D=NaN(2048,8); Dnew=NaN(8,2048);
for z=1:q
for n=1:8
    R=import_abf(A(z).name,n,0.005);
    %leak subtraction
    D(:,n)=R(:,2);
    T=R(:,1);
    ydata=[D(1:81,n); D(end-81:end,n)];
    xdata=[T(1:81,1); T(end-81:end,1)];
    nm=fit(xdata,ydata,g,'Startpoint',[1,1]);
    y=nm.a*T(:,1)+nm.b;
    Dnew(n,:)=D(:,n)-y;
    Snew(z,n,:)=Dnew(n,:);
    %subtract baseline IV
    Snew(z,n,533:633)=Snew(z,n,533:633)-Snew(z,n,1733:1833);
    Snew(z,n,1733:1833)=Snew(z,n,1733:1833)-Snew(z,n,1733:1833);
end
end

%split into normal and low [ion] traces
a=q/2;
S=NaN(a,8,101); L=NaN(a,8,101);
for n=1:8;
    L(:,n,:)=Snew(1:a,n,533:633);     %Low [ion]
    S(:,n,:)=Snew(a+1:q,n,533:633);   %Saline normal
end

%normalize each trace to Imax of corresponding normal saline trace
Smin=NaN(a,8);Speak=NaN(a,1);
SP=NaN(a,8,101);LP=NaN(a,8,101);
Sp=NaN(a,8,101);Lp=NaN(a,8,101);
for s=1:a;
for n=1:8;
    Smin(s,n)=S(s,n,1);     %I
    SP(s,n,:)=S(s,n,:)./-Smin(s,n);  %I/I_slosh
    LP(s,n,:)=L(s,n,:)./-Smin(s,n);  %I/I_slosh
end
    Speak(s,1)=min(Smin(s,:));      %Imax
    Sp(s,:,:)=S(s,:,:)./-Speak(s,1);  %All/Imax
    Lp(s,:,:)=L(s,:,:)./-Speak(s,1);  %All/Imax
end

Sp_mean=mean(Sp,1); Sp_sem=std(Sp)/sqrt(size(Sp,1));
Lp_mean=mean(Lp,1); Lp_sem=std(Lp)/sqrt(size(Lp,1));

SP_mean=mean(SP,1); SP_sem=std(SP)/sqrt(size(SP,1));
LP_mean=mean(LP,1); LP_sem=std(LP)/sqrt(size(LP,1));
```

```
%Erev
[butter_b butter_a]=butter(2,10/100,'low');    %filtering at 10Hz
                                               %10/100=0.1 ratio to the
Nyquist
Vu=(-60:2.4:60);Vd=(57.6:-2.4:-60);
V=[Vu Vd];
Vd=(60:-2.4:-60);

%determine Reversal Potential for traces filtered at 10Hz
Su=NaN(a,8,51);Sd=NaN(a,8,51);
YSu=NaN(a,8,51);YSd=NaN(a,8,51);
RevSu=NaN(a,8);RevSd=NaN(a,8);RevS=NaN(a,8);
RI_S=NaN(a,8);RI_L=NaN(a,8);
Lu=NaN(a,8,51);Ld=NaN(a,8,51);
YLu=NaN(a,8,51);YLd=NaN(a,8,51);
RevLu=NaN(a,8);RevLd=NaN(a,8);RevL=NaN(a,8);
for n=1:8;
    for z=1:a;
    Su(z,n,:)=Sp(z,n,1:51);Sd(z,n,:)=Sp(z,n,51:101);
    YSu(z,n,:)=filtfilt(butter_b,butter_a,squeeze(Su(z,n,:)));
    YSd(z,n,:)=filtfilt(butter_b,butter_a,squeeze(Sd(z,n,:)));
    RevSu(z,n)=interp1(squeeze(YSu(z,n,:)),Vu,0);
    RevSd(z,n)=interp1(squeeze(YSd(z,n,:)),Vd,0);
    RevS(z,n)=(RevSu(z,n)+RevSd(z,n))/2;
if ((((YSu(z,n,1)+YSd(z,n,51))/2)<0)&&(YSu(z,n,51)>0));
    RI_S(z,n)=abs((YSu(z,n,1)+YSd(z,n,51))/2)/YSu(z,n,51);
end
    end
end
Vu=(-30:2.4:90);Vd=(87.6:-2.4:-30);
V=[Vu Vd];
Vd=(90:-2.4:-30);
for n=1:8;
    for z=1:a;
    Lu(z,n,:)=Lp(z,n,1:51);Ld(z,n,:)=Lp(z,n,51:101);
    YLu(z,n,:)=filtfilt(butter_b,butter_a,squeeze(Lu(z,n,:)));
    YLd(z,n,:)=filtfilt(butter_b,butter_a,squeeze(Ld(z,n,:)));
    RevLu(z,n)=interp1(squeeze(YLu(z,n,:)),Vu,0);
    RevLd(z,n)=interp1(squeeze(YLd(z,n,:)),Vd,0);
    RevL(z,n)=(RevLu(z,n)+RevLd(z,n))/2;
if ((((YLu(z,n,1)+YLd(z,n,51))/2)<0)&&(YLu(z,n,51)>0));
    RI_L(z,n)=abs((YLu(z,n,1)+YLd(z,n,51))/2)/YLu(z,n,51);
end
    end
end
Erev=RevL-RevS;


str2=input('SAVE AS:   '_N' or '_C');
save(str2);
```

[6] Statistics

```
%for all tests ('alpha',0.05)

%Students t-test
%define input
```

```
x=1;y=1;
%input data for comparison

%paired t-test
[h]=ttest(x,y);

%independent t-test
[h]=ttest2(x,y);

%output
h=1 reject the null hypothesis; groups are significantly different
h=0 failure to reject the null hypothesis



%analysis of variance
%define input
x=1;groups=1;

%input data for comparison
% x is numerical data
% groups is numerical or character descriptor of data
[p,table,stats]=anova1(x,groups);

%post hoc comparison with 'tukey-kramer'
[c,m] = multcompare(stats);

%post hoc comparison with 'dunnett'
[c,m] = dunnett(stats);
```

[7] Sequence Alignment

```
%get sequences from NCBI database
%GABA_AR αβγδεθπ
A1=getgenpept('NP_000797');  A2=getgenpept('NP_000798');
A3=getgenpept('NP_000799');  A4=getgenpept('NP_000800');
A5=getgenpept('NP_000801');  A6=getgenpept('NP_000802');

B1=getgenpept('NP_000803');
B2s=getgenpept('NP_000804'); B2L=getgenpept('NP_068711');
B3=getgenpept('NP_000805');

G1=getgenpept('NP_775807');
G2s=getgenpept('NP_000807'); G2L=getgenpept('NP_944494');
G3=getgenpept('NP_150092');

D=getgenpept('NP_000806');   E=getgenpept('NP_004952');
Q=getgenpept('NP_061028');   P=getgenpept('NP_055026');

%define and align sequences with 'BLOSUM80' to 'BLOSUM30' scoring
seq={A1.Sequence,A2.Sequence,A3.Sequence,A4.Sequence,A5.Sequence,A6.Seq
uence,B1.Sequence,B2s.Sequence,B2L.Sequence,B3.Sequence,G1.Sequence,G2s
.Sequence,G2L.Sequence,G3.Sequence};
ma=multialign(seq); multialignviewer(ma);

seq={A1.Sequence,A2.Sequence,A3.Sequence,A4.Sequence,A5.Sequence,A6.Seq
uence,B1.Sequence,B2s.Sequence,B2L.Sequence,B3.Sequence,G1.Sequence,G2s
.Sequence,G2L.Sequence,G3.Sequence,D.Sequence,Q.Sequence,E.Sequence,P.S
equence};
ma=multialign(seq); multialignviewer(ma);

%view phylogenetic tree of alignment
Display → View Tree → All… or Selected…

%get sequences from NCBI database
%GABA_AR α1 vs nAChR αβδγ
A1=getgenpept('NP_000797');
A=getgenpept('AAA96705'); B=getgenpept('AAA49274');
D=getgenpept('AAA49275'); G=getgenpept('AAA49276');

%define and align sequences with 'BLOSUM80' to 'BLOSUM30' scoring
seq={A1.Sequence, A.Sequence, B.Sequence, D.Sequence, G.Sequence};
ma=multialign(seq); multialignviewer(ma);

%pairwise alignment with Needleman-Wunsch global alignment
%to determine percent identity and similarity between two sequences
[s a]=nwalign(A1.Sequence,A.Sequence);showalignment(a);
[s a]=nwalign(A1.Sequence,B.Sequence);showalignment(a);
[s a]=nwalign(A1.Sequence,D.Sequence);showalignment(a);
[s a]=nwalign(A1.Sequence,G.Sequence);showalignment(a);
```

Appendix E: QuB Protocol

I. Determine single channel current amplitudes

Idl Idealize data with the segmental k-means (SKM) method to fit to a C-O model
Set each state of the model with the Grab function (right click and highlight ideal segments)

Histogram Create a histogram of SKM results and export to MicroSoft Excel

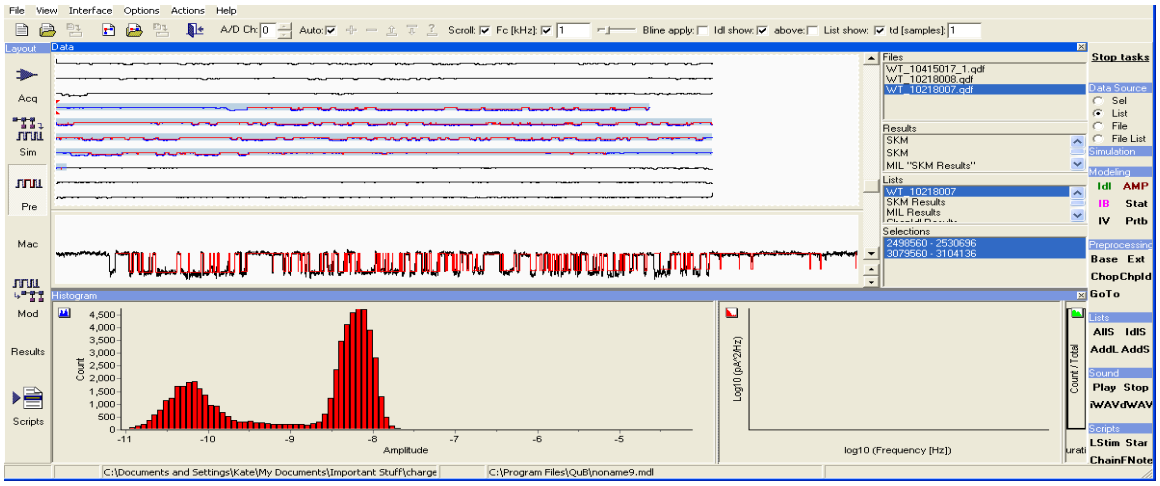

Matlab Subtract baseline for each patch and re-bin by 0.1 pA
Fit data to Gaussian curve (*Gauss2*) with curve fitting tool (*cftool*) guided user interface

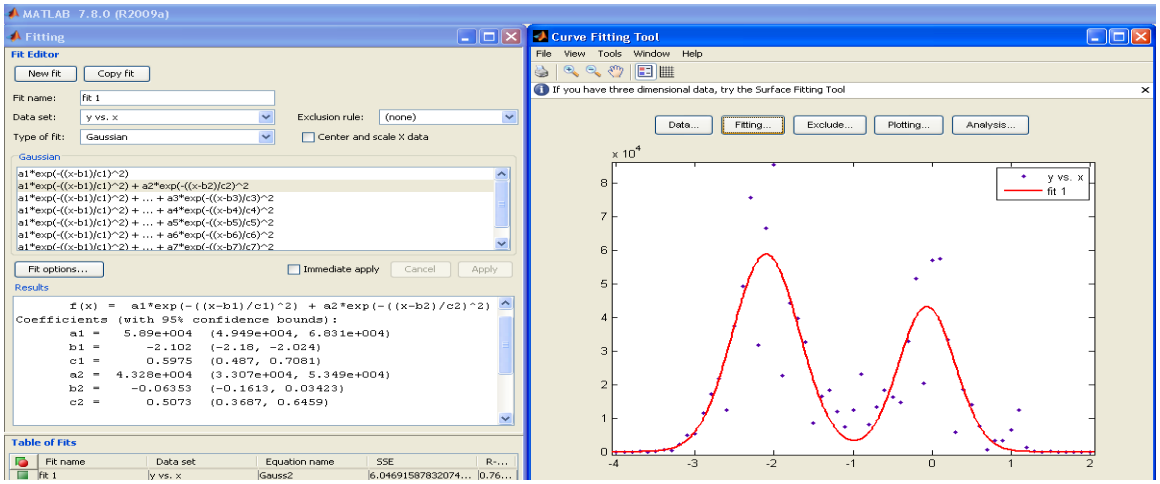

II. **Determine open probability (P_O) of bursts**

Idl Idealize data with the segmental k-means (SKM) method to fit to a C-O-C model
Set each state of the model with the Grab function (right click and highlight ideal segments)

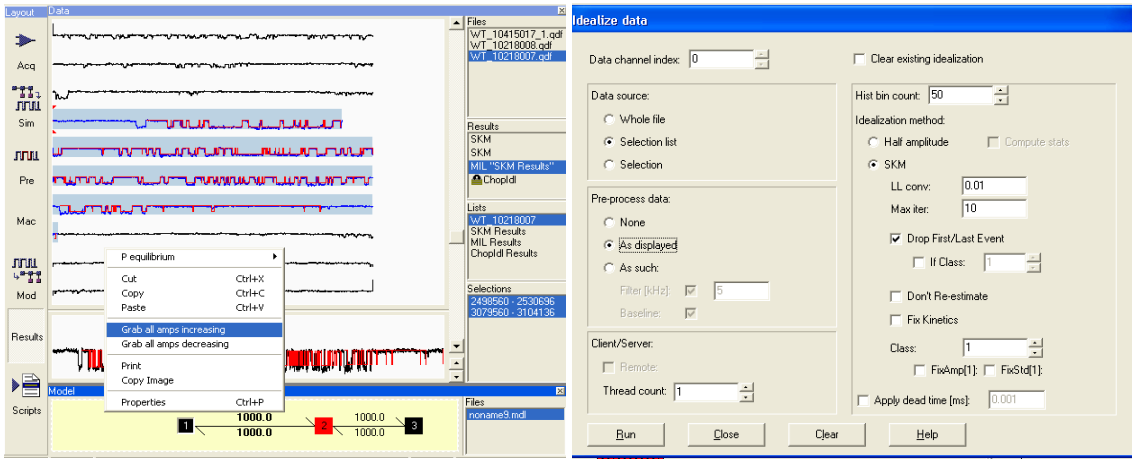

MIL Use Maximum Interval Likelihood algorithm to determine the critical time (T_{crit}) that defines a burst of openings

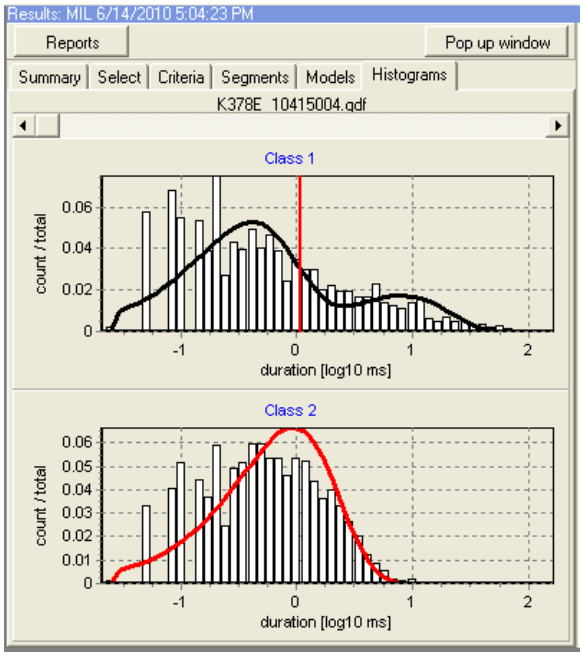

ChpId Chop Idealized data into bursts using T_{crit} to calculate P_O from output statistics (Stats)

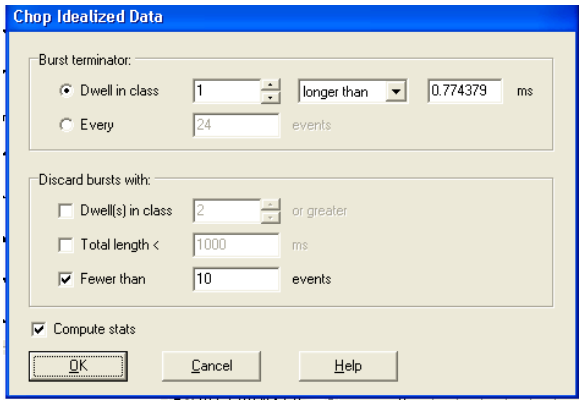

References

Adusei, D. C., L. K. Pacey, et al. (2010). "Early developmental alterations in GABAergic protein expression in fragile X knockout mice." Neuropharmacology **59**(3): 167-171.

Akk, G., D. F. Covey, et al. (2010). "Kinetic and Structural Determinants for GABA-A Receptor Potentiation by Neuroactive Steroids." Curr Neuropharmacol **8**(1): 18-25.

Akk, G. and J. H. Steinbach (2000). "Structural elements near the C-terminus are responsible for changes in nicotinic receptor gating kinetics following patch excision." J Physiol **527 Pt 3**: 405-417.

Amin, J. and D. S. Weiss (1993). "GABAA receptor needs two homologous domains of the beta-subunit for activation by GABA but not by pentobarbital." Nature **366**(6455): 565-569.

Andriotis, A. N., M. Menon, et al. (2001). "Rectification properties of carbon nanotube "Y-junctions"." Phys Rev Lett **87**(6): 066802.

Angelotti, T. P. and R. L. Macdonald (1993). "Assembly of GABAA receptor subunits: alpha 1 beta 1 and alpha 1 beta 1 gamma 2S subunits produce unique ion channels with dissimilar single-channel properties." J Neurosci **13**(4): 1429-1440.

Arnold, K., L. Bordoli, et al. (2006). "The SWISS-MODEL workspace: a web-based environment for protein structure homology modelling." Bioinformatics **22**(2): 195-201.

Backus, K. H., M. Arigoni, et al. (1993). "Stoichiometry of a recombinant GABAA receptor deduced from mutation-induced rectification." Neuroreport **5**(3): 285-288.

Baker, D. and A. Sali (2001). "Protein structure prediction and structural genomics." Science **294**(5540): 93-96.

Barker, J. L. and N. L. Harrison (1988). "Outward rectification of inhibitory postsynaptic currents in cultured rat hippocampal neurones." J Physiol **403**: 41-55.

Baulac, S., G. Huberfeld, et al. (2001). "First genetic evidence of GABA(A) receptor dysfunction in epilepsy: a mutation in the gamma2-subunit gene." Nat Genet **28**(1): 46-48.

Bennetts, B., G. Y. Rychkov, et al. (2005). "Cytoplasmic ATP-sensing domains regulate gating of skeletal muscle ClC-1 chloride channels." J Biol Chem **280**(37): 32452-32458.

Bertaccini, E. and J. R. Trudell (2002). "Predicting the transmembrane secondary structure of ligand-gated ion channels." Protein Eng **15**(6): 443-454.

Bocquet, N., H. Nury, et al. (2009). "X-ray structure of a pentameric ligand-gated ion channel in an apparently open conformation." Nature **457**(7225): 111-114.

Bocquet, N., L. Prado de Carvalho, et al. (2007). "A prokaryotic proton-gated ion channel from the nicotinic acetylcholine receptor family." Nature **445**(7123): 116-119.

Boileau, A. J., A. R. Evers, et al. (1999). "Mapping the agonist binding site of the GABAA receptor: evidence for a beta-strand." J Neurosci **19**(12): 4847-4854.

Boileau, A. J., T. Li, et al. (2003). "Effects of gamma2S subunit incorporation on GABAA receptor macroscopic kinetics." Neuropharmacology **44**(8): 1003-1012.

Boileau, A. J., J. G. Newell, et al. (2002). "GABA(A) receptor beta 2 Tyr97 and Leu99 line the GABA-binding site. Insights into mechanisms of agonist and antagonist actions." J Biol Chem **277**(4): 2931-2937.

Bordoli, L., F. Kiefer, et al. (2009). "Protein structure homology modeling using SWISS-MODEL workspace." Nat Protoc **4**(1): 1-13.

Bormann, J. (1988). "Electrophysiology of GABAA and GABAB receptor subtypes." Trends Neurosci **11**(3): 112-116.

Bormann, J. (1988). "Patch-clamp analysis of GABA- and glycine-gated chloride channels." Adv Biochem Psychopharmacol **45**: 47-60.

Bormann, J., O. P. Hamill, et al. (1987). "Mechanism of anion permeation through channels gated by glycine and gamma-aminobutyric acid in mouse cultured spinal neurones." J Physiol **385**: 243-286.

Brandon, N. J., F. K. Bedford, et al. (1999). "Synaptic targeting and regulation of GABA(A) receptors." Biochem Soc Trans **27**(4): 527-530.

Brandon, N. J., P. Delmas, et al. (2000). "GABAA receptor phosphorylation and functional modulation in cortical neurons by a protein kinase C-dependent pathway." J Biol Chem **275**(49): 38856-38862.

Brejc, K., W. J. van Dijk, et al. (2001). "Crystal structure of an ACh-binding protein reveals the ligand-binding domain of nicotinic receptors." Nature **411**(6835): 269-276.

Brown, A. M., A. G. Hope, et al. (1998). "Ion permeation and conduction in a human recombinant 5-HT3 receptor subunit (h5-HT3A)." J Physiol **507 (Pt 3)**: 653-665.

Carland, J. E., M. A. Cooper, et al. (2009). "Characterization of the effects of charged residues in the intracellular loop on ion permeation in alpha1 glycine receptor channels." J Biol Chem **284**(4): 2023-2030.

Chen, C. and H. Okayama (1987). "High-efficiency transformation of mammalian cells by plasmid DNA." Mol Cell Biol **7**(8): 2745-2752.

Chen, Z. W. and R. W. Olsen (2007). "GABAA receptor associated proteins: a key factor regulating GABAA receptor function." J Neurochem **100**(2): 279-294.

Chisari, M., H. J. Shu, et al. (2010). "Structurally diverse amphiphiles exhibit biphasic modulation of GABAA receptors: similarities and differences with neurosteroid actions." Br J Pharmacol **160**(1): 130-141.

Chothia, C. and A. M. Lesk (1986). "The relation between the divergence of sequence and structure in proteins." Embo J **5**(4): 823-826.

Chou, P. Y. and G. D. Fasman (1978). "Prediction of the secondary structure of proteins from their amino acid sequence." Adv. Enzym. **47**: 45-148.

Chou, P. Y. and G. D. Fasman (1978). "Prediction of the secondary structure of proteins from their amino acid sequence." Adv Enzymol Relat Areas Mol Biol **47**: 45-148.

Cole, C., J. D. Barber, et al. (2008). "The Jpred 3 secondary structure prediction server." Nucleic Acids Res **36**(Web Server issue): W197-201.

Colquhoun, D. (1998). "Binding, gating, affinity and efficacy: the interpretation of structure-activity relationships for agonists and of the effects of mutating receptors." Br J Pharmacol **125**(5): 924-947.

Connolly, C. N. (2008). "Trafficking of 5-HT(3) and GABA(A) receptors (Review)." Mol Membr Biol **25**(4): 293-301.

Connolly, C. N., J. T. Kittler, et al. (1999). "Cell surface stability of gamma-aminobutyric acid type A receptors. Dependence on protein kinase C activity and subunit composition." J Biol Chem **274**(51): 36565-36572.

Corringer, P. J., M. Baaden, et al. (2010). "Atomic structure and dynamics of pentameric ligand-gated ion channels: new insight from bacterial homologues." J Physiol **588**(Pt 4): 565-572.

Croarkin, P. E., A. J. Levinson, et al. (2011). "Evidence for GABAergic inhibitory deficits in major depressive disorder." Neurosci Biobehav Rev **35**(3): 818-825.

Cromer, B. A., C. J. Morton, et al. (2002). "Anxiety over GABA(A) receptor structure relieved by AChBP." Trends Biochem Sci **27**(6): 280-287.

Dalton, J. A. and R. M. Jackson (2007). "An evaluation of automated homology modelling methods at low target template sequence similarity." Bioinformatics **23**(15): 1901-1908.

Daskalakis, Z. J., P. B. Fitzgerald, et al. (2007). "The role of cortical inhibition in the pathophysiology and treatment of schizophrenia." Brain Res Rev **56**(2): 427-442.

Davies, P. A., E. B. Hoffmann, et al. (2000). "The influence of an endogenous beta3 subunit on recombinant GABA(A) receptor assembly and pharmacology in WSS-1 cells and transiently transfected HEK293 cells." Neuropharmacology **39**(4): 611-620.

Davies, P. A., M. Pistis, et al. (1999). "The 5-HT3B subunit is a major determinant of serotonin-receptor function." Nature **397**(6717): 359-363.

Deeb, T. Z., J. E. Carland, et al. (2007). "Dynamic modification of a mutant cytoplasmic cysteine residue modulates the conductance of the human 5-HT3A receptor." J Biol Chem **282**(9): 6172-6182.

Delorenzi, M. and T. Speed (2002). "An HMM model for coiled-coil domains and a comparison with PSSM-based predictions." Bioinformatics **18**(4): 617-625.

DeLorey, T. M., A. Handforth, et al. (1998). "Mice lacking the beta3 subunit of the GABAA receptor have the epilepsy phenotype and many of the behavioral characteristics of Angelman syndrome." J Neurosci **18**(20): 8505-8514.

Ding, L., H. J. Feng, et al. (2010). "GABA(A) receptor alpha1 subunit mutation A322D associated with autosomal dominant juvenile myoclonic epilepsy reduces the expression and alters the composition of wild type GABA(A) receptors." J Biol Chem **285**(34): 26390-26405.

Duret, G., C. Van Renterghem, et al. (2011). "Functional prokaryotic-eukaryotic chimera from the pentameric ligand-gated ion channel family." Proc Natl Acad Sci U S A **108**(29): 12143-12148.

Essrich, C., M. Lorez, et al. (1998). "Postsynaptic clustering of major GABAA receptor subtypes requires the gamma 2 subunit and gephyrin." Nat Neurosci **1**(7): 563-571.

Farrant, M. and Z. Nusser (2005). "Variations on an inhibitory theme: phasic and tonic activation of GABA(A) receptors." Nat Rev Neurosci **6**(3): 215-229.

Fatima-Shad, K. and P. H. Barry (1993). "Anion permeation in GABA- and glycine-gated channels of mammalian cultured hippocampal neurons." Proc Biol Sci **253**(1336): 69-75.

Finer-Moore, J. and R. M. Stroud (1984). "Amphipathic analysis and possible formation of the ion channel in an acetylcholine receptor." Proc Natl Acad Sci U S A **81**(1): 155-159.

Fisher, J. L. (2004). "The alpha 1 and alpha 6 subunit subtypes of the mammalian GABA(A) receptor confer distinct channel gating kinetics." J Physiol **561**(Pt 2): 433-448.

Fisher, R. S., W. van Emde Boas, et al. (2005). "Epileptic seizures and epilepsy: definitions proposed by the International League Against Epilepsy (ILAE) and the International Bureau for Epilepsy (IBE)." Epilepsia **46**(4): 470-472.

Franks, N. P. (2008). "General anaesthesia: from molecular targets to neuronal pathways of sleep and arousal." Nat Rev Neurosci **9**(5): 370-386.

Franks, N. P. and W. R. Lieb (1994). "Molecular and cellular mechanisms of general anaesthesia." Nature **367**(6464): 607-614.

Fritschy, J. M. and H. Mohler (1995). "GABAA-receptor heterogeneity in the adult rat brain: differential regional and cellular distribution of seven major subunits." J Comp Neurol **359**(1): 154-194.

Fuchs, K., J. Zezula, et al. (1995). "Endogenous [3H]flunitrazepam binding in human embryonic kidney cell line 293." Eur J Pharmacol **289**(1): 87-95.

Gage, P. W. and S. H. Chung (1994). "Influence of membrane potential on conductance sublevels of chloride channels activated by GABA." Proc Biol Sci **255**(1343): 167-172.

Gallagher, M. J., L. Ding, et al. (2007). "The GABAA receptor alpha1 subunit epilepsy mutation A322D inhibits transmembrane helix formation and causes proteasomal degradation." Proc Natl Acad Sci U S A **104**(32): 12999-13004.

Galvan, A., M. Kuwajima, et al. (2006). "Glutamate and GABA receptors and transporters in the basal ganglia: what does their subsynaptic localization reveal about their function?" Neuroscience **143**(2): 351-375.

Gasteiger, E., C. Hoogland, et al. (2005). Protein Identification and Analysis Tools on the ExPASy Server. New York, Humana Press.

Glausier, J. R. and D. A. Lewis (2011). "Selective Pyramidal Cell Reduction of GABA(A) Receptor alpha1 Subunit Messenger RNA Expression in Schizophrenia." Neuropsychopharmacology.

Goldman, D. E. (1943). "Potential, Impedance, and Rectification in Membranes." J Gen Physiol **27**(1): 37-60.

Gonnet, G. H., M. A. Cohen, et al. (1992). "Exhaustive matching of the entire protein sequence database." Science **256**(5062): 1443-1445.

Gonzalez-Burgos, G., T. Hashimoto, et al. (2011). "Alterations of cortical GABA neurons and network oscillations in schizophrenia." Curr Psychiatry Rep **12**(4): 335-344.

Gordon, F. J. (1997). Analysis of Variance: Designs, computations, and multiple comparisons. Atlanta Emory University**:** 41.

Goyal, R., A. A. Salahudeen, et al. (2011). "Engineering a prokaryotic Cys-loop receptor with a third functional domain." J Biol Chem.

Graham, F. L., J. Smiley, et al. (1977). "Characteristics of a human cell line transformed by DNA from human adenovirus type 5." J Gen Virol **36**(1): 59-74.

Hague, C., M. A. Uberti, et al. (2004). "Cell surface expression of alpha1D-adrenergic receptors is controlled by heterodimerization with alpha1B-adrenergic receptors." J Biol Chem **279**(15): 15541-15549.

Hales, T. G., J. I. Dunlop, et al. (2006). "Common determinants of single channel conductance within the large cytoplasmic loop of 5-hydroxytryptamine type 3 and alpha4beta2 nicotinic acetylcholine receptors." J Biol Chem **281**(12): 8062-8071.

Hampson, D. R., D. C. Adusei, et al. (2011). "The neurochemical basis for the treatment of autism spectrum disorders and Fragile X Syndrome." Biochem Pharmacol **81**(9): 1078-1086.

Hansen, S. B., H. L. Wang, et al. (2008). "An ion selectivity filter in the extracellular domain of Cys-loop receptors reveals determinants for ion conductance." J Biol Chem **283**(52): 36066-36070.

Hardison, R. (1998). "Hemoglobins from bacteria to man: evolution of different patterns of gene expression." J Exp Biol **201**(Pt 8): 1099-1117.

Harkin, L. A., D. N. Bowser, et al. (2002). "Truncation of the GABA(A)-receptor gamma2 subunit in a family with generalized epilepsy with febrile seizures plus." Am J Hum Genet **70**(2): 530-536.

Henikoff, S. and J. G. Henikoff (1992). "Amino acid substitution matrices from protein blocks." Proc Natl Acad Sci U S A **89**(22): 10915-10919.

Hilf, R. J. and R. Dutzler (2008). "X-ray structure of a prokaryotic pentameric ligand-gated ion channel." Nature **452**(7185): 375-379.

Hilf, R. J. and R. Dutzler (2009). "Structure of a potentially open state of a proton-activated pentameric ligand-gated ion channel." Nature **457**(7225): 115-118.

Hille, B. (2001). Ion Channels of Excitable Membranes. Sunderland, MA, Sinauer Associates, Inc.

Hodgkin, A. L. and B. Katz (1949). "The effect of sodium ions on the electrical activity of giant axon of the squid." J Physiol **108**(1): 37-77.

Hoffman, W. E., I. V. Balyasnikova, et al. (2002). "GABA alpha6 receptors mediate midazolam-induced anxiolysis." J Clin Anesth **14**(3): 206-209.

Howard, R. J., S. Murail, et al. (2011). "Structural basis for alcohol modulation of a pentameric ligand-gated ion channel." Proc Natl Acad Sci U S A **108**(29): 12149-12154.

Imoto, K., C. Busch, et al. (1988). "Rings of negatively charged amino acids determine the acetylcholine receptor channel conductance." Nature **335**(6191): 645-648.

Iwata, N., D. S. Cowley, et al. (1999). "Relationship between a GABAA alpha 6 Pro385Ser substitution and benzodiazepine sensitivity." Am J Psychiatry **156**(9): 1447-1449.

Jansen, M., M. Bali, et al. (2008). "Modular design of Cys-loop ligand-gated ion channels: functional 5-HT3 and GABA rho1 receptors lacking the large cytoplasmic M3M4 loop." J Gen Physiol **131**(2): 137-146.

Jensen, M. L., L. N. Pedersen, et al. (2005). "Mutational studies using a cation-conducting GABAA receptor reveal the selectivity determinants of the Cys-loop family of ligand-gated ion channels." J Neurochem **92**(4): 962-972.

Jensen, M. L., A. Schousboe, et al. (2005). "Charge selectivity of the Cys-loop family of ligand-gated ion channels." J Neurochem **92**(2): 217-225.

Jensen, M. L., D. B. Timmermann, et al. (2002). "The beta subunit determines the ion selectivity of the GABAA receptor." J Biol Chem **277**(44): 41438-41447.

Jensen, M. O., D. W. Borhani, et al. (2010). "Principles of conduction and hydrophobic gating in K+ channels." Proc Natl Acad Sci U S A **107**(13): 5833-5838.

Jones, M. V. and G. L. Westbrook (1995). "Desensitized states prolong GABAA channel responses to brief agonist pulses." Neuron **15**(1): 181-191.

Jovanovic, J. N. (2006). "Phosphorylation Site-Specific Antibodies as Research Tools in Studies of Native GABAA Receptors."

Jovanovic, J. N., P. Thomas, et al. (2004). "Brain-derived neurotrophic factor modulates fast synaptic inhibition by regulating GABA(A) receptor phosphorylation, activity, and cell-surface stability." J Neurosci **24**(2): 522-530.

Kakar, S., F. G. Hoffman, et al. (2010). "Structure and reactivity of hexacoordinate hemoglobins." Biophys Chem **152**(1-3): 1-14.

Kang, J. Q., W. Shen, et al. (2009). "The GABRG2 mutation, Q351X, associated with generalized epilepsy with febrile seizures plus, has both loss of function and dominant-negative suppression." J Neurosci **29**(9): 2845-2856.

Karlin, A., M. H. Akabas, et al. (1994). "Structures involved in binding, gating, and conduction in nicotinic acetylcholine receptors." Ren Physiol Biochem **17**(3-4): 184-186.

Kash, T. L., A. Jenkins, et al. (2003). "Coupling of agonist binding to channel gating in the GABA(A) receptor." Nature **421**(6920): 272-275.

Kash, T. L., J. R. Trudell, et al. (2004). "Structural elements involved in activation of the gamma-aminobutyric acid type A (GABAA) receptor." Biochem Soc Trans **32**(Pt3): 540-546.

Kelley, S. P., J. I. Dunlop, et al. (2003). "A cytoplasmic region determines single-channel conductance in 5-HT3 receptors." Nature **424**(6946): 321-324.

Kendrew, J. C., G. Bodo, et al. (1958). "A three-dimensional model of the myoglobin molecule obtained by x-ray analysis." Nature **181**(4610): 662-666.

Keramidas, A. and N. L. Harrison (2008). "Agonist-dependent single channel current and gating in alpha4beta2delta and alpha1beta2gamma2S GABAA receptors." J Gen Physiol **131**(2): 163-181.

Keramidas, A., T. L. Kash, et al. (2006). "The pre-M1 segment of the alpha1 subunit is a transduction element in the activation of the GABAA receptor." J Physiol **575**(Pt 1): 11-22.

Keramidas, A., A. J. Moorhouse, et al. (2002). "Cation-selective mutations in the M2 domain of the inhibitory glycine receptor channel reveal determinants of ion-charge selectivity." J Gen Physiol **119**(5): 393-410.

Keramidas, A., A. J. Moorhouse, et al. (2004). "Ligand-gated ion channels: mechanisms underlying ion selectivity." Prog Biophys Mol Biol **86**(2): 161-204.

Kiefer, F., K. Arnold, et al. (2009). "The SWISS-MODEL Repository and associated resources." Nucleic Acids Res **37**(Database issue): D387-392.

Kienker, P. K., W. F. DeGrado, et al. (1994). "A helical-dipole model describes the single-channel current rectification of an uncharged peptide ion channel." Proc Natl Acad Sci U S A **91**(11): 4859-4863.

Kneussel, M., J. H. Brandstatter, et al. (1999). "Loss of postsynaptic GABA(A) receptor clustering in gephyrin-deficient mice." J Neurosci **19**(21): 9289-9297.

Kopp, J. and T. Schwede (2004). "The SWISS-MODEL Repository of annotated three-dimensional protein structure homology models." Nucleic Acids Res **32**(Database issue): D230-234.

Kopp, J. and T. Schwede (2006). "The SWISS-MODEL Repository: new features and functionalities." Nucleic Acids Res **34**(Database issue): D315-318.

Kovarik, M. L., K. Zhou, et al. (2009). "Effect of conical nanopore diameter on ion current rectification." J Phys Chem B **113**(49): 15960-15966.

Krasowski, M. D. and N. L. Harrison (1999). "General anaesthetic actions on ligand-gated ion channels." Cell Mol Life Sci **55**(10): 1278-1303.

Krishek, B. J. and T. G. Smart (2001). "Proton sensitivity of rat cerebellar granule cell GABAA receptors: dependence on neuronal development." J Physiol **530**(Pt 2): 219-233.

Langosch, D., B. Laube, et al. (1994). "Decreased agonist affinity and chloride conductance of mutant glycine receptors associated with human hereditary hyperekplexia." Embo J **13**(18): 4223-4228.

Laurie, D. J., P. H. Seeburg, et al. (1992). "The distribution of 13 GABAA receptor subunit mRNAs in the rat brain. II. Olfactory bulb and cerebellum." J Neurosci **12**(3): 1063-1076.

Lavoie, A. M., J. J. Tingey, et al. (1997). "Activation and deactivation rates of recombinant GABA(A) receptor channels are dependent on alpha-subunit isoform." Biophys J **73**(5): 2518-2526.

Lee, D., O. Redfern, et al. (2007). "Predicting protein function from sequence and structure." Nat Rev Mol Cell Biol **8**(12): 995-1005.

Leidenheimer, N. J., M. D. Browning, et al. (1991). "GABAA receptor phosphorylation: multiple sites, actions and artifacts." Trends Pharmacol Sci **12**(3): 84-87.

Levi, S., S. M. Logan, et al. (2004). "Gephyrin is critical for glycine receptor clustering but not for the formation of functional GABAergic synapses in hippocampal neurons." J Neurosci **24**(1): 207-217.

Livesey, M. R., M. A. Cooper, et al. (2008). "Structural determinants of Ca2+ permeability and conduction in the human 5-hydroxytryptamine type 3A receptor." J Biol Chem **283**(28): 19301-19313.

Lo, W. S., C. F. Lau, et al. (2004). "Association of SNPs and haplotypes in GABAA receptor beta2 gene with schizophrenia." Mol Psychiatry **9**(6): 603-608.

Lo, W. S., Z. Xu, et al. (2007). "Positive selection within the Schizophrenia-associated GABA(A) receptor beta(2) gene." PLoS One **2**(5): e462.

Lupas, A., M. Van Dyke, et al. (1991). "Predicting coiled coils from protein sequences." Science **252**(5010): 1162-1164.

Macdonald, R. L., J. Q. Kang, et al. (2010). "Mutations in GABAA receptor subunits associated with genetic epilepsies." J Physiol **588**(Pt 11): 1861-1869.

Macdonald, R. L., C. J. Rogers, et al. (1989). "Kinetic properties of the GABAA receptor main conductance state of mouse spinal cord neurones in culture." J Physiol **410**: 479-499.

Maljevic, S., K. Krampfl, et al. (2006). "A mutation in the GABA(A) receptor alpha(1)-subunit is associated with absence epilepsy." Ann Neurol **59**(6): 983-987.

Martin, D. L. and R. W. Olsen (2000). GABA in the nervous system: The view at fifty years. Philadelphia, Lippincott Williams & Wilkins.

McKernan, R. M. and P. J. Whiting (1996). "Which GABAA-receptor subtypes really occur in the brain?" Trends Neurosci **19**(4): 139-143.

Mellor, J. R. and A. D. Randall (1998). "Voltage-dependent deactivation and desensitization of GABA responses in cultured murine cerebellar granule cells." J Physiol **506 (Pt 2)**: 377-390.

Melo, F. and E. Feytmans (1998). "Assessing protein structures with a non-local atomic interaction energy." J Mol Biol **277**(5): 1141-1152.

Mercado, J. and C. Czajkowski (2006). "Charged residues in the alpha1 and beta2 pre-M1 regions involved in GABAA receptor activation." J Neurosci **26**(7): 2031-2040.

Michels, G. and S. J. Moss (2007). "GABAA receptors: properties and trafficking." Crit Rev Biochem Mol Biol **42**(1): 3-14.

Mizokami, A., T. Kanematsu, et al. (2007). "Phospholipase C-related inactive protein is involved in trafficking of gamma2 subunit-containing GABA(A) receptors to the cell surface." J Neurosci **27**(7): 1692-1701.

Mody, I. (2001). "Distinguishing between GABA(A) receptors responsible for tonic and phasic conductances." Neurochem Res **26**(8-9): 907-913.

Mohler, H. and T. Okada (1977). "Benzodiazepine receptor: demonstration in the central nervous system." Science **198**(4319): 849-851.

Mokrab, Y., V. N. Bavro, et al. (2007). "Exploring ligand recognition and ion flow in comparative models of the human GABA type A receptor." J Mol Graph Model **26**(4): 760-774.

Moorhouse, A. J., A. Keramidas, et al. (2002). "Single channel analysis of conductance and rectification in cation-selective, mutant glycine receptor channels." J Gen Physiol **119**(5): 411-425.

Mortensen, M., B. Ebert, et al. (2010). "Distinct activities of GABA agonists at synaptic- and extrasynaptic-type GABAA receptors." J Physiol **588**(Pt 8): 1251-1268.

Mortensen, M., U. Kristiansen, et al. (2004). "Activation of single heteromeric GABA(A) receptor ion channels by full and partial agonists." J Physiol **557**(Pt 2): 389-413.

Mortensen, M. and T. G. Smart (2006). "Extrasynaptic alphabeta subunit GABAA receptors on rat hippocampal pyramidal neurons." J Physiol **577**(Pt 3): 841-856.

Mukherjee J., K. K., Maric H.-M., Harvey K., Schindelin H., Moss S. J. (2010). "Cdk5-dependent phosphorylation regulates the gephyrin-dependent clustering of α1-containing GABAARs at inhibitory synapses " **239.4**.

Nury, H., C. Van Renterghem, et al. (2011). "X-ray structures of general anaesthetics bound to a pentameric ligand-gated ion channel." Nature **469**(7330): 428-431.

Nusser, Z., W. Sieghart, et al. (1998). "Segregation of different GABAA receptors to synaptic and extrasynaptic membranes of cerebellar granule cells." J Neurosci **18**(5): 1693-1703.

Nymann-Andersen, J., G. W. Sawyer, et al. (2002). "Interaction between GABAA receptor subunit intracellular loops: implications for higher order complex formation." J Neurochem **83**(5): 1164-1171.

O'Shea, S. M. and N. L. Harrison (2000). "Arg-274 and Leu-277 of the gamma-aminobutyric acid type A receptor alpha 2 subunit define agonist efficacy and potency." J Biol Chem **275**(30): 22764-22768.

Olsen, R. W. and W. Sieghart (2008). "International Union of Pharmacology. LXX. Subtypes of gamma-aminobutyric acid(A) receptors: classification on the basis of subunit composition, pharmacology, and function. Update." Pharmacol Rev **60**(3): 243-260.

Pavlov, I., L. P. Savtchenko, et al. (2009). "Outwardly rectifying tonically active GABAA receptors in pyramidal cells modulate neuronal offset, not gain." J Neurosci **29**(48): 15341-15350.

Peran, M., B. W. Hicks, et al. (2001). "Lateral mobility and anchoring of recombinant GABAA receptors depend on subunit composition." Cell Motil Cytoskeleton **50**(2): 89-100.

Peran, M., H. Hooper, et al. (2006). "The M3/M4 cytoplasmic loop of the alpha1 subunit restricts GABAARs lateral mobility: a study using fluorescence recovery after photobleaching." Cell Motil Cytoskeleton **63**(12): 747-757.

Peters, J. A., M. A. Cooper, et al. (2010). "Novel structural determinants of single channel conductance and ion selectivity in 5-hydroxytryptamine type 3 and nicotinic acetylcholine receptors." J Physiol **588**(Pt 4): 587-596.

Picton, A. J. and J. L. Fisher (2007). "Effect of the alpha subunit subtype on the macroscopic kinetic properties of recombinant GABA(A) receptors." Brain Res **1165**: 40-49.

Pirker, S., C. Schwarzer, et al. (2000). "GABA(A) receptors: immunocytochemical distribution of 13 subunits in the adult rat brain." Neuroscience **101**(4): 815-850.

Pritchett, D. B., H. Sontheimer, et al. (1988). "Transient expression shows ligand gating and allosteric potentiation of GABAA receptor subunits." Science **242**(4883): 1306-1308.

Pritchett, D. B., H. Sontheimer, et al. (1989). "Importance of a novel GABAA receptor subunit for benzodiazepine pharmacology." Nature **338**(6216): 582-585.

Pytel, M., K. Mercik, et al. (2006). "Membrane voltage modulates the GABA(A) receptor gating in cultured rat hippocampal neurons." Neuropharmacology **50**(2): 143-153.

Qin, F. (2004). "Restoration of single-channel currents using the segmental k-means method based on hidden Markov modeling." Biophys J **86**(3): 1488-1501.

Qin, F., A. Auerbach, et al. (1996). "Estimating single-channel kinetic parameters from idealized patch-clamp data containing missed events." Biophys J **70**(1): 264-280.

Qin, F., A. Auerbach, et al. (1997). "Maximum likelihood estimation of aggregated Markov processes." Proc Biol Sci **264**(1380): 375-383.

Ratnam, M., D. L. Nguyen, et al. (1986). "Transmembrane topography of nicotinic acetylcholine receptor: immunochemical tests contradict theoretical predictions based on hydrophobicity profiles." Biochemistry **25**(9): 2633-2643.

Robinson, R. A. and R. H. Stokes (1965). Electrolyte Solutions. London, Butterworths.

Saitou, N. and M. Nei (1987). "The neighbor-joining method: a new method for reconstructing phylogenetic trees." Mol Biol Evol **4**(4): 406-425.

Schwede, T., J. Kopp, et al. (2003). "SWISS-MODEL: An automated protein homology-modeling server." Nucleic Acids Res **31**(13): 3381-3385.

Sen, S., S. Villafuerte, et al. (2004). "Serotonin transporter and GABAA alpha 6 receptor variants are associated with neuroticism." Biol Psychiatry **55**(3): 244-249.

Shaw, G., S. Morse, et al. (2002). "Preferential transformation of human neuronal cells by human adenoviruses and the origin of HEK 293 cells." Faseb J **16**(8): 869-871.

Shen, H., Q. H. Gong, et al. (2007). "Reversal of neurosteroid effects at alpha4beta2delta GABAA receptors triggers anxiety at puberty." Nat Neurosci **10**(4): 469-477.

Sherman-Gold, R., A. S. Finkel, et al. (1993). The Axon Guide for Electrophysiology and Biophysics Laboratory Techniques. Foster City, CA, Axon Instruments, Inc.

Shiang, R., S. G. Ryan, et al. (1993). "Mutations in the alpha 1 subunit of the inhibitory glycine receptor cause the dominant neurologic disorder, hyperekplexia." Nat Genet **5**(4): 351-358.

Sigel, E., R. Baur, et al. (1992). "Point mutations affecting antagonist affinity and agonist dependent gating of GABAA receptor channels." Embo J **11**(6): 2017-2023.

Sine, S. M., H. L. Wang, et al. (2010). "On the origin of ion selectivity in the Cys-loop receptor family." J Mol Neurosci **40**(1-2): 70-76.

Smart, T. G. (1997). "Regulation of excitatory and inhibitory neurotransmitter-gated ion channels by protein phosphorylation." Curr Opin Neurobiol **7**(3): 358-367.

Smith, G. B. and R. W. Olsen (1994). "Identification of a [3H]muscimol photoaffinity substrate in the bovine gamma-aminobutyric acidA receptor alpha subunit." J Biol Chem **269**(32): 20380-20387.

Smith, K. R., K. McAinsh, et al. (2008). "Regulation of inhibitory synaptic transmission by a conserved atypical interaction of GABA(A) receptor beta- and gamma-subunits with the clathrin AP2 adaptor." Neuropharmacology **55**(5): 844-850.

Smith, R. M. and W. Sadee (2011). "Synaptic signaling and aberrant RNA splicing in autism spectrum disorders." Front Synaptic Neurosci **3**: 1.

Straub, R. E., B. K. Lipska, et al. (2007). "Allelic variation in GAD1 (GAD67) is associated with schizophrenia and influences cortical function and gene expression." Mol Psychiatry **12**(9): 854-869.

Student (1908). "Probable error of a correlation coefficient." Biometrika **6**: 302-310.

Student (1908). "The probable error of a mean." Biometrika **6**: 1-25.

Studier, J. A. and K. J. Keppler (1988). "A note on the neighbor-joining algorithm of Saitou and Nei." Mol Biol Evol **5**(6): 729-731.

Sun, H., Y. Zhang, et al. (2008). "[Analysis of the GABRG2 gene mutation in a Chinese family with generalized epilepsy with febrile seizures plus]." Zhonghua Yi Xue Yi Chuan Xue Za Zhi **25**(6): 611-615.

Tallman, J. F., J. W. Thomas, et al. (1978). "GABAergic modulation of benzodiazepine binding site sensitivity." Nature **274**(5669): 383-385.

Taylor, P. M., P. Thomas, et al. (1999). "Identification of amino acid residues within GABA(A) receptor beta subunits that mediate both homomeric and heteromeric receptor expression." J Neurosci **19**(15): 6360-6371.

Teissere, J. A. and C. Czajkowski (2001). "A (beta)-strand in the (gamma)2 subunit lines the benzodiazepine binding site of the GABA A receptor: structural rearrangements detected during channel gating." J Neurosci **21**(14): 4977-4986.

Terunuma, M., J. Xu, et al. (2008). "Deficits in phosphorylation of GABA(A) receptors by intimately associated protein kinase C activity underlie compromised synaptic inhibition during status epilepticus." J Neurosci **28**(2): 376-384.

Thomas, P. and T. G. Smart (2005). "HEK293 cell line: a vehicle for the expression of recombinant proteins." J Pharmacol Toxicol Methods **51**(3): 187-200.

Tretter, V., T. C. Jacob, et al. (2008). "The clustering of GABA(A) receptor subtypes at inhibitory synapses is facilitated via the direct binding of receptor alpha 2 subunits to gephyrin." J Neurosci **28**(6): 1356-1365.

Trudell, J. R. and E. Bertaccini (2004). "Comparative modeling of a GABAA alpha1 receptor using three crystal structures as templates." J Mol Graph Model **23**(1): 39-49.

Ueno, S., C. Zorumski, et al. (1996). "Endogenous subunits can cause ambiguities in the pharmacology of exogenous gamma-aminobutyric acidA receptors expressed in human embryonic kidney 293 cells." Mol Pharmacol **50**(4): 931-938.

Unwin, N. (1993). "Nicotinic acetylcholine receptor at 9 A resolution." J Mol Biol **229**(4): 1101-1124.

Unwin, N. (1998). "The nicotinic acetylcholine receptor of the Torpedo electric ray." J Struct Biol **121**(2): 181-190.

Unwin, N. (2000). "The Croonian Lecture 2000. Nicotinic acetylcholine receptor and the structural basis of fast synaptic transmission." Philos Trans R Soc Lond B Biol Sci **355**(1404): 1813-1829.

Unwin, N. (2005). "Refined structure of the nicotinic acetylcholine receptor at 4A resolution." J Mol Biol **346**(4): 967-989.

vanGunsteren, W. F., S. R. Billeter, et al. (1996). Biomolecular Simulations: The GROMOS96 Manual and User Guide. Zurich, VdF Hochschulverlag ETHZ.

Wagner, D. A. and C. Czajkowski (2001). "Structure and dynamics of the GABA binding pocket: A narrowing cleft that constricts during activation." J Neurosci **21**(1): 67-74.

Wang, H. L., X. Cheng, et al. (2008). "Control of cation permeation through the nicotinic receptor channel." PLoS Comput Biol **4**(2): e41.

Weiss, D. S. (1988). "Membrane potential modulates the activation of GABA-gated channels." J Neurophysiol **59**(2): 514-527.

Weiss, D. S., E. M. Barnes, Jr., et al. (1988). "Whole-cell and single-channel recordings of GABA-gated currents in cultured chick cerebral neurons." J Neurophysiol **59**(2): 495-513.

Westh-Hansen, S. E., P. B. Rasmussen, et al. (1997). "Decreased agonist sensitivity of human GABA(A) receptors by an amino acid variant, isoleucine to valine, in the alpha1 subunit." Eur J Pharmacol **329**(2-3): 253-257.

Westh-Hansen, S. E., M. R. Witt, et al. (1999). "Arginine residue 120 of the human GABAA receptor alpha 1, subunit is essential for GABA binding and chloride ion current gating." Neuroreport **10**(11): 2417-2421.

Williams, D. B. and M. H. Akabas (1999). "gamma-aminobutyric acid increases the water accessibility of M3 membrane-spanning segment residues in gamma-aminobutyric acid type A receptors." Biophys J **77**(5): 2563-2574.

Wisden, W., D. J. Laurie, et al. (1992). "The distribution of 13 GABAA receptor subunit mRNAs in the rat brain. I. Telencephalon, diencephalon, mesencephalon." J Neurosci **12**(3): 1040-1062.

Wooltorton, J. R., S. J. Moss, et al. (1997). "Pharmacological and physiological characterization of murine homomeric beta3 GABA(A) receptors." Eur J Neurosci **9**(11): 2225-2235.

Xiu, X., A. P. Hanek, et al. (2005). "A unified view of the role of electrostatic interactions in modulating the gating of Cys loop receptors." J Biol Chem **280**(50): 41655-41666.

Xu, M. and M. H. Akabas (1993). "Amino acids lining the channel of the gamma-aminobutyric acid type A receptor identified by cysteine substitution." J Biol Chem **268**(29): 21505-21508.

Xu, M. and M. H. Akabas (1996). "Identification of channel-lining residues in the M2 membrane-spanning segment of the GABA(A) receptor alpha1 subunit." J Gen Physiol **107**(2): 195-205.

Xu, M., D. F. Covey, et al. (1995). "Interaction of picrotoxin with GABAA receptor channel-lining residues probed in cysteine mutants." Biophys J **69**(5): 1858-1867.

Zhao, C., Z. Xu, et al. (2006). "Two isoforms of GABA(A) receptor beta2 subunit with different electrophysiological properties: Differential expression and genotypical correlations in schizophrenia." Mol Psychiatry **11**(12): 1092-1105.

Zhao, C., Z. Xu, et al. (2009). "Alternative-splicing in the exon-10 region of GABA(A) receptor beta(2) subunit gene: relationships between novel isoforms and psychotic disorders." PLoS One **4**(9): e6977.

Zimmermann, I. and R. Dutzler (2011). "Ligand Activation of the Prokaryotic Pentameric Ligand-Gated Ion Channel ELIC." PLoS Biol **9**(6): e1001101.

Acknowledgements

"It's supposed to be hard. If it wasn't hard, everyone would do it. The hard... is what makes it great."

~A League of Their Own

I have been very lucky in my life to be surrounded by people who love me and have supported me when things got "hard". First and foremost, I would be nothing without my family and my friends who have become my family. Mom, Dad, Kim… I love you so much! Thank you for always believing in me and telling me how smart I am even when you had no idea what I was talking about. To all of my neuro-buddies… you have made these six years amazing and I can't wait to have y'all in my life for sixty more years. Thank you for all the good times, all the memories, and all the adventures ahead.

Second, I would like to acknowledge all of the teachers who have made me strive to become a life-long learner and inspired me to become an educator myself: Mr. John Finch, Caywood Elementary, Ms. Barbara Sumpter, River Ridge Intermediate, Ms. Shelly Rodenkirchen, Villa Madonna Academy, Sr. Nancy Kordenbrock O.S.B., Villa Madonna Academy, Patrick Schultheis Ph.D., Northern Kentucky University, Tom Zaniello Ph.D., Northern Kentucky University, Diana McGill Ph.D., Northern Kentucky University, Patricia Marstellar Ph.D., Emory University, and Jordan Rose M.P.H., Emory University.

Thank you to my thesis committee for all of your support over the years: Ron Calabrese Ph.D., Victor Faundez Ph.D., Andrew Jenkins Ph.D., Yoland Smith Ph.D. and Steve Traynelis Ph.D. Under your guidance I have been encouraged to think independently and have grown into a more mature scientist ready for the next phase of my career. And finally to my thesis advisor and mentor, Andy, it may be the "end" of my time in the Jenko lab, but I hope just the beginning of our friendship. I think I finally understand. Thank you for everything!